An entropy stable nodal discontinuous Galerkin method for the resistive MHD equations

vorgelegt von

Marvin Bohm

aus Bielefeld

Köln, 2018

Berichterstatter:	Prof. Dr. Gregor Gassner
	Prof. Dr. Christian Klingenberg
Tag der mündlichen Prüfung:	15. Februar 2019

Abstract

We present a discretely entropy stable discontinuous Galerkin (DG) method for the resistive magneto-hydrodynamic (MHD) equations on three-dimensional curvilinear unstructured hexahedral meshes. Compared to other fluid dynamics systems such as the shallow water equations or the compressible Navier-Stokes equations, the resistive MHD equations need special considerations because of the divergence-free constraint on the magnetic field. For instance, it is well known that for the symmetrization of the ideal MHD system as well as the continuous entropy analysis a non-conservative term proportional to the divergence of the magnetic field, typically referred to as the Powell term, must be included. As a consequence, the mimicry of the continuous entropy analysis in the discrete sense demands a suitable DG approximation of the non-conservative terms in addition to the ideal MHD terms.

We focus on the *resistive* MHD equations. Subsequently, our first result is a proof that the resistive terms are symmetric and positive-definite when formulated in entropy space as gradients of the entropy variables. This enables us to show that the entropy inequality holds for the resistive MHD equations. The continuous analysis is the key for our DG discretization and guides the path for the construction of an approximation that discretely mimics the entropy inequality, typically termed *entropy stability*. The discrete analysis relies on the summation-by-parts (SBP) property, which is satisfied by the DG spectral element method (DGSEM) with Legendre-Gauss-Lobatto (LGL) nodes. With the help of a resulting split form approximation and by incorporating specific dicretizations of the non-conservative terms, we obtain an overall entropy conservative DG scheme for the ideal MHD equations. We extend the scheme to an entropy stable approximation by adding appropriate dissipation terms. Further, we provide a detailed derivation and analysis of the entropy stable discretization on three-dimensional curvilinear meshes.

Although the divergence-free constraint is included in the non-conservative terms, the resulting method has no particular treatment to control the magnetic field divergence errors, which pollute the solution quality. Hence, we also extend the standard resistive MHD equations and the according DG approximation with a divergence cleaning mechanism that is based on a generalized Lagrange multiplier (GLM). Moreover, we equip the resulting scheme with certain shock capturing methods in order to regularize the approximation in oscillatory regions close to discontinuities.

We provide numerical examples that verify the theoretical properties of the entropy stable method. Also, we demonstrate the increased robustness of the entropy stable method with a series of challenging numerical results, before we finally apply it to a real space physics model describing atmospheric plasma interactions.

Kurzzusammenfassung

Diese Arbeit beschäftigt sich mit der Konstruktion eines Entropie-stabilen Discontinuous Galerkin (DG) Verfahrens für die resistiven magnetohydrodynamischen (MHD) Gleichungen auf dreidimensionalen, gekrümmten und unstrukturierten Gittern. Im Gegensatz zu anderen Systemen der Strömungsmechanik, wie z.B. die Flachwasser Gleichungen oder die Navier-Stokes Gleichungen, muss bei den resistiven MHD Gleichungen die Divergenz-Freiheit des Magnetfeldes zusätzlich berücksichtigt werden. Diesbezüglich werden sogenannte nicht-erhaltende Terme eingeführt, welche für die Symmetrisierung sowie die kontinuierliche Entropie-Analyse der Gleichungen eine entscheidende Rolle spielen. Folglich ist eine entsprechende Approximation dieser zusätzlichen Terme in der diskreten Herleitung des Entropie-stabilen DG Verfahrens essentiell.

Der Fokus dieser Arbeit liegt auf den *resistiven* MHD Gleichungen. Deswegen wird zunächst bewiesen, dass sich die resistiven Terme als Produkt von symmetrisch positiv-definiten Matrizen und Gradienten der Entropie-Variablen darstellen lassen. Somit lässt sich zeigen, dass die Entropie-Ungleichung für die resistiven MHD Gleichungen gilt. Mit Hilfe der kontinuierlichen Ergebnisse wird ein numerisches Verfahren hergeleitet, welches im Diskreten die Entropie-Ungleichung erfüllt und allgemein als *Entropie-stabil* bezeichnet wird. Die diskrete Entropie-Analyse beruht auf der summation-by-parts (SBP) Eigenschaft, welche beim Discontinuous Galerkin Spektrale Elemente Verfahren (DGSEM) mit Legendre-Gauß-Lobatto (LGL) Stützstellen erfüllt ist. Durch die daraus resultierende Split-Formulierung sowie entsprechende Approximationen der nicht-erhaltenden Terme ergibt sich ein Entropie-erhaltendes DG Verfahren für die idealen MHD Gleichungen. Dieses wird zu einem Entropie-stabilen Verfahren erweitert, indem letztendlich geeignete Dissipationsterme hinzugefügt werden. Insbesondere erfolgt die gesamte Herleitung der Entropie-stabilen Näherung für dreidimensionale, gekrümmte Gitterelemente.

Obgleich die Divergenz-Bedingung bereits in den nicht-erhaltenden Termen berücksichtigt wird, beinhaltet das Gesamtverfahren keinen Mechanismus zur Kontrolle von Divergenzfehlern in den Magnetfeldern. Aufgrund dessen werden die resistiven MHD Gleichungen sowie deren Diskretisierung mit einem zusätzlichen Divergenz Cleaning Algorithmus basierend auf verallgemeinerten Lagrange-Multiplikatoren (GLM) ausgestattet. Zudem werden verschiedene Shock Capturing Verfahren vorgestellt, um durch Stöße hervorgerufene Oszillationen zu dämpfen.

Des Weiteren werden numerische Tests bereit gestellt, welche die theoretischen Ausführungen verifizieren. Insbesondere wird die erhöhte Robustheit des Entropie-stabilen Verfahrens belegt, bevor dieses abschließend auf eine geophysikalische Problemstellung hinsichtlich atmosphärischer Wechselwirkungen von Plasmen angewandt wird.

Danksagung

An erster Stelle möchte ich mich bei Gregor Gassner bedanken, der mir die Möglichkeit zur Promotion gegeben hat. Nicht nur durch seine fachliche Unterstützung und exzellente Betreuung hat er mich stets begeistert, sondern vor allem auch durch seine lässige Art. Ebenso dankbar bin ich für das gemeinsame Arbeiten mit Andrew Winters, der mir sowohl im Büro als auch beim gelegentlichen Feierabendbier stets zur Seite stand. Insgesamt hatte ich in den letzten vier Jahren unheimliches Glück, dass ich Teil einer Arbeitsgruppe sein durfte, die auch privat super harmonierte und die ich mit Sicherheit vermissen werde. Dafür bedanke ich mich insbesondere auch bei Niklas und Lucas, obgleich der eine brutal schwach am Glas ist und der andere wohl immer noch unter dem Schnitzel-Oasen-Trauma leidet.

Im Laufe meiner Promotion habe ich mit vielen anderen Forschern kooperieren dürfen. Ich möchte mich daher vor allem bei Joachim Saur bedanken, der dieses Forschungsprojekt mit gefördert hat. Auch seinen Mitarbeitern gilt besonderer Dank, da Aljona Blöcker und Justus Sagemüller mich das ein oder andere Mal aus dem Sumpf der Physik gezogen haben. Zudem möchte ich mich bei Florian Hindenlang bedanken, ohne dessen Hilfestellungen hinsichtlich Implementierungsfragen und Gittergeneration diese Arbeit nicht möglich gewesen wäre.

Auf privater Ebene möchte ich mich als Erstes bei dem Menschen bedanken, der in meinem Leben am meisten für mich getan hat: Meinem Vater Thomas. Ohne dich wäre ich nicht da, wo ich heute bin. Du bist der Beste! Für ihren seelischen Beistand in den letzten Jahren gilt meiner Mutter Sabine ein großes Dankeschön. Auch bei meinem Bruder Yannick und meiner Oma Roswitha möchte ich mich herzlich für alles bedanken. Jan, Luis, Raphael und Sliman könnte ich aus vielerlei Gründen danken, aber hauptsächlich für jahrelange freundschaftliche Treue.

Abschließend möchte ich der Person danken, die in den letzten Jahren einen besonderen Platz in meinem Leben und auch meinem Herzen eingenommen hat: Juliana, du hast in meinen beruflichen und privaten Krisen trotz meines Gejammers immer zu mir gehalten. Die Erfahrungen in unserer gemeinsamen Zeit - ob gut oder schlecht - haben mich dir so nahe gebracht wie ich keinem anderen Menschen je zuvor war. Ich kann dir nicht genug danken für die wunderschönen Momente und ich freue mich auf alle weiteren gemeinsamen Jahre mit dir. Ich liebe dich!

Contents

Contents

Nomenclature

In this work one-dimensional continuous functions and scalars are denoted by small letters, e.g. t, ϱ, whereas vectors in three-dimensional space are provided with a superscript arrow, e.g. $\vec{x}, \vec{v}$. Continuous state vectors, which consist of several system variables, are given by bold letters, e.g. $\mathbf{u}, \mathbf{r}$, and their discrete approximations are represented by capital bold letters, e.g. $\mathbf{U}, \mathbf{R}$.

Throughout this work we consider three-dimensional problems, so that especially in the discrete sections the equations and proofs become quite complex. Hence, for compact notation and in order to simplify the discussion and analysis of the equations, we define block vectors with the double arrow as

$$\overset{\leftrightarrow}{\mathbf{f}} = \begin{bmatrix} \mathbf{f}_1 \\ \mathbf{f}_2 \\ \mathbf{f}_3 \end{bmatrix} \tag{1}$$

and the spatial gradient of a state vector describing the set of considered variables as

$$\vec{\nabla}\mathbf{u} = \begin{bmatrix} \mathbf{u}_x \\ \mathbf{u}_y \\ \mathbf{u}_z \end{bmatrix}. \tag{2}$$

Moreover, the gradient of a spatial vector is a second order tensor, written in matrix form as

$$\vec{\nabla}\vec{v} = \begin{bmatrix} \frac{\partial v_1}{\partial x} & \frac{\partial v_1}{\partial y} & \frac{\partial v_1}{\partial z} \\ \frac{\partial v_2}{\partial x} & \frac{\partial v_2}{\partial y} & \frac{\partial v_2}{\partial z} \\ \frac{\partial v_3}{\partial x} & \frac{\partial v_2}{\partial y} & \frac{\partial v_3}{\partial z} \end{bmatrix}, \tag{3}$$

which is the Jacobian of $\vec{v}$ and will be needed later in order to define second derivatives.

The dot product of two block vectors is a scalar defined by

$$\overset{\leftrightarrow}{\mathbf{f}} \cdot \overset{\leftrightarrow}{\mathbf{g}} = \sum_{i=1}^{3} \mathbf{f}_i{}^T \mathbf{g}_i, \tag{4}$$

and the dot product of a block vector with a spatial vector is a state vector

$$\vec{g} \cdot \overset{\leftrightarrow}{\mathbf{f}} = \sum_{i=1}^{3} g_i \mathbf{f}_i. \tag{5}$$

Finally, these definitions also allow a compact notation for the divergence of a flux written as a block vector, i.e.

$$\vec{\nabla} \cdot \overset{\leftrightarrow}{\mathbf{f}} = (\mathbf{f}_1)_x + (\mathbf{f}_2)_y + (\mathbf{f}_3)_z = \sum_{i=1}^{3} \frac{\partial \mathbf{f}_i}{\partial x_i}. \tag{6}$$

Further, we denote contra-variant space and block vectors by the tilde notation, e.g. $\vec{\tilde{v}}, \overset{\leftrightarrow}{\tilde{\mathbf{f}}}$, and define different underline and typeset notations for matrices, i.e. $\underline{B}$ is a 3×3 matrix, B denotes a 9×9 matrix, $\underline{\mathsf{B}}$ a 27×27 block matrix and $\mathcal{B}$ a $(N{+}1) \times (N{+}1)$ matrix. The most important notational conventions of this work are summarized in the following table:

Notational conventions

t	Scalar quantity
$\mathfrak{A}$	Subset of three dimensional space
$\vec{v}$	Vector in three dimensional space
$\vec{\tilde{v}}$	Contra-variant space vector
$\mathbf{u}$	Continuous state vector
$\mathbf{U}$	Polynomial approximation of state vector
$\overset{\leftrightarrow}{\mathbf{f}}$	Block vector
$\overset{\leftrightarrow}{\tilde{\mathbf{f}}}$	Contra-variant block vector
$\overset{\leftrightarrow}{\mathbf{F}}$	Polynomial approximation of block vector
$\underline{B}$	3×3 matrix
B	9×9 matrix
$\underline{\mathsf{B}}$	27×27 block matrix
$\mathcal{B}$	$(N{+}1) \times (N{+}1)$ matrix

For completeness and survey, we also provide tables with alphanumeric symbols and abbreviations used in this work. We note, that only the most significant symbols are listed below. Some symbols are even defined multiple times, but only locally and their meaning should be clear in the given contexts.

Alphanumeric Symbols

$\vec{a}_i, \vec{a}^{\,i}$	Co-variant and contra-variant basis vectors
A	Flux Jacobians
$\mathfrak{A}$	Atmosphere
$\vec{B}$	Magnetic field vector
$\mathcal{B}$	Discrete boundary matrix
c	Speed of sound
c^A	Alfvén wave speed
c^f	Fast magneto-acoustic wave speed
c_h	GLM divergence cleaning speed
c^s	Slow magneto-acoustic wave speed
CFL	CFL number for advective time step
d	Dilatation factor of ionosphere
$\mathcal{D}$	Discrete derivative matrix
$\hat{\mathcal{D}}$	Modified derivative matrix for quasi-weak form
$\mathbb{D}$	Derivative projection operators
DFL	CFL number for diffusive time step
e	Specific inner energy
E	Total energy
$\mathfrak{E}$	Reference element
$\vec{E}$	Electric field vector
$\vec{f}^{\,S}$	Entropy flux
$\overset{\leftrightarrow}{\mathbf{f}}{}^{a}$	Block vector of advective fluxes
$\overset{\leftrightarrow}{\mathbf{f}}{}^{v}$	Block vector of viscous fluxes
$\overset{\leftrightarrow}{\mathbf{f}}{}^{v,\nu}$	Block vector of viscous fluxes with artificial viscosity
$\overset{\leftrightarrow}{\mathbf{f}}{}^{\mathrm{EC}}$	Entropy conservative fluxes
$\overset{\leftrightarrow}{\mathbf{f}}{}^{\mathrm{ES}}$	Entropy stable fluxes
$\bar{\mathbf{F}}$	Flux interpolation on staggered grid
$\mathbf{F}^{\#}$	Two-point volume flux
h	Minimum element size
$\underline{I}$	Identity matrix
$\mathfrak{I}$	Ionosphere
$\mathbb{I}^N$	Polynomial interpolation operator of degree N
J	Jacobian of element mapping
$\vec{J}$	Current density vector
G	Entropy contributions of element surfaces
H	Entropy Jacobian
$\hat{\mathsf{H}}$	Interface approximation of entropy Jacobian

$\underline{\mathsf{K}}$	Block dissipation matrix for entropy variables
l	Characteristic length
ℓ	Lagrange polynomials
L	Legendre polynomials
$\mathcal{L}$	Discrete operator for advective flux contributions
$\underline{M}$	Transformation matrix for space vectors
$\underline{\mathsf{M}}$	Transformation matrix for block vectors
$\mathcal{M}$	Discrete mass matrix
Ma	Mach number
$\mathrm{Ma_m}$	Magnetic Mach number
$\vec{n}$	Physical space normal vector
$\hat{n}$	Cartesian space normal vector
N	Polynomial degree
N_{el}	Total number of elements
p	Pressure
$\mathbb{P}^N$	Space of polynomials of degree $\leq N$
Pr	Prandtl number
$\vec{q}_h$	Heat flux
$\overset{\leftrightarrow}{\mathbf{q}}$	Gradient of entropy variables
$\mathcal{Q}$	Discrete SBP matrix
$r_{\mathfrak{A}}$	Radius of atmosphere
$\mathbf{r}$	Damping source term
$\mathbf{r}_{\mathrm{c}}$	Collision source term
R	Universal gas constant
R	Interface approximation of eigenvector matrices
Re	Reynolds number
$\mathrm{Re_m}$	Magnetic Reynolds number
$\mathbf{u}$	Conserved variables
$\vec{v}$	Velocity vector
$\mathcal{V}$	Discrete Vandermonde matrix
s	Thermodynamic entropy
$\hat{s}$	Surface element
S	Entropy function
$\bar{S}$	Total discrete entropy
t	Time
T	Final time
T	Interface scaling matrix
TOL	Error tolerance for filtering
$\mathbf{w}$	Entropy variables
$\vec{x} = (x, y, z)^T$	Physical spatial coordinates
$\vec{X}$	Element mapping

α	Damping parameter
β	Convenience variable for one half density over pressure
β_{m}	Plasma beta
δ	Dirac-delta polynomial
Δt	Time step
$\Delta x, \Delta y$	Element size for Cartesian mesh
ϵ_0	Upper bound for artificial viscosity
ϵ_S	Discrete entropy conservation error
ϵ_{FIL}	Maximum error between filtered and unfiltered approximations
ε	Stencil of Dirac-delta kernel
γ	Adiabatic coefficient
Γ	Curved element surface
θ	Involution multiplier contracted into entropy space
$\overset{\leftrightarrow}{\boldsymbol{\vartheta}}$	Test function for viscous parts
κ	Thermal conductivity
$\varkappa$	Convex parameter for adaptive filtering
λ	Eigenvalues of flux Jacobians
λ_{max}	Maximum eigenvalue of flux Jacobians
Λ_n	Dissipation matrix in normal flow direction
$\hat{\Lambda}$	Interface approximation of diagonal eigenvalue matrices
μ_{NS}	Viscosity
μ_{R}	Resistivity
ν	Artificial viscosity
ν^*	Scaling of artificial viscosity
$\vec{\xi} = (\xi, \eta, \zeta)^T$	Spatial coordinates in the reference domain
$\bar{\bar{\xi}}$	Staggered grid points
Ξ	Global filter matrix
$\boldsymbol{\Xi}$	Local filter matrix
ϱ	Density
σ^{DOF}	DOF energy indicator
$\sigma^{\mathrm{DOF}}_{\mathrm{min}}$	Minimum threshold for adding artificial viscosity
$\sigma^{\mathrm{DOF}}_{\mathrm{max}}$	Maximum threshold for adding artificial viscosity
σ^{FIL}	SIAC filter indicator
$\sigma^{\mathrm{FIL}}_{\mathrm{min}}$	Minimum threshold for adaptive filtering
$\sigma^{\mathrm{FIL}}_{\mathrm{max}}$	Maximum threshold for adaptive filtering
ϖ	Collision frequency
ϖ_{in}	Inner collision frequency
$\underline{\tau}$	Viscous stress tensor
υ	Estimation of viscous eigenvalues
$\boldsymbol{\Upsilon}$	Non-conservative terms

$\mathbf{\Upsilon}^{\mathrm{GLM}}$	GLM non-conservative term
$\mathbf{\Upsilon}^{\mathrm{MHD}}$	MHD non-conservative term (Powell term)
$\overset{\leftrightarrow}{\boldsymbol{\phi}}{}^{\mathrm{GLM}}$	Derivative-free part of GLM non-conservative term
$\boldsymbol{\phi}^{\mathrm{MHD}}$	Derivative-free part of MHD non-conservative term
$\boldsymbol{\varphi}$	Test function for advective parts
ψ	GLM divergence cleaning variable
$\vec{\Psi}$	Entropy potential
ω	Quadrature weights
Ω	Computational domain

$(\cdot)^-$	Primary state at element interface
$(\cdot)^+$	Secondary state at element interface
$(\cdot)^*$	Interface coupling by numerical flux
$(\cdot)^\diamond$	Interface coupling of non-conservative term
$\langle \cdot, \cdot \rangle$	Inner product of two Lebesgue integrable functions
$\|\cdot\|$	L_2 norm of Lebesgue integrable function
$\langle \cdot, \cdot \rangle_N$	Discrete inner product of two approximations
$\|\cdot\|_N$	Discrete L_2 norm of approximation
$[\![\cdot]\!]$	Jump between two states
$\{\!\{\cdot\}\!\}$	Arithmetic mean of two states
$(\cdot)^{\ln}$	Logarithmic mean of two states

Abbreviations

BR1	Bassi-Rebay type one
CFL	Courant-Friedrichs-Lewy
DG	Discontinuous Galerkin
DGSEM	Discontinuous Galerkin spectral element method
DOF	Degree of freedom
EC	Entropy conservative
EOC	Experimental order of convergence
ES	Entropy stable
GLF	Global Lax-Friedrichs
GLM	Generalized Lagrangian multiplier
HPC	High performance computing
LGL	Legendre-Gauss-Lobatto
LLF	Local Lax-Friedrichs
MHD	Magnetohydrodynamics
MPI	Message passing interface
NSE	Navier-Stokes equations
NW	Nine-wave
OTV	Orszag-Tang vortex
PDE	Partial differential equation
PID	Performance index
RKM	Runge-Kutta method
SIAC	Smoothness increasing accuracy conserving
SBP	Summation-by-parts
SSP	Strong stability preserving
TGV	Taylor-Green vortex

1. Introduction

Numerical methods are a powerful tool for simulating real world problems and in some applications have become an attractive alternative for expensive experiments. In fact, they are even more valuable when it comes to investigations of large scale processes, e.g. in space, for which experiments are impossible to perform in a laboratory. Moreover, the trend of relying on numerical schemes to simulate physical problems has even intensified, since the power of computers has increased drastically over the last decades.

Speaking about numerical simulations of physical processes, one has a broad variety of numerical methods, from which to choose. The decision for one particular method depends on many aspects like the problem setup and the user defined goals. For instance, low-order finite volume schemes are some of the most reliable schemes available and applicable to many flow phenomena due to their simplicity of implementation and robustness, e.g. [96]. However, the drawback of these methods is an inadequate solution quality especially in flow regimes with fine features or turbulent structures. On the other hand, more accurate schemes often suffer from stability or robustness issues [121]. In the end, one has to balance these properties such that the optimal numerical approach for the considered problem is found. Consequently, a shared purpose of the entire numerics community is the development and improvement of numerical schemes with respect to their accuracy, robustness and applicability.

Pursuing this goal, one has to start with the mathematical model describing the underlying physics. In this work, we focus on systems of conservation laws, which are built from partial differential equations (PDE) connecting temporal and spatial evolutions in the considered physical variables. Systems of conservation laws cover a broad range of physical processes such as fluid dynamics, e.g. [9, 95, 102, 132]. In particular, the fluid behavior is determined by tracking the evolution of variables such as density or total energy over time. These conserved variables are strongly coupled to each other and can only change in time depending on the fluid flow into or out of the system.

The resistive magneto-hydrodynamic (MHD) equations are among these systems of conservation laws and of great interest in many areas of plasma, space and astrophysics, e.g. [78]. This stems from a wide range of applications such as electromagnetic turbulence in conducting fluids, magnetically confined fusion for power generation, modeling the action of dynamos and predicting the interaction of the solar wind with planets or moons, e.g. [31, 45, 116, 119]. The governing equations describe electrically conducted fluids, termed as *plasma*, which are not only influenced by the hydrodynamic fluid forces, but also by electromagnetic field forces. MHD covers both, dense and thin plasmas, that

are time dependent and include motions with a wide range of temporal and spatial scales, e.g. compressible MHD turbulence [12, 138]. In contrast to the *ideal* MHD equations, which comprise the advective terms of the system, the *resistive* MHD equations also account for viscous and resistive effects.

Another important property, in a closed physical system, is the second law of thermodynamics, i.e. the evolution of the entropy. In the absence of resistivity and viscosity, that is for the ideal MHD model, and for smooth solutions, the entropy of the system is an additional conserved quantity, although not explicitly built into the mathematical model [9]. Further, in the presence of shocks, the second law of thermodynamics becomes the entropy inequality, e.g. [65], which guarantees that entropy is always dissipated with the correct sign. Herein, we extend the continuous entropy analysis to the resistive MHD equations by proving that the additional resistive terms have a purely entropy dissipative effect as well.

A complication arising from the entropy analysis of MHD models is the involution, that is, the divergence-free constraint of the magnetic field, which is an additional partial differential equation not explicitly built into the resistive MHD equations similar to the entropy inequality, e.g. [23]. However, it is well known that an additional non-conservative PDE term proportional to the divergence-free constraint is necessary for the entropy analysis of the ideal MHD equations, see e.g. Godunov [55]. There are different variants in how to construct such non-conservative terms, e.g. Powell [109] and Janhunen [75]. On the continuous level, adding a non-conservative term scaled by the divergence of the magnetic fields is a clever way of adding zero to the model. But, for numerical approximations, there are known stability and accuracy issues that differ between the three types of non-conservative terms [124].

Mimicking the continuous entropy analysis in the discrete sense is a promising way to enhance the robustness of the resulting numerical approximation, which is a desirable goal for all numerical schemes as pointed out earlier. A numerical scheme that satisfies a discrete entropy inequality is often referred to as an *entropy stable* scheme, [65, 90, 128].

In this thesis, we focus on discontinuous Galerkin (DG) methods, which are based on element-wise polynomial approximations coupled by numerical surface fluxes, e.g. [27, 67, 81]. Particularly, we consider a nodal discontinuous Galerkin spectral element method (DGSEM) on unstructured conforming hexahedral grids, as it is able to handle curved elements in a natural way while providing high computational efficiency [69]. The geometric flexibility offered by unstructured curvilinear meshes is needed to decompose e.g. domains around spherical objects without singularities [35] or a torus-shaped Tokamak reactor [71].

In practice, entropy stable DG schemes show enhanced robustness compared to the standard DGSEM for fluid dynamics problems with weak shocks and especially for compressible (under-resolved) turbulence, e.g. [20, 41, 54], as entropy stability provides the desired in-built de-aliasing. At the end of this work, we show that these positive properties indeed carry over to simulations of magnetized fluid dynamics.

Hence, the main focus of this thesis is the derivation of an entropy stable DG method with special focus on the discretization of the non-conservative terms unique to MHD models and its extension to fully three-dimensional curvilinear unstructured hexahedral meshes. The key to *discrete* entropy stability on curvilinear meshes is to mimic the integration-by-parts property with the DG operators and satisfy the metric identities [16]. This enables the construction of DG methods that are entropy stable without the assumption of exact evaluation of the variational forms. Discrete integration-by-parts, or summation-by-parts (SBP), is naturally obtained when using the Legendre-Gauss-Lobatto (LGL) nodes in the nodal DG approximation [51]. Furthermore, we extend the recent results from Gassner et al. [20, 53] to show that it is possible to construct nodal DG discretizations with LGL nodes that are discretely entropy stable for the viscous and resistive terms of the MHD equations.

As noted, an important difference to the construction of entropy stable DG schemes for non-magnetized fluid dynamics is the necessity to include the divergence-free constraint as a non-conservative term for the continuous and discrete entropy analysis. However, it is well known in the MHD numerics community that even if the magnetic field is initially divergence-free, it is not guaranteed that the discrete evolution of the magnetized fluid will remain divergence-free in the magnetic field without additional mechanisms [18]. Therefore, many numerical techniques have been devised to control errors introduced into the divergence-free constraint by a numerical discretization [8, 38, 79, 133]. One possibility to counteract the generation of divergence errors is the method of hyperbolic divergence cleaning, which is based on a generalized Lagrangian multiplier (GLM) technique [30]. Recent work by Derigs et al. [34] modified the additional GLM divergence cleaning system in such a way that the resulting ideal GLM-MHD system is consistent with the continuous entropy analysis and provides in-built divergence cleaning capabilities. The novel entropy stable GLM-MHD system includes the Powell non-conservative term and a non-conservative GLM term in the energy equation, which is necessary for Galilean invariance. Overall, we present a discontinuous Galerkin spectral element method for the resistive MHD equations, which is high-order accurate, discretely entropy stable on curvilinear elements and has an in-built GLM divergence cleaning mechanism.

An additional issue arises from the fact, that for systems of non-linear conservation laws, like the resistive GLM-MHD equations, shocks might develop in finite time even from smooth initial data, e.g. [40]. In combination with a high-order approximation this leads to de-stabilizing oscillations in the interpolating polynomials, which cause unphysical solution states or, even worse, simulation crashes due to e.g. negative pressure values [57]. Hence, we equip the final entropy stable DGSEM with additional shock capturing mechanisms in order to regularize the discretization in shocked regions. Particularly, we present three approaches to treat such unfavorable situations based on artificial viscosity, smoothness increasing filters and simple positivity limiters.

Finally, we use the novel solver to simulate a space physics flow, which belongs to the category of physical processes one cannot investigate in a laboratory. Since observation data from spacecraft flybys is not always available and expensive, we rely on numerical simulations to study such physical situations. The considered setup involves atmospheric plasma interactions in the orbit of planetary moons like Io, Europa or Enceladus. These sub-alfvénic plasma interactions exhibit exceptionally interesting flow characteristics containing steep gradients and discontinuities [118]. We show simulation results of the entropy stable DG solver and compare them against the standard DG version as well as state-of-the-art solver commonly used to simulate such space plasma flows.

The outline of this thesis is as follows. In Chapter 2, we start with an introduction of the mathematical model, from which we incrementally build up the final system of the three-dimensional resistive GLM-MHD equations. Further, we present the continuous entropy analysis, which demonstrates that the model indeed satisfies the entropy inequality. Next, we introduce the specific split form DGSEM on curvilinear hexahedral elements in Chapter 3. With that at hand, we prove the entropy stability of the numerical approximation in Chapter 4 by discretely mimicking the continuous entropy analysis with special attention given to the metric terms, GLM divergence cleaning and the resistive terms. In Chapter 5, we introduce and discuss the shock capturing methods as well as their compatibility with entropy stability. Next, we provide some details on the actual implementation, parallelization aspects and efficiency in Chapter 6. By many numerical tests we verify the theoretical properties of the scheme in Chapter 7. Amongst others, we use several benchmark examples from the literature to validate the accuracy, entropy conservation, GLM divergence cleaning capabilities and increased robustness of the method on both, two-dimensional Cartesian and three-dimensional hexahedral curved meshes. Finally, we apply the entropy stable solver to the geophysics problem in Chapter 8, where we first clarify the physical background and present simulation results as well as comparisons for a simplified version of the problem, before we apply it to a more realistic setup. Lastly, Chapter 9 gives concluding remarks and an outlook on possible further research projects.

2. Physical model

In general, natural scientists are interested in the behavior and functionality of the world surrounding them. Besides observations and laboratory experiments, numerical simulations are a helpful tool of understanding these processes. In order to set up such simulations we need a mathematical model, which describes the underlying physics sufficiently well. Consequently, we have to convert the quantities and characteristics of the considered system into abstract mathematical concepts and equations.

Thus, as a starting point for the discussion we outline a general mathematical framework to describe the considered physics. In particular, we describe these physics in terms of partial differential equations (PDE) linking temporal and spatial changes of the considered variables in *systems of conservation laws*. After discussing some general properties of these systems, we introduce the governing equations under consideration incrementally by building their complexity as well as their applicability to capture as much physics as possible. The incremental splitting of the governing mathematical equations is useful to discuss the main focus of this work. That is, the investigation and proof that the resulting system remains thermodynamically consistent presented in the continuous entropy analysis at the end of this chapter. This structure will be helpful throughout this work when constructing entropy aware numerical discretizations to model the complex flow phenomena governed by these systems.

2.1. Governing equations

On a three-dimensional domain $\Omega \subset \mathbb{R}^3$ we consider systems of non-linear conservation laws

$$\mathbf{u}_t + \vec{\nabla} \cdot \overset{\leftrightarrow}{\mathbf{f}} = \mathbf{0} \tag{2.1}$$

with $t \in [0, T] \subset \mathbb{R}$ and appropriate initial and boundary conditions. Here $\mathbf{u}$ denotes the vector of conserved variables and $\overset{\leftrightarrow}{\mathbf{f}}$ the multidimensional flux vector. The conservative nature of (2.1), meaning the total change of the conserved variables only depends on its boundary conditions, can be verified by integrating over Ω and applying the divergence theorem, i.e.

$$\int_\Omega \mathbf{u}_t \ \mathrm{dV} = - \oint_{\partial\Omega} \overset{\leftrightarrow}{\mathbf{f}} \cdot \vec{n} \ \mathrm{dS}. \tag{2.2}$$

There is a wide range of physical applications, that are mathematically described by equation (2.1), e.g. water height in a tub, mass in chemical processes or energy in electrical heating [88, 89].

Alternatively, by applying the chain rule onto the fluxes we rewrite (2.1) in its quasi-linear form, i.e.

$$\mathbf{u}_t + \sum_{i=1}^{3} \mathsf{A}_i \, \frac{\partial \mathbf{u}}{\partial x_i} = \mathbf{0} \tag{2.3}$$

with the diagonalizable flux Jacobians A_i in each spatial direction $i = 1, 2, 3$. These are particularly interesting, since their eigenvalues give important information about the characteristics of the considered system. If all eigenvalues of the three flux Jacobians are real numbers, then (2.1) is a system of *hyperbolic* conservation laws. We can interpret the solutions of such systems as waves traveling along characteristics [132].

Additionally, the three-dimensional fluxes are, in general, dependent of the solution itself in a non-linear way. Due to the hyperbolic nature of these non-linear conservation laws it is well known, that discontinuities in terms of shocks may form regardless on the smoothness of the initial data [40]. By analyzing the characteristics of the considered system it is possible to derive the shock speed with the help of the Rankine-Hugoniot condition, see e.g. [44].

Once discontinuities are present in the solution of (2.1), the concept of classical solutions breaks, since classical derivatives no longer apply. Hence, the weak form of the conservation law is introduced, which is obtained by integration of the original conservation law and multiplying by a smooth test function $\boldsymbol{\varphi} \in C^1(\Omega \times [0, T))$ with compact support. Then integration-by-parts is applied to find the conservation law in weak form

$$\int_0^T \int_\Omega \left(\mathbf{u}\boldsymbol{\varphi}_t + \overset{\leftrightarrow}{\mathbf{f}} \cdot \vec{\nabla}\boldsymbol{\varphi} \right) \, \mathrm{dV}\mathrm{d}t = \int_\Omega \mathbf{u}(\vec{x}, 0)\boldsymbol{\varphi}(\vec{x}, 0)\mathrm{dV}. \tag{2.4}$$

We call $\mathbf{u}(\vec{x}, t)$ a weak solution of (2.1) if it satisfies the weak form conservation law (2.4) for all feasible test functions $\boldsymbol{\varphi} \in C^1(\Omega \times [0, T))$ with compact support [39]. Unfortunately, this approach creates new issues finding the (physically) correct solution out of the pool of weak solutions. So, we lose uniqueness of our solution in the weak formulation. We address this matter in Sec. 2.2, when we introduce the concept of entropy.

Furthermore, we are particularly interested in weak solutions of (2.4), since our numerical method is also built from a weak formulation and we will revisit the issue of discontinuities and shocks from a numerical perspective in Sec. 5. But first, we introduce the considered system of governing equations in this work, the resistive GLM-MHD equations, step-by-step.

2.1.1. Euler equations

Since magnetohydrodynamics is the study of electrically conducting fluids, it combines both principles of fluid dynamics and electromagnetism [11]. Thus, we start off with the well known compressible Euler equations, which are the mathematical baseline model for fluid dynamics and cover a bulk of physical flow motions like laminar flows as well as inviscid turbulence in technical pipes or around airfoils. In contrast to particle based models the Euler equations are a macroscopic approach including the continuum assumption [88]. Essentially, they combine three physical principles: conservation of mass, momenta and energy. For going their derivation, we can write them as a system of conservation laws as in (2.1) with the conserved variables and advective fluxes

$$\mathbf{u} = \begin{pmatrix} \varrho \\ \varrho\vec{v} \\ E \end{pmatrix}, \qquad \overset{\leftrightarrow}{\mathbf{f}} = \overset{\leftrightarrow}{\mathbf{f}}^{\text{Euler}} = \begin{pmatrix} \varrho\vec{v} \\ \varrho(\vec{v}\vec{v}^T) + p\underline{I} \\ \vec{v}\left(\frac{1}{2}\varrho\,\|\vec{v}\|^2 + \frac{\gamma p}{\gamma-1}\right) \end{pmatrix}. \tag{2.5}$$

Here, ϱ, $\vec{v} = (v_1, v_2, v_3)^T$, p, E are the mass density, fluid velocities, pressure and total energy, respectively, and $\underline{I}$ denotes the 3×3 identity matrix. We close the system with the ideal gas assumption, which relates the total energy and pressure

$$p = (\gamma - 1)\left(E - \frac{1}{2}\varrho\,\|\vec{v}\|^2\right), \tag{2.6}$$

where γ denotes the adiabatic coefficient.

Moreover, we can express the eigenvalues of the flux Jacobian in the i-th direction [132] from (2.3) as

$$(\lambda_i)_{1,5} = v_i \pm c, \quad (\lambda_i)_{2,3,4} = v_i \quad \text{with } c = \sqrt{\frac{\gamma p}{\varrho}}, \quad i = 1, 2, 3, \tag{2.7}$$

so that the maximum eigenvalue of the entire system is bounded by

$$\lambda^{\max} = \max_{i=1,2,3} |v_i| + c. \tag{2.8}$$

We see, that the compressible Euler equations are a hyperbolic system of conservation laws under the physical assumptions, that $\varrho, p > 0$.

An additional quantity often stated in the context of the Euler equations is the Mach number, i.e.

$$\text{Ma} = \frac{\|\vec{v}\|}{c}, \tag{2.9}$$

which is a dimensionless variable relating the characteristic velocity of the fluid to the speed of sound and, thus, indicates the strength of arising shocks. Further, inflow and outflow boundary condition can be determined by the Mach number, which helps to distinguish between sub- and supersonic flow configurations [132].

2.1.2. Ideal MHD equations

The MHD equations mathematically describe the evolution of plasmas (electrically ionized gases) such that we can model flow configurations, e.g. in space or fusion reactors. These plasmas are assumed to be strongly collisional, electrically neutral and perfectly conductive [31, 45, 111]. Neglecting both, viscous stresses and resistive effects of the magnetic fields, we first consider the ideal MHD equations.

As mentioned at the beginning of the previous section, the ideal MHD equations are a combination of fluid dynamics and electromagnetism. Since we already addressed the hydrodynamic part, we now add the electric and magnetic components and couple them with the Euler equations. Hence, we next look at Maxwell's equations of electromagnetism and derive the ideal MHD equations by consulting several additional physical laws. Note, for the following derivations we assume many physical restrictions, e.g. non-dimensionality, no resistivity and no relativistic effects. For now, we also assume divergence free magnetic fields $\vec{\nabla} \cdot \vec{B} = 0$ and, thus, vanishing magnetic charges and current densities.

We begin with the induction equation of Maxwell's model arising from Faraday's law, which reads

$$\frac{\partial \vec{B}}{\partial t} + \vec{\nabla} \times \vec{E} = \vec{0} \tag{2.10}$$

and basically states that temporal changes in the magnetic field $\vec{B} = (B_1, B_2, B_3)^T$ create electric fields $\vec{E} = (E_1, E_2, E_3)^T$ and not only vice versa. Next, we insert Ohm's law

$$\vec{E} = -\left(\vec{v} \times \vec{B} \right) \tag{2.11}$$

into (2.10) and use vector calculus manipulations to obtain a conservation law for the magnetic field variables

$$\frac{\partial \vec{B}}{\partial t} - \vec{\nabla} \times \left(\vec{v} \times \vec{B} \right) = \frac{\partial \vec{B}}{\partial t} + \vec{\nabla} \cdot \left(\vec{v} \vec{B}^T - \vec{B} \vec{v}^T \right) = \vec{0}. \tag{2.12}$$

Additionally, in order to couple the electric and magnetic components with the Euler equations we consider the low-frequency Ampere's law

$$\vec{J} = \vec{\nabla} \times \vec{B} \tag{2.13}$$

with the current density $\vec{J}$ and insert it into the Lorentz force

$$\vec{F}_L = \vec{J} \times \vec{B} = \left(\vec{\nabla} \times \vec{B} \right) \times \vec{B} = \vec{\nabla} \cdot \left(\vec{B} \vec{B}^T - \frac{1}{2} \|\vec{B}\|^2 \underline{I} \right). \tag{2.14}$$

We include this external force on the right-hand-side of the momenta equations to obtain

$$\frac{\partial (\varrho \vec{v})}{\partial t} + \vec{\nabla} \cdot \left(\varrho (\vec{v} \vec{v}^T) + p\underline{I} + \frac{1}{2} \|\vec{B}\|^2 \underline{I} - \vec{B} \vec{B}^T \right) = \vec{0}. \tag{2.15}$$

Finally, we adapt the energy conservation by simply adding the magnetic energy, i.e.

$$E = \varrho e + \frac{1}{2} \varrho \|\vec{v}\|^2 + \frac{1}{2} \|\vec{B}\|^2 \tag{2.16}$$

with the specific inner energy e. Taking the time derivative of (2.16), inserting the derived new conservation laws (2.12) as well as (2.15) and after many manipulations (see e.g. [29]) we find

$$\frac{\partial E}{\partial t} + \vec{\nabla} \cdot \left[\vec{v} \left(\frac{1}{2} \varrho \|\vec{v}\|^2 + \frac{\gamma p}{\gamma - 1} + \|\vec{B}\|^2 \right) - \vec{B} \left(\vec{v} \cdot \vec{B} \right) \right] = \vec{0}. \tag{2.17}$$

Overall, we express the ideal MHD equation as a system of conservation laws as in (2.1) with

$$\mathbf{u} = \begin{pmatrix} \varrho \\ \varrho \vec{v} \\ E \\ \vec{B} \end{pmatrix}, \qquad \overset{\leftrightarrow}{\mathbf{f}} = \overset{\leftrightarrow}{\mathbf{f}}^{\text{Euler}} + \overset{\leftrightarrow}{\mathbf{f}}^{\text{MHD}} = \begin{pmatrix} \varrho \vec{v} \\ \varrho (\vec{v} \vec{v}^T) + p \underline{I} \\ \vec{v} \left(\frac{1}{2} \varrho \|\vec{v}\|^2 + \frac{\gamma p}{\gamma - 1} \right) \\ \underline{0} \end{pmatrix} + \begin{pmatrix} \vec{0} \\ \frac{1}{2} \|\vec{B}\|^2 \underline{I} - \vec{B} \vec{B}^T \\ \vec{v} \|\vec{B}\|^2 - \vec{B} \left(\vec{v} \cdot \vec{B} \right) \\ \vec{v} \vec{B}^T - \vec{B} \vec{v}^T \end{pmatrix} \tag{2.18}$$

and the new equation of state

$$p = (\gamma - 1) \left(E - \frac{1}{2} \varrho \|\vec{v}\|^2 - \frac{1}{2} \|\vec{B}\|^2 \right). \tag{2.19}$$

However, the eigenstructure of the flux Jacobians gets more complicated. In fact, we now have eight different eigenvalues in each spatial direction

$$
\begin{aligned}
\lambda_i^{\pm f} &= v_i \pm c_i^f & \text{(fast magneto-acoustic waves)}, \\
\lambda_i^{\pm A} &= v_i \pm c^A & \text{(Alfvén waves)}, \\
\lambda_i^{\pm s} &= v_i \pm c_i^s & \text{(slow magneto-acoustic waves)}, \\
\lambda_i^E = v_i, \ \lambda_i^D &= 0 & \text{(entropy and divergence wave)}
\end{aligned}
\tag{2.20}
$$

for $i = 1, 2, 3$, which not only include the sound speed c but also the Alfvén wave as well as slow and fast magneto-acoustic wave speeds [12, 29, 31, 45, 112], i.e.

$$c_i^{f,s} = \sqrt{\frac{1}{2} \left(a + b \pm \sqrt{(a+b)^2 - 4a \left(c_i^A \right)^2} \right)}, \quad i = 1, 2, 3 \tag{2.21}$$

with

$$a = c^2 = \frac{\gamma p}{\varrho} \qquad b = \frac{\|\vec{B}\|^2}{\varrho} \qquad c_i^A = \frac{B_i}{\sqrt{\varrho}}, \quad i = 1, 2, 3. \tag{2.22}$$

Here, c_i^A denotes the Alfvén wave speed and we note again, that positivity of density and pressure are crucial requirements for maintaining the hyperbolicity of the PDE. For the actual implementation we bound the maximum eigenvalue of the system by

$$\lambda^{\max} = \max_{i=1,2,3} \left\{ |v_i| + c_i^f \right\}. \tag{2.23}$$

We also introduce the magnetic Mach number

$$\mathrm{Ma_m} = \max_{i=1,2,3} \frac{v_i}{c_i^A} \tag{2.24}$$

and the plasma beta

$$\beta_\mathrm{m} = \frac{2p}{\|\vec{B}\|^2}, \tag{2.25}$$

which are important variables to characterize the considered MHD problems.

2.1.3. Ideal GLM-MHD equations

There is an additional constraint that is not explicitly built into the ideal MHD equations, albeit necessary to accurately model the evolution of magnetized fluid dynamics. We must ensure that the divergence on the magnetic field is zero, as is dictated by Gauss' law of magnetism

$$\vec{\nabla} \cdot \vec{B} = 0. \tag{2.26}$$

We refer to this property as the *divergence-free condition*. The geometrical meaning of (2.26) is that magnetic field lines have "no ends," i.e., regions of reduced field strength cannot be local, since magnetic field lines are not allowed to meet any monopolar singularities. So, in contrast to other macroscopic quantities like density, a change in magnetic field strength must be accommodated by changes in the field morphology on a larger scale, which introduces additional difficulties in the numerical modeling.

On the continuous level (2.26) is assumed to always be satisfied. However, even if the divergence-free constraint is satisfied with the initial conditions, it is not necessarily true that it will remain satisfied through the *discrete* evolution of the equations [18]. So, we see that the divergence-free constraint provides an important indicator to decide if flows remain physically meaningful during their numerical approximation. Thus, we already build this additional condition (2.26) into the model on a continuous level, even though its significance is numerically motivated.

There are many available techniques to restore the divergence-free condition discretely. These include the source term approach of Powell [109], the projection approach of Brackhill and Barnes [18], the method of constrained transport introduced by Evans and Hawley [38] or Balsara and Spicer [8], and the hyperbolic divergence cleaning technique of Dedner et al. [30]. A thorough review of all these techniques (except hyperbolic divergence cleaning) is provided by Tóth [133].

Due to its relative ease of implementation and its computational efficiency we select the method of hyperbolic divergence cleaning to address the numerical issues stemming from the discrete divergence-free condition. This technique is based on a generalized Lagrangian Multiplier (GLM), that minimizes the error in the magnetic field divergence [30, 79, 134]. Recently, Derigs et al. [34] extended the system of ideal MHD equations to include the GLM divergence cleaning methodology while guaranteeing that the governing equations remained consistent to the second law of thermodynamics (entropy). We postpone the specific discussion of the entropic properties of the system to Sec. 2.2.

We now assume $\vec{\nabla} \cdot \vec{B} \neq 0$ and start by introducing an auxiliary variable ψ that keeps track of the divergence error as suggested by Dedner et al. [30]. In particular, this new variable propagates the divergence error through the domain away from its source by the yet arbitrary propagation speed c_h. Consequently, we build an additional conservation law into our system, i.e.

$$\frac{\partial \psi}{\partial t} + \vec{\nabla} \cdot \left(c_h \vec{B} \right) = 0. \tag{2.27}$$

We couple the new variable with the magnetic fields and, thus, modify the fluxes in (2.12) by

$$\frac{\partial \vec{B}}{\partial t} + \vec{\nabla} \cdot \left(\vec{v}\,\vec{B}^T - \vec{B}\,\vec{v}^T + c_h\psi\underline{I} \right) = \vec{0}. \tag{2.28}$$

Furthermore, Derigs et al. [34] again adapted the energy equation by

$$E = \varrho e + \frac{1}{2}\varrho\,\|\vec{v}\|^2 + \frac{1}{2}\|\vec{B}\|^2 + \frac{1}{2}\psi^2 \tag{2.29}$$

in order to include the new contributions from the divergence correction into the total energy rather than ignoring it, which would have generated spurious thermal energy. Finally, this changes the energy update to be

$$\frac{\partial E}{\partial t} + \vec{\nabla} \cdot \left[\vec{v}\left(\frac{1}{2}\varrho\,\|\vec{v}\|^2 + \frac{\gamma p}{\gamma - 1} + \|\vec{B}\|^2 \right) - \vec{B}\left(\vec{v} \cdot \vec{B} \right) + c_h\psi\vec{B} \right] = \vec{0}. \tag{2.30}$$

However, one major problem occurs, if we now re-consider the derivations of the previous section. Since we assume $\vec{\nabla} \cdot \vec{B} \neq 0$, some of the physical laws do not hold anymore. Particularly, we get additional terms on the right hand side of Faraday's law (2.10) dependent on $\vec{\nabla} \cdot \vec{B}$ and in the computation of the Lorentz force (2.14), see e.g. [34]. Due to these changes we obtain a *non-conservative term* $\boldsymbol{\Upsilon}$ in the resulting ideal GLM-MHD system, which we split into two parts $\boldsymbol{\Upsilon} = \boldsymbol{\Upsilon}^{\mathrm{MHD}} + \boldsymbol{\Upsilon}^{\mathrm{GLM}}$ with

$$\boldsymbol{\Upsilon}^{\mathrm{MHD}} = (\vec{\nabla} \cdot \vec{B})\boldsymbol{\phi}^{\mathrm{MHD}} = \left(\vec{\nabla} \cdot \vec{B} \right) \left(0\,,\, B_1\,,\, B_2\,,\, B_3\,,\, \vec{v} \cdot \vec{B}\,,\, v_1\,,\, v_2\,,\, v_3\,,\, 0 \right)^T\,, \tag{2.31}$$

$$\boldsymbol{\Upsilon}^{\mathrm{GLM}} = \overset{\leftrightarrow}{\boldsymbol{\phi}}^{\mathrm{GLM}} \cdot \vec{\nabla}\psi \quad = \phi_1^{\mathrm{GLM}}\frac{\partial \psi}{\partial x} + \phi_2^{\mathrm{GLM}}\frac{\partial \psi}{\partial y} + \phi_3^{\mathrm{GLM}}\frac{\partial \psi}{\partial z}\,, \tag{2.32}$$

where $\overset{\leftrightarrow}{\phi}^{\mathrm{GLM}}$ again is a 27 block vector with

$$\phi_i^{\mathrm{GLM}} = (0,\, 0,\, 0,\, 0,\, v_i\psi,\, 0,\, 0,\, 0,\, v_i)^T, \quad i = 1, 2, 3. \tag{2.33}$$

As presented in [34], the first non-conservative term $\boldsymbol{\Upsilon}^{\mathrm{MHD}}$ is the well-known Powell term [109], and the second term $\boldsymbol{\Upsilon}^{\mathrm{GLM}}$ results from Galilean invariance of the full GLM-MHD system [34]. It turns out, that these physically motivated non-conservative terms are not only related to the GLM extension of the system, but are also important for the entropic properties of the system as will be discussed later.

Moreover, we reject the choice of alternative non-conservative terms as the one suggested by Janhunen [75] or Brackhill and Barnes [18] instead of the Powell term, even though they have the same entropic properties. This is due to the previous derivations as well as numerical tests, in which we see, that only the Powell term reproduces the Lorentz force (2.14) correctly.

Finally, the overall ideal GLM-MHD system reads

$$\mathbf{u}_t + \vec{\nabla} \cdot \overset{\leftrightarrow}{\mathbf{f}}(\mathbf{u}) + \boldsymbol{\Upsilon} = \mathbf{0} \tag{2.34}$$

with the vector of conserved variables $\mathbf{u} = (\varrho, \varrho\vec{v}, E, \vec{B}, \psi)^T$, the advective fluxes

$$\overset{\leftrightarrow}{\mathbf{f}} = \overset{\leftrightarrow}{\mathbf{f}}^{\mathrm{Euler}} + \overset{\leftrightarrow}{\mathbf{f}}^{\mathrm{MHD}} + \overset{\leftrightarrow}{\mathbf{f}}^{\mathrm{GLM}} = \begin{pmatrix} \varrho\vec{v} \\ \varrho(\vec{v}\,\vec{v}^T) + p\underline{I} \\ \vec{v}\left(\frac{1}{2}\varrho\,\|\vec{v}\|^2 + \frac{\gamma p}{\gamma-1}\right) \\ \underline{0} \\ \vec{0} \end{pmatrix} + \begin{pmatrix} \vec{0} \\ \frac{1}{2}\|\vec{B}\|^2\underline{I} - \vec{B}\vec{B}^T \\ \vec{v}\|\vec{B}\|^2 - \vec{B}\left(\vec{v}\cdot\vec{B}\right) \\ \vec{v}\,\vec{B}^T - \vec{B}\,\vec{v}^T \\ \vec{0} \end{pmatrix} + \begin{pmatrix} \vec{0} \\ \underline{0} \\ c_h\psi\vec{B} \\ c_h\psi\underline{I} \\ c_h\vec{B} \end{pmatrix} \tag{2.35}$$

and the non-conservative term $\boldsymbol{\Upsilon} = \boldsymbol{\Upsilon}^{\mathrm{MHD}} + \boldsymbol{\Upsilon}^{\mathrm{GLM}}$ defined in (2.31)-(2.33). The adapted pressure now reads

$$p = (\gamma - 1)\left(E - \frac{1}{2}\varrho\,\|\vec{v}\|^2 - \frac{1}{2}\|\vec{B}\|^2 - \frac{1}{2}\psi^2\right). \tag{2.36}$$

We note, for $\vec{\nabla} \cdot \vec{B} = 0$ all ψ contributions as well as both non-conservative terms are zero and, thus, in the continuous case the resulting system reduces to the original ideal MHD equations. A complete derivation and discussion of the GLM-MHD system can be found in [34].

Advantageously, the spectra of the flux Jacobians do not change significantly, though we get two GLM waves dependent on $\pm c_h$ from the new equation and instead of the divergence wave in the original MHD equations (2.20). Thus, we select the correction speed to be

$$c_h \le \max_{i=1,2,3} c_i^f \tag{2.37}$$

with c_i^f from (2.21). If we do so, the upper bound for the maximum eigenvalue (2.23) still holds, which is particularly important for the numerical scheme in order to avoid additional time step restrictions.

In the ideal GLM-MHD equations (2.34) the divergence error is solely propagated through the domain, which might be insufficient especially for periodic boundaries. Hence, we introduce an additional purely algebraic source term $\mathbf{r}$ on the right hand side of the ideal GLM-MHD system in order to damp the divergence error [30, 34]

$$\mathbf{r} = (0\,,\,0\,,0\,,\,0\,,\,0\,,\,0\,,\,0\,,\,0\,,\,-\alpha\psi)^T\,, \tag{2.38}$$

with $\alpha \geq 0$. We note, that the choice of the damping parameter α is arbitrary and not related to any physical motivation [30].

2.1.4. Resistive GLM-MHD equations

The final step in building the system of equations considered in this work is to introduce the viscous and resistive effects into the fluid model. These include those which arise from the compressible Navier-Stokes equations (NSE) through viscous stresses and heat fluxes as well as the resistive effects that arise in the induction equations, e.g. terms that can possibly warp and alter the topology of the magnetic field. In this work, we refer to the complete system as the *resistive GLM-MHD equations*, which are, without the GLM modification, also known as the visco-resistive MHD equations in the literature, e.g. [103]. The applications of these governing equations are vast, e.g. modeling electromagnetic turbulence in conducting fluids [12, 17, 93, 94] or solar wind interaction with planets and moons [13, 117, 118].

The equations that govern resistive, conducting fluids depend on the solution as well as its gradient [138] and still include the derived GLM-MHD framework. The complete mathematical model considered in this work is

$$\mathbf{u}_t + \vec{\nabla} \cdot \overset{\leftrightarrow}{\mathbf{f}}^a(\mathbf{u}) - \vec{\nabla} \cdot \overset{\leftrightarrow}{\mathbf{f}}^v(\mathbf{u}, \vec{\nabla}\mathbf{u}) + \mathbf{\Upsilon} = \mathbf{r} \tag{2.39}$$

with the advective flux $\overset{\leftrightarrow}{\mathbf{f}}^a(\mathbf{u})$ from (2.35) and the viscous flux

$$\overset{\leftrightarrow}{\mathbf{f}}^v(\mathbf{u}, \vec{\nabla}\mathbf{u}) = \overset{\leftrightarrow}{\mathbf{f}}^{v,\text{NSE}} + \overset{\leftrightarrow}{\mathbf{f}}^{v,\text{MHD}} = \begin{pmatrix} \vec{0} \\ \underline{\tau} \\ \underline{\tau}\vec{v} - \vec{q}_h \\ \underline{0} \\ \vec{0} \end{pmatrix} + \begin{pmatrix} \vec{0} \\ \underline{0} \\ -\mu_{\text{R}}\left((\vec{\nabla} \times \vec{B}) \times \vec{B}\right) \\ \mu_{\text{R}}\left((\vec{\nabla}\vec{B})^T - \vec{\nabla}\vec{B}\right) \\ \vec{0} \end{pmatrix}. \tag{2.40}$$

Here, the viscous stress tensor reads [88]

$$\underline{\tau} = \mu_{\text{NS}}((\vec{\nabla}\vec{v})^T + \vec{\nabla}\vec{v}) - \frac{2}{3}\mu_{\text{NS}}(\vec{\nabla} \cdot \vec{v})\underline{I} \tag{2.41}$$

and the heat flux is defined as

$$\vec{q}_h = -\kappa \vec{\nabla}\left(\frac{p}{R\varrho}\right). \tag{2.42}$$

The introduced constants $\mu_{\mathrm{NS}}, \mu_{\mathrm{R}}, \kappa, R > 0$ describe the viscosity from the Navier-Stokes equations, resistivity of the plasma, thermal conductivity and the universal gas constant, respectively. In particular, the constants μ_{NS} and μ_{R} are first-order transport coefficients that describe the kinematic viscosity and the diffusivity of the magnetic field [144].

Instead of defining the thermal conductivity and universal gas constant separately, we usually state the Prandtl number, which is determined by these quantities, the kinematic viscosity and the ratio of specific heat, i.e.

$$\mathrm{Pr} = \frac{\gamma R \mu_{\mathrm{NS}}}{(\gamma - 1)\kappa}. \tag{2.43}$$

The governing equations (2.39) describing resistive plasmas are still time-dependent and feature a wide range of temporal and spatial scales. The pressure remains unchanged as in (2.36) and for $\vec{B} = \vec{0}$ we obtain the well-known Navier-Stokes equations. Also, the inclusion of viscous effects means that the system exhibits a mixed hyperbolic/parabolic structure introducing additional complications when deriving numerical methods. In order to classify the viscous effects of the system, we define the Reynolds number

$$\mathrm{Re} = \frac{\|\vec{v}\| \, l}{\mu_{\mathrm{NS}}} \tag{2.44}$$

with the characteristic length l. Analogously, we have the magnetic Reynolds number

$$\mathrm{Re_m} = \frac{\|\vec{v}\| \, l}{\mu_{\mathrm{R}}}, \tag{2.45}$$

which measures the influence of resistive effects.

With the final system of governing equations at hand, we are now prepared to analyze the thermodynamical properties of the resistive GLM-MHD equations (2.39).

2.2. Entropic properties

In this section we consider the entropy of the derived system, which is a thermodynamical quantity. Even though most physical variables used in thermodynamics analysis are intuitive, the entropy is a slightly esoteric quantity as we do not use it in everyday life. Besides the energy and temperature, the entropy is an important indicator in thermodynamics describing irreversible processes.

Thermodynamics is a branch of physics, that investigates conversion between different forms of energies using balance equations. Most importantly, these fundamentals

are described in three laws solely based on empirical observations which have not yet been disproved. The first law of thermodynamics states, that for any physical process the total energy of a closed system remains conserved, which is obviously satisfied by the Euler and ideal MHD systems from the previous section. The second law of thermodynamics, in which we are particularly interested, states that the entropy of a closed physical system not in equilibrium tends to increase over time, approaching its maximum value at equilibrium, i.e. it cannot shrink. However, in the mathematical analogy of this second law, we use a different sign convention [129] and thus want the total entropy of the system to be non-increasing over time. This difference in notation is largely due to the fact that mathematicians want an upper bound on the entropy [100]. Since it is not of particular interest in this work, we neglect the third law concerning the temperature.

2.2.1. General motivation

Overall, the three laws of thermodynamics provide an important role in selecting the tiny subset of physically feasible solutions from all imaginable state configurations. So, we are in particular interested in the entropy of the system because it helps to distinguish between physically meaningful and unphysical flow states. More precisely, we exclude solutions, that are not thermodynamically relevant with respect to the entropy, because such solution states are physically not possible. Consequently, from a numerical point of view, it has been shown in many contexts [23, 43, 51, 130, 141], that entropy aware discretizations have an increased robustness, since they more likely converge against a physical solution.

At this point, we recall the weak formulation (2.4) from Sec. 2.1 and the downside of this approach, that the uniqueness of the solution is lost, which creates the new problem of how to find the correct weak solution. Here, the entropy comes into play. In the case of one-dimensional scalar equations it is indeed possible to solve this problem and prove existence and uniqueness of a solution by Lax and Oleinik's entropy conditions [91]. Moreover, this result could be extended to multiple dimensions for scalar conservation laws [87].

In this work we consider general three-dimensional systems of conservation laws as in (2.1), for which there is no general uniqueness, not even existence, proof for an entropy solution [26]. Nevertheless, we focus on the entropy analysis for non-linear systems of conservation laws in a mathematical language by introducing the concept of entropy functions, i.e. we define a scalar entropy function $S(\mathbf{u})$ that satisfies the following conditions:

- S is a strongly convex function of $\mathbf{u}$.

- S is augmented with corresponding entropy flux functions $\vec{f}^S$ in each spatial direction such that
$$\left(\frac{\partial S}{\partial \mathbf{u}}\right)^T \frac{\partial \mathbf{f}_i}{\partial \mathbf{u}} = \left(\frac{\partial f_i^S}{\partial \mathbf{u}}\right)^T \quad i = 1, 2, 3. \tag{2.46}$$

These conditions are referred to as the *convexity condition* and the *compatibility condition*. Moreover, the entropy function S and its corresponding entropy flux $\vec{f}^S$ form an entropy-entropy flux pair $(S, \vec{f}^S)$, which need not be unique [65, 102, 129].

From the entropy function we define a new vector of entropy variables

$$\mathbf{w} = \frac{\partial S}{\partial \mathbf{u}} \tag{2.47}$$

in order to contract the hyperbolic conservation laws (2.1) into entropy space. In particular, we apply the convexity and compatibility conditions, that define a one-to-one mapping and, thus, give us the entropy conservation law for smooth solutions

$$\mathbf{w}^T \left(\mathbf{u}_t + \vec{\nabla} \cdot \overleftrightarrow{\mathbf{f}} \right) = S_t + \vec{\nabla} \cdot \vec{f}^S = 0. \tag{2.48}$$

If we account for discontinuous solutions as well then the entropy equality becomes the entropy inequality [91], i.e.

$$S_t + \vec{\nabla} \cdot \vec{f}^S \leq 0, \tag{2.49}$$

where we use the mathematical convention of a decreasing entropy as mentioned above. But, we have to be careful here, because for discontinuous solutions the classical derivatives are not valid any more, as mentioned above. Hence, we consider an integral statement of (2.49)

$$\int_\Omega S_t \, \mathrm{dV} + \int_\Omega \vec{\nabla} \cdot \vec{f}^S \, \mathrm{dV} \leq 0, \tag{2.50}$$

which is equivalent to the weak formulation. This we obtain by multiplying with the distributions $\varphi \in C^1 (\Omega \times (0, T))$ with compact support as well as $\varphi \geq 0$ and integrating by parts, i.e.

$$\int_0^T \int_\Omega S \varphi_t \, \mathrm{dV}\mathrm{d}t + \int_0^T \int_\Omega \vec{f}^S \cdot \vec{\nabla} \varphi \, \mathrm{dV}\mathrm{d}t \geq 0. \tag{2.51}$$

This way we build the second law of thermodynamics into the system in a mathematically consistent way. Albeit the incomplete theory for three-dimensional systems of hyperbolic conservation laws, we can still utilize the entropy to determine a set of meaningful solutions.

For completeness and later analysis, we define some more quantities related to the mathematical entropy such as the entropy flux potential [128], which reads

$$\vec{\Psi} := \mathbf{w}^T \overleftrightarrow{\mathbf{f}} - \vec{f}^S. \tag{2.52}$$

Particularly in the discrete entropy investigations, we need the entropy flux potential, though it differs in case of the MHD equations.

Additionally, due to the strong convexity of the entropy function there exist symmetric positive-definite Jacobian matrices, which transform back and forth between the

variable spaces. The Jacobian matrix to move from conservative space to entropy space is found by computing the Hessian of the entropy function

$$\mathsf{H}^{-1} = \frac{\partial^2 S}{\partial \mathbf{u}^2} = \frac{\partial \mathbf{w}}{\partial \mathbf{u}}. \tag{2.53}$$

This matrix can be used to symmetrize the system [90] and we can immediately compute the other entropy Jacobian through inversion of (2.53) to obtain

$$\mathsf{H} = \frac{\partial \mathbf{u}}{\partial \mathbf{w}}. \tag{2.54}$$

Both Jacobians are important as they are used for theoretical derivations, e.g. in Sec. 5.1.2, as well as in the actual implementation, e.g. in Sec. 4.1.2.

Next, we apply the discussed entropy framework to the resistive GLM-MHD equations derived in the previous sections in order to investigate the entropic properties of this particular system of governing equations.

2.2.2. Entropy definitions for the GLM-MHD equations

In order to discuss the thermodynamic properties of the resistive GLM-MHD equations (2.39) we use the mathematical concepts of the first and second law of thermodynamics from the previous section. To do so, we first define the necessary quantities in a MHD context. Next, we exclusively examine the advective and non-conservative terms, before we show, that the resistive terms are also consistent with the second law of thermodynamics.

For the ideal and the resistive GLM-MHD equations, a suitable entropy function is the thermodynamical entropy density divided by the constant $(\gamma - 1)$ for convenience

$$S(\mathbf{u}) = -\frac{\varrho s}{\gamma - 1} \quad \text{with} \quad s = \ln\left(p\varrho^{-\gamma}\right), \tag{2.55}$$

where s is the thermodynamic entropy [89] with the physical assumptions $\varrho, p > 0$. From the entropy function we obtain the entropy variables from (2.47)

$$\mathbf{w} = \frac{\partial S}{\partial \mathbf{u}} = \left(\frac{\gamma - s}{\gamma - 1} - \beta \left\| \vec{v} \right\|^2, \ 2\beta v_1, \ 2\beta v_2, \ 2\beta v_3, \ -2\beta, \ 2\beta B_1, \ 2\beta B_2, \ 2\beta B_3, \ 2\beta\psi \right)^T \tag{2.56}$$

with $\beta = \frac{\varrho}{2p}$, which is proportional to the inverse temperature and simplifies the notation.

Furthermore, the corresponding entropy fluxes are defined as

$$\vec{f}^S = \vec{v}S, \tag{2.57}$$

as they satisfy (2.46) for the ideal MHD equations [9].

Since it will be necessary in later derivations and the proof of discrete entropy stability, we define the MHD entropy flux potential to be

$$\vec{\Psi} := \mathbf{w}^T \overleftrightarrow{\mathbf{f}}^a - \vec{f}^S + \theta \vec{B}. \tag{2.58}$$

We note, that in contrast to the general entropy flux potential (2.52) we now have an additional term on the right hand side, which comes from the Powell term (2.31) contracted into entropy space [23, 55] and is defined by

$$\theta = \mathbf{w}^T \boldsymbol{\phi}^{\text{MHD}} = 2\beta(\vec{v} \cdot \vec{B}). \tag{2.59}$$

Moreover, we see that the GLM part of the non-conservative term in (2.32) cancels internally, when contracted in entropy space, i.e.

$$\mathbf{w}^T \boldsymbol{\Upsilon}^{\text{GLM}} = \mathbf{w}^T \overleftrightarrow{\boldsymbol{\phi}}^{\text{GLM}} \cdot \vec{\nabla}\psi = \vec{0} \cdot \vec{\nabla}\psi = 0. \tag{2.60}$$

As introduced in the previous sections, we split the advective flux part into three terms to simplify the derivations and keep track of the individual contributions. This will be useful in the entire entropy analysis. Hence, we analogously split the total entropy flux potential $\vec{\Psi}$ into Euler, ideal MHD and GLM components

$$\vec{\Psi} = \vec{\Psi}^{\text{Euler}} + \vec{\Psi}^{\text{MHD}} + \vec{\Psi}^{\text{GLM}}, \tag{2.61}$$

where

$$\vec{\Psi}^{\text{Euler}} = \mathbf{w}^T \overleftrightarrow{\mathbf{f}}^{a,\text{Euler}} - \vec{f}^S, \tag{2.62}$$

$$\vec{\Psi}^{\text{MHD}} = \mathbf{w}^T \overleftrightarrow{\mathbf{f}}^{a,\text{MHD}} + \theta \vec{B}, \tag{2.63}$$

$$\vec{\Psi}^{\text{GLM}} = \mathbf{w}^T \overleftrightarrow{\mathbf{f}}^{a,\text{GLM}}. \tag{2.64}$$

With all these definitions we are now equipped to examine the entropic properties of the advective and resistive parts of the resistive GLM-MHD equations separately.

2.2.3. Continuous entropy analysis of the ideal GLM-MHD equations

The ideal GLM-MHD equations satisfy the first law of thermodynamics, because the evolution of the total fluid energy is one of the conserved quantities. This is true for our choice of the vector $\boldsymbol{\Upsilon}$ because it vanishes in the continuous analysis, even though on the discrete level, this is not the case as noted by many authors [34, 109, 75, 133]. However, the mathematical description of the second law of thermodynamics is more subtle, because the entropy is not explicitly built into the system. Thus, we use the defined entropy variables to present the first important statement in this work:

Lemma 1 (Entropy conservation for the ideal GLM-MHD equations)**.**
Smooth solutions of the ideal GLM-MHD equations (2.34) *with the non-conservative terms* (2.31) *and* (2.32) *are entropy conservative in terms of* (2.48) *on periodic domains.*

Proof. We start by contracting the ideal GLM-MHD system (2.34) with the entropy variables (2.56)

$$\mathbf{w}^T \mathbf{u}_t + \mathbf{w}^T \left(\vec{\nabla} \cdot \overset{\leftrightarrow}{\mathbf{f}}^a(\mathbf{u}) + \boldsymbol{\Upsilon} \right) = 0. \tag{2.65}$$

From the definition of the entropy variables (2.56) and the chain rule we have

$$\mathbf{w}^T \mathbf{u}_t = \left(\frac{\partial S}{\partial \mathbf{u}} \right)^T \mathbf{u}_t = S_t. \tag{2.66}$$

Next, for clarity, we separate the advective flux into Euler, ideal MHD and GLM parts defined in (2.35)

$$\overset{\leftrightarrow}{\mathbf{f}}^a(\mathbf{u}) = \overset{\leftrightarrow}{\mathbf{f}}^{a,\text{Euler}} + \overset{\leftrightarrow}{\mathbf{f}}^{a,\text{MHD}} + \overset{\leftrightarrow}{\mathbf{f}}^{a,\text{GLM}}. \tag{2.67}$$

The Euler terms generate the divergence of the entropy flux, e.g., [65]

$$\mathbf{w}^T \left(\vec{\nabla} \cdot \overset{\leftrightarrow}{\mathbf{f}}^{a,\text{Euler}} \right) = \vec{\nabla} \cdot \vec{f}^S, \tag{2.68}$$

the ideal MHD and non-conservative term cancel, e.g., [9, 97]

$$\mathbf{w}^T \left(\vec{\nabla} \cdot \overset{\leftrightarrow}{\mathbf{f}}^{a,\text{MHD}} + \boldsymbol{\Upsilon}^{\text{MHD}} \right) = 0 \tag{2.69}$$

and the GLM terms vanish as shown in [34]

$$\mathbf{w}^T \left(\vec{\nabla} \cdot \overset{\leftrightarrow}{\mathbf{f}}^{a,\text{GLM}} + \boldsymbol{\Upsilon}^{\text{GLM}} \right) = 0. \tag{2.70}$$

So, assuming smoothness of the solution and a periodic domain, we have

$$S_t + \vec{\nabla} \cdot \vec{f}^S = 0. \tag{2.71}$$

$\square$

Corollary 1. *When we consider discontinuous solutions in a weak formulation or include the damping* (2.38)*, we obtain the entropy inequality* (2.49) *as the final result of Lemma 1.*

Again we note, that the non-conservative term $\boldsymbol{\Upsilon}$ is necessary to obtain entropy conservation for $\vec{\nabla} \cdot \vec{B} \neq 0$ as is usually the case on the discrete level. Remarkably, Godunov found the same Powell source term (2.31) in order to symmetrize the non-divergence-free MHD system [55], whereas Derigs et al. derived it from the physics as pointed out in Sec. 2.1.3. Powell himself, first found this term in order to avoid singularities in the flux Jacobians for the primitive variables [109]. However, incorporating this term on the continuous level makes sense, since it will simplify the later analysis of the ideal GLM-MHD approximations.

2.2.4. Continuous entropy analysis of the resistive GLM-MHD equations

Next, we account for the resistive terms to demonstrate the entropy behavior for the resistive GLM-MHD equations as in [16]. To do so, we require a suitable representation of the resistive terms to discuss how they affect (2.49).

Lemma 2 (Entropy representation of viscous and resistive fluxes)**.**
The viscous and resistive fluxes of the resistive GLM-MHD equations in (2.40) *can be expressed by gradients of the entropy variables as*

$$\overset{\leftrightarrow}{\mathbf{f}}^v(\mathbf{u}, \vec{\nabla}\mathbf{u}) = \underline{\mathsf{K}}\vec{\nabla}\mathbf{w} \tag{2.72}$$

with a block matrix $\underline{\mathsf{K}} \in \mathbb{R}^{27 \times 27}$ *that is symmetric and positive semi-definite, i.e,*

$$\mathsf{q}^T\underline{\mathsf{K}}\mathsf{q} \geq 0, \quad \forall \mathsf{q} \in \mathbb{R}^{27}. \tag{2.73}$$

Proof. We consider the viscous and resistive fluxes of the resistive GLM-MHD system in (2.40)

$$\overset{\leftrightarrow}{\mathbf{f}}^v(\mathbf{u}, \vec{\nabla}\mathbf{u}) = [\mathbf{f}_1^v, \mathbf{f}_2^v, \mathbf{f}_3^v]^T . \tag{2.74}$$

Using the vector of entropy variables from (2.56)

$$\mathbf{w} = (w_1, \ldots, w_9)^T, \tag{2.75}$$

we find the following relations:

$$\vec{\nabla}v_i = -\frac{1}{w_5}\vec{\nabla}w_{1+i} + \frac{w_{1+i}}{w_5^2}\vec{\nabla}w_5, \quad \vec{\nabla}B_i = -\frac{1}{w_5}\vec{\nabla}w_{5+i} + \frac{w_{5+i}}{w_5^2}\vec{\nabla}w_5, \quad i = 1, 2, 3,$$

$$\vec{\nabla}\left(\frac{p}{\varrho}\right) = \frac{1}{w_5^2}\vec{\nabla}w_5.$$

With some algebraic effort we determine the matrices $\mathsf{K}_{ij} \in \mathbb{R}^{9 \times 9}, (i, j = 1, 2, 3)$ to express the viscous fluxes in terms of matrices times the gradients of entropy variables:

$$\mathbf{f}_1^v = \mathsf{K}_{11}\frac{\partial \mathbf{w}}{\partial x} + \mathsf{K}_{12}\frac{\partial \mathbf{w}}{\partial y} + \mathsf{K}_{13}\frac{\partial \mathbf{w}}{\partial z}, \tag{2.76}$$

$$\mathbf{f}_2^v = \mathsf{K}_{21}\frac{\partial \mathbf{w}}{\partial x} + \mathsf{K}_{22}\frac{\partial \mathbf{w}}{\partial y} + \mathsf{K}_{23}\frac{\partial \mathbf{w}}{\partial z}, \tag{2.77}$$

$$\mathbf{f}_3^v = \mathsf{K}_{31}\frac{\partial \mathbf{w}}{\partial x} + \mathsf{K}_{32}\frac{\partial \mathbf{w}}{\partial y} + \mathsf{K}_{33}\frac{\partial \mathbf{w}}{\partial z}. \tag{2.78}$$

We collect all these 9×9 block matrices into the matrix $\underline{\mathsf{K}} \in \mathbb{R}^{27 \times 27}$

$$\underline{\mathsf{K}} = \begin{pmatrix} \mathsf{K}_{11} & \mathsf{K}_{12} & \mathsf{K}_{13} \\ \mathsf{K}_{21} & \mathsf{K}_{22} & \mathsf{K}_{23} \\ \mathsf{K}_{31} & \mathsf{K}_{32} & \mathsf{K}_{33} \end{pmatrix}, \tag{2.79}$$

which clearly yields

$$\overset{\leftrightarrow}{\mathbf{f}}^v = \overset{\leftrightarrow}{\mathbf{f}}^v(\mathbf{u}, \vec{\nabla}\mathbf{u}) = \underline{\mathsf{K}}\vec{\nabla}\mathbf{w}. \tag{2.80}$$

For clarification, we present the first matrix

$$\mathsf{K}_{11} = \frac{1}{w_5}\begin{pmatrix} 0 & 0 & 0 & 0 & 0 & 0 & 0 & 0 & 0 \\ 0 & -\frac{4\mu_{\mathrm{NS}}}{3} & 0 & 0 & \frac{4\mu_{\mathrm{NS}}w_2}{3w_5} & 0 & 0 & 0 & 0 \\ 0 & 0 & -\mu_{\mathrm{NS}} & 0 & \frac{\mu_{\mathrm{NS}}w_3}{w_5} & 0 & 0 & 0 & 0 \\ 0 & 0 & 0 & -\mu_{\mathrm{NS}} & \frac{\mu_{\mathrm{NS}}w_4}{w_5} & 0 & 0 & 0 & 0 \\ 0 & \frac{4\mu_{\mathrm{NS}}w_2}{3w_5} & \frac{\mu_{\mathrm{NS}}w_3}{w_5} & \frac{\mu_{\mathrm{NS}}w_4}{w_5} & -\frac{4\mu_{\mathrm{NS}}w_2^2}{3w_5^2} - \frac{\mu_{\mathrm{NS}}w_3^2}{w_5^2} - \frac{\mu_{\mathrm{NS}}w_4^2}{w_5^2} + \frac{\kappa}{Rw_5} - \frac{\mu_{\mathrm{R}}w_7^2}{w_5^2} - \frac{\mu_{\mathrm{R}}w_8^2}{w_5^2} & 0 & \frac{\mu_{\mathrm{R}}w_7}{w_5} & \frac{\mu_{\mathrm{R}}w_8}{w_5} & 0 \\ 0 & 0 & 0 & 0 & 0 & 0 & 0 & 0 & 0 \\ 0 & 0 & 0 & 0 & \frac{\mu_{\mathrm{R}}w_7}{w_5} & 0 & -\mu_{\mathrm{R}} & 0 & 0 \\ 0 & 0 & 0 & 0 & \frac{\mu_{\mathrm{R}}w_8}{w_5} & 0 & 0 & -\mu_{\mathrm{R}} & 0 \\ 0 & 0 & 0 & 0 & 0 & 0 & 0 & 0 & 0 \end{pmatrix}. \tag{2.81}$$

The other matrices $\mathsf{K}_{12}, \ldots, \mathsf{K}_{33}$ are explicitly stated in appendix A.1. It is straightforward to verify that the matrix $\underline{\mathsf{K}}$ is symmetric by inspecting the block matrices listed in (2.81) and (A.1) - (A.8) where the following relationships hold

$$\mathsf{K}_{11} = \mathsf{K}_{11}^T, \ \mathsf{K}_{22} = \mathsf{K}_{22}^T, \ \mathsf{K}_{33} = \mathsf{K}_{33}^T, \ \mathsf{K}_{12} = \mathsf{K}_{21}^T, \ \mathsf{K}_{13} = \mathsf{K}_{31}^T, \ \mathsf{K}_{23} = \mathsf{K}_{32}^T. \tag{2.82}$$

To show that the matrix $\underline{\mathsf{K}}$ is positive semi-definite is more involved. We first note that it is possible to split the matrix (2.79) into the viscous terms associated with the Navier-Stokes equations and the resistive terms from the GLM-MHD equations as we also did with the viscous fluxes in (2.40). Therefore, we can rewrite the total diffusion matrix into two pieces

$$\underline{\mathsf{K}} = \underline{\mathsf{K}}^{\mathrm{NSE}} + \underline{\mathsf{K}}^{\mathrm{MHD}}, \tag{2.83}$$

where all terms with μ_{NS} are put in $\underline{\mathsf{K}}^{\mathrm{NSE}}$ and all terms with μ_{R} are in $\underline{\mathsf{K}}^{\mathrm{MHD}}$. It is easy to verify that the NSE and MHD block matrices are symmetric, as both satisfy (2.82). A further convenience is that the Navier-Stokes part, $\underline{\mathsf{K}}^{\mathrm{NSE}}$, is known to be positive semi-definite [36]

$$\mathsf{q}^T\underline{\mathsf{K}}^{\mathrm{NSE}}\mathsf{q} \geq 0, \quad \forall \mathsf{q} \in \mathbb{R}^{27}. \tag{2.84}$$

Thus, all that remains is to demonstrate that the additional resistive dissipation matrix, $\underline{\mathsf{K}}^{\mathrm{MHD}}$, is positive semi-definite. To do so, we examine the eigenvalues of the system. We use the computer algebra system Maxima [99] to find an explicit expression of the eigenvalues to be

$$\lambda_0^{\mathrm{MHD}} = 0, \ \lambda_1^{\mathrm{MHD}} = \frac{2\mu_{\mathrm{R}}p}{\varrho}, \ \lambda_2^{\mathrm{MHD}} = \frac{\mu_{\mathrm{R}}p\left(\|\vec{B}\|^2 + 2\right)}{\varrho}, \quad \text{multiplicity: } \{24, 1, 2\}. \tag{2.85}$$

Under the physical assumptions that $p, \varrho > 0$ and $\mu_{\mathrm{R}} \geq 0$ we see that the eigenvalues (2.85) of the matrix $\underline{\mathsf{K}}^{\mathrm{MHD}}$ are all non-negative. Hence, we have

$$\mathsf{q}^T \underline{\mathsf{K}} \mathsf{q} = \mathsf{q}^T \left(\underline{\mathsf{K}}^{\mathrm{NSE}} + \underline{\mathsf{K}}^{\mathrm{MHD}} \right) \mathsf{q} = \mathsf{q}^T \underline{\mathsf{K}}^{\mathrm{NSE}} \mathsf{q} + \mathsf{q}^T \underline{\mathsf{K}}^{\mathrm{MHD}} \mathsf{q} \geq 0, \quad \forall \mathsf{q} \in \mathbb{R}^{27}, \qquad (2.86)$$

so the block matrix $\underline{\mathsf{K}}$ is symmetric and positive semi-definite. $\qquad \square$

With the ability to rewrite the viscous fluxes as a combination of the entropy variable gradients, we can now address the entropic properties of the resistive GLM-MHD equations. In particular, we combine the results of Lemmas 1 and 2 to summarize our first main result:

Theorem 1 (Entropy inequality for the resistive GLM-MHD equations)**.**
Solutions of the resistive GLM-MHD equations (2.39) *with the non-conservative terms* (2.31), (2.32) *and* $\alpha \geq 0$ *in* (2.38) *satisfy the entropy inequality*

$$\int\limits_{\Omega} S_t \, \mathrm{dV} + \int\limits_{\partial\Omega} (\vec{f}^S \cdot \vec{n}) - \mathbf{w}^T (\overset{\leftrightarrow}{\mathbf{f}}^v \cdot \vec{n}) \, \mathrm{dS} \leq 0. \qquad (2.87)$$

Proof. We start by contracting the resistive GLM-MHD system (2.39) with the entropy variables (2.56):

$$\mathbf{w}^T \mathbf{u}_t + \mathbf{w}^T \left(\vec{\nabla} \cdot \overset{\leftrightarrow}{\mathbf{f}}^a (\mathbf{u}) + \boldsymbol{\Upsilon} \right) = \mathbf{w}^T \vec{\nabla} \cdot \overset{\leftrightarrow}{\mathbf{f}}^v (\mathbf{u}, \vec{\nabla}\mathbf{u}) + \mathbf{w}^T \mathbf{r}. \qquad (2.88)$$

From Lemma 1 we know, that the ideal GLM-MHD part yields

$$\mathbf{w}^T \mathbf{u}_t + \mathbf{w}^T \left(\vec{\nabla} \cdot \overset{\leftrightarrow}{\mathbf{f}}^a (\mathbf{u}) + \boldsymbol{\Upsilon} \right) = S_t + \vec{\nabla} \cdot \vec{f}^S. \qquad (2.89)$$

The damping source term for the GLM divergence cleaning is zero in all but its ninth component, so we see

$$\mathbf{w}^T \mathbf{r} = -2\alpha\beta\psi^2. \qquad (2.90)$$

Thus, we have

$$S_t + \vec{\nabla} \cdot \vec{f}^S = \mathbf{w}^T \vec{\nabla} \cdot \overset{\leftrightarrow}{\mathbf{f}}^v - 2\alpha\beta\psi^2. \qquad (2.91)$$

Since we are interested in weak solutions, we consider the integral statement of the continuous entropy inequality (2.50), i.e.

$$\int\limits_{\Omega} S_t \, \mathrm{dV} + \int\limits_{\Omega} \vec{\nabla} \cdot \vec{f}^S \, \mathrm{dV} = \int\limits_{\Omega} \mathbf{w}^T \vec{\nabla} \cdot \overset{\leftrightarrow}{\mathbf{f}}^v \, \mathrm{dV} - \int\limits_{\Omega} 2\alpha\beta\psi^2 \, \mathrm{dV}. \qquad (2.92)$$

Next, we apply Gauss' law to the entropy flux divergence and integration-by-parts to the viscous and resistive flux contributions to obtain

$$\int\limits_{\Omega} S_t \, \mathrm{dV} + \int\limits_{\partial\Omega} (\vec{f}^S \cdot \vec{n}) - \mathbf{w}^T (\overset{\leftrightarrow}{\mathbf{f}}^v \cdot \vec{n}) \, \mathrm{dS} = -\int\limits_{\Omega} (\vec{\nabla}\mathbf{w})^T \overset{\leftrightarrow}{\mathbf{f}}^v \, \mathrm{dV} - \int\limits_{\Omega} 2\alpha\beta\psi^2 \, \mathrm{dV}. \qquad (2.93)$$

Using the representation of the viscous flux in entropy variable gradients from Lemma 2, the viscous and resistive flux contribution in the domain become

$$-\int_\Omega (\vec{\nabla}\mathbf{w})^T \overset{\leftrightarrow}{\mathbf{f}}{}^v \, \mathrm{dV} = -\int_\Omega (\vec{\nabla}\mathbf{w})^T \underline{\mathsf{K}} \, \vec{\nabla}\mathbf{w} \, \mathrm{dV} \leq 0. \tag{2.94}$$

Assuming the damping parameter $\alpha \geq 0$ and a positive temperature, i.e. $\beta > 0$, the contribution of the damping term to the total entropy evolution is guaranteed negative $-2\alpha\beta\psi^2 \leq 0$, which finalizes the proof of Theorem 1. $\qquad\square$

Corollary 2. *If we consider a closed system, e.g. periodic boundary conditions, Theorem 1 shows that the total entropy is a decreasing function*

$$\int_\Omega S_t \, dV \leq 0. \tag{2.95}$$

In summary, we demonstrated that the resistive GLM-MHD equations satisfy an entropy inequality. To do so, we separated the advective contributions into Euler, ideal MHD and GLM pieces and considered the viscous contributions separately, which served to clarify how each term contributed to the entropy analysis. A major result is that it is possible to rewrite the resistive terms of the three-dimensional system in an entropy consistent way to demonstrate that those terms are entropy dissipative. We will use an identical splitting of the advective and diffusive terms in the discrete entropy stability proofs in Sec. 4 to directly mimic the continuous analysis.

3. Curved split form discontinuous Galerkin method

The numerical scheme considered in this work is the discontinuous Galerkin spectral element method (DGSEM), because it is not only high-order accurate and geometrically flexible, but also well suited for parallelization in an high performance computing (HPC) environment. Moreover, many extensions of DG discretization to obtain entropy aware solvers have recently been investigated and studied for different systems of equations [51, 139]. Hence, we seek for an entropy stable DGSEM on curvilinear geometries for the resistive GLM-MHD equations.

In the early 1970s discontinuous Galerkin methods were first proposed by Reed and Hill in the context of linear steady hyperbolic problems [110]. In the ensuing decades many researchers extended and improved this idea like Cockburn and Shu, who combined the spatial DG discretization with an high-order explicit Runge-Kutta time integration, see e.g. [27, 28]. The resulting scheme yields a powerful numerical framework to compute solutions of non-linear hyperbolic conservation laws. Even in the past years, DG methods remain a popular field of numerical research and recent publications still provide significant modifications and enhancements to the schemes [20, 51, 54, 85], e.g. the split form and flux differencing approximations discussed later.

In a MHD context, many DG methods have recently been developed for the ideal, e.g. [9, 113], as well as for the complete resistive system, e.g. [3, 138]. An extension including several divergence cleaning approaches and adaptive mesh refinement can be found in Guillet et al. [60]. Additional modifications of the scheme with respect to the entropic properties have been studied in e.g. [22, 97]. In this thesis we construct the entropy stable split form DGSEM on curvilinear meshes as presented in Bohm et al. [16].

In this chapter, we introduce the building blocks of our entropy stable DGSEM on three-dimensional curvilinear hexahedral meshes. Thus, we begin with the geometrical mapping of the equations, before we present the discrete operators and derive our DGSEM. Next, we account for the equivalent split form discretizations of the volume contributions, which are crucial for the discrete entropy analysis in the next chapter. Finally, we conclude with a brief discussion of the time integration for the resulting system of ordinary differential equations.

3.1. Mapping the equations

As a starting point for our numerical approximation, we subdivide the physical domain $\Omega \subset \mathbb{R}^3$ into N_{el} non-overlapping hexahedral elements $\mathfrak{E}_\iota$, $\iota = 1, 2, \ldots, N_{el}$. In particular, we use hexahedras and not tetrahedras, since our entire discretization is based on a tensor product ansatz. Furthermore, we are free to distribute our elements in the physical domain however we want, as long as they are conforming, such that neighboring elements have exactly one joint surface termed as interface. Due to the geometric flexibility of the DGSEM we are not restricted to structured meshes, but, in general, consider unstructured meshes, where an example is illustrated in Fig.3.1 for the two-dimensional case. The main difference between both grid types is, that for structured meshes a numbering of the elements comes naturally, since the elements are well ordered, whereas for unstructured meshes special algorithms and data structures are necessary e.g. to determine neighboring elements.
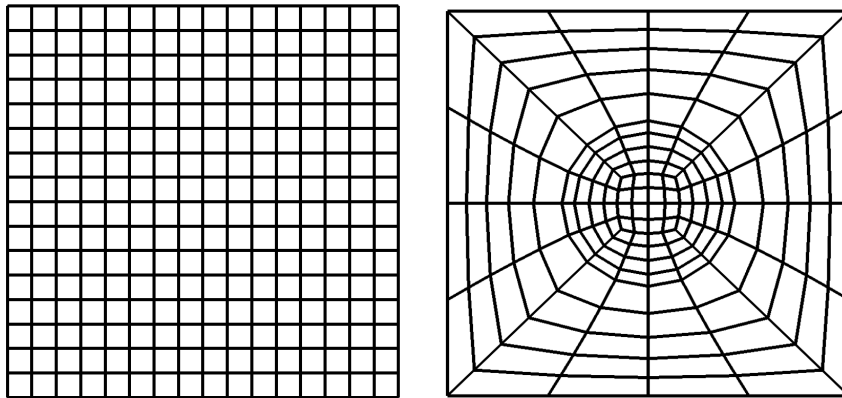
Figure 3.1.: Two-dimensional structured (left) and unstructured mesh (right).

Additionally, we allow the hexahedral elements to have curved faces if necessary, which is advantageous to accurately approximate certain physical structures [69]. Especially, the geometric flexibility offered by unstructured curvilinear meshes is needed to decompose, e.g., a domain around a spherical object without singularities [35] or a torus-shaped Tokamak reactor [71].

For the construction of curved and unstructured meshes, we create transformations $\vec{x} = \vec{X}^\iota(\vec{\xi})$ for all elements $\iota = 1, 2, \ldots, N_{el}$ from the reference space to these elements. Here, we use the notation for computational coordinates $\vec{\xi} = (\xi_1, \xi_2, \xi_3)^T = (\xi, \eta, \zeta)^T$ in the reference element $\mathfrak{E} = [-1, 1]^3$ and physical coordinates $\vec{x} = (x_1, x_2, x_3)^T = (x, y, z)^T$ in the original domain Ω. Since the discrete DG operators are solely defined in reference space, we require these mappings to rewrite the governing equations (2.39) in reference

25

space, too. In the following we consider one particular element and, thus, suppress the element index ι as well as the vector notation for the mapping.
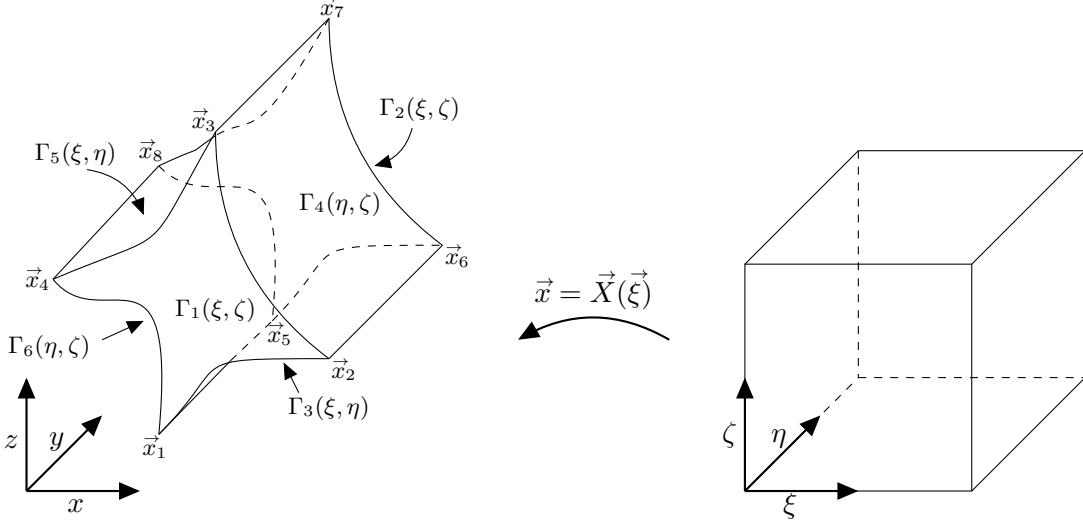

Figure 3.2.: Three-dimensional mapping from computational coordinates (right) to physical coordinates (left).

Commonly, the element mapping illustrated in Fig. 3.2 is a three-dimensional transfinite interpolation with linear blending [81, 140]. We assume, we have a representation of the curved surfaces $\Gamma_k, k = 1, \ldots, 6$, that bound an element, and build our mapping by linear interpolations between opposing faces, i.e.

$$X_{12}(\xi, \zeta) = \frac{1}{2} \left[(1 - \eta)\Gamma_1(\xi, \zeta) + (1 + \eta)\Gamma_2(\xi, \zeta) \right], \tag{3.1}$$

$$X_{35}(\xi, \eta) = \frac{1}{2} \left[(1 - \zeta)\Gamma_3(\xi, \eta) + (1 + \zeta)\Gamma_5(\xi, \eta) \right], \tag{3.2}$$

$$X_{64}(\eta, \zeta) = \frac{1}{2} \left[(1 - \xi)\Gamma_6(\eta, \zeta) + (1 + \xi)\Gamma_4(\eta, \zeta) \right]. \tag{3.3}$$

The final mapping will be a combination of the six interpolations, starting with the sum

$$
\begin{aligned}
\Sigma(\xi, \eta, \zeta) &= X_{12}(\xi, \zeta) + X_{35}(\xi, \eta) + X_{64}(\eta, \zeta) \\
&= \frac{1}{2} [(1 - \xi)\Gamma_6(\eta, \zeta) + (1 + \xi)\Gamma_4(\eta, \zeta) + (1 - \eta)\Gamma_1(\xi, \zeta) \\
&\quad + (1 + \eta)\Gamma_2(\xi, \zeta) + (1 - \zeta)\Gamma_3(\xi, \eta) + (1 + \zeta)\Gamma_5(\xi, \eta)].
\end{aligned}
\tag{3.4}
$$

In general, the combination (3.4) no longer matches the faces, e.g. for $\eta = -1$ we do not

obtain the corresponding surface Γ_1, i.e.

$$\Sigma(\xi, -1, \zeta) = \Gamma_1(\xi, \zeta) + \frac{1}{2}[(1-\xi)\Gamma_6(-1,\zeta) + (1+\xi)\Gamma_4(-1,\zeta)$$
$$+ (1-\zeta)\Gamma_3(\xi,-1) + (1+\zeta)\Gamma_5(\xi,-1)] \neq \Gamma_1(\xi, \zeta). \tag{3.5}$$

To match the faces, in each direction ξ, η and ζ, we subtract of the additional terms that appear in the braces of (3.5) as well as the ones occurring from the other five faces. We find these linear interpolants to be

$$\Pi_\xi = \left(\frac{1-\xi}{2}\right)\left[\frac{1}{2}\{(1-\eta)\Gamma_1(-1,\zeta) + (1+\eta)\Gamma_2(-1,\zeta) + (1-\zeta)\Gamma_3(-1,\eta)\right.$$
$$\left. + (1+\zeta)\Gamma_5(-1,\eta)\} + \left(\frac{1+\xi}{2}\right)\left[\frac{1}{2}\{(1-\eta)\Gamma_1(1,\zeta)\right.$$
$$\left. + (1+\eta)\Gamma_2(1,\zeta) + (1-\zeta)\Gamma_3(1,\eta) + (1+\zeta)\Gamma_5(1,\eta)\}\right], \tag{3.6}$$

$$\Pi_\eta = \left(\frac{1-\eta}{2}\right)\left[\frac{1}{2}\{(1-\xi)\Gamma_6(-1,\zeta) + (1+\xi)\Gamma_4(-1,\zeta) + (1-\zeta)\Gamma_3(\xi,-1)\right.$$
$$\left. + (1+\zeta)\Gamma_5(\xi,-1)\} + \left(\frac{1+\eta}{2}\right)\left[\frac{1}{2}\{(1-\xi)\Gamma_6(1,\zeta)\right.$$
$$\left. + (1+\xi)\Gamma_4(1,\zeta) + (1-\zeta)\Gamma_3(\xi,1) + (1+\zeta)\Gamma_5(\xi,1)\}\right], \tag{3.7}$$

and

$$\Pi_\zeta = \left(\frac{1-\zeta}{2}\right)\left[\frac{1}{2}\{(1-\eta)\Gamma_1(\xi,-1) + (1+\eta)\Gamma_2(\xi,-1) + (1-\xi)\Gamma_6(\eta,-1)\right.$$
$$\left. + (1+\xi)\Gamma_4(\eta,-1)\} + \left(\frac{1+\zeta}{2}\right)\left[\frac{1}{2}\{(1-\eta)\Gamma_1(\xi,1)\right.$$
$$\left. + (1+\eta)\Gamma_2(\xi,1) + (1-\xi)\Gamma_6(\eta,1) + (1+\xi)\Gamma_4(\eta,1)\}\right]. \tag{3.8}$$

However, subtracting the correction terms (3.6), (3.7), and (3.8) from (3.4) removes the interior contributions twice. Thus, to complete the correction to (3.4), we add the transfinite map of the reference cube to a straight-sided hexahedral element

$$X_H(\vec{\xi}, t) = \frac{1}{8}\{\vec{x}_1(1-\xi)(1-\eta)(1-\zeta) + \vec{x}_2(1+\xi)(1-\eta)(1-\zeta)$$
$$+ \vec{x}_3(1+\xi)(1+\eta)(1-\zeta) + \vec{x}_4(1-\xi)(1+\eta)(1-\zeta)$$
$$+ \vec{x}_5(1-\xi)(1-\eta)(1+\zeta) + \vec{x}_6(1+\xi)(1-\eta)(1+\zeta)$$
$$+ \vec{x}_7(1+\xi)(1+\eta)(1+\zeta) + \vec{x}_8(1-\xi)(1+\eta)(1+\zeta)\}, \tag{3.9}$$

where $\vec{x}_i$, $i = 1, \ldots, 8$ are the corners of the hexahedron. We arrive at the final transfinite interpolation with linear blending for a curved-sided hexahedron

$$X(\vec{\xi}) = \Sigma(\vec{\xi}) - \frac{1}{2}\left[\Pi_\xi + \Pi_\eta + \Pi_\zeta\right] + X_H(\vec{\xi}), \tag{3.10}$$

where we divide the correction terms (3.6), (3.7), and (3.8) in half as they count the contribution from each of the twelve faces twice.

As presented in the next section, the faces are approximated by polynomials, so the calculation of the *metric terms*

$$\vec{X}_\xi = \frac{\partial \vec{X}}{\partial \xi}, \quad \vec{X}_\eta = \frac{\partial \vec{X}}{\partial \eta}, \quad \vec{X}_\zeta = \frac{\partial \vec{X}}{\partial \zeta} \tag{3.11}$$

is straightforward. We particularly need these metric terms to approximate the co-variant basis vectors

$$\vec{a}_i = \frac{\partial \vec{X}}{\partial \xi^i}, \quad i = 1, 2, 3, \tag{3.12}$$

and volume-weighted contra-variant vectors

$$J\vec{a}^i = \vec{a}_j \times \vec{a}_k, \quad (i, j, k) \text{ cyclic}, \tag{3.13}$$

where the Jacobian of the transformation is given by

$$J = \vec{a}_i \cdot (\vec{a}_j \times \vec{a}_k), \quad (i, j, k) \text{ cyclic}. \tag{3.14}$$

We require these vectors as well as the Jacobian to transform derivatives and integrals back and forth between the reference element and physical space. Essentially, they occur from the chain rule and, in general, vary on curved elements. But still, the divergence of a constant flux vanishes in the reference cube, i.e. the contra-variant vectors satisfy the metric identities [80]

$$\sum_{i=1}^{3} \frac{\partial (Ja_n^i)}{\partial \xi^i} = 0, \quad n = 1, 2, 3. \tag{3.15}$$

We note, that our discrete entropy analysis reveals that the proper discretization of the metric identities is crucial.

In order to express the transformation of the gradient and divergence operators compactly, we define two different matrices dependent on the metric terms

$$\underline{\mathsf{M}} = \begin{bmatrix} Ja_1^1\,\mathsf{I}_9 & Ja_1^2\,\mathsf{I}_9 & Ja_1^3\,\mathsf{I}_9 \\ Ja_2^1\,\mathsf{I}_9 & Ja_2^2\,\mathsf{I}_9 & Ja_2^3\,\mathsf{I}_9 \\ Ja_3^1\,\mathsf{I}_9 & Ja_3^2\,\mathsf{I}_9 & Ja_3^3\,\mathsf{I}_9 \end{bmatrix}, \qquad \underline{M} = \begin{bmatrix} Ja_1^1 & Ja_1^2 & Ja_1^3 \\ Ja_2^1 & Ja_2^2 & Ja_2^3 \\ Ja_3^1 & Ja_3^2 & Ja_3^3 \end{bmatrix} \tag{3.16}$$

with the 9×9 unit matrix I_9, as 9 is the size of the GLM-MHD system. Applying these matrices, the transformation of the gradient of a state or a scalar is

$$\vec{\nabla}_x \mathbf{u} = \begin{bmatrix} \mathbf{u}_x \\ \mathbf{u}_y \\ \mathbf{u}_z \end{bmatrix} = \frac{1}{J}\mathsf{M}\begin{bmatrix} \mathbf{u}_\xi \\ \mathbf{u}_\eta \\ \mathbf{u}_\zeta \end{bmatrix} = \frac{1}{J}\mathsf{M}\vec{\nabla}_\xi \mathbf{u}, \quad \vec{\nabla}_x h = \frac{1}{J}\underline{M}\vec{\nabla}_\xi h, \tag{3.17}$$

and the transformation of the divergence is

$$\vec{\nabla}_x \cdot \overset{\leftrightarrow}{\mathbf{g}} = \frac{1}{J}\vec{\nabla}_\xi \cdot \left(\mathsf{M}^T \overset{\leftrightarrow}{\mathbf{g}}\right), \quad \vec{\nabla}_x \cdot \vec{h} = \frac{1}{J}\vec{\nabla}_\xi \cdot \left(\underline{M}^T \vec{h}\right). \tag{3.18}$$

Similarly, we define contra-variant block vectors and contra-variant spatial vectors, e.g.

$$\overset{\leftrightarrow}{\tilde{\mathbf{g}}} = \underline{\mathsf{M}}^T \overset{\leftrightarrow}{\mathbf{g}}, \qquad \vec{\tilde{h}} = \underline{M}^T \vec{h}. \tag{3.19}$$

For the discretization of the viscous and resistive terms we introduce the gradient of the entropy variables as an additional unknown $\overset{\leftrightarrow}{\mathbf{q}}$. Applying the transformations to the divergence and the gradient, we get the transformed resistive GLM-MHD equations

$$J\mathbf{u}_t + \vec{\nabla}_\xi \cdot \overset{\leftrightarrow}{\tilde{\mathbf{f}}}{}^a + \left(\vec{\nabla}_\xi \cdot \vec{\tilde{B}}\right)\phi^{\mathrm{MHD}} + \overset{\leftrightarrow}{\tilde{\phi}}{}^{\mathrm{GLM}} \cdot \vec{\nabla}_\xi \psi = \vec{\nabla}_\xi \cdot \overset{\leftrightarrow}{\tilde{\mathbf{f}}}{}^v\left(\mathbf{u}, \overset{\leftrightarrow}{\mathbf{q}}\right) + J\mathbf{r} \tag{3.20}$$

$$J\overset{\leftrightarrow}{\mathbf{q}} = \underline{\mathsf{M}}\vec{\nabla}_\xi \mathbf{w}.$$

The next step is the weak formulation of the transformed equations (3.20), for which we multiply by test functions $\boldsymbol{\varphi}$ and $\overset{\leftrightarrow}{\boldsymbol{\vartheta}}$. Next, we use integration-by-parts for the flux divergence as well as for the non-conservative term to arrive at

$$\langle J\mathbf{u}_t, \boldsymbol{\varphi}\rangle + \int_{\partial\mathfrak{E}} \boldsymbol{\varphi}^T \left\{\overset{\leftrightarrow}{\tilde{\mathbf{f}}}{}^a - \overset{\leftrightarrow}{\tilde{\mathbf{f}}}{}^v\right\} \cdot \vec{n}\,\hat{s}\,\mathrm{dS} - \left\langle \overset{\leftrightarrow}{\tilde{\mathbf{f}}}{}^a, \vec{\nabla}_\xi \boldsymbol{\varphi}\right\rangle$$

$$+ \int_{\partial\mathfrak{E}} \boldsymbol{\varphi}^T \phi^{\mathrm{MHD}}(\vec{\tilde{B}} \cdot \vec{n})\hat{s}\,\mathrm{dS} - \left\langle \vec{\tilde{B}}, \vec{\nabla}_\xi(\boldsymbol{\varphi}^T \phi^{\mathrm{MHD}})\right\rangle$$

$$+ \int_{\partial\mathfrak{E}} \boldsymbol{\varphi}^T (\overset{\leftrightarrow}{\tilde{\phi}}{}^{\mathrm{GLM}} \cdot \vec{n})\psi\hat{s}\,\mathrm{dS} - \left\langle \psi, \vec{\nabla}_\xi \cdot (\boldsymbol{\varphi}^T \overset{\leftrightarrow}{\tilde{\phi}}{}^{\mathrm{GLM}})\right\rangle = -\left\langle \overset{\leftrightarrow}{\tilde{\mathbf{f}}}{}^v, \vec{\nabla}_\xi \boldsymbol{\varphi}\right\rangle + \langle J\mathbf{r}, \boldsymbol{\varphi}\rangle$$

$$\left\langle J\overset{\leftrightarrow}{\mathbf{q}}, \overset{\leftrightarrow}{\boldsymbol{\vartheta}}\right\rangle = \int_{\partial\mathfrak{E}} \mathbf{w}^T \left(\overset{\leftrightarrow}{\boldsymbol{\vartheta}} \cdot \vec{n}\right)\hat{s}\,\mathrm{dS} - \left\langle \mathbf{w}, \vec{\nabla}_\xi \cdot \left(\underline{\mathsf{M}}^T \overset{\leftrightarrow}{\boldsymbol{\vartheta}}\right)\right\rangle.$$

$$\tag{3.21}$$

Here, we introduced the inner product notation on the reference element for state and block vectors

$$\langle \mathbf{u}, \mathbf{v}\rangle = \int_E \mathbf{u}^T \mathbf{v}\,\mathrm{d}\xi\mathrm{d}\eta\mathrm{d}\zeta \quad \text{and} \quad \left\langle \overset{\leftrightarrow}{\mathbf{f}}, \overset{\leftrightarrow}{\mathbf{g}}\right\rangle = \int_E \sum_{i=1}^3 \mathbf{f}_i^T \mathbf{g}_i\,\mathrm{d}\xi\mathrm{d}\eta\mathrm{d}\zeta \tag{3.22}$$

as well as the surface element $\hat{s}$ and the outward pointing unit normal vector $\vec{n}$ in physical space. In particular, these are defined for all faces of the reference element as

$$
\begin{aligned}
\xi = \pm 1 \quad &: \quad \hat{s}(\eta,\zeta) := \left|J\vec{a}^1(\pm 1,\eta,\zeta)\right|, \quad \vec{n}(\eta,\zeta) := \pm J\vec{a}^1(\pm 1,\eta,\zeta)/\hat{s}(\eta,\zeta), \\
\eta = \pm 1 \quad &: \quad \hat{s}(\xi,\zeta) := \left|J\vec{a}^2(\xi,\pm 1,\zeta)\right|, \quad \vec{n}(\xi,\zeta) := \pm J\vec{a}^2(\xi,\pm 1,\zeta)/\hat{s}(\xi,\zeta), \quad (3.23)\\
\zeta = \pm 1 \quad &: \quad \hat{s}(\xi,\eta) := \left|J\vec{a}^3(\xi,\eta,\pm 1)\right|, \quad \vec{n}(\xi,\eta) := \pm J\vec{a}^3(\xi,\eta,\pm 1)/\hat{s}(\xi,\eta).
\end{aligned}
$$

It is important to note, that under the assumption of a conforming mesh, the surface element $\hat{s}$ is continuous across the element interface and the normal vector only changes sign.

3.2. Spectral element approximation

We now introduce all necessary dicretization tools in the reference space $\mathfrak{E} = [-1,1]^3$ to derive the spectral element method. First, for a local approximation with polynomial degree N, we define $N+1$ Legendre-Gauss-Lobatto (LGL) nodes and weights, ξ_i and ω_i, $i = 0, \dots, N$, on the unit interval $[-1,1]$. The LGL nodes are computed as roots of the Legendre polynomials [81], include the boundaries and are internally not uniformly distributed as illustrated in Fig. 3.3.

Figure 3.3.: Legendre-Gauss-Lobatto nodes for $N = 3$.

Next, we span the one-dimensional nodal Lagrange basis functions

$$
\ell_i(\xi) = \prod_{\substack{j=0 \\ j \neq i}}^{N} \frac{\xi - \xi_j}{\xi_i - \xi_j} \quad \text{for } i = 0, \dots, N, \quad (3.24)
$$

which satisfy the Kronecker-delta property, i.e. $\ell_j(\xi_i) = \delta_{ij}$ with $\delta_{ij} = 1$ for $i = j$ and $\delta_{ij} = 0$ for $i \neq j$. These one-dimensional basis functions are extended to the three-dimensional reference element by a tensor product ansatz [81]. We approximate the state vector in one element with a polynomial interpolation on the LGL nodes denoted by capital letters, i.e.

$$
\mathbf{u}(x,y,z,t)|_{\mathfrak{E}_\iota} = \mathbf{u}^\iota(\xi,\eta,\zeta,t) \approx \sum_{i,j,k=0}^{N} \mathbf{U}^\iota_{ijk}(t)\ell_i(\xi)\ell_j(\eta)\ell_k(\zeta) \equiv \mathbf{U}^\iota(\xi,\eta,\zeta,t). \quad (3.25)
$$

Here, $\mathbf{U}_{ijk}^{\iota}(t)$ are the time-dependent nodal degrees of freedom for the considered element $\mathfrak{E}_{\iota}$, time t and $i, j, k = 0, \ldots, N$. Alternatively, we write the interpolation of a function g through those nodes as $G = \mathbb{I}^N(g) \in \mathbb{P}^N(E)$. Further, we interpolate the fluxes the same way, i.e.

$$
\begin{aligned}
\overleftrightarrow{\mathbf{f}}(x, y, z, t)|_{\mathfrak{E}_{\iota}} = \overleftrightarrow{\mathbf{f}}^{\iota}(\xi, \eta, \zeta, t) &\approx \sum_{i,j,k=0}^{N} \overleftrightarrow{\mathbf{F}}(\mathbf{U}_{ijk}^{\iota}(t)) \ell_i(\xi) \ell_j(\eta) \ell_k(\zeta) \\
&= \sum_{i,j,k=0}^{N} \overleftrightarrow{\mathbf{F}}_{ijk}^{\iota}(t) \ell_i(\xi) \ell_j(\eta) \ell_k(\zeta) \equiv \overleftrightarrow{\mathbf{F}}^{\iota}(\xi, \eta, \zeta, t).
\end{aligned}
\tag{3.26}
$$

Due to the non-linearity of the fluxes aliasing errors might arise from this interpolation, which leads to an inexact flux evaluation. However, this issue is well-known from spectral methods and the introduced errors are usually small [50, 77]. In the following derivations we focus on the approximation in one particular element and, thus, suppress the superscript for the element index.

Moreover, spatial derivatives now fall on the local polynomial basis of degree N. Thus, we define the discrete derivative operator, which in one spatial dimension reads as

$$
\mathcal{D}_{ij} := \left. \frac{\partial \ell_j}{\partial \xi} \right|_{\xi = \xi_i}, \qquad i, j = 0, \ldots, N.
\tag{3.27}
$$

Before we introduce the quadratures and discretize the weak form of the governing equations (3.21), we address the geometrical components from the previous section. For instance, the proper computation of the metric terms is crucial to guarantee that the *discrete metric identities* hold

$$
\sum_{i=1}^{3} \frac{\partial \mathbb{I}^N(Ja_n^i)}{\partial \xi^i} = 0, \quad n = 1, 2, 3.
\tag{3.28}
$$

We ensure this property if we compute the metric terms as curl [80], i.e.

$$
Ja_n^i = -\hat{x}_i \cdot \nabla_{\xi} \times \left(\mathbb{I}^N(X_l \nabla_{\xi} X_m) \right), \quad i = 1, 2, 3, \ n = 1, 2, 3, \ (n, m, l) \text{ cyclic}.
\tag{3.29}
$$

In particular, we use the discrete derivative matrix from (3.27) to evaluate the gradients in (3.29), which guarantees free stream preservation discretely and has already been shown to be important for numerical stability, e.g. [53, 83, 139].

Additionally, we use two-dimensional isoparametric approximations to construct the surfaces of the mapping in (3.1)-(3.3), e.g.

$$
\Gamma_1(\xi, \zeta) = \sum_{i,j=0}^{M} \Gamma_1(\xi_i, \zeta_j) \ell_i(\xi) \ell_j(\zeta)
\tag{3.30}
$$

with suitable interpolation nodes $\xi_i, \zeta_j \in [-1, 1]$, $i, j = 0, \ldots, M$ and the one-dimensional Lagrange basis as in (3.24). We note, that these surface interpolations are of degree $M+1$ with $M \leq N$ to maintain the overall order of the approximation as well as free stream preservation [81].

In general, integrals in the variational form are approximated by the according LGL quadrature rule. Consequently, the collocation of the LGL polynomial approximation ansatz and the quadrature leads to a discretely orthogonal mass matrix, which in one spatial dimension is

$$\mathcal{M} = \operatorname{diag}(\omega_0, \ldots, \omega_N). \tag{3.31}$$

As mentioned above, this particular choice of the DG derivative operator yields the summation-by-parts (SBP) property [51]

$$(\mathcal{M}\mathcal{D}) + (\mathcal{M}\mathcal{D})^T = \mathcal{Q} + \mathcal{Q}^T = \mathcal{B}, \tag{3.32}$$

where we introduce the notation of the SBP matrix, $\mathcal{Q}$, as well as the boundary matrix

$$\mathcal{B} = \operatorname{diag}(-1, 0, \ldots, 0, 1). \tag{3.33}$$

We stress again, that the SBP property is crucial for the stability proofs presented in this work. Furthermore, we note, that it is also important for our proofs on curvilinear meshes, that the mass matrix, also known as the norm matrix in the language of SBP finite difference methods, is diagonal.

Tensor product extension is used to approximate integrals in multiple spatial dimensions. As such we express the discrete inner product between two functions f and g in three space dimensions as

$$\langle f, g \rangle_N = \sum_{n,m,l=0}^{N} f_{nml} g_{nml} \omega_n \omega_m \omega_l \equiv \sum_{n,m,l=0}^{N} f_{nml} g_{nml} \omega_{nml}, \tag{3.34}$$

where $f_{nml} = f(\xi_n, \eta_m, \zeta_l)$, etc.

A consequence of the SBP property is a discrete version of the extended Gauss Law [82]. That is, for any $V = \mathbb{I}^N(v)$

$$\left\langle \vec{\nabla}_\xi \cdot \overleftrightarrow{\vec{\mathbf{F}}}, V \right\rangle_N = \int_{\partial\mathfrak{E}, N} V^T \left(\overleftrightarrow{\vec{\mathbf{F}}} \cdot \hat{n} \right) \mathrm{dS} - \left\langle \overleftrightarrow{\vec{\mathbf{F}}}, \vec{\nabla}_\xi V \right\rangle_N = \int_{\partial\mathfrak{E}, N} V^T \left(\overleftrightarrow{\vec{\mathbf{F}}} \cdot \vec{n} \right) \hat{s} \, \mathrm{dS} - \left\langle \overleftrightarrow{\vec{\mathbf{F}}}, \vec{\nabla}_\xi V \right\rangle_N, \tag{3.35}$$

which we can apply to mimic integration-by-parts in the continuous derivations. Here, the discrete surface integral is also defined via LGL quadrature, and the integrand is

transformed with the collocated surface metrics from (3.23), yielding

$$
\int\limits_{\partial\mathfrak{E},N} V^T\left(\overset{\leftrightarrow}{\mathbf{F}}\cdot\hat{n}\right)\mathrm{dS} = \int\limits_{\partial\mathfrak{E},N} V^T\left(\sum_{i=1}^{3}\left(J\vec{a}^{\,i}\cdot\overset{\leftrightarrow}{\mathbf{F}}\right)\hat{n}_i\right)\,\mathrm{dS}
$$

$$
\equiv \sum_{j,k=0}^{N}\omega_{jk}\left[V^T\left(\overset{\leftrightarrow}{\mathbf{F}}\cdot\vec{n}\right)\hat{s}\right]_{\eta_j,\zeta_k}^{\xi=\pm1} + \sum_{i,k=0}^{N}\omega_{ik}\left[V^T\left(\overset{\leftrightarrow}{\mathbf{F}}\cdot\vec{n}\right)\hat{s}\right]_{\xi_i,\zeta_k}^{\eta=\pm1} + \sum_{i,j=0}^{N}\omega_{ij}\left[V^T\left(\overset{\leftrightarrow}{\mathbf{F}}\cdot\vec{n}\right)\hat{s}\right]_{\xi_i,\eta_j}^{\zeta=\pm1}
$$

$$
= \int\limits_{\partial\mathfrak{E},N} V^T\left(\overset{\leftrightarrow}{\mathbf{F}}\cdot\vec{n}\right)\hat{s}\,\mathrm{dS}\,.
$$

(3.36)

With all these definitions at hand, we next replace the Jacobian, the metric terms as well as the solution vector, its time derivative, the fluxes, the test functions and non-conservative terms by polynomial interpolations in (3.21), to obtain the *discrete weak form* of the DGSEM

$$
\left\langle \mathbb{I}^N(J)\,\mathbf{U}_t,\boldsymbol{\varphi}\right\rangle_N + \int\limits_{\partial\mathfrak{E},N}\boldsymbol{\varphi}^T\left\{\mathbf{F}_n^a - \mathbf{F}_n^v\right\}\hat{s}\,\mathrm{dS} - \left\langle \overset{\leftrightarrow}{\mathbf{F}}^a - \overset{\leftrightarrow}{\mathbf{F}}^v,\vec{\nabla}_\xi\boldsymbol{\varphi}\right\rangle_N
$$

$$
+ \int\limits_{\partial\mathfrak{E},N}\boldsymbol{\varphi}^T\boldsymbol{\Phi}^{\mathrm{MHD}}B_n\hat{s}\,\mathrm{dS} - \left\langle \vec{\tilde{B}},\vec{\nabla}_\xi(\boldsymbol{\varphi}^T\boldsymbol{\Phi}^{\mathrm{MHD}})\right\rangle_N
$$

$$
+ \int\limits_{\partial\mathfrak{E},N}\boldsymbol{\varphi}^T\boldsymbol{\Phi}_n^{\mathrm{GLM}}\psi\hat{s}\,\mathrm{dS} - \left\langle \psi,\vec{\nabla}_\xi\cdot\mathbb{I}^N\left(\boldsymbol{\varphi}^T\overset{\leftrightarrow}{\boldsymbol{\Phi}}^{\mathrm{GLM}}\right)\right\rangle_N = \left\langle \mathbb{I}^N(J)\,\mathbf{R},\boldsymbol{\varphi}\right\rangle_N\,,
$$

$$
\left\langle \mathbb{I}^N(J)\,\overset{\leftrightarrow}{\mathbf{Q}},\overset{\leftrightarrow}{\boldsymbol{\vartheta}}\right\rangle_N = \int\limits_{\partial\mathfrak{E},N}\mathbf{W}^T\left(\overset{\leftrightarrow}{\boldsymbol{\vartheta}}\cdot\vec{n}\right)\hat{s}\,\mathrm{dS} - \left\langle \mathbf{W},\vec{\nabla}_\xi\cdot\mathbb{I}^N\left(\underline{\mathsf{M}}^T\overset{\leftrightarrow}{\boldsymbol{\vartheta}}\right)\right\rangle_N\,,
$$

(3.37)

where we introduced compact notation for normal quantities, e.g. the normal flux in physical space $\mathbf{F}_n = \left(\overset{\leftrightarrow}{\mathbf{F}}\cdot\vec{n}\right)$.

Due to the discontinuous nature of our local polynomial ansatz, values at the element interfaces are not uniquely defined. The elements are coupled through the boundary terms by way of consistent *numerical fluxes*, which we denote as $\mathbf{F}_n^{a,*}$, $\mathbf{F}_n^{v,*}$ and $\mathbf{W}^*$. For now, we postpone the selection of these numerical flux functions to the next chapter. Further, the non-conservative terms also couple elements through the boundary. Again, for now, the definition of the non-conservative terms at the boundary is left ambiguous and we denote these unknowns at the element interface by $\left(\boldsymbol{\Phi}^{\mathrm{MHD}}B_n\right)^{\lozenge}$ and $\left(\boldsymbol{\Phi}_n^{\mathrm{GLM}}\psi\right)^{\lozenge}$ to obtain

$$\left\langle \mathbb{I}^N(J)\,\mathbf{U}_t, \boldsymbol{\varphi} \right\rangle_N + \int_{\partial\mathfrak{E},N} \boldsymbol{\varphi}^T \left\{ \mathbf{F}_n^{a,*} - \mathbf{F}_n^{v,*} \right\} \hat{s}\,\mathrm{dS} - \left\langle \overleftrightarrow{\mathbf{F}}^a - \overleftrightarrow{\mathbf{F}}^v, \vec{\nabla}_\xi \boldsymbol{\varphi} \right\rangle_N$$

$$+ \int_{\partial\mathfrak{E},N} \boldsymbol{\varphi}^T \left(\boldsymbol{\Phi}^{\mathrm{MHD}} B_n \right)^{\lozenge} \hat{s}\,\mathrm{dS} - \left\langle \vec{B}, \vec{\nabla}_\xi \left(\boldsymbol{\varphi}^T \boldsymbol{\Phi}^{\mathrm{MHD}} \right) \right\rangle_N$$

$$+ \int_{\partial\mathfrak{E},N} \boldsymbol{\varphi}^T \left(\boldsymbol{\Phi}_n^{\mathrm{GLM}} \psi \right)^{\lozenge} \hat{s}\,\mathrm{dS} - \left\langle \psi, \vec{\nabla}_\xi \cdot \mathbb{I}^N\left(\boldsymbol{\varphi}^T \overleftrightarrow{\boldsymbol{\Phi}}^{\mathrm{GLM}} \right) \right\rangle_N = \left\langle \mathbb{I}^N(J)\,\mathbf{R}, \boldsymbol{\varphi} \right\rangle_N,$$

$$\left\langle \mathbb{I}^N(J)\,\overleftrightarrow{\mathbf{Q}}, \overleftrightarrow{\boldsymbol{\vartheta}} \right\rangle_N = \int_{\partial\mathfrak{E},N} \mathbf{W}^{*,T} \left(\overleftrightarrow{\boldsymbol{\vartheta}} \cdot \vec{n} \right) \hat{s}\,\mathrm{dS} - \left\langle \mathbf{W}, \vec{\nabla}_\xi \cdot \mathbb{I}^N\!\left(\underline{\mathsf{M}}^T \overleftrightarrow{\boldsymbol{\vartheta}} \right) \right\rangle_N.$$

$$(3.38)$$

Applying the discrete extended Gauss law (3.35) to the flux and non-conservative terms of the first equation in (3.38) gives the *strong form* of the DGSEM, which we use in this work to approximate solutions of the resistive GLM-MHD equations

$$\left\langle \mathbb{I}^N(J)\,\mathbf{U}_t, \boldsymbol{\varphi} \right\rangle_N + \left\langle \vec{\nabla}_\xi \cdot \mathbb{I}^N\!\left(\overleftrightarrow{\mathbf{F}}^a \right), \boldsymbol{\varphi} \right\rangle_N + \int_{\partial\mathfrak{E},N} \boldsymbol{\varphi}^T \left\{ \left(\mathbf{F}_n^{a,*} - \mathbf{F}_n^a \right) \right\} \hat{s}\,\mathrm{dS}$$

$$- \left\langle \vec{\nabla}_\xi \cdot \mathbb{I}^N\!\left(\overleftrightarrow{\mathbf{F}}^v \right), \boldsymbol{\varphi} \right\rangle_N - \int_{\partial\mathfrak{E},N} \boldsymbol{\varphi}^T \left\{ \mathbf{F}_n^{v,*} - \mathbf{F}_n^v \right\} \hat{s}\,\mathrm{dS}$$

$$+ \left\langle \boldsymbol{\Phi}^{\mathrm{MHD}} \vec{\nabla}_\xi \cdot \mathbb{I}^N\!\left(\vec{B} \right), \boldsymbol{\varphi} \right\rangle_N + \int_{\partial\mathfrak{E},N} \boldsymbol{\varphi}^T \left\{ \left(\boldsymbol{\Phi}^{\mathrm{MHD}} B_n \right)^{\lozenge} - \boldsymbol{\Phi}^{\mathrm{MHD}} B_n \right\} \hat{s}\,\mathrm{dS}$$

$$+ \left\langle \overleftrightarrow{\boldsymbol{\Phi}}^{\mathrm{GLM}} \cdot \vec{\nabla}_\xi \mathbb{I}^N(\psi), \boldsymbol{\varphi} \right\rangle_N + \int_{\partial\mathfrak{E},N} \boldsymbol{\varphi}^T \left\{ \left(\boldsymbol{\Phi}_n^{\mathrm{GLM}} \psi \right)^{\lozenge} - \boldsymbol{\Phi}_n^{\mathrm{GLM}} \psi \right\} \hat{s}\,\mathrm{dS}$$

$$= \left\langle \mathbb{I}^N(J)\,\mathbf{R}, \boldsymbol{\varphi} \right\rangle_N,$$

$$\left\langle \mathbb{I}^N(J)\,\overleftrightarrow{\mathbf{Q}}, \overleftrightarrow{\boldsymbol{\vartheta}} \right\rangle_N = \int_{\partial\mathfrak{E},N} \mathbf{W}^{*,T} \left(\overleftrightarrow{\boldsymbol{\vartheta}} \cdot \vec{n} \right) \hat{s}\,\mathrm{dS} - \left\langle \mathbf{W}, \vec{\nabla}_\xi \cdot \mathbb{I}^N\!\left(\underline{\mathsf{M}}^T \overleftrightarrow{\boldsymbol{\vartheta}} \right) \right\rangle_N.$$

$$(3.39)$$

3.3. Split form approximation

In this section we consider the discretizations of the volume terms needed in (3.39). For a standard strong form DG approximation these are evaluated in a tensor product fashion by simply multiplying the polynomial flux approximations (3.26) with the derivative matrix (3.27), i.e.

$$
\left[\vec{\nabla}_\xi \cdot \mathbb{I}^N\!\left(\overset{\leftrightarrow}{\tilde{\mathbf{F}}}\right)\right]_{ijk} \approx \left[\vec{\mathbb{D}}^{\mathrm{S}}\!\cdot\!\overset{\leftrightarrow}{\tilde{\mathbf{F}}}\right]_{ijk}
$$
$$
= \sum_{m=0}^{N} \mathcal{D}_{im}\left(\tilde{\mathbf{F}}_1\right)_{mjk} + \sum_{m=0}^{N} \mathcal{D}_{jm}\left(\tilde{\mathbf{F}}_2\right)_{imk} + \sum_{m=0}^{N} \mathcal{D}_{km}\left(\tilde{\mathbf{F}}_3\right)_{ijm} \tag{3.40}
$$

for $i,j,k = 0,\dots,N$.

But, especially for an entropy compatible discretization of the advective flux divergence as well as the non-conservative volume terms we require a different representation based on the works of Fisher et al. and Carpenter et al. [20, 42, 51]. Referring to this, the key concept is to rewrite the volume integrals into an equivalent sub-cell finite volume differencing form. Therefore, we introduce a staggered grid, which consists of $N{+}2$ nodes $\bar{\xi}_i, i = 0,\dots,N{+}1$ for the given LGL nodes $\xi_i, i = 0,\dots,N$ and is illustrated for the case $N = 3$ in Fig.3.4.
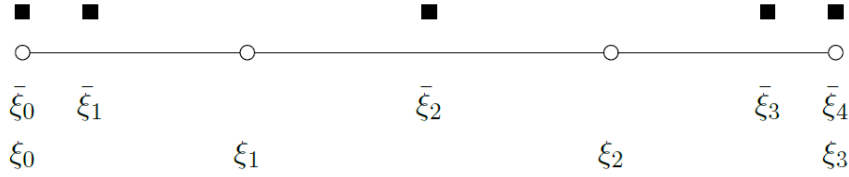
Figure 3.4.: Staggered grid for $N = 3$.

In general, the staggered grid nodes are defined by

$$
\bar{\xi}_0 = \xi_0, \quad \bar{\xi}_{N+1} = \xi_N \quad \text{and} \quad \bar{\xi}_i - \bar{\xi}_{i-1} = \mathcal{M}_{ii} = \omega_i \quad \text{for } i = 1,\dots,N. \tag{3.41}
$$

We note, that the inclusion of the boundary nodes is crucial, since the flux differencing framework is based on the SBP property (3.32). This also enables us to interpolate the auxiliary fluxes onto the staggered grid by $\bar{\mathbf{F}} = \mathbb{I}^{N+1}(\mathbf{F})$ [42], so that we can reformulate the one-dimensional and unmapped volume term as

$$
\sum_{m=0}^{N} \mathcal{D}_{im}\,\mathbf{F}_m = \frac{\bar{\mathbf{F}}_{i+1} - \bar{\mathbf{F}}_i}{\omega_i} \tag{3.42}
$$

for $i = 0, \ldots, N$. For diagonal norm SBP operators this formulation directly states conservation of the volume discretizations in the sense of Lax-Wendroff due to the telescoping flux differencing [42, 92].

Remarkably, Fisher and Carpenter [42] specified the fluxes on the right-hand-side of (3.42) to be $\bar{\mathbf{F}}_0 = \mathbf{F}_0, \bar{\mathbf{F}}_{N+1} = \mathbf{F}_N$ and

$$\bar{\mathbf{F}}_i \approx \sum_{k=i}^{N} \sum_{l=0}^{i-1} 2\, \mathcal{Q}_{lk} \mathbf{F}^{\#}(\mathbf{U}_l, \mathbf{U}_k) \quad \text{for } i = 1, \ldots, N, \tag{3.43}$$

which introduces the two-point volume flux $\mathbf{F}^{\#}$. This additional numerical flux has to be consistent $\mathbf{F}^{\#}(\mathbf{U}, \mathbf{U}) = \mathbf{F}(\mathbf{U})$ as well as symmetric $\mathbf{F}^{\#}(\mathbf{U}, \mathbf{V}) = \mathbf{F}^{\#}(\mathbf{V}, \mathbf{U})$ and is extended to high-order by (3.43). If we insert this particular choice of $\bar{\mathbf{F}}$ into (3.42) and use some algebraic manipulations, we finally obtain the alternative volume discretization

$$\sum_{m=0}^{N} \mathcal{D}_{im}\, \mathbf{F}_m = \frac{\bar{\mathbf{F}}_{i+1} - \bar{\mathbf{F}}_i}{\omega_i} \approx \sum_{m=0}^{N} 2\, \mathcal{D}_{im} \mathbf{F}^{\#}(\mathbf{U}_i, \mathbf{U}_m) \tag{3.44}$$

for $i = 0, \ldots, N$. Considering the standard volume form on the left side and the flux differencing form on the right side we notice, that, except for a factor of two, we solely replace the original flux approximation by the new two-point numerical volume flux. Most notably, this formulation allows us to build any consistent and symmetric numerical flux function in our volume approximation, whereas the final discretization is not only high-order accurate, but also maintains certain flux related properties.

The simplest choice for the volume flux is the central flux $\mathbf{F}^{\#} = \mathbf{F}^{\text{central}}$ with

$$\mathbf{F}^{\text{central}}(\mathbf{U}, \mathbf{V}) = \frac{1}{2} \left[\mathbf{F}(\mathbf{U}) + \mathbf{F}(\mathbf{V}) \right] \equiv \{\!\{ \mathbf{F} \}\!\}, \tag{3.45}$$

which collapses to the standard DGSEM volume approximation (3.40). Moreover, we can construct plenty of other choices for the numerical volume fluxes, where each volume flux results in a different scheme [54]. For instance, if we are interested in the kinetic energy of the Euler equations, we can create kinetic energy preserving fluxes for the Euler equations like the ones of Pirozzili [108] or Kenndy and Gruber [76]. Recently, Gassner et al. [54] investigated on possible volume flux approximations, their properties and special relation to the underlying splittings in the flux components. At least for simple products in the fluxes they demonstrated a connection between the averaging of the discrete states and the continuous split formulations by the product rule, which does not hold discretely. Hence, we obtain different approximations, e.g. the continuous flux $(\varrho v_1)_x$ corresponds to the discrete evaluation of $\{\!\{ \varrho v_1 \}\!\}$ in the volume flux, and the continuously equivalent flux $\frac{1}{2} \left[(\varrho v_1)_x + \varrho (v_1)_x + (\varrho)_x v_1 \right]$ corresponds to the discrete evaluation of $\{\!\{ \varrho \}\!\} \{\!\{ v_1 \}\!\}$ in the volume flux. Due to this strong relation, such discretizations of the volume terms as in (3.44) are called split forms, even though the actual splitting on the continuous level is not always known.

The main goal in this work is to find a numerical volume flux, which has certain entropic properties and will be introduced in next chapter. The overall split form DG approximation then has two numerical fluxes, one at the surface and the other inside the volume.

Recalling our strong form DGSEM (3.39), we define the special split form volume integral for the advective flux divergence as

$$
\left[\vec{\nabla}_\xi \cdot \mathbb{I}^N\!\left(\overset{\leftrightarrow}{\mathbf{F}}{}^a\right)\right]_{ijk} \approx \left[\vec{\mathbb{D}}\cdot\overset{\leftrightarrow}{\mathbf{F}}{}^{a,\#}\right]_{ijk} = 2\sum_{m=0}^{N} \mathcal{D}_{im}\, \overset{\leftrightarrow}{\mathbf{F}}{}^{a,\#}(\mathbf{U}_{ijk}, \mathbf{U}_{mjk}) \cdot \left\{\!\!\left\{ J\vec{a}^{\,1} \right\}\!\!\right\}_{(i,m)jk}
$$
$$
+\, 2\sum_{m=0}^{N} \mathcal{D}_{jm}\, \overset{\leftrightarrow}{\mathbf{F}}{}^{a,\#}(\mathbf{U}_{ijk}, \mathbf{U}_{imk}) \cdot \left\{\!\!\left\{ J\vec{a}^{\,2} \right\}\!\!\right\}_{i(j,m)k} \qquad (3.46)
$$
$$
+\, 2\sum_{m=0}^{N} \mathcal{D}_{km}\, \overset{\leftrightarrow}{\mathbf{F}}{}^{a,\#}(\mathbf{U}_{ijk}, \mathbf{U}_{ijm}) \cdot \left\{\!\!\left\{ J\vec{a}^{\,3} \right\}\!\!\right\}_{ij(k,m)}
$$

at each point $i,j,k = 0,\ldots,N$ of an element. The arithmetic mean of the metric terms in each spatial direction is written compactly, e.g. using the notation in the ξ-direction

$$
\left\{\!\!\left\{ \cdot \right\}\!\!\right\}_{(i,m)jk} = \frac{1}{2}\left((\cdot)_{ijk} + (\cdot)_{mjk} \right). \qquad (3.47)
$$

Particularly, we split away the metric terms for reasons of geometrical de-aliasing and as it is an important component of the proofs in the next chapter [16].

In a similar fashion, the volume contributions of the non-conservative terms are approximated by

$$
\left[\mathbf{\Phi}^{\mathrm{MHD}}\vec{\nabla}_\xi \cdot \mathbb{I}^N\!\left(\vec{B}\right)\right]_{ijk} \approx \left[\mathbf{\Phi}^{\mathrm{MHD}}\vec{\mathbb{D}}_{\mathrm{div}}^{\mathrm{NC}}\cdot\vec{B}\right]_{ijk} = \sum_{m=0}^{N} \mathcal{D}_{im}\, \mathbf{\Phi}_{ijk}^{\mathrm{MHD}}\left(\vec{B}_{mjk}\cdot\left\{\!\!\left\{ J\vec{a}^{\,1} \right\}\!\!\right\}_{(i,m)jk}\right)
$$
$$
+ \sum_{m=0}^{N} \mathcal{D}_{jm}\, \mathbf{\Phi}_{ijk}^{\mathrm{MHD}}\left(\vec{B}_{imk}\cdot\left\{\!\!\left\{ J\vec{a}^{\,2} \right\}\!\!\right\}_{i(j,m)k}\right)
$$
$$
+ \sum_{m=0}^{N} \mathcal{D}_{km}\, \mathbf{\Phi}_{ijk}^{\mathrm{MHD}}\left(\vec{B}_{ijm}\cdot\left\{\!\!\left\{ J\vec{a}^{\,3} \right\}\!\!\right\}_{ij(k,m)}\right)
$$
$$
(3.48)
$$

and

$$
\left[\overset{\leftrightarrow}{\tilde{\mathbf{\Phi}}}{}^{\mathrm{GLM}} \cdot \vec{\nabla}_\xi \mathbb{I}^N(\psi)\right]_{ijk} \approx \left[\overset{\leftrightarrow}{\tilde{\mathbf{\Phi}}}{}^{\mathrm{GLM}} \cdot \vec{\mathbb{D}}_{\mathrm{grad}}^{\mathrm{NC}}\psi\right]_{ijk} = \sum_{m=0}^{N} \mathcal{D}_{im}\left(J\vec{a}_{ijk}^{\,1}\cdot\overset{\leftrightarrow}{\mathbf{\Phi}}{}_{ijk}^{\mathrm{GLM}}\right)\psi_{mjk}
$$
$$
+ \sum_{m=0}^{N} \mathcal{D}_{jm}\left(J\vec{a}_{ijk}^{\,2}\cdot\overset{\leftrightarrow}{\mathbf{\Phi}}{}_{ijk}^{\mathrm{GLM}}\right)\psi_{imk} \qquad (3.49)
$$
$$
+ \sum_{m=0}^{N} \mathcal{D}_{km}\left(J\vec{a}_{ijk}^{\,3}\cdot\overset{\leftrightarrow}{\mathbf{\Phi}}{}_{ijk}^{\mathrm{GLM}}\right)\psi_{ijm}
$$

for $i, j, k = 0, \ldots, N$, which introduces compact notation for the discrete divergence and gradient on the non-conservative terms. We will also show in the discrete entropy proofs, that it is important to separate the derivative on the magnetic field components and the metric terms.

Next, we address the discretization of the viscous terms in the resistive MHD equations. The volume contributions are computed as in the standard DGSEM (3.40), such that

$$
\left[\vec{\nabla}_\xi \cdot \mathbb{I}^N\!\left(\overset{\leftrightarrow}{\tilde{\mathbf{F}}}{}^v \right) \right]_{ijk} \approx \left[\vec{\mathbb{D}}^{\mathrm{S}} \!\cdot\! \overset{\leftrightarrow}{\tilde{\mathbf{F}}}{}^v \right]_{ijk}
$$
$$
= \sum_{m=0}^{N} \mathcal{D}_{im} \left(\tilde{\mathbf{F}}_1^v \right)_{mjk} + \sum_{m=0}^{N} \mathcal{D}_{jm} \left(\tilde{\mathbf{F}}_2^v \right)_{imk} + \sum_{m=0}^{N} \mathcal{D}_{km} \left(\tilde{\mathbf{F}}_3^v \right)_{ijm}
\tag{3.50}
$$

for $i, j, k = 0, \ldots, N$, where the metric terms are included in the transformed viscous fluxes $\tilde{\mathbf{F}}_l^v$, $l = 1, 2, 3$. Inserting the volume discretizations (3.46), (3.48), (3.49) and (3.50) into (3.39) we obtain the final split form DGSEM:

$$
\left\langle \mathbb{I}^N(J)\, \mathbf{U}_t, \boldsymbol{\varphi} \right\rangle_N + \left\langle \vec{\mathbb{D}} \!\cdot\! \overset{\leftrightarrow}{\tilde{\mathbf{F}}}{}^{a,\#}, \boldsymbol{\varphi} \right\rangle_N + \int_{\partial \mathfrak{E}, N} \boldsymbol{\varphi}^T \left\{ \mathbf{F}_n^{a,*} - \mathbf{F}_n^a \right\} \hat{s}\, \mathrm{dS}
$$
$$
- \left\langle \vec{\mathbb{D}}^{\mathrm{S}} \!\cdot\! \overset{\leftrightarrow}{\tilde{\mathbf{F}}}{}^v, \boldsymbol{\varphi} \right\rangle_N - \int_{\partial \mathfrak{E}, N} \boldsymbol{\varphi}^T \left\{ \mathbf{F}_n^{v,*} - \mathbf{F}_n^v \right\} \hat{s}\, \mathrm{dS}
$$
$$
+ \left\langle \boldsymbol{\Phi}^{\mathrm{MHD}} \vec{\mathbb{D}}_{\mathrm{div}}^{\mathrm{NC}} \!\cdot\! \vec{B}, \boldsymbol{\varphi} \right\rangle_N + \int_{\partial \mathfrak{E}, N} \boldsymbol{\varphi}^T \left\{ \left(\boldsymbol{\Phi}^{\mathrm{MHD}} B_n \right)^{\Diamond} - \boldsymbol{\Phi}^{\mathrm{MHD}} B_n \right\} \hat{s}\, \mathrm{dS}
$$
$$
+ \left\langle \overset{\leftrightarrow}{\tilde{\boldsymbol{\Phi}}}{}^{\mathrm{GLM}} \cdot \vec{\mathbb{D}}_{\mathrm{grad}}^{\mathrm{NC}} \psi, \boldsymbol{\varphi} \right\rangle_N + \int_{\partial \mathfrak{E}, N} \boldsymbol{\varphi}^T \left\{ \left(\boldsymbol{\Phi}_n^{\mathrm{GLM}} \psi \right)^{\Diamond} - \boldsymbol{\Phi}_n^{\mathrm{GLM}} \psi \right\} \hat{s}\, \mathrm{dS}
\tag{3.51}
$$
$$
= \left\langle \mathbb{I}^N(J)\, \mathbf{R}, \boldsymbol{\varphi} \right\rangle_N,
$$

$$
\left\langle \mathbb{I}^N(J)\, \overset{\leftrightarrow}{\mathbf{Q}}, \overset{\leftrightarrow}{\boldsymbol{\vartheta}} \right\rangle_N = \int_{\partial \mathfrak{E}, N} \mathbf{W}^{*,T} \left(\overset{\leftrightarrow}{\boldsymbol{\vartheta}} \cdot \vec{n} \right) \hat{s}\, \mathrm{dS} - \left\langle \mathbf{W}, \vec{\nabla}_\xi \cdot \mathbb{I}^N\!\left(\underline{\mathsf{M}}^T \overset{\leftrightarrow}{\boldsymbol{\vartheta}} \right) \right\rangle_N .
$$

3.4. Time integration

The resulting semi-discrete formulation in the first equation of (3.51) is a system of time-dependent ordinary differential equations. Hence, in order to advance these approximations in time, we need an appropriate time integration method.

For this purpose, there are many numerical procedures available in the literature like explicit, implicit or semi-implicit time integrators. Whereas the latter two are well-suited for steady problems with possibly larger time steps [84], an explicit solver is a more preferable choice for our scheme, because the herein considered solutions of the resistive GLM-MHD equations are compressible and advection dominated. In particular, we use the explicit 4th order low storage Runge-Kutta method (RKM) of Carpenter and Kennedy [21] to advance the element-wise approximations in time for each element $\iota = 1, \ldots, N_{\text{el}}$. An additional advantage of such an high-order accurate RKM is, that its explicit and local nature results in a very efficient method for massively parallel computations [70]. We note, that investigations on other suitable time integrators for DG methods is ongoing research such as strong stability preserving Runge-Kutta schemes [58], local time stepping methods [50, 52, 142] or the recently developed entropy stable space-time DG methods [46].

If we equip the overall discretization with an explicit Runge-Kutta method, the maximum allowable time step is restricted to guarantee stability [61]. The selection of the time step for hyperbolic systems is equation-dependent as it involves the fastest wave speed. In order for the results of the numerical approximation to remain relevant we select the advective time step using the Courant, Friedrichs, and Lewy (CFL) condition. One version of the CFL condition for DG type approximations in three spatial dimensions on curved hexahedral meshes is [50]

$$\Delta t^a \leq \frac{\text{CFL}}{|\lambda_{\max}^a|} \left(\frac{h}{2N + 1} \right), \tag{3.52}$$

where $\lambda_{\max}^a$ is the largest advective wave speed at the current time from (2.23). Particularly, we approximate these eigenvalues locally by the velocities, fast magneto-acoustic wave speeds (2.21) and the contra-variant vectors (3.13). The CFL condition (3.52) ensures that the spectrum of the DG operator is contained in the stability region of the time integrator guaranteeing a stable time step selection. We note again, that for the GLM-MHD equations, the correction speed c_h also appears in the spectra of the flux Jacobians and, thus, must be bounded.

Moreover, we scale the advective time step by the polynomial degree N and an approximation of the minimum element size

$$h = \min_{\iota = 1, \ldots, N_{\text{el}}} h_\iota, \tag{3.53}$$

whereas the extent of single elements can be computed by e.g.

$$h_\iota = \min_{i,j,k=0,\ldots,N} \frac{J_{ijk}}{2}. \tag{3.54}$$

The well CFL number $\texttt{CFL} \in (0,1]$ in (3.52) is an adjustable coefficient.

For explicit time integration of the viscous terms there is an additional constraint on selecting the time step. Hence, a similar condition as the CFL condition for the advective terms (3.52) is used for the viscous time step selection [52]

$$\Delta t^v \leq \frac{\texttt{DFL}}{|\lambda_{\max}^v|} \left(\frac{h}{2N+1}\right)^2, \tag{3.55}$$

where $\lambda_{\max}^v$ is an approximation to the largest eigenvalue of the viscous flux Jacobians, N is the polynomial order of the approximation and $\texttt{DFL} \in (0,1]$ is an adjustable coefficient. One possible choice for the diffusive eigenvalues is [3]

$$\lambda_{\max}^v = \max_{\iota=1,\ldots,N_{\mathrm{el}}} \tilde{v}^\iota \tag{3.56}$$

with the element-wise approximations

$$v^\iota = \max\left\{\mu_{\mathrm{R}}, \mu_{\mathrm{NS}} \max\left[\frac{\gamma}{\mathrm{Pr}}, \frac{4}{3}\right] \max_{i,j,k=0,\ldots,N} \frac{1}{\varrho_{ijk}}\right\} \tag{3.57}$$

scaled by the contra-variant vectors (3.13).

The complete explicit time step is then selected to be

$$\Delta t = \min\{\Delta t^a, \Delta t^v\}. \tag{3.58}$$

Obviously, a major drawback of an explicit RKM is that the minimal time step over the whole domain has to be used during the entire simulation, which is especially troublesome if the magnitude of the local resolution varies drastically over the computational domain. Thus, advancing with the minimum time step might result in high decrease in efficiency of such methods. However, the DGSEM combined with the presented explicit low storage RKM provides a numerical method, that is highly parallelizable and remains applicable to model a wide variety of compressible flows [70]. Especially, we are interested in advection driven problems, so that the advective time step (3.52) dominates the viscous timestep (3.55) in most applications and, thus, the considered problems are not stiff for a physical reason.

4. Entropy stable DG scheme for the resistive GLM-MHD equations

The goal of this chapter is the design of a high-order discontinuous Galerkin method to solve either, the ideal GLM-MHD system (2.34) in an entropy conservative (EC) or the resistive GLM-MHD system (2.39) in an entropy stable (ES) fashion, respectively. In both cases, we extend the resulting scheme to an overall entropy stable nodal DG method by adding appropriate dissipation terms to the entropy conservative formulation at element boundaries in order to satisfy the second law of thermodynamics. Thus, the entropy stable numerical method produces physically meaningful approximations, which are particularly desired in the presence of discontinuities or shocks.

Much work in the numerics community has been invested over the years to develop approximations of non-linear hyperbolic PDE systems that remain thermodynamically consistent, e.g. [23, 43, 47, 51, 130, 141]. This began with the pioneering work of Tadmor [126, 127] to develop low-order finite volume approximations. Extension to higher spatial order was recently achieved in the context of DG methods for the Shallow-Water equations [139] as well as the compressible Navier-Stokes equations [20, 53]. Moreover, there is recent work on entropy stable DG methods applied to the ideal MHD equations by Rossmanith [113], Gallego-Valencia [48] and most notably the recent work by Liu et al. [97], who introduced an entropy stable DG discretization on Cartesian meshes of the non-conservative PDE term proportional to the divergence-free constraint. Remarkably, Carpenter et al. inspired most of these works by showing that the conditions to develop entropy stable approximations at low-order immediately apply to high-order methods provided the derivative approximation satisfies the SBP property as shown in [20, 41, 42].

The derivations and discussion in this chapter are divided into digestible pieces to highlight the construction of each part of the final numerical scheme. We begin with contracting the split form DG formulation into entropy space and defining the total discrete entropy of the approximation in Sec. 4.1. Next, we construct the necessary conditions for an EC low-order finite volume scheme in Sec. 4.1.1, which is a critical first step as obtaining a high-order approximation requires this low-order analysis. With the help of this condition we derive numerical fluxes in Sec. 4.1.2, that are discretely entropy conservative for the convective part of the considered system and can be extended to entropy stable fluxes by adding special dissipation terms. The remaining structure of this section is very similar to that of Sec. 2.1, where the governing equations of interest were

built incrementally, so too will the numerical approximation. The high-order EC DG scheme for the ideal GLM-MHD equations on three dimensional unstructured curvilinear meshes is presented in Sec. 4.2, where the analysis is divided into volume and surface contributions. Finally, the novel entropy stable scheme for the resistive GLM-MHD system is presented in Sec. 4.3.

4.1. Discrete entropy definitions

In order to obtain entropy stability, we start with the split form DG approximation (3.51) and contract into entropy space by replacing the first test function with the interpolant of the entropy variables and the second one with the interpolant of the viscous fluxes:

$$
\begin{aligned}
\left\langle \mathbb{I}^N(J)\,\mathbf{U}_t, \mathbf{W} \right\rangle_N &= -\left\langle \vec{\mathbb{D}}\cdot\overleftrightarrow{\mathbf{F}}^{a,\#}, \mathbf{W} \right\rangle_N - \left\langle \mathbf{\Phi}^{\mathrm{MHD}}\vec{\mathbb{D}}_{\mathrm{div}}^{\mathrm{NC}}\cdot\vec{B}, \mathbf{W} \right\rangle_N - \left\langle \vec{\overleftrightarrow{\mathbf{\Phi}}}^{\mathrm{GLM}}\cdot\vec{\mathbb{D}}_{\mathrm{grad}}^{\mathrm{NC}}\psi, \mathbf{W} \right\rangle_N \\
&\quad -\int_{\partial\mathfrak{E},N}\mathbf{W}^T\left[\mathbf{F}_n^{a,*}-\mathbf{F}_n^a\right]\hat{s}\,\mathrm{dS} - \int_{\partial\mathfrak{E},N}\mathbf{W}^T\left\{\left(\mathbf{\Phi}^{\mathrm{MHD}}B_n\right)^\Diamond-\mathbf{\Phi}^{\mathrm{MHD}}B_n\right\}\hat{s}\,\mathrm{dS} - \int_{\partial\mathfrak{E},N}\mathbf{W}^T\left\{\left(\mathbf{\Phi}_n^{\mathrm{GLM}}\psi\right)^\Diamond-\mathbf{\Phi}_n^{\mathrm{GLM}}\psi\right\}\hat{s}\,\mathrm{dS} \\
&\quad +\left\langle \vec{\mathbb{D}}^{\mathrm{S}}\cdot\overleftrightarrow{\mathbf{F}}^v, \mathbf{W} \right\rangle_N + \int_{\partial\mathfrak{E},N}\mathbf{W}^T\left[\mathbf{F}_n^{v,*}-\mathbf{F}_n^v\right]\hat{s}\,\mathrm{dS} + \left\langle \mathbb{I}^N(J)\,\mathbf{R}, \mathbf{W} \right\rangle_N \\[2mm]
\left\langle \mathbb{I}^N(J)\,\overleftrightarrow{\mathbf{Q}}, \overleftrightarrow{\mathbf{F}}^v \right\rangle_N &= \int_{\partial\mathfrak{E},N}\mathbf{W}^{*,T}\left(\overleftrightarrow{\mathbf{F}}^v\cdot\vec{n}\right)\hat{s}\,\mathrm{dS} - \left\langle \mathbf{W}, \vec{\mathbb{D}}^{\mathrm{S}}\cdot\overleftrightarrow{\mathbf{F}}^v \right\rangle_N
\end{aligned}
$$

(4.1)

Here, we have intentionally arranged the advective plus non-conservative volume parts, the advective plus non-conservative surface parts and the viscous parts plus the damping source term of the first equation into separate rows.

The time derivative term in (4.1) is the rate of change of the entropy in the element. Assuming that the chain rule with respect to differentiation in time holds (time continuity), we use the contraction property of the entropy variable (2.66) at each LGL node within the element to see that on each element $\iota = 1, \ldots, N_{\mathrm{el}}$ we have

$$
\left\langle \mathbb{I}^N(J)\,\mathbf{U}_t, \mathbf{W} \right\rangle_N = \sum_{i,j,k=0}^N J_{ijk}\omega_i\omega_j\omega_k\mathbf{W}_{ijk}^T\frac{d\mathbf{U}_{ijk}}{dt} = \sum_{i,j,k=0}^N J_{ijk}\omega_{ijk}\frac{dS_{ijk}}{dt} = \left\langle \mathbb{I}^N(J)\,S_t, 1 \right\rangle_N.
$$

(4.2)

To obtain the time derivative of the total discrete entropy we sum over all elements

$$
\frac{d\overline{S}}{dt} \equiv \sum_{\iota=1}^{N_{\mathrm{el}}}\left\langle J^\iota S_t^\iota, 1 \right\rangle_N.
$$

(4.3)

The final goal of this chapter is to demonstrate the entropy stability of the contracted DG approximation (4.1) for the resistive GLM-MHD system. That is, we want the discrete total entropy in a closed system (periodic boundary conditions) to be a decreasing

function

$$\frac{d\overline{S}}{dt} \leq 0. \tag{4.4}$$

To get the result (4.4) we examine each row in the first equation of (4.1) incrementally. We demonstrate the behavior of the advective as well as non-conservative volume contributions (first row) in Sec. 4.2.1 and the according interface contributions (second row) in in Sec. 4.2.2. Throughout these sections, we highlight how the metric terms and the GLM divergence cleaning parts affect the approximation. Then, in Sec. 4.3, we assess the contribution of the viscous and resistive terms (third row) by using the results of Lemma 2 and a proof of entropy stability for the Bassi-Rebay type one (BR1) [10] scheme presented in Gassner et al. [53]. But first, we introduce the numerical fluxes needed to guarantee entropy conservation and stability for the advective volume and surface contributions.

4.1.1. Discrete entropy conservation condition

The starting point of our discrete entropy analysis is analogous to the general entropy potential definition (2.52), which for the Euler and Navier-Stokes equations results in the so-called Tadmor shuffle condition [127]. Due to the presence of the non-conservative terms in the ideal and resistive GLM-MHD equations, this condition is not sufficient and, thus, we consider the adapted potential from (2.58). Furthermore, we know from the split forms in Sec. 3.3 of the previous chapter, that we solely need a first order numerical EC flux. Hence, for the discrete entropy analysis of the ideal GLM-MHD system we first develop the entropy conservation constraint in the finite volume context. To do so, we restrict to one spatial dimension and assume, that we have two adjacent states (L, R) with uniform cell areas Δx. We discretize the ideal GLM-MHD equations semi-discretely and examine the approximation at one particular interface. For convenience we suppress the interface index and introduce the short notations for the jump and the arithmetic mean between a left and right state, a_L and a_R, i.e.

$$[\![a]\!] := a_R - a_L, \qquad \{\!\{a\}\!\} := \frac{1}{2}(a_L + a_R). \tag{4.5}$$

Similar to the derivations in [32, 34, 141] we consider the Riemann problem at one particular interface between two adjacent cells, which reads

$$
\begin{aligned}
\Delta x \frac{\partial \mathbf{u}_L}{\partial t} &= \mathbf{f}_L - \mathbf{f}^* - \frac{1}{2}\Delta x \boldsymbol{\phi}_L^{\mathrm{MHD}} \frac{[\![B_1]\!]}{\Delta x} - \frac{1}{2}\Delta x (\boldsymbol{\phi}_1^{\mathrm{GLM}})_L \frac{[\![\psi]\!]}{\Delta x}, \\
\Delta x \frac{\partial \mathbf{u}_R}{\partial t} &= \mathbf{f}^* - \mathbf{f}_R - \frac{1}{2}\Delta x \boldsymbol{\phi}_R^{\mathrm{MHD}} \frac{[\![B_1]\!]}{\Delta x} - \frac{1}{2}\Delta x (\boldsymbol{\phi}_1^{\mathrm{GLM}})_R \frac{[\![\psi]\!]}{\Delta x},
\end{aligned}
\tag{4.6}
$$

where we use a first order approximation of the derivative on B_1 to be $\frac{[\![B_1]\!]}{\Delta x} \approx (B_1)_x$ and the derivative on ψ to be $\frac{[\![\psi]\!]}{\Delta x} \approx \psi_x$, respectively. Further, we suppress the indices

of the fluxes in the following one-dimensional analysis for reasons of survey. We can interpret the update (4.6) as a finite volume scheme, where we have left and right cell-averaged values separated by a common flux interface. Moreover, we have introduced the numerical flux function $\mathbf{f}^* = \mathbf{f}^*(\mathbf{u}_L, \mathbf{u}_R)$, which is symmetric in its arguments and consistent. In order to also obtain an entropy conservative finite volume approximation, we present the following additional condition for $\mathbf{f}^*$:

Lemma 3 (Discrete entropy conservation condition for the first order numerical flux)**.** *The one-dimensional finite volume approximation for the ideal GLM-MHD equations (2.34) is entropy conservative, if the symmetric and consistent numerical flux function satisfies the condition*

$$\llbracket \mathbf{w} \rrbracket^T \mathbf{f}^* = \llbracket \Psi_1 \rrbracket - \{\!\{B_1\}\!\} \llbracket \theta \rrbracket, \tag{4.7}$$

where $\mathbf{w}$ denotes the vector of entropy variables (2.56), Ψ_1 the entropy flux potential (2.58) and $\theta = \mathbf{w}^T \boldsymbol{\phi}^{\mathrm{MHD}}$ the contracted Powell term (2.59).

Proof. We premultiply the expressions (4.6) by the entropy variables to convert to entropy space. From the chain rule we know that $S_t = \mathbf{w}^T \mathbf{u}_t$, hence a semi-discrete entropy update is

$$
\begin{aligned}
\Delta x \frac{\partial S_L}{\partial t} &= \mathbf{w}_L^T \left(\mathbf{f}_L - \mathbf{f}^* - \frac{1}{2} \boldsymbol{\phi}_L^{\mathrm{MHD}} \llbracket B_1 \rrbracket - \frac{1}{2} (\boldsymbol{\phi}_1^{\mathrm{GLM}})_L \llbracket \psi \rrbracket \right), \\
\Delta x \frac{\partial S_R}{\partial t} &= \mathbf{w}_R^T \left(\mathbf{f}^* - \mathbf{f}_R - \frac{1}{2} \boldsymbol{\phi}_R^{\mathrm{MHD}} \llbracket B_1 \rrbracket - \frac{1}{2} (\boldsymbol{\phi}_1^{\mathrm{GLM}})_R \llbracket \psi \rrbracket \right).
\end{aligned}
\tag{4.8}
$$

If we contract the Powell term $\boldsymbol{\phi}^{\mathrm{MHD}}$ from (2.59) into entropy space, we obtain θ, whereas the the second non-conservative term cancels internally as in (2.60). Therefore, we rewrite (4.8) to be

$$
\begin{aligned}
\Delta x \frac{\partial S_L}{\partial t} &= \mathbf{w}_L^T \left(\mathbf{f}_L - \mathbf{f}^* \right) - \frac{1}{2} \theta_L \llbracket B_1 \rrbracket, \\
\Delta x \frac{\partial S_R}{\partial t} &= \mathbf{w}_R^T \left(\mathbf{f}^* - \mathbf{f}_R \right) - \frac{1}{2} \theta_R \llbracket B_1 \rrbracket.
\end{aligned}
\tag{4.9}
$$

We add the two contributions from (4.9) to obtain the total entropy update

$$\Delta x \frac{\partial}{\partial t} \left(S_L + S_R \right) = \llbracket \mathbf{w} \rrbracket^T \mathbf{f}^* - \llbracket \mathbf{w} \cdot \mathbf{f} \rrbracket - \{\!\{\theta\}\!\} \llbracket B_1 \rrbracket. \tag{4.10}$$

To ensure that the discrete entropy update satisfies the finite volume approximation of the entropy conservation law (2.48), we require that the right hand side generates the negative jump of the entropy flux, i.e.

$$\llbracket \mathbf{w} \rrbracket^T \mathbf{f}^* - \llbracket \mathbf{w} \cdot \mathbf{f} \rrbracket - \{\!\{\theta\}\!\} \llbracket B_1 \rrbracket = - \llbracket f^S \rrbracket. \tag{4.11}$$

Rearranging terms and adding $\pm [\![\theta B_1]\!]$ to the right hand side of (4.11) we have

$$[\![\mathbf{w}]\!]^T \mathbf{f}^* = [\![\mathbf{w} \cdot \mathbf{f}]\!] + \{\!\{ \theta \}\!\} [\![B_1]\!] - [\![f^S]\!] + [\![\theta B_1]\!] - [\![\theta B_1]\!] . \qquad (4.12)$$

However, from the previous definition of the entropy flux potential and properties of the jump operator we know

$$\Psi_1 = \mathbf{w} \cdot \mathbf{f} + \theta B_1 - f^S, \quad [\![\theta B_1]\!] = \{\!\{ \theta \}\!\} [\![B_1]\!] + \{\!\{ B_1 \}\!\} [\![\theta]\!] . \qquad (4.13)$$

Thus, we arrive at the new discrete entropy conservation condition for the numerical flux function

$$[\![\mathbf{w}]\!]^T \mathbf{f}^* = [\![\Psi_1]\!] - \{\!\{ B_1 \}\!\} [\![\theta]\!] . \qquad (4.14)$$

$\square$

Similar conditions can be derived for the numerical fluxes in y- and z-directions [23, 34, 48, 97] stating

$$[\![\mathbf{w}]\!]^T \mathbf{f}_l^{\mathrm{EC}} = [\![\Psi_l]\!] - \{\!\{ B_l \}\!\} [\![\theta]\!] , \quad l = 1, 2, 3. \qquad (4.15)$$

However, we restrict to one spatial dimension for now and next use the derived discrete entropy conservation condition (4.7) from Lemma 3 to introduce one possible choice for an entropy conservative numerical flux function.

4.1.2. Entropy conservative numerical flux

A consistent, symmetric numerical flux function, which is entropy conservative for the ideal GLM-MHD equations, is derived in [34] and serves as the backbone for the high-order entropy stable DGSEM considered in this work.

In addition to the already defined notation for the jump and arithmetic mean operators in (4.5) we will also require the logarithmic mean between a left and right state, a_L and a_R, i.e.

$$a^{\mathrm{ln}} := [\![a]\!] / [\![\ln(a)]\!] , \qquad (4.16)$$

where a numerically stable procedure to evaluate the logarithmic mean can be found in e.g. [73].

Then, we present the EC numerical flux in the first spatial direction:

Lemma 4 (Entropy conservative flux for the ideal GLM-MHD equations)**.**
*An entropy conservative numerical flux function for two adjacent solution states $\mathbf{u}_L, \mathbf{u}_R$
of the one-dimensional ideal GLM-MHD equations is given as*

$$
\mathbf{f}^{\mathrm{EC}}(\mathbf{u}_L, \mathbf{u}_R) =
\begin{pmatrix}
\varrho^{\ln} \{\!\{v_1\}\!\} \\
\varrho^{\ln} \{\!\{v_1\}\!\}^2 - \{\!\{B_1\}\!\}^2 + \overline{p} + \frac{1}{2}\left(\{\!\{B_1^2\}\!\} + \{\!\{B_2^2\}\!\} + \{\!\{B_3^2\}\!\} \right) \\
\varrho^{\ln} \{\!\{v_1\}\!\} \{\!\{v_2\}\!\} - \{\!\{B_1\}\!\} \{\!\{B_2\}\!\} \\
\varrho^{\ln} \{\!\{v_1\}\!\} \{\!\{v_3\}\!\} - \{\!\{B_1\}\!\} \{\!\{B_3\}\!\} \\
f_5^{\mathrm{EC}} \\
c_h \{\!\{\psi\}\!\} \\
\{\!\{v_1\}\!\} \{\!\{B_2\}\!\} - \{\!\{v_2\}\!\} \{\!\{B_1\}\!\} \\
\{\!\{v_1\}\!\} \{\!\{B_3\}\!\} - \{\!\{v_3\}\!\} \{\!\{B_1\}\!\} \\
c_h \{\!\{B_1\}\!\}
\end{pmatrix}
\tag{4.17}
$$

with

$$
\begin{aligned}
f_5^{\mathrm{EC}} = &\, f_1^{\mathrm{EC}}\left[\frac{1}{2(\gamma-1)\beta^{\ln}} - \frac{1}{2}\left(\{\!\{v_1^2\}\!\} + \{\!\{v_2^2\}\!\} + \{\!\{v_3^2\}\!\} \right) \right] + f_2^{\mathrm{EC}} \{\!\{v_1\}\!\} + f_3^{\mathrm{EC}} \{\!\{v_2\}\!\} + f_4^{\mathrm{EC}} \{\!\{v_3\}\!\} \\
&+ f_6^{\mathrm{EC}} \{\!\{B_1\}\!\} + f_7^{\mathrm{EC}} \{\!\{B_2\}\!\} + f_8^{\mathrm{EC}} \{\!\{B_3\}\!\} + f_9^{\mathrm{EC}} \{\!\{\psi\}\!\} - \frac{1}{2}\left(\{\!\{v_1 B_1^2\}\!\} + \{\!\{v_1 B_2^2\}\!\} + \{\!\{v_1 B_3^2\}\!\} \right) \\
&+ \{\!\{v_1 B_1\}\!\} \{\!\{B_1\}\!\} + \{\!\{v_2 B_2\}\!\} \{\!\{B_1\}\!\} + \{\!\{v_3 B_3\}\!\} \{\!\{B_1\}\!\} - c_h \{\!\{B_1 \psi\}\!\}
\end{aligned}
\tag{4.18}
$$

and

$$
\overline{p} = \frac{\{\!\{\varrho\}\!\}}{2\{\!\{\beta\}\!\}}.
\tag{4.19}
$$

Proof. The simple way of proving the entropy conservation for the numerical flux (4.17) is straightforward by inserting it into the discrete entropy conservation condition (4.7). However, for clarity, we present the reverse procedure to demonstrate the derivation of such a flux starting with the discrete entropy conservation condition (4.7) and a yet arbitrary numerical flux function. Therefore, we use the properties of the linear jump operator

$$
[\![ab]\!] = \{\!\{b\}\!\} [\![a]\!] + \{\!\{a\}\!\} [\![b]\!], \quad [\![a^2]\!] = 2\{\!\{a\}\!\} [\![a]\!].
\tag{4.20}
$$

We first expand the jump in entropy variables by

$$
[\![\mathbf{w}]\!] =
\begin{bmatrix}
[\![w_1]\!] \\
[\![2\beta v_1]\!] \\
[\![2\beta v_2]\!] \\
[\![2\beta v_3]\!] \\
-[\![2\beta]\!] \\
[\![2\beta B_1]\!] \\
[\![2\beta B_2]\!] \\
[\![2\beta B_3]\!] \\
[\![2\beta \psi]\!]
\end{bmatrix}
=
\begin{bmatrix}
[\![w_1]\!] \\
2\{\!\{\beta\}\!\} [\![v_1]\!] + 2\{\!\{v_1\}\!\} [\![\beta]\!] \\
2\{\!\{\beta\}\!\} [\![v_2]\!] + 2\{\!\{v_2\}\!\} [\![\beta]\!] \\
2\{\!\{\beta\}\!\} [\![v_3]\!] + 2\{\!\{v_3\}\!\} [\![\beta]\!] \\
-2[\![\beta]\!] \\
2\{\!\{\beta\}\!\} [\![B_1]\!] + 2\{\!\{B_1\}\!\} [\![\beta]\!] \\
2\{\!\{\beta\}\!\} [\![B_2]\!] + 2\{\!\{B_2\}\!\} [\![\beta]\!] \\
2\{\!\{\beta\}\!\} [\![B_3]\!] + 2\{\!\{B_3\}\!\} [\![\beta]\!] \\
2\{\!\{\beta\}\!\} [\![\psi]\!] + 2\{\!\{\psi\}\!\} [\![\beta]\!]
\end{bmatrix}
\tag{4.21}
$$

with

$$\llbracket w_1 \rrbracket = \left\llbracket \frac{\gamma - s}{\gamma - 1} - \beta \|\vec{v}\|^2 \right\rrbracket = \frac{\llbracket \varrho \rrbracket}{\varrho^{\ln}} + \frac{\llbracket \beta \rrbracket}{\beta^{\ln}(\gamma - 1)} - \left(\{\!\{ v_1^2 \}\!\} + \{\!\{ v_2^2 \}\!\} + \{\!\{ v_3^2 \}\!\} \right) \llbracket \beta \rrbracket$$
$$- 2 \{\!\{ \beta \}\!\} \left(\{\!\{ v_1 \}\!\} \llbracket v_1 \rrbracket + \{\!\{ v_2 \}\!\} \llbracket v_2 \rrbracket + \{\!\{ v_3 \}\!\} \llbracket v_3 \rrbracket \right). \tag{4.22}$$

Now we can write the left hand side of (4.7) component-wise to find

$$\llbracket \mathbf{w} \rrbracket^T \mathbf{f}^* = f_1^* \left(\frac{\llbracket \varrho \rrbracket}{\varrho^{\ln}} + \frac{\llbracket \beta \rrbracket}{\beta^{\ln}(\gamma - 1)} - \left(\{\!\{ v_1^2 \}\!\} + \{\!\{ v_2^2 \}\!\} + \{\!\{ v_3^2 \}\!\} \right) \llbracket \beta \rrbracket - 2 \{\!\{ \beta \}\!\} \left(\{\!\{ v_1 \}\!\} \llbracket v_1 \rrbracket + \{\!\{ v_2 \}\!\} \llbracket v_2 \rrbracket + \{\!\{ v_3 \}\!\} \llbracket v_3 \rrbracket \right) \right)$$
$$+ f_2^* \left(2 \{\!\{ \beta \}\!\} \llbracket v_1 \rrbracket + 2 \{\!\{ v_1 \}\!\} \llbracket \beta \rrbracket \right) + f_3^* \left(2 \{\!\{ \beta \}\!\} \llbracket v_2 \rrbracket + 2 \{\!\{ v_2 \}\!\} \llbracket \beta \rrbracket \right) + f_4^* \left(2 \{\!\{ \beta \}\!\} \llbracket v_3 \rrbracket + 2 \{\!\{ v_3 \}\!\} \llbracket \beta \rrbracket \right) + f_5^* \left(-2 \llbracket \beta \rrbracket \right)$$
$$+ f_6^* \left(2 \{\!\{ \beta \}\!\} \llbracket B_1 \rrbracket + 2 \{\!\{ B_1 \}\!\} \llbracket \beta \rrbracket \right) + f_7^* \left(2 \{\!\{ \beta \}\!\} \llbracket B_2 \rrbracket + 2 \{\!\{ B_2 \}\!\} \llbracket \beta \rrbracket \right) + f_8^* \left(2 \{\!\{ \beta \}\!\} \llbracket B_3 \rrbracket + 2 \{\!\{ B_3 \}\!\} \llbracket \beta \rrbracket \right)$$
$$+ f_9^* \left(2 \{\!\{ \beta \}\!\} \llbracket \psi \rrbracket + 2 \{\!\{ \psi \}\!\} \llbracket \beta \rrbracket \right). \tag{4.23}$$

Next, we expand the the right hand side of (4.7) to combinations of linear jumps

$$\llbracket \Psi_1 \rrbracket - \{\!\{ B_1 \}\!\} \llbracket \theta \rrbracket = \llbracket \varrho v_1 + \beta v_1 \|\vec{B}\|^2 + 2\beta c_h B_1 \psi \rrbracket - \llbracket 2\beta(\vec{v} \cdot \vec{B}) \rrbracket \{\!\{ B_1 \}\!\}$$
$$= \llbracket \varrho v_1 \rrbracket + \llbracket \beta v_1 \|\vec{B}\|^2 \rrbracket + 2 c_h \llbracket \beta B_1 \psi \rrbracket - 2 \llbracket \beta(\vec{v} \cdot \vec{B}) \rrbracket \{\!\{ B_1 \}\!\} \tag{4.24}$$

with

$$\llbracket \varrho v_1 \rrbracket = \{\!\{ v_1 \}\!\} \llbracket \varrho \rrbracket + \{\!\{ \varrho \}\!\} \llbracket v_1 \rrbracket,$$

$$\llbracket \beta v_1 \|\vec{B}\|^2 \rrbracket = \llbracket \beta v_1 B_1^2 \rrbracket + \llbracket \beta v_1 B_2^2 \rrbracket + \llbracket \beta v_1 B_3^2 \rrbracket$$
$$= \{\!\{ v_1 B_1^2 \}\!\} \llbracket \beta \rrbracket + \{\!\{ \beta \}\!\} \left(\{\!\{ B_1^2 \}\!\} \llbracket v_1 \rrbracket + 2 \{\!\{ v_1 \}\!\} \{\!\{ B_1 \}\!\} \llbracket B_1 \rrbracket \right)$$
$$+ \{\!\{ v_1 B_2^2 \}\!\} \llbracket \beta \rrbracket + \{\!\{ \beta \}\!\} \left(\{\!\{ B_2^2 \}\!\} \llbracket v_1 \rrbracket + 2 \{\!\{ v_1 \}\!\} \{\!\{ B_2 \}\!\} \llbracket B_2 \rrbracket \right)$$
$$+ \{\!\{ v_1 B_3^2 \}\!\} \llbracket \beta \rrbracket + \{\!\{ \beta \}\!\} \left(\{\!\{ B_3^2 \}\!\} \llbracket v_1 \rrbracket + 2 \{\!\{ v_1 \}\!\} \{\!\{ B_3 \}\!\} \llbracket B_3 \rrbracket \right)$$
$$= \llbracket \beta \rrbracket \left(\{\!\{ v_1 B_1^2 \}\!\} + \{\!\{ v_1 B_2^2 \}\!\} + \{\!\{ v_1 B_3^2 \}\!\} \right)$$
$$+ \llbracket v_1 \rrbracket \left(\{\!\{ \beta \}\!\} \{\!\{ B_1^2 \}\!\} + \{\!\{ \beta \}\!\} \{\!\{ B_2^2 \}\!\} + \{\!\{ \beta \}\!\} \{\!\{ B_3^2 \}\!\} \right)$$
$$+ \llbracket B_1 \rrbracket \left(2 \{\!\{ \beta \}\!\} \{\!\{ v_1 \}\!\} \{\!\{ B_1 \}\!\} \right) + \llbracket B_2 \rrbracket \left(2 \{\!\{ \beta \}\!\} \{\!\{ v_1 \}\!\} \{\!\{ B_2 \}\!\} \right)$$
$$+ \llbracket B_3 \rrbracket \left(2 \{\!\{ \beta \}\!\} \{\!\{ v_1 \}\!\} \{\!\{ B_3 \}\!\} \right),$$

$$\llbracket \beta B_1 \psi \rrbracket = \{\!\{ \beta \}\!\} \llbracket B_1 \psi \rrbracket + \{\!\{ B_1 \psi \}\!\} \llbracket \beta \rrbracket = \{\!\{ \beta \}\!\} \left(\{\!\{ B_1 \}\!\} \llbracket \psi \rrbracket + \{\!\{ \psi \}\!\} \llbracket B_1 \rrbracket \right) + \{\!\{ B_1 \psi \}\!\} \llbracket \beta \rrbracket$$
$$= \llbracket \psi \rrbracket \{\!\{ \beta \}\!\} \{\!\{ B_1 \}\!\} + \llbracket B_1 \rrbracket \{\!\{ \beta \}\!\} \{\!\{ \psi \}\!\} + \llbracket \beta \rrbracket \{\!\{ B_1 \psi \}\!\} \tag{4.25}$$

and

$$\left[\!\left[\beta(\vec{v_1}\cdot\vec{B})\right]\!\right]\{\!\{B_1\}\!\} = \{\!\{B_1\}\!\}\left(\left[\!\left[\beta v_1 B_1\right]\!\right] + \left[\!\left[\beta v_2 B_2\right]\!\right] + \left[\!\left[\beta v_3 B_3\right]\!\right]\right)$$

$$= \{\!\{B_1\}\!\}\left(\{\!\{v_1 B_1\}\!\}\left[\!\left[\beta\right]\!\right] + \{\!\{\beta\}\!\}\left[\!\left[v_1 B_1\right]\!\right] + \{\!\{v_2 B_2\}\!\}\left[\!\left[\beta\right]\!\right] + \{\!\{\beta\}\!\}\left[\!\left[v_2 B_2\right]\!\right]\right.$$
$$\left. + \{\!\{v_3 B_3\}\!\}\left[\!\left[\beta\right]\!\right] + \{\!\{\beta\}\!\}\left[\!\left[v_3 B_3\right]\!\right]\right)$$

$$= \{\!\{B_1\}\!\}\left(\left[\!\left[\beta\right]\!\right]\left(\{\!\{v_1 B_1\}\!\} + \{\!\{v_2 B_2\}\!\} + \{\!\{v_3 B_3\}\!\}\right) + \{\!\{\beta\}\!\}\left(\left[\!\left[v_1\right]\!\right]\{\!\{B_1\}\!\}\right.\right.$$
$$\left.\left. + \left[\!\left[B_1\right]\!\right]\{\!\{v_1\}\!\} + \left[\!\left[v_2\right]\!\right]\{\!\{B_2\}\!\} + \left[\!\left[B_2\right]\!\right]\{\!\{v_2\}\!\} + \left[\!\left[v_3\right]\!\right]\{\!\{B_3\}\!\} + \left[\!\left[B_3\right]\!\right]\{\!\{v_3\}\!\}\right)\right)$$

$$= \left[\!\left[\beta\right]\!\right]\{\!\{B_1\}\!\}\left(\{\!\{v_1 B_1\}\!\} + \{\!\{v_2 B_2\}\!\} + \{\!\{v_3 B_3\}\!\}\right)$$
$$+ \left[\!\left[v_1\right]\!\right]\{\!\{\beta\}\!\}\{\!\{B_1\}\!\}^2 + \left[\!\left[B_1\right]\!\right]\{\!\{\beta\}\!\}\{\!\{B_1\}\!\}\{\!\{v_1\}\!\}$$
$$+ \left[\!\left[v_2\right]\!\right]\{\!\{\beta\}\!\}\{\!\{B_1\}\!\}\{\!\{B_2\}\!\} + \left[\!\left[B_2\right]\!\right]\{\!\{\beta\}\!\}\{\!\{B_1\}\!\}\{\!\{v_2\}\!\}$$
$$+ \left[\!\left[v_3\right]\!\right]\{\!\{\beta\}\!\}\{\!\{B_1\}\!\}\{\!\{B_3\}\!\} + \left[\!\left[B_3\right]\!\right]\{\!\{\beta\}\!\}\{\!\{B_1\}\!\}\{\!\{v_3\}\!\}\,.$$

(4.26)

After having rewritten every term in the discrete entropy conservation equation (4.7) into linear jumps, we can obtain the yet unknown components of the entropy conserving ideal GLM-MHD flux function from a coefficient comparison, i.e.

$$\left[\!\left[\varrho\right]\!\right] : f_1^* \frac{\left[\!\left[\varrho\right]\!\right]}{\varrho^{\ln}} = \{\!\{v_1\}\!\}\left[\!\left[\varrho\right]\!\right]$$

$$\left[\!\left[v_1\right]\!\right] : -2f_1^*\{\!\{\beta\}\!\}\{\!\{v_1\}\!\}\left[\!\left[v_1\right]\!\right] + 2f_2^*\{\!\{\beta\}\!\}\left[\!\left[v_1\right]\!\right] = \{\!\{\varrho\}\!\}\left[\!\left[v_1\right]\!\right] + \{\!\{\beta\}\!\}\left(\{\!\{B_1^2\}\!\} + \{\!\{B_2^2\}\!\} + \{\!\{B_3^2\}\!\}\right)\left[\!\left[v_1\right]\!\right]$$
$$- 2\{\!\{\beta\}\!\}\{\!\{B_1\}\!\}^2\left[\!\left[v_1\right]\!\right]$$

$$\left[\!\left[v_2\right]\!\right] : -2f_1^*\{\!\{\beta\}\!\}\{\!\{v_2\}\!\}\left[\!\left[v_2\right]\!\right] + 2f_3^*\{\!\{\beta\}\!\}\left[\!\left[v_2\right]\!\right] = -2\{\!\{\beta\}\!\}\{\!\{B_1\}\!\}\{\!\{B_2\}\!\}\left[\!\left[v_2\right]\!\right]$$

$$\left[\!\left[v_3\right]\!\right] : -2f_1^*\{\!\{\beta\}\!\}\{\!\{v_3\}\!\}\left[\!\left[v_3\right]\!\right] + 2f_4^*\{\!\{\beta\}\!\}\left[\!\left[v_3\right]\!\right] = -2\{\!\{\beta\}\!\}\{\!\{B_1\}\!\}\{\!\{B_3\}\!\}\left[\!\left[v_3\right]\!\right]$$

$$\left[\!\left[B_1\right]\!\right] : 2f_6^*\{\!\{\beta\}\!\}\left[\!\left[B_1\right]\!\right] = 2\{\!\{\beta\}\!\}\{\!\{B_1\}\!\}\{\!\{v_1\}\!\}\left[\!\left[B_1\right]\!\right] + 2c_h\{\!\{\beta\}\!\}\{\!\{\psi\}\!\}\left[\!\left[B_1\right]\!\right] - 2\{\!\{\beta\}\!\}\{\!\{B_1\}\!\}\{\!\{v_1\}\!\}\left[\!\left[B_1\right]\!\right]$$
$$= 2c_h\{\!\{\beta\}\!\}\{\!\{\psi\}\!\}\left[\!\left[B_1\right]\!\right]$$

$$\left[\!\left[B_2\right]\!\right] : 2f_7^*\{\!\{\beta\}\!\}\left[\!\left[B_2\right]\!\right] = 2\{\!\{\beta\}\!\}\{\!\{B_2\}\!\}\{\!\{v_1\}\!\}\left[\!\left[B_2\right]\!\right] - 2\{\!\{\beta\}\!\}\{\!\{B_1\}\!\}\{\!\{v_2\}\!\}\left[\!\left[B_2\right]\!\right]$$

$$\left[\!\left[B_3\right]\!\right] : 2f_8^*\{\!\{\beta\}\!\}\left[\!\left[B_3\right]\!\right] = 2\{\!\{\beta\}\!\}\{\!\{B_3\}\!\}\{\!\{v_1\}\!\}\left[\!\left[B_3\right]\!\right] - 2\{\!\{\beta\}\!\}\{\!\{B_1\}\!\}\{\!\{v_3\}\!\}\left[\!\left[B_3\right]\!\right]$$

$$\left[\!\left[\psi\right]\!\right] : 2f_9^*\{\!\{\beta\}\!\} = 2c_h\{\!\{\beta\}\!\}\{\!\{B_1\}\!\}$$

$$\left[\!\left[\beta\right]\!\right] : \frac{f_1^*}{\beta^{\ln}(\gamma-1)}\left[\!\left[\beta\right]\!\right] - f_1^*\left(\{\!\{v_1^2\}\!\} + \{\!\{v_2^2\}\!\} + \{\!\{v_3^2\}\!\}\right)\left[\!\left[\beta\right]\!\right] + 2f_2^*\{\!\{v_1\}\!\}\left[\!\left[\beta\right]\!\right] + 2f_3^*\{\!\{v_2\}\!\}\left[\!\left[\beta\right]\!\right]$$
$$+ 2f_4^*\{\!\{v_3\}\!\}\left[\!\left[\beta\right]\!\right] - 2f_5^*\left[\!\left[\beta\right]\!\right] + 2f_6^*\{\!\{B_1\}\!\}\left[\!\left[\beta\right]\!\right] + 2f_7^*\{\!\{B_2\}\!\}\left[\!\left[\beta\right]\!\right] + 2f_8^*\{\!\{B_3\}\!\}\left[\!\left[\beta\right]\!\right] + 2f_9^*\{\!\{\psi\}\!\}\left[\!\left[\beta\right]\!\right]$$
$$= \left(\{\!\{v_1 B_1^2\}\!\} + \{\!\{v_1 B_2^2\}\!\} + \{\!\{v_1 B_3^2\}\!\}\right)\left[\!\left[\beta\right]\!\right] + 2c_h\{\!\{B_1\psi\}\!\}\left[\!\left[\beta\right]\!\right]$$
$$- 2\{\!\{B_1\}\!\}\left(\{\!\{v_1 B_1\}\!\} + \{\!\{v_2 B_2\}\!\} + \{\!\{v_3 B_3\}\!\}\right)\left[\!\left[\beta\right]\!\right]$$

Solving these equations gives the numerical entropy conserving flux function (4.17). $\quad\square$

By arranging the hydrodynamic contributions, the magnetic field parts and the GLM components in (4.17) separately, we split the advective EC numerical flux function, as in the continuous analysis, into three components

$$\mathbf{f}^{\text{EC}} = \mathbf{f}^{\text{EC,Euler}} + \mathbf{f}^{\text{EC,MHD}} + \mathbf{f}^{\text{EC,GLM}} \tag{4.27}$$

with

$$\mathbf{f}^{\text{EC,Euler}} = \begin{pmatrix} \varrho^{\ln} \{\!\{v_1\}\!\} \\ \varrho^{\ln} \{\!\{v_1\}\!\}^2 + \overline{p} \\ \varrho^{\ln} \{\!\{v_1\}\!\} \{\!\{v_2\}\!\} \\ \varrho^{\ln} \{\!\{v_1\}\!\} \{\!\{v_3\}\!\} \\ f_5^{\text{EC,Euler}} \\ 0 \\ 0 \\ 0 \\ 0 \end{pmatrix}, \quad \mathbf{f}^{\text{EC,MHD}} = \begin{pmatrix} 0 \\ -\{\!\{B_1\}\!\}^2 + \frac{1}{2}\Big(\{\!\{B_1^2\}\!\} + \{\!\{B_2^2\}\!\} + \{\!\{B_3^2\}\!\} \Big) \\ -\{\!\{B_1\}\!\} \{\!\{B_2\}\!\} \\ -\{\!\{B_1\}\!\} \{\!\{B_3\}\!\} \\ f_5^{\text{EC,MHD}} \\ 0 \\ \{\!\{v_1\}\!\} \{\!\{B_2\}\!\} - \{\!\{v_2\}\!\} \{\!\{B_1\}\!\} \\ \{\!\{v_1\}\!\} \{\!\{B_3\}\!\} - \{\!\{v_3\}\!\} \{\!\{B_1\}\!\} \\ 0 \end{pmatrix},$$

$$\mathbf{f}^{\text{EC,GLM}} = \begin{pmatrix} 0 \\ 0 \\ 0 \\ 0 \\ c_h \{\!\{B_1\}\!\} \{\!\{\psi\}\!\} - c_h \{\!\{B_1 \psi\}\!\} \\ c_h \{\!\{\psi\}\!\} \\ 0 \\ 0 \\ c_h \{\!\{B_1\}\!\} \end{pmatrix}$$

$$\tag{4.28}$$

and

$$f_5^{\text{EC,Euler}} = f_1^{\text{EC,Euler}} \left[\frac{1}{2(\gamma - 1)\beta^{\ln}} - \frac{1}{2}\left(\{\!\{v_1^2\}\!\} + \{\!\{v_2^2\}\!\} + \{\!\{v_3^2\}\!\} \right) \right]$$
$$+ f_2^{\text{EC,Euler}} \{\!\{v_1\}\!\} + f_3^{\text{EC,Euler}} \{\!\{v_2\}\!\} + f_4^{\text{EC,Euler}} \{\!\{v_3\}\!\},$$

$$f_5^{\text{EC,MHD}} = f_2^{\text{EC,MHD}} \{\!\{v_1\}\!\} + f_3^{\text{EC,MHD}} \{\!\{v_2\}\!\} + f_4^{\text{EC,MHD}} \{\!\{v_3\}\!\} \tag{4.29}$$
$$f_6^{\text{EC,MHD}} \{\!\{B_1\}\!\} + f_7^{\text{EC,MHD}} \{\!\{B_2\}\!\} + f_8^{\text{EC,MHD}} \{\!\{B_3\}\!\}$$
$$- \frac{1}{2}\left(\{\!\{v_1 B_1^2\}\!\} + \{\!\{v_1 B_2^2\}\!\} + \{\!\{v_1 B_3^2\}\!\} \right)$$
$$+ \{\!\{v_1 B_1\}\!\} \{\!\{B_1\}\!\} + \{\!\{v_2 B_2\}\!\} \{\!\{B_1\}\!\} + \{\!\{v_3 B_3\}\!\} \{\!\{B_1\}\!\}.$$

Furthermore, this also defines appropriate split entropy conservation conditions for the numerical flux functions in the first spatial direction, i.e.

$$[\![\mathbf{w}]\!]^T \mathbf{f}^{\text{EC,Euler}} = [\![\Psi_1^{\text{Euler}}]\!] \,, \tag{4.30}$$

$$[\![\mathbf{w}]\!]^T \mathbf{f}^{\text{EC,MHD}} = [\![\Psi_1^{\text{MHD}}]\!] - \{\!\{B_1\}\!\} [\![\theta]\!] \,, \tag{4.31}$$

$$[\![\mathbf{w}]\!]^T \mathbf{f}^{\text{EC,GLM}} = [\![\Psi_1^{\text{GLM}}]\!] \,, \tag{4.32}$$

where we use the previously defined split entropy flux potentials from the continuous analysis (2.61).

Remark 1. Technically, the splitting of the entropy conservative flux into separate Euler, MHD and GLM parts as stated in (4.28) does not work on the discrete level, since the EC Euler flux implicitly still includes magnetic and GLM contributions in the pressure, i.e. in the second and fifth components hidden in $\bar{p}$ and β^{ln}. Nevertheless, the discrete entropy conditions (4.30)-(4.32) hold, because the pressure-dependent variables in the Euler EC flux cancel internally when contracted into entropy space. Further, we compute the numerical fluxes in terms of the primitive variables, where the pressure is a purely hydrodynamic quantity.

Similar to the proof of Lemma 4, it is possible to derive suitable entropy conservative fluxes in the y- and z-directions. The final three-dimensional *EC flux* can be written in the compact block vector notation

$$\overset{\leftrightarrow}{\mathbf{f}}^{\text{EC}} = \left(\mathbf{f}_1^{\text{EC}}, \mathbf{f}_2^{\text{EC}}, \mathbf{f}_3^{\text{EC}}\right)^T \tag{4.33}$$

and satisfies the three-dimensional entropy conservation conditions, i.e.

$$[\![\mathbf{w}]\!]^T \overset{\leftrightarrow}{\mathbf{f}}^{\text{EC,Euler}} = [\![\vec{\Psi}^{\text{Euler}}]\!] \,, \tag{4.34}$$

$$[\![\mathbf{w}]\!]^T \overset{\leftrightarrow}{\mathbf{f}}^{\text{EC,MHD}} = [\![\vec{\Psi}^{\text{MHD}}]\!] - \{\!\{\vec{B}\}\!\} [\![\theta]\!] \,, \tag{4.35}$$

$$[\![\mathbf{w}]\!]^T \overset{\leftrightarrow}{\mathbf{f}}^{\text{EC,GLM}} = [\![\vec{\Psi}^{\text{GLM}}]\!] \,. \tag{4.36}$$

Recalling the contracted DG approximation (4.1) we select both the two point volume fluxes $\overset{\leftrightarrow}{\mathbf{F}}^{a,\#}$ and the advective surface fluxes $\mathbf{F}_n^{a,*}$ to be the EC fluxes

$$\overset{\leftrightarrow}{\mathbf{F}}^{a,\#}(\mathbf{U}_{ijk}, \mathbf{U}_{mjk}) = \overset{\leftrightarrow}{\mathbf{f}}^{\text{EC}}(\mathbf{U}_{ijk}, \mathbf{U}_{mjk}) \,, \quad \mathbf{F}_n^{a,*} = \overset{\leftrightarrow}{\mathbf{F}}^{\text{EC}} \cdot \vec{n} = \overset{\leftrightarrow}{\mathbf{f}}^{\text{EC}}(\mathbf{U}_L, \mathbf{U}_R) \cdot \vec{n}. \tag{4.37}$$

We note, that the latter can also include stabilization terms as discussed next.

4.1.3. Entropy stable numerical fluxes

Especially, in the presence of shocks or discontinuities, we must add dissipation to the interface fluxes in terms of the entropy variables to ensure we do not violate the entropy inequality (2.49). In order to create such an entropy stable scheme, we use the EC flux in (4.33) as a baseline flux and add a general form of numerical dissipation at the interfaces to get an entropy stable *ES flux* that is applicable to arbitrary flows

$$\overset{\leftrightarrow}{\mathbf{f}}^{\mathrm{ES}} \cdot \vec{n} = \overset{\leftrightarrow}{\mathbf{f}}^{\mathrm{EC}} \cdot \vec{n} - \frac{1}{2}\Lambda_n \hat{\mathsf{H}} \left[\!\left[\mathbf{w} \right]\!\right], \tag{4.38}$$

where Λ_n is the dissipation matrix in the normal direction and $\hat{\mathsf{H}}$ is a matrix, that relates the variables in conserved and entropy space. In particular, this reformulation in terms of the jump in entropy variables is necessary to ensure entropy stability by guaranteeing a negative contribution in the entropy inequality (2.49). Even though the entropy Jacobian H from (2.54) is easy to derive in the continuous space, it is non-trivial to discretize this matrix for use in a numerical scheme [33]. An approximation to the entropy Jacobian has been derived in [34], that satisfies

$$\left(\left[\!\left[\mathbf{u} \right]\!\right]\right)_i = \left(\hat{\mathsf{H}} \left[\!\left[\mathbf{w} \right]\!\right]\right)_i, \quad i = 1, 2, 3, 4, 6, 7, 8, 9 \quad \text{and} \quad \left(\left[\!\left[\mathbf{u} \right]\!\right]\right)_5 \simeq \left(\hat{\mathsf{H}} \left[\!\left[\mathbf{w} \right]\!\right]\right)_5. \tag{4.39}$$

So, the equality holds for each term except for the jump in total energy. Further, the discrete matrix is still symmetric positive-definite and reads

$$\hat{\mathsf{H}} = \begin{bmatrix} \varrho^{\ln} & \varrho^{\ln} \{\!\{v_1\}\!\} & \varrho^{\ln} \{\!\{v_2\}\!\} & \varrho^{\ln} \{\!\{v_3\}\!\} & \bar{E} & 0 & 0 & 0 & 0 \\ \varrho^{\ln} \{\!\{v_1\}\!\} & \varrho^{\ln} \{\!\{v_1\}\!\}^2 + \bar{p} & \varrho^{\ln} \{\!\{v_1\}\!\} \{\!\{v_2\}\!\} & \varrho^{\ln} \{\!\{v_1\}\!\} \{\!\{v_3\}\!\} & \left(\bar{E}+\bar{p}\right)\{\!\{v_1\}\!\} & 0 & 0 & 0 & 0 \\ \varrho^{\ln} \{\!\{v_2\}\!\} & \varrho^{\ln} \{\!\{v_2\}\!\} \{\!\{v_1\}\!\} & \varrho^{\ln} \{\!\{v_2\}\!\}^2 + \bar{p} & \varrho^{\ln} \{\!\{v_2\}\!\} \{\!\{v_3\}\!\} & \left(\bar{E}+\bar{p}\right)\{\!\{v_2\}\!\} & 0 & 0 & 0 & 0 \\ \varrho^{\ln} \{\!\{v_3\}\!\} & \varrho^{\ln} \{\!\{v_3\}\!\} \{\!\{v_1\}\!\} & \varrho^{\ln} \{\!\{v_3\}\!\} \{\!\{v_2\}\!\} & \varrho^{\ln} \{\!\{v_3\}\!\}^2 + \bar{p} & \left(\bar{E}+\bar{p}\right)\{\!\{v_3\}\!\} & 0 & 0 & 0 & 0 \\ \bar{E} & \left(\bar{E}+\bar{p}\right)\{\!\{v_1\}\!\} & \left(\bar{E}+\bar{p}\right)\{\!\{v_2\}\!\} & \left(\bar{E}+\bar{p}\right)\{\!\{v_3\}\!\} & \hat{\mathsf{H}}_{5,5} & \tau \{\!\{B_1\}\!\} & \tau \{\!\{B_2\}\!\} & \tau \{\!\{B_3\}\!\} & \tau \{\!\{\psi\}\!\} \\ 0 & 0 & 0 & 0 & \tau \{\!\{B_1\}\!\} & \tau & 0 & 0 & 0 \\ 0 & 0 & 0 & 0 & \tau \{\!\{B_2\}\!\} & 0 & \tau & 0 & 0 \\ 0 & 0 & 0 & 0 & \tau \{\!\{B_3\}\!\} & 0 & 0 & \tau & 0 \\ 0 & 0 & 0 & 0 & \tau \{\!\{\psi\}\!\} & 0 & 0 & 0 & \tau \end{bmatrix}, \tag{4.40}$$

with

$$\begin{aligned} \bar{E} &= \varrho^{\ln} \left[\{\!\{v_1\}\!\}^2 + \{\!\{v_2\}\!\}^2 + \{\!\{v_3\}\!\}^2 - \frac{1}{2} \left(\{\!\{v_1^2\}\!\} + \{\!\{v_2^2\}\!\} + \{\!\{v_3^2\}\!\} \right) \right] + \frac{\varrho^{\ln}}{2\beta^{\ln}(\gamma-1)}, \\ \tau &= \frac{\{\!\{p\}\!\}}{\{\!\{\varrho\}\!\}} = \frac{1}{2\{\!\{\beta\}\!\}}, \end{aligned} \tag{4.41}$$

$\bar{p}$ from (4.19) and

$$\hat{\mathsf{H}}_{5,5} = \frac{1}{\varrho^{\ln}} \left(\frac{(\varrho^{\ln})^2}{4(\beta^{\ln})^2(\gamma-1)} + \bar{E}^2 \right) + \bar{p} \left(\{\!\{v_1\}\!\}^2 + \{\!\{v_2\}\!\}^2 + \{\!\{v_3\}\!\}^2 \right) + \tau \sum_{l=1}^{3} \{\!\{B_l\}\!\}^2 + \tau \{\!\{\psi\}\!\}^2. \tag{4.42}$$

Next, we address the dissipation matrix Λ, for which there are many possible choices available. The easiest option is to define the dissipation by a *global Lax-Friedrichs* (GLF) stabilization term [132], i.e.

$$\Lambda_n^{\mathrm{GLF}} = |\lambda_{\max}^{\mathrm{global}}| \, \mathsf{I}, \tag{4.43}$$

where $\lambda_{\max}^{\mathrm{global}}$ is the largest eigenvalue of the ideal GLM-MHD system from (2.23) in the entire computational domain. Consequently, this choice results in a high diffusivity due to its global nature. Indeed, Rusanov [114] showed that a less diffusive, yet stable scheme can be built using a local wave speed measure. The resulting dissipation term is called *Rusanov* or *local Lax-Friedrichs* (LLF) stabilization term, i.e.

$$\Lambda_n^{\mathrm{LLF}} = |\lambda_{\max}^{\mathrm{local}}| \, \mathsf{I}. \tag{4.44}$$

Here, $\lambda_{\max}^{\mathrm{local}} = \max\left[\lambda_{\max}(\mathbf{u}_L), \lambda_{\max}(\mathbf{u}_R)\right]$ is the largest eigenvalue from (2.23) at the particular evaluation point of the flux. We note, that in the computation of the eigenvalues we solely consider the contributions in the normal flow direction, which can be implemented using the rotational invariance of the numerical flux function.

We can create an even more selective dissipation operator if we take all nine waves of the system into account and define the dissipation matrix in (4.38) to have the form

$$\Lambda_n^{\mathrm{NW}} = \mathsf{R}|\hat{\Lambda}|\mathsf{R}^{-1}, \tag{4.45}$$

where R is the matrix of right eigenvectors and $\hat{\Lambda}$ is the diagonal matrix containing the eigenvalues of the flux Jacobian for the ideal GLM-MHD system. Remarkably, for entropy stable schemes there exists a particular scaling of the eigenvectors that relates the matrix R to the entropy Jacobian such that

$$\hat{\mathsf{H}} = \mathsf{R}\mathsf{T}\mathsf{R}^T, \tag{4.46}$$

where T is a positive diagonal scaling matrix [9]. From this we can rewrite the dissipation term

$$\begin{aligned}
\frac{1}{2}\Lambda_n^{\mathrm{NW}} [\![\mathbf{u}]\!] &\approx \frac{1}{2}\mathsf{R}|\hat{\Lambda}|\mathsf{R}^{-1}\hat{\mathsf{H}} \, [\![\mathbf{w}]\!] \\
&= \frac{1}{2}\mathsf{R}|\hat{\Lambda}|\mathsf{R}^{-1}\mathsf{R}\mathsf{T}\mathsf{R}^T \, [\![\mathbf{w}]\!] \\
&= \frac{1}{2}\mathsf{R}|\hat{\Lambda}|\mathsf{T}\mathsf{R}^T \, [\![\mathbf{w}]\!] .
\end{aligned} \tag{4.47}$$

The final form of the entropy stable numerical flux with the matrix dissipation term then takes the equivalent form [9, 141]

$$\overleftrightarrow{\mathbf{f}}^{\mathrm{ES,NW}} \cdot \vec{n} = \overleftrightarrow{\mathbf{f}}^{\mathrm{EC}} \cdot \vec{n} - \frac{1}{2}\mathsf{R}|\hat{\Lambda}|\mathsf{T}\mathsf{R}^T \, [\![\mathbf{w}]\!] . \tag{4.48}$$

Details on the discrete evaluations of the matrices $\mathsf{R}, \hat{\Lambda}$ and T can be found in appendix A.2.

In this work, we choose the local Lax-Friedrichs type dissipation (4.44) for most applications. But for now, we ignore the dissipation terms in the numerical fluxes and focus on the purely entropy conservative discretization in order to prove discrete entropy conservation for the ideal GLM-MHD equations.

4.2. Discrete entropy analysis of the ideal GLM-MHD equations

This section focuses on the advective parts in the contracted DG approximation (4.1). With the help of the advective interface and volume numerical fluxes from the previous section, we are now prepared to examine these contributions. In Sec. 4.2.1, we show that the volume contributions with the inserted entropy conservative flux of the Euler terms become the entropy flux at the surfaces, the ideal MHD terms cancel and the GLM terms vanish. By splitting the entropy conservative flux into three terms as in (4.34)‐(4.36) we explicitly see how the discrete contraction into entropy space mimics the results of the continuous analysis, i.e. (2.68)‐(2.70). Next, with the knowledge that the volume contributions move to the interfaces, Sec. 4.2.2 addresses all the surface contributions and we select the form of the coupling for the non-conservative terms. By summing over all the elements and applying the definition of the entropy conservative fluxes we cancel all the remaining advective and non-conservative terms for a closed system (periodic boundary conditions).

4.2.1. Volume contributions

First, we focus on the advective volume discretizations as well as on the non-conservative volume terms in the first row of (4.1). Using (4.27) we split the advective fluxes to determine the contributions from the Euler, MHD and GLM parts, separately. Since the contribution of the curvilinear Euler components has been investigated in the DG context, see e.g. [20, 53], we address the curvilinear ideal MHD and GLM parts first.

Lemma 5 (Entropy contribution of the curvilinear ideal MHD volume terms)**.**
The curvilinear volume contributions of the ideal MHD equations in (4.1) *cancel in entropy space. That is,*

$$\left\langle \vec{\mathbb{D}} \cdot \overset{\leftrightarrow}{\mathbf{F}}^{\mathrm{EC,MHD}}, \mathbf{W} \right\rangle_N + \left\langle \mathbf{\Phi}^{\mathrm{MHD}} \vec{\mathbb{D}}_{\mathrm{div}}^{\mathrm{NC}} \cdot \vec{\mathbb{B}}, \mathbf{W} \right\rangle_N = 0. \tag{4.49}$$

Proof. We first expand each of the volume contribution from the advective terms

$$
\left\langle \vec{\mathbb{D}} \cdot \overleftrightarrow{\vec{\mathbf{F}}}^{\text{EC,MHD}}, \mathbf{W} \right\rangle_N = \sum_{i,j,k=0}^{N} \omega_{ijk} \mathbf{W}_{ijk}^T \Bigg[2 \sum_{m=0}^{N} \mathcal{D}_{im} \bigg(\overleftrightarrow{\vec{\mathbf{F}}}^{\text{EC,MHD}}(\mathbf{U}_{ijk}, \mathbf{U}_{mjk}) \cdot \left\{\!\!\left\{ J\vec{a}^1 \right\}\!\!\right\}_{(i,m)jk} \bigg)
$$
$$
+ 2 \sum_{m=0}^{N} \mathcal{D}_{jm} \bigg(\overleftrightarrow{\vec{\mathbf{F}}}^{\text{EC,MHD}}(\mathbf{U}_{ijk}, \mathbf{U}_{imk}) \cdot \left\{\!\!\left\{ J\vec{a}^2 \right\}\!\!\right\}_{i(j,m)k} \bigg)
$$
$$
+ 2 \sum_{m=0}^{N} \mathcal{D}_{km} \bigg(\overleftrightarrow{\vec{\mathbf{F}}}^{\text{EC,MHD}}(\mathbf{U}_{ijk}, \mathbf{U}_{ijm}) \cdot \left\{\!\!\left\{ J\vec{a}^3 \right\}\!\!\right\}_{ij(k,m)} \bigg) \Bigg]
$$
(4.50)

and the non-conservative term

$$
\left\langle \mathbf{\Phi}^{\text{MHD}} \vec{\mathbb{D}}_{\text{div}}^{\text{NC}} \cdot \vec{B}, \mathbf{W} \right\rangle_N = \sum_{i,j,k=0}^{N} \omega_{ijk} \mathbf{W}_{ijk}^T \Bigg[\sum_{m=0}^{N} \mathcal{D}_{im} \mathbf{\Phi}_{ijk}^{\text{MHD}} \bigg(\vec{B}_{mjk} \cdot \left\{\!\!\left\{ J\vec{a}^1 \right\}\!\!\right\}_{(i,m)jk} \bigg)
$$
$$
+ \sum_{m=0}^{N} \mathcal{D}_{jm} \mathbf{\Phi}_{ijk}^{\text{MHD}} \bigg(\vec{B}_{imk} \cdot \left\{\!\!\left\{ J\vec{a}^2 \right\}\!\!\right\}_{i(j,m)k} \bigg)
$$
$$
+ \sum_{m=0}^{N} \mathcal{D}_{km} \mathbf{\Phi}_{ijk}^{\text{MHD}} \bigg(\vec{B}_{ijm} \cdot \left\{\!\!\left\{ J\vec{a}^3 \right\}\!\!\right\}_{ij(k,m)} \bigg) \Bigg].
$$
(4.51)

We then focus on the ξ-direction term of the volume integral approximations, which greatly simplifies the analysis (as the other directions are done in an analogous manner). The sum of (4.50) can be written in terms of the SBP matrix (3.32), $\mathcal{Q}_{im} = \omega_i \mathcal{D}_{im}$,

$$
\sum_{i,j,k=0}^{N} \omega_{ijk} \mathbf{W}_{ijk}^T 2 \sum_{m=0}^{N} \mathcal{D}_{im} \bigg(\overleftrightarrow{\vec{\mathbf{F}}}^{\text{EC,MHD}}(\mathbf{U}_{ijk}, \mathbf{U}_{mjk}) \cdot \left\{\!\!\left\{ J\vec{a}^1 \right\}\!\!\right\}_{(i,m)jk} \bigg)
$$
$$
= \sum_{j,k=0}^{N} \omega_{jk} \sum_{i=0}^{N} \mathbf{W}_{ijk}^T \sum_{m=0}^{N} 2\omega_i \mathcal{D}_{im} \bigg(\overleftrightarrow{\vec{\mathbf{F}}}^{\text{EC,MHD}}(\mathbf{U}_{ijk}, \mathbf{U}_{mjk}) \cdot \left\{\!\!\left\{ J\vec{a}^1 \right\}\!\!\right\}_{(i,m)jk} \bigg)
$$
$$
= \sum_{j,k=0}^{N} \omega_{jk} \sum_{i=0}^{N} \mathbf{W}_{ijk}^T \sum_{m=0}^{N} 2\mathcal{Q}_{im} \bigg(\overleftrightarrow{\vec{\mathbf{F}}}^{\text{EC,MHD}}(\mathbf{U}_{ijk}, \mathbf{U}_{mjk}) \cdot \left\{\!\!\left\{ J\vec{a}^1 \right\}\!\!\right\}_{(i,m)jk} \bigg).
$$
(4.52)

We use the summation-by-parts property $2\mathcal{Q}_{im} = \mathcal{Q}_{im} - \mathcal{Q}_{mi} + \mathcal{B}_{im}$, perform a re-indexing of i and m to subsume the $\mathcal{Q}_{mi}$ term and use the facts that $\overleftrightarrow{\vec{\mathbf{F}}}^{\text{EC,MHD}}(\mathbf{U}_{ijk}, \mathbf{U}_{mjk})$ and the average operator of the metric term $\left\{\!\!\left\{ Ja^1 \right\}\!\!\right\}_{(i,m)jk}$ are symmetric with respect to the index i and m to rewrite the ξ-direction contribution to the volume integral

54

approximation as

$$
\sum_{i=0}^{N} \mathbf{W}_{ijk}^T \sum_{m=0}^{N} 2\mathcal{Q}_{im} \left(\overset{\leftrightarrow}{\mathbf{F}}^{\text{EC,MHD}}(\mathbf{U}_{ijk}, \mathbf{U}_{mjk}) \cdot \left\{\!\!\left\{ J\vec{a}^1 \right\}\!\!\right\}_{(i,m)jk} \right)
$$

$$
= \sum_{i,m=0}^{N} \mathbf{W}_{ijk}^T \left(\mathcal{Q}_{im} - \mathcal{Q}_{mi} + \mathcal{B}_{im} \right) \left(\overset{\leftrightarrow}{\mathbf{F}}^{\text{EC,MHD}}(\mathbf{U}_{ijk}, \mathbf{U}_{mjk}) \cdot \left\{\!\!\left\{ J\vec{a}^1 \right\}\!\!\right\}_{(i,m)jk} \right) \tag{4.53}
$$

$$
= \sum_{i,m=0}^{N} \mathcal{Q}_{im} (\mathbf{W}_{ijk} - \mathbf{W}_{mjk})^T \left(\overset{\leftrightarrow}{\mathbf{F}}^{\text{EC,MHD}}(\mathbf{U}_{ijk}, \mathbf{U}_{mjk}) \cdot \left\{\!\!\left\{ J\vec{a}^1 \right\}\!\!\right\}_{(i,m)jk} \right)
$$

$$
+ \mathcal{B}_{im} \mathbf{W}_{ijk}^T \left(\overset{\leftrightarrow}{\mathbf{F}}^{\text{EC,MHD}}(\mathbf{U}_{ijk}, \mathbf{U}_{mjk}) \cdot \left\{\!\!\left\{ J\vec{a}^1 \right\}\!\!\right\}_{(i,m)jk} \right).
$$

Because the proof at hand only concerns ideal MHD terms, we are only concerned with the entropy conservation condition (4.35), which we use to replace the first terms in (4.53) with

$$
(\mathbf{W}_{ijk} - \mathbf{W}_{mjk})^T \mathbf{F}_l^{\text{EC,MHD}}(\mathbf{U}_{ijk}, \mathbf{U}_{mjk}) = \left(\Psi_l^{\text{MHD}} \right)_{ijk} - \left(\Psi_l^{\text{MHD}} \right)_{mjk}
$$

$$
- \frac{1}{2} \left((B_l)_{ijk} + (B_l)_{mjk} \right) (\theta_{ijk} - \theta_{mjk}) \tag{4.54}
$$

for $l = 1, 2, 3$.

Furthermore, note that the entries of the boundary matrix $\mathcal{B}$ are only non-zero when $i = m = 0$ or $i = m = N$, so

$$
\mathcal{B}_{im} \mathbf{W}_{ijk}^T \mathbf{F}_l^{\text{EC,MHD}}(\mathbf{U}_{ijk}, \mathbf{U}_{mjk}) = \mathcal{B}_{im} \left(\left(\Psi_l^{\text{MHD}} \right)_{ijk} - \theta_{ijk} (B_l)_{ijk} \right) \tag{4.55}
$$

for $l = 1, 2, 3$.

We substitute (4.54) and (4.55) into the final line of (4.53) to find

$$
\sum_{i=0}^{N} \mathbf{W}_{ijk}^T \sum_{m=0}^{N} 2\mathcal{Q}_{im} \left(\overset{\leftrightarrow}{\mathbf{F}}^{\text{EC,MHD}}(\mathbf{U}_{ijk}, \mathbf{U}_{mjk}) \cdot \left\{\!\!\left\{ J\vec{a}^1 \right\}\!\!\right\}_{(i,m)jk} \right)
$$

$$
= \sum_{i,m=0}^{N} \mathcal{Q}_{im} \left(\left[\vec{\Psi}_{ijk}^{\text{MHD}} - \vec{\Psi}_{mjk}^{\text{MHD}} - \frac{1}{2} \left(\vec{B}_{ijk} + \vec{B}_{mjk} \right) (\theta_{ijk} - \theta_{mjk}) \right] \cdot \left\{\!\!\left\{ J\vec{a}^1 \right\}\!\!\right\}_{(i,m)jk} \right)
$$

$$
+ \mathcal{B}_{im} \left(\left[\vec{\Psi}_{ijk}^{\text{MHD}} - \theta_{ijk} \vec{B}_{ijk} \right] \cdot \left\{\!\!\left\{ J\vec{a}^1 \right\}\!\!\right\}_{(i,m)jk} \right).
$$

$$
\tag{4.56}
$$

We next examine the terms of the sum (4.56) systematically from left to right.

Now, because the derivative of a constant is zero (i.e. the rows of $\mathcal{Q}$ sum to zero),

$$
\begin{aligned}
\sum_{i,m=0}^{N} \mathcal{Q}_{im} \left(\vec{\Psi}_{ijk}^{\mathrm{MHD}} \cdot \left\{\!\!\left\{ J\vec{a}^1 \right\}\!\!\right\}_{(i,m)jk} \right) &= \frac{1}{2} \sum_{i=0}^{N} \left(\vec{\Psi}_{ijk}^{\mathrm{MHD}} \cdot \left(J\vec{a}^1 \right)_{ijk} \right) \sum_{m=0}^{N} \mathcal{Q}_{im} \\
&+ \frac{1}{2} \sum_{i,m=0}^{N} \mathcal{Q}_{im} \left(\vec{\Psi}_{ijk}^{\mathrm{MHD}} \cdot \left(J\vec{a}^1 \right)_{mjk} \right) \qquad (4.57) \\
&= \frac{1}{2} \sum_{i,m=0}^{N} \mathcal{Q}_{im} \left(\vec{\Psi}_{ijk}^{\mathrm{MHD}} \cdot \left(J\vec{a}^1 \right)_{mjk} \right).
\end{aligned}
$$

Next, on the second term, we use the summation by parts property (3.32), re-index on the $\mathcal{Q}_{mi}$ term, and the symmetric property of the arithmetic mean to rewrite

$$
\begin{aligned}
-\sum_{i,m=0}^{N} \mathcal{Q}_{im} \left(\vec{\Psi}_{mjk}^{\mathrm{MHD}} \cdot \left\{\!\!\left\{ J\vec{a}^1 \right\}\!\!\right\}_{(i,m)jk} \right) &= -\sum_{i,m=0}^{N} \left(\mathcal{B}_{im} - \mathcal{Q}_{mi} \right) \left(\vec{\Psi}_{mjk}^{\mathrm{MHD}} \cdot \left\{\!\!\left\{ J\vec{a}^1 \right\}\!\!\right\}_{(i,m)jk} \right) \\
&= -\sum_{i,m=0}^{N} \left(\mathcal{B}_{im} - \mathcal{Q}_{im} \right) \left(\vec{\Psi}_{ijk}^{\mathrm{MHD}} \cdot \left\{\!\!\left\{ J\vec{a}^1 \right\}\!\!\right\}_{(i,m)jk} \right) \\
&= -\sum_{i,m=0}^{N} \mathcal{B}_{im} \left(\vec{\Psi}_{ijk}^{\mathrm{MHD}} \cdot \left\{\!\!\left\{ J\vec{a}^1 \right\}\!\!\right\}_{(i,m)jk} \right) \\
&+ \sum_{i,m=0}^{N} \mathcal{Q}_{im} \left(\vec{\Psi}_{ijk}^{\mathrm{MHD}} \cdot \left\{\!\!\left\{ J\vec{a}^1 \right\}\!\!\right\}_{(i,m)jk} \right) \\
&= -\sum_{i,m=0}^{N} \mathcal{B}_{im} \left(\vec{\Psi}_{ijk}^{\mathrm{MHD}} \cdot \left\{\!\!\left\{ J\vec{a}^1 \right\}\!\!\right\}_{(i,m)jk} \right) \\
&+ \frac{1}{2} \sum_{i,m=0}^{N} \mathcal{Q}_{im} \left(\vec{\Psi}_{ijk}^{\mathrm{MHD}} \cdot \left(J\vec{a}^1 \right)_{mjk} \right),
\end{aligned}
$$
$$(4.58)$$

where, again, one term in the second arithmetic mean drops out due to consistency of the matrix $\mathcal{Q}$.

We come next to the terms involving $\vec{B}$ and θ in (4.56). We leave these terms grouped for convenience and first expand to find

$$
\begin{aligned}
\sum_{i,m=0}^{N} \mathcal{Q}_{im} & \left(\left[-\frac{1}{2} \left(\vec{B}_{ijk} + \vec{B}_{mjk} \right) \left(\theta_{ijk} - \theta_{mjk} \right) \right] \cdot \left\{\!\!\left\{ J\vec{a}^1 \right\}\!\!\right\}_{(i,m)jk} \right) \\
&= -\frac{1}{2} \sum_{i,m=0}^{N} \mathcal{Q}_{im} \left(\left[\theta_{ijk}\vec{B}_{ijk} + \theta_{ijk}\vec{B}_{mjk} - \theta_{mjk}\vec{B}_{ijk} - \theta_{mjk}\vec{B}_{mjk} \right] \cdot \left\{\!\!\left\{ J\vec{a}^1 \right\}\!\!\right\}_{(i,m)jk} \right).
\end{aligned}
$$
$$(4.59)$$

We examine each term from (4.59): for the first term we use the consistency of $\mathcal{Q}$, the second term is left alone, the third term makes a re-indexing of i and m, and the fourth term applies the SBP property to obtain

$$
\begin{aligned}
-\frac{1}{2} \sum_{i,m=0}^{N} & \mathcal{Q}_{im} \left(\left[\theta_{ijk}\vec{B}_{ijk} + \theta_{ijk}\vec{B}_{mjk} - \theta_{mjk}\vec{B}_{ijk} - \theta_{mjk}\vec{B}_{mjk} \right] \cdot \left\{\!\!\left\{ J\vec{a}^{1} \right\}\!\!\right\}_{(i,m)jk} \right) \\
&= -\frac{1}{4} \sum_{i,m=0}^{N} \mathcal{Q}_{im}\theta_{ijk} \left(\vec{B}_{ijk} \cdot \left(J\vec{a}^{1} \right)_{mjk} \right) \\
&\quad -\frac{1}{2} \sum_{i,m=0}^{N} (\mathcal{Q}_{im} - \mathcal{Q}_{mi})\theta_{ijk} \left(\vec{B}_{mjk} \cdot \left\{\!\!\left\{ J\vec{a}^{1} \right\}\!\!\right\}_{(i,m)jk} \right) \\
&\quad +\frac{1}{2} \sum_{i,m=0}^{N} (\mathcal{B}_{im} - \mathcal{Q}_{mi})\theta_{mjk} \left(\vec{B}_{mjk} \cdot \left\{\!\!\left\{ J\vec{a}^{1} \right\}\!\!\right\}_{(i,m)jk} \right).
\end{aligned} \tag{4.60}
$$

Next, we use the SBP property on the $\mathcal{Q}_{mi}$ term in the second sum of (4.60) and re-index i and m in the third term to get

$$
\begin{aligned}
-\frac{1}{2} \sum_{i,m=0}^{N} & \mathcal{Q}_{im} \left(\left[\theta_{ijk}\vec{B}_{ijk} + \theta_{ijk}\vec{B}_{mjk} - \theta_{mjk}\vec{B}_{ijk} - \theta_{mjk}\vec{B}_{mjk} \right] \cdot \left\{\!\!\left\{ J\vec{a}^{1} \right\}\!\!\right\}_{(i,m)jk} \right) \\
&= -\frac{1}{4} \sum_{i,m=0}^{N} \mathcal{Q}_{im}\theta_{ijk} \left(\vec{B}_{ijk} \cdot \left(J\vec{a}^{1} \right)_{mjk} \right) \\
&\quad -\frac{1}{2} \sum_{i,m=0}^{N} (2\mathcal{Q}_{im} - \mathcal{B}_{im})\theta_{ijk} \left(\vec{B}_{mjk} \cdot \left\{\!\!\left\{ J\vec{a}^{1} \right\}\!\!\right\}_{(i,m)jk} \right) \\
&\quad +\frac{1}{2} \sum_{i,m=0}^{N} (\mathcal{B}_{im} - \mathcal{Q}_{im})\theta_{ijk} \left(\vec{B}_{ijk} \cdot \left\{\!\!\left\{ J\vec{a}^{1} \right\}\!\!\right\}_{(i,m)jk} \right).
\end{aligned} \tag{4.61}
$$

It is clear now that the terms with the boundary matrix, $\mathcal{B}$, combine from the second and third terms of (4.61). Also, the i term of the $\mathcal{Q}_{im}$ piece of the third term cancels due to consistency (similar to (4.57)). The remaining part of the third term then combines

with the first term arriving at

$$-\frac{1}{2}\sum_{i,m=0}^{N}\mathcal{Q}_{im}\left(\left[\theta_{ijk}\vec{B}_{ijk}+\theta_{ijk}\vec{B}_{mjk}-\theta_{mjk}\vec{B}_{ijk}-\theta_{mjk}\vec{B}_{mjk}\right]\cdot\left\{\!\!\left\{J\vec{a}^1\right\}\!\!\right\}_{(i,m)jk}\right)$$

$$=-\frac{1}{2}\sum_{i,m=0}^{N}\mathcal{Q}_{im}\theta_{ijk}\left(\vec{B}_{ijk}\cdot\left(J\vec{a}^1\right)_{mjk}\right)-\sum_{i,m=0}^{N}\mathcal{Q}_{im}\theta_{ijk}\left(\vec{B}_{mjk}\cdot\left\{\!\!\left\{J\vec{a}^1\right\}\!\!\right\}_{(i,m)jk}\right)$$

$$+\sum_{i,m=0}^{N}\mathcal{B}_{im}\theta_{ijk}\left(\vec{B}_{ijk}\cdot\left\{\!\!\left\{J\vec{a}^1\right\}\!\!\right\}_{(i,m)jk}\right).$$

$$(4.62)$$

Combining the results of (4.57), (4.58), and (4.62), we rewrite (4.56) to have

$$\sum_{i=0}^{N}\mathbf{W}_{ijk}^{T}\sum_{m=0}^{N}2\mathcal{Q}_{im}\left(\overset{\leftrightarrow}{\mathbf{F}}^{\text{EC,MHD}}(\mathbf{U}_{ijk},\mathbf{U}_{mjk})\cdot\left\{\!\!\left\{J\vec{a}^1\right\}\!\!\right\}_{(i,m)jk}\right)$$

$$=-\sum_{i,m=0}^{N}\mathcal{B}_{im}\left(\vec{\Psi}_{ijk}^{\text{MHD}}\cdot\left\{\!\!\left\{J\vec{a}^1\right\}\!\!\right\}_{(i,m)jk}\right)+\sum_{i,m=0}^{N}\mathcal{Q}_{im}\left(\vec{\Psi}_{ijk}^{\text{MHD}}\cdot\left(J\vec{a}^1\right)_{mjk}\right)$$

$$-\frac{1}{2}\sum_{i,m=0}^{N}\mathcal{Q}_{im}\theta_{ijk}\left(\vec{B}_{ijk}\cdot\left(J\vec{a}^1\right)_{mjk}\right)-\sum_{i,m=0}^{N}\mathcal{Q}_{im}\theta_{ijk}\left(\vec{B}_{mjk}\cdot\left\{\!\!\left\{J\vec{a}^1\right\}\!\!\right\}_{(i,m)jk}\right)$$

$$+\sum_{i,m=0}^{N}\mathcal{B}_{im}\theta_{ijk}\left(\vec{B}_{ijk}\cdot\left\{\!\!\left\{J\vec{a}^1\right\}\!\!\right\}_{(i,m)jk}\right)+\sum_{i,m=0}^{N}\mathcal{B}_{im}\left(\left[\vec{\Psi}_{ijk}^{\text{MHD}}-\theta_{ijk}\vec{B}_{ijk}\right]\cdot\left\{\!\!\left\{J\vec{a}^1\right\}\!\!\right\}_{(i,m)jk}\right).$$

$$(4.63)$$

Conveniently, several terms in (4.63) cancel to leave

$$\sum_{i=0}^{N}\mathbf{W}_{ijk}^{T}\sum_{m=0}^{N}2\mathcal{Q}_{im}\left(\overset{\leftrightarrow}{\mathbf{F}}^{\text{EC,MHD}}(\mathbf{U}_{ijk},\mathbf{U}_{mjk})\cdot\left\{\!\!\left\{J\vec{a}^1\right\}\!\!\right\}_{(i,m)jk}\right)$$

$$=\sum_{i,m=0}^{N}\mathcal{Q}_{im}\left(\vec{\Psi}_{ijk}^{\text{MHD}}\cdot\left(J\vec{a}^1\right)_{mjk}\right)-\frac{1}{2}\sum_{i,m=0}^{N}\mathcal{Q}_{im}\theta_{ijk}\left(\vec{B}_{ijk}\cdot\left(J\vec{a}^1\right)_{mjk}\right)\qquad(4.64)$$

$$-\sum_{i,m=0}^{N}\mathcal{Q}_{im}\theta_{ijk}\left(\vec{B}_{mjk}\cdot\left\{\!\!\left\{J\vec{a}^1\right\}\!\!\right\}_{(i,m)jk}\right).$$

We are now prepared to revisit the contributions from the non-conservative volume

terms (4.51), which read in the ξ-direction as

$$
\sum_{i,j,k=0}^{N} \omega_{ijk} \mathbf{W}_{ijk}^{T} \sum_{m=0}^{N} \mathcal{D}_{im} \mathbf{\Phi}_{ijk}^{\mathrm{MHD}} \left(\vec{B}_{mjk} \cdot \left\{\!\!\left\{ J\vec{a}^{1} \right\}\!\!\right\}_{(i,m)jk} \right)
$$
$$
= \sum_{j,k=0}^{N} \omega_{jk} \sum_{i,m=0}^{N} \omega_{i} \mathcal{D}_{im} \mathbf{W}_{ijk}^{T} \mathbf{\Phi}_{ijk}^{\mathrm{MHD}} \left(\vec{B}_{mjk} \cdot \left\{\!\!\left\{ J\vec{a}^{1} \right\}\!\!\right\}_{(i,m)jk} \right)
$$
$$
= \sum_{j,k=0}^{N} \omega_{jk} \sum_{i,m=0}^{N} \mathcal{Q}_{im} \mathbf{W}_{ijk}^{T} \mathbf{\Phi}_{ijk}^{\mathrm{MHD}} \left(\vec{B}_{mjk} \cdot \left\{\!\!\left\{ J\vec{a}^{1} \right\}\!\!\right\}_{(i,m)jk} \right)
$$
$$
= \sum_{j,k=0}^{N} \omega_{jk} \sum_{i,m=0}^{N} \mathcal{Q}_{im} \theta_{ijk} \left(\vec{B}_{mjk} \cdot \left\{\!\!\left\{ J\vec{a}^{1} \right\}\!\!\right\}_{(i,m)jk} \right),
\tag{4.65}
$$

where we use the definition of the SBP matrix and the property (2.59) contracting the non-conservative term into entropy space. Comparing the result (4.65) and the last term of (4.64) we see that they cancel when added together. Thus, the contribution in the ξ-direction is

$$
\sum_{j,k=0}^{N} \omega_{jk} \sum_{i=0}^{N} \mathbf{W}_{ijk}^{T} \left[\sum_{m=0}^{N} 2\mathcal{Q}_{im} \left(\overset{\leftrightarrow}{\mathbf{F}}^{\mathrm{EC,MHD}}(\mathbf{U}_{ijk}, \mathbf{U}_{mjk}) \cdot \left\{\!\!\left\{ J\vec{a}^{1} \right\}\!\!\right\}_{(i,m)jk} \right) \right.
$$
$$
\left. + \sum_{m=0}^{N} \mathcal{Q}_{im} \theta_{ijk} \left(\vec{B}_{mjk} \cdot \left\{\!\!\left\{ J\vec{a}^{1} \right\}\!\!\right\}_{(i,m)jk} \right) \right]
$$
$$
= \sum_{j,k=0}^{N} \omega_{jk} \left[\sum_{i,m=0}^{N} \mathcal{Q}_{im} \left(\vec{\overset{\leftrightarrow}{\Psi}}_{ijk}^{\mathrm{MHD}} \cdot \left(J\vec{a}^{1} \right)_{mjk} \right) - \frac{1}{2} \sum_{i,m=0}^{N} \mathcal{Q}_{im} \theta_{ijk} \left(\vec{B}_{ijk} \cdot \left(J\vec{a}^{1} \right)_{mjk} \right) \right].
\tag{4.66}
$$

Summarized, the total contribution of the ξ-direction of (4.50) and (4.51) in the volume term is

$$
\sum_{i,j,k=0}^{N} \omega_{ijk} \mathbf{W}_{ijk}^{T} 2 \sum_{m=0}^{N} \mathcal{D}_{im} \left(\left[\overset{\leftrightarrow}{\mathbf{F}}^{\mathrm{EC,MHD}}(\mathbf{U}_{ijk}, \mathbf{U}_{mjk}) + \mathbf{\Phi}_{ijk}^{\mathrm{MHD}} \vec{B}_{mjk} \right] \cdot \left\{\!\!\left\{ J\vec{a}^{1} \right\}\!\!\right\}_{(i,m)jk} \right)
$$
$$
= \sum_{i,j,k=0}^{N} \omega_{ijk} \sum_{m=0}^{N} \mathcal{D}_{im} \left(\left[\vec{\overset{\leftrightarrow}{\Psi}}_{ijk}^{\mathrm{MHD}} - \frac{1}{2} \theta_{ijk} \vec{B}_{ijk} \right] \cdot \left(J\vec{a}^{1} \right)_{mjk} \right),
\tag{4.67}
$$

where we returned the polynomial derivative matrix due to the property $\mathcal{Q}_{im} = \omega_i \mathcal{D}_{im}$.

Similar results hold for the η- and ζ-directions of the volume integral approximations

leading to

$$
\left\langle \vec{\mathbb{D}} \cdot \vec{\overset{\leftrightarrow}{\mathbf{F}}}^{\mathrm{EC,MHD}}, \mathbf{W} \right\rangle_N + \left\langle \boldsymbol{\Phi}^{\mathrm{MHD}} \vec{\mathbb{D}}_{\mathrm{div}}^{\mathrm{NC}} \cdot \vec{B}, \mathbf{W} \right\rangle_N
$$

$$
= \sum_{i,j,k0}^{N} \omega_{ijk} \sum_{m=0}^{N} \mathcal{D}_{im} \left(\left[\vec{\Psi}_{ijk}^{\mathrm{MHD}} - \frac{1}{2}\theta_{ijk}\vec{B}_{ijk} \right] \cdot \left(J\vec{a}^1 \right)_{mjk} \right)
$$

$$
+ \sum_{i,j,k=0}^{N} \omega_{ijk} \sum_{m=0}^{N} \mathcal{D}_{jm} \left(\left[\vec{\Psi}_{ijk}^{\mathrm{MHD}} - \frac{1}{2}\theta_{ijk}\vec{B}_{ijk} \right] \cdot \left(J\vec{a}^2 \right)_{imk} \right) \tag{4.68}
$$

$$
+ \sum_{i,j,k=0}^{N} \omega_{ijk} \sum_{m=0}^{N} \mathcal{D}_{km} \left(\left[\vec{\Psi}_{ijk}^{\mathrm{MHD}} - \frac{1}{2}\theta_{ijk}\vec{B}_{ijk} \right] \cdot \left(J\vec{a}^3 \right)_{ijm} \right).
$$

Regrouping these volume terms we have shown that

$$
\left\langle \vec{\mathbb{D}} \cdot \vec{\overset{\leftrightarrow}{\mathbf{F}}}^{\mathrm{EC,MHD}}, \mathbf{W} \right\rangle_N + \left\langle \boldsymbol{\Phi}^{\mathrm{MHD}} \vec{\mathbb{D}}_{\mathrm{div}}^{\mathrm{NC}} \cdot \vec{B}, \mathbf{W} \right\rangle_N
$$

$$
= \sum_{i,j,k=0}^{N} \omega_{ijk} \left(\left(\Psi_1^{\mathrm{MHD}} \right)_{ijk} - \frac{1}{2}\theta_{ijk}(B_1)_{ijk} \right) \left\{ \sum_{m=0}^{N} \mathcal{D}_{im}\left(Ja_1^1 \right)_{mjk} + \sum_{m=0}^{N} \mathcal{D}_{jm}\left(Ja_1^2 \right)_{imk} + \sum_{m=0}^{N} \mathcal{D}_{km}\left(Ja_1^3 \right)_{ijm} \right\}
$$

$$
+ \sum_{i,j,k=0}^{N} \omega_{ijk} \left(\left(\Psi_2^{\mathrm{MHD}} \right)_{ijk} - \frac{1}{2}\theta_{ijk}(B_2)_{ijk} \right) \left\{ \sum_{m=0}^{N} \mathcal{D}_{im}\left(Ja_2^1 \right)_{mjk} + \sum_{m=0}^{N} \mathcal{D}_{jm}\left(Ja_2^2 \right)_{imk} + \sum_{m=0}^{N} \mathcal{D}_{km}\left(Ja_2^3 \right)_{ijm} \right\}
$$

$$
+ \sum_{i,j,k=0}^{N} \omega_{ijk} \left(\left(\Psi_3^{\mathrm{MHD}} \right)_{ijk} - \frac{1}{2}\theta_{ijk}(B_3)_{ijk} \right) \left\{ \sum_{m=0}^{N} \mathcal{D}_{im}\left(Ja_3^1 \right)_{mjk} + \sum_{m=0}^{N} \mathcal{D}_{jm}\left(Ja_3^2 \right)_{imk} + \sum_{m=0}^{N} \mathcal{D}_{km}\left(Ja_3^3 \right)_{ijm} \right\},
$$

$$
\tag{4.69}
$$

which gives the desired result (4.49), provided the metric identities are satisfied discretely, i.e., that

$$
\sum_{m=0}^{N} \mathcal{D}_{im}\left(Ja_n^1 \right)_{mjk} + \mathcal{D}_{jm}\left(Ja_n^2 \right)_{imk} + \mathcal{D}_{km}\left(Ja_n^3 \right)_{ijm} = \sum_{l=1}^{3} \frac{\partial}{\partial \xi^l} \mathbb{I}^N \left(Ja_n^l \right) = 0 \tag{4.70}
$$

for $n = 1, 2, 3$ at all LGL nodes $i, j, k = 0, \ldots, N$ within an element.

$\square$

Remark 2. In the proof we use the SBP property (3.32) repeatedly as well as the discrete version of the MHD entropy potential condition (4.35). Moreover, a crucial condition to obtain the desired result on curved elements is that the discrete metric identities (3.28) are satisfied.

Lemma 6 (Entropy contribution of the curvilinear GLM volume terms)**.**
The curvilinear GLM volume contributions of (4.1) reduce to zero in entropy space. That is,

$$
\left\langle \vec{\mathbb{D}} \cdot \vec{\overset{\leftrightarrow}{\mathbf{F}}}^{\mathrm{EC,GLM}}, \mathbf{W} \right\rangle_N + \left\langle \vec{\overset{\leftrightarrow}{\boldsymbol{\Phi}}}^{\mathrm{GLM}} \cdot \vec{\mathbb{D}}_{\mathrm{grad}}^{\mathrm{NC}} \psi, \mathbf{W} \right\rangle_N = 0. \tag{4.71}
$$

Proof. We begin with the term arising from the $\overset{\leftrightarrow}{\mathbf{F}}^{\mathrm{EC,GLM}}$. Similar to the previous proof, we first expand each of the volume contributions

$$
\left\langle \vec{\mathbb{D}} \cdot \overset{\leftrightarrow}{\mathbf{F}}^{\mathrm{EC,GLM}}, \mathbf{W} \right\rangle_N = \sum_{i,j,k=0}^{N} \omega_{ijk} \mathbf{W}_{ijk}^{T} \left[2 \sum_{m=0}^{N} \mathcal{D}_{im} \left(\overset{\leftrightarrow}{\mathbf{F}}^{\mathrm{EC,GLM}}(\mathbf{U}_{ijk}, \mathbf{U}_{mjk}) \cdot \left\{\!\!\left\{ J\vec{a}^{\,1} \right\}\!\!\right\}_{(i,m)jk} \right) \right.
$$

$$
+ 2 \sum_{m=0}^{N} \mathcal{D}_{jm} \left(\overset{\leftrightarrow}{\mathbf{F}}^{\mathrm{EC,GLM}}(\mathbf{U}_{ijk}, \mathbf{U}_{imk}) \cdot \left\{\!\!\left\{ J\vec{a}^{\,2} \right\}\!\!\right\}_{i(j,m)k} \right)
$$

$$
\left. + 2 \sum_{m=0}^{N} \mathcal{D}_{km} \left(\overset{\leftrightarrow}{\mathbf{F}}^{\mathrm{EC,GLM}}(\mathbf{U}_{ijk}, \mathbf{U}_{ijm}) \cdot \left\{\!\!\left\{ J\vec{a}^{\,3} \right\}\!\!\right\}_{ij(k,m)} \right) \right].
$$

$$(4.72)$$

Again, focus is given to the ξ-direction term, as the other spatial directions follow from an analogous argument. The sum can be written in terms of the SBP matrix (3.32), $\mathcal{Q}_{im} = \omega_i \mathcal{D}_{im}$,

$$
\sum_{i,j,k=0}^{N} \omega_{ijk} \mathbf{W}_{ijk}^{T} 2 \sum_{m=0}^{N} \mathcal{D}_{im} \left(\overset{\leftrightarrow}{\mathbf{F}}^{\mathrm{EC,GLM}}(\mathbf{U}_{ijk}, \mathbf{U}_{mjk}) \cdot \left\{\!\!\left\{ J\vec{a}^{\,1} \right\}\!\!\right\}_{(i,m)jk} \right)
$$

$$
= \sum_{j,k=0}^{N} \omega_{jk} \sum_{i=0}^{N} \mathbf{W}_{ijk}^{T} \sum_{m=0}^{N} 2\omega_i \mathcal{D}_{im} \left(\overset{\leftrightarrow}{\mathbf{F}}^{\mathrm{EC,GLM}}(\mathbf{U}_{ijk}, \mathbf{U}_{mjk}) \cdot \left\{\!\!\left\{ J\vec{a}^{\,1} \right\}\!\!\right\}_{(i,m)jk} \right)
$$

$$
= \sum_{j,k=0}^{N} \omega_{jk} \sum_{i=0}^{N} \mathbf{W}_{ijk}^{T} \sum_{m=0}^{N} 2\mathcal{Q}_{im} \left(\overset{\leftrightarrow}{\mathbf{F}}^{\mathrm{EC,GLM}}(\mathbf{U}_{ijk}, \mathbf{U}_{mjk}) \cdot \left\{\!\!\left\{ J\vec{a}^{\,1} \right\}\!\!\right\}_{(i,m)jk} \right).
$$

$$(4.73)$$

We apply the summation-by-parts property $2\mathcal{Q}_{im} = \mathcal{Q}_{im} - \mathcal{Q}_{mi} + \mathcal{B}_{im}$, perform a re-indexing of i and m to subsume the $\mathcal{Q}_{mi}$ term and use the symmetry with respect to the index i and m of $\overset{\leftrightarrow}{\mathbf{F}}^{\mathrm{EC,GLM}}(\mathbf{U}_{ijk}, \mathbf{U}_{mjk})$ and the average operator of the metric term $\left\{\!\!\left\{ Ja^{1} \right\}\!\!\right\}_{(i,m)jk}$ to rewrite the ξ-direction contribution as

$$
\sum_{i=0}^{N} \mathbf{W}_{ijk}^{T} \sum_{m=0}^{N} 2\mathcal{Q}_{im} \left(\overset{\leftrightarrow}{\mathbf{F}}^{\mathrm{EC,GLM}}(\mathbf{U}_{ijk}, \mathbf{U}_{mjk}) \cdot \left\{\!\!\left\{ J\vec{a}^{\,1} \right\}\!\!\right\}_{(i,m)jk} \right)
$$

$$
= \sum_{i,m=0}^{N} \mathbf{W}_{ijk}^{T} \left(\mathcal{Q}_{im} - \mathcal{Q}_{mi} + \mathcal{B}_{im} \right) \left(\overset{\leftrightarrow}{\mathbf{F}}^{\mathrm{EC,GLM}}(\mathbf{U}_{ijk}, \mathbf{U}_{mjk}) \cdot \left\{\!\!\left\{ J\vec{a}^{\,1} \right\}\!\!\right\}_{(i,m)jk} \right)
$$

$$
= \sum_{i,m=0}^{N} \mathcal{Q}_{im} \left(\mathbf{W}_{ijk} - \mathbf{W}_{mjk} \right)^{T} \left(\overset{\leftrightarrow}{\mathbf{F}}^{\mathrm{EC,GLM}}(\mathbf{U}_{ijk}, \mathbf{U}_{mjk}) \cdot \left\{\!\!\left\{ J\vec{a}^{\,1} \right\}\!\!\right\}_{(i,m)jk} \right)
$$

$$
+ \mathcal{B}_{im} \mathbf{W}_{ijk}^{T} \left(\overset{\leftrightarrow}{\mathbf{F}}^{\mathrm{EC,GLM}}(\mathbf{U}_{ijk}, \mathbf{U}_{mjk}) \cdot \left\{\!\!\left\{ J\vec{a}^{\,1} \right\}\!\!\right\}_{(i,m)jk} \right).
$$

$$(4.74)$$

The current proof only contains GLM terms, so we are only concerned with the entropy conservation condition (4.36), which we use to replace the first terms in (4.74)

with

$$(\mathbf{W}_{ijk} - \mathbf{W}_{mjk})^T \mathbf{F}_l^{\mathrm{EC,GLM}}(\mathbf{U}_{ijk}, \mathbf{U}_{mjk}) = \left(\Psi_l^{\mathrm{GLM}}\right)_{ijk} - \left(\Psi_l^{\mathrm{GLM}}\right)_{mjk}, \quad l = 1, 2, 3.$$
(4.75)

Furthermore, recall that the entries of the boundary matrix $\mathcal{B}$ are only non-zero when $i = m = 0$ or $i = m = N$, thus

$$\mathcal{B}_{im} \mathbf{W}_{ijk}^T \mathbf{F}_l^{\mathrm{EC,GLM}}(\mathbf{U}_{ijk}, \mathbf{U}_{mjk}) = \mathcal{B}_{im}\left(\Psi_l^{\mathrm{GLM}}\right)_{ijk}, \quad l = 1, 2, 3.$$
(4.76)

We substitute (4.75) and (4.76) into the final line of (4.74) to find

$$\sum_{i=0}^N \mathbf{W}_{ijk}^T \sum_{m=0}^N 2\mathcal{Q}_{im}\left(\overset{\leftrightarrow}{\mathbf{F}}^{\mathrm{EC,GLM}}(\mathbf{U}_{ijk}, \mathbf{U}_{mjk}) \cdot \left\{\!\!\left\{ J\vec{a}^1 \right\}\!\!\right\}_{(i,m)jk}\right)$$

$$= \sum_{i,m=0}^N \mathcal{Q}_{im}\left(\left[\vec{\Psi}_{ijk}^{\mathrm{GLM}} - \vec{\Psi}_{mjk}^{\mathrm{GLM}}\right] \cdot \left\{\!\!\left\{ J\vec{a}^1 \right\}\!\!\right\}_{(i,m)jk}\right) + \mathcal{B}_{im}\left(\vec{\Psi}_{ijk}^{\mathrm{GLM}} \cdot \left\{\!\!\left\{ J\vec{a}^1 \right\}\!\!\right\}_{(i,m)jk}\right).$$
(4.77)

We individually examine the terms of the sum (4.77) from left to right. Due to the consistency of the SBP matrix (i.e. the rows of $\mathcal{Q}$ sum to zero),

$$\sum_{i,m=0}^N \mathcal{Q}_{im}\left(\vec{\Psi}_{ijk}^{\mathrm{GLM}} \cdot \left\{\!\!\left\{ J\vec{a}^1 \right\}\!\!\right\}_{(i,m)jk}\right) = \frac{1}{2}\sum_{i=0}^N \left(\vec{\Psi}_{ijk}^{\mathrm{GLM}} \cdot \left(J\vec{a}^1\right)_{ijk}\right)\sum_{m=0}^N \mathcal{Q}_{im}$$

$$+ \frac{1}{2}\sum_{i,m=0}^N \mathcal{Q}_{im}\left(\vec{\Psi}_{ijk}^{\mathrm{GLM}} \cdot \left(J\vec{a}^1\right)_{mjk}\right)$$
(4.78)

$$= \frac{1}{2}\sum_{i,m=0}^N \mathcal{Q}_{im}\left(\vec{\Psi}_{ijk}^{\mathrm{GLM}} \cdot \left(J\vec{a}^1\right)_{mjk}\right).$$

On the second term, we apply the summation by parts property (3.32), re-index on the $\mathcal{Q}_{mi}$ term, and utilize the symmetric property of the arithmetic mean to rewrite

$$-\sum_{i,m=0}^N \mathcal{Q}_{im}\left(\vec{\Psi}_{mjk}^{\mathrm{GLM}} \cdot \left\{\!\!\left\{ J\vec{a}^1 \right\}\!\!\right\}_{(i,m)jk}\right) = -\sum_{i,m=0}^N (\mathcal{B}_{im} - \mathcal{Q}_{mi})\left(\vec{\Psi}_{mjk}^{\mathrm{GLM}} \cdot \left\{\!\!\left\{ J\vec{a}^1 \right\}\!\!\right\}_{(i,m)jk}\right)$$

$$= -\sum_{i,m=0}^N (\mathcal{B}_{im} - \mathcal{Q}_{im})\left(\vec{\Psi}_{ijk}^{\mathrm{GLM}} \cdot \left\{\!\!\left\{ J\vec{a}^1 \right\}\!\!\right\}_{(i,m)jk}\right)$$

$$= -\sum_{i,m=0}^N \mathcal{B}_{im}\left(\vec{\Psi}_{ijk}^{\mathrm{GLM}} \cdot \left\{\!\!\left\{ J\vec{a}^1 \right\}\!\!\right\}_{(i,m)jk}\right) + \sum_{i,m=0}^N \mathcal{Q}_{im}\left(\vec{\Psi}_{ijk}^{\mathrm{GLM}} \cdot \left\{\!\!\left\{ J\vec{a}^1 \right\}\!\!\right\}_{(i,m)jk}\right)$$

$$= -\sum_{i,m=0}^N \mathcal{B}_{im}\left(\vec{\Psi}_{ijk}^{\mathrm{GLM}} \cdot \left\{\!\!\left\{ J\vec{a}^1 \right\}\!\!\right\}_{(i,m)jk}\right) + \frac{1}{2}\sum_{i,m=0}^N \mathcal{Q}_{im}\left(\vec{\Psi}_{ijk}^{\mathrm{GLM}} \cdot \left(J\vec{a}^1\right)_{mjk}\right),$$
(4.79)

where, again, one term in the second arithmetic mean drops out due to consistency of the matrix $\mathcal{Q}$.

Substituting the results (4.78) and (4.79) into (4.77) we find the terms containing the boundary matrix, $\mathcal{B}$, cancel and the remaining terms combine to become

$$\sum_{i=0}^{N} \mathbf{W}_{ijk}^{T} \sum_{m=0}^{N} 2\mathcal{Q}_{im}\left(\overset{\leftrightarrow}{\mathbf{F}}^{\text{EC,GLM}}(\mathbf{U}_{ijk}, \mathbf{U}_{mjk}) \cdot \left\{\!\!\left\{ J\vec{a}^{1} \right\}\!\!\right\}_{(i,m)jk} \right) = \sum_{i,m=0}^{N} \mathcal{Q}_{im}\left(\vec{\overset{\leftrightarrow}{\Psi}}_{ijk}^{\text{GLM}} \cdot \left(J\vec{a}^{1} \right)_{mjk} \right) \tag{4.80}$$

Thus, the total contribution in the ξ-direction is found to be

$$\sum_{j,k=0}^{N} \omega_{jk} \sum_{i=0}^{N} \mathbf{W}_{ijk}^{T} \sum_{m=0}^{N} 2\mathcal{Q}_{im}\left(\overset{\leftrightarrow}{\mathbf{F}}^{\text{EC,GLM}}(\mathbf{U}_{ijk}, \mathbf{U}_{mjk}) \cdot \left\{\!\!\left\{ J\vec{a}^{1} \right\}\!\!\right\}_{(i,m)jk} \right)$$
$$= \sum_{j,k=0}^{N} \omega_{jk} \sum_{i,m=0}^{N} \mathcal{Q}_{im}\left(\vec{\overset{\leftrightarrow}{\Psi}}_{ijk}^{\text{GLM}} \cdot \left(J\vec{a}^{1} \right)_{mjk} \right) \tag{4.81}$$
$$= \sum_{i,j,k=0}^{N} \omega_{ijk} \sum_{m=0}^{N} \mathcal{D}_{im}\left(\vec{\overset{\leftrightarrow}{\Psi}}_{ijk}^{\text{GLM}} \cdot \left(J\vec{a}^{1} \right)_{mjk} \right),$$

where we reintroduce the derivative matrix instead of the SBP matrix from the property $\mathcal{Q}_{im} = \omega_i \mathcal{D}_{im}$.

Similar results hold for the η- and ζ-directions of the GLM volume integral approximations leading to

$$\left\langle \vec{\mathbb{D}} \cdot \overset{\leftrightarrow}{\vec{\mathbf{F}}}^{\text{EC,GLM}}, \mathbf{W} \right\rangle_{N} = \sum_{i,j,k=0}^{N} \omega_{ijk} \sum_{m=0}^{N} \mathcal{D}_{im}\left(\vec{\overset{\leftrightarrow}{\Psi}}_{ijk}^{\text{GLM}} \cdot \left(J\vec{a}^{1} \right)_{mjk} \right)$$
$$+ \sum_{i,j,k=0}^{N} \omega_{ijk} \sum_{m=0}^{N} \mathcal{D}_{jm}\left(\vec{\overset{\leftrightarrow}{\Psi}}_{ijk}^{\text{GLM}} \cdot \left(J\vec{a}^{2} \right)_{imk} \right) \tag{4.82}$$
$$+ \sum_{i,j,k=0}^{N} \omega_{ijk} \sum_{m=0}^{N} \mathcal{D}_{km}\left(\vec{\overset{\leftrightarrow}{\Psi}}_{ijk}^{\text{GLM}} \cdot \left(J\vec{a}^{3} \right)_{ijm} \right).$$

Regrouping these volume terms we have shown that

$$
\left\langle \vec{\mathbb{D}} \cdot \overset{\leftrightarrow}{\tilde{\mathbf{F}}}^{\mathrm{EC,GLM}}, \mathbf{W} \right\rangle_N
$$

$$
= \sum_{i,j,k=0}^{N} \omega_{ijk} \Psi_{1,ijk}^{\mathrm{GLM}} \left\{ \sum_{m=0}^{N} \mathcal{D}_{im} \left(Ja_1^1 \right)_{mjk} + \sum_{m=0}^{N} \mathcal{D}_{jm} \left(Ja_1^2 \right)_{imk} + \sum_{m=0}^{N} \mathcal{D}_{km} \left(Ja_1^3 \right)_{ijm} \right\}
$$

$$
+ \sum_{i,j,k=0}^{N} \omega_{ijk} \Psi_{2,ijk}^{\mathrm{GLM}} \left\{ \sum_{m=0}^{N} \mathcal{D}_{im} \left(Ja_2^1 \right)_{mjk} + \sum_{m=0}^{N} \mathcal{D}_{jm} \left(Ja_2^2 \right)_{imk} + \sum_{m=0}^{N} \mathcal{D}_{km} \left(Ja_2^3 \right)_{ijm} \right\}
$$

$$
+ \sum_{i,j,k=0}^{N} \omega_{ijk} \Psi_{3,ijk}^{\mathrm{GLM}} \left\{ \sum_{m=0}^{N} \mathcal{D}_{im} \left(Ja_3^1 \right)_{mjk} + \sum_{m=0}^{N} \mathcal{D}_{jm} \left(Ja_3^2 \right)_{imk} + \sum_{m=0}^{N} \mathcal{D}_{km} \left(Ja_3^3 \right)_{ijm} \right\},
\tag{4.83}
$$

which makes this term vanish, provided the metric identities are satisfied discretely, i.e., that

$$
\sum_{m=0}^{N} \mathcal{D}_{im} \left(Ja_n^1 \right)_{mjk} + \mathcal{D}_{jm} \left(Ja_n^2 \right)_{imk} + \mathcal{D}_{km} \left(Ja_n^3 \right)_{ijm} = 0
\tag{4.84}
$$

for $n = 1, 2, 3$ at all LGL nodes $i, j, k = 0, \ldots, N$ within an element.

Next, we verify that the non-conservative GLM volume term vanishes. So, we consider the following

$$
\left\langle \overset{\leftrightarrow}{\tilde{\boldsymbol{\Phi}}}^{\mathrm{GLM}} \cdot \vec{\mathbb{D}}_{\mathrm{grad}}^{\mathrm{NC}} \psi, \mathbf{W} \right\rangle_N = \sum_{i,j,k=0}^{N} \omega_{ijk} \mathbf{W}_{ijk}^{T} \left[\sum_{m=0}^{N} \mathcal{D}_{im} \psi_{mjk} \left(\overset{\leftrightarrow}{\tilde{\boldsymbol{\Phi}}}_{ijk}^{\mathrm{GLM}} \cdot J\vec{a}_{ijk}^{1} \right) \right.
$$

$$
+ \sum_{m=0}^{N} \mathcal{D}_{jm} \psi_{imk} \left(\overset{\leftrightarrow}{\tilde{\boldsymbol{\Phi}}}_{ijk}^{\mathrm{GLM}} \cdot J\vec{a}_{ijk}^{2} \right)
\tag{4.85}
$$

$$
\left. + \sum_{m=0}^{N} \mathcal{D}_{km} \psi_{ijm} \left(\overset{\leftrightarrow}{\tilde{\boldsymbol{\Phi}}}_{ijk}^{\mathrm{GLM}} \cdot J\vec{a}_{ijk}^{3} \right) \right].
$$

We factor out the $\overset{\leftrightarrow}{\tilde{\boldsymbol{\Phi}}}^{\mathrm{GLM}}$ term because it has no m dependence to find

$$
\left\langle \overset{\leftrightarrow}{\tilde{\boldsymbol{\Phi}}}^{\mathrm{GLM}} \cdot \vec{\mathbb{D}}_{\mathrm{grad}}^{\mathrm{NC}} \psi, \mathbf{W} \right\rangle_N
$$

$$
= \sum_{i,j,k=0}^{N} \omega_{ijk} \left(\mathbf{W}_{ijk}^{T} \overset{\leftrightarrow}{\tilde{\boldsymbol{\Phi}}}_{ijk}^{\mathrm{GLM}} \right) \cdot \left[\sum_{m=0}^{N} \mathcal{D}_{im} \psi_{mjk} J\vec{a}_{ijk}^{1} + \sum_{m=0}^{N} \mathcal{D}_{jm} \psi_{imk} J\vec{a}_{ijk}^{2} + \sum_{m=0}^{N} \mathcal{D}_{km} \psi_{ijm} J\vec{a}_{ijk}^{3} \right].
\tag{4.86}
$$

As in the continuous case (2.60), $\left(\mathbf{W}_{ijk}^{T} \overset{\leftrightarrow}{\tilde{\boldsymbol{\Phi}}}_{ijk}^{\mathrm{GLM}} \right) = 0$ holds point-wise, leading to the desired result

$$
\left\langle \overset{\leftrightarrow}{\tilde{\boldsymbol{\Phi}}}^{\mathrm{GLM}} \cdot \vec{\mathbb{D}}_{\mathrm{grad}}^{\mathrm{NC}} \psi, \mathbf{W} \right\rangle_N = 0.
\tag{4.87}
$$

$\square$

Remark 3. Again, the most important requirements for the proof are the SBP property (3.32), the discrete GLM entropy flux condition (4.36) and the discrete metric identities (3.28).

Remark 4. If we also take the damping source term of the GLM divergence cleaning into account, the statement of Lemma 6 becomes an inequality, i.e.

$$-\left\langle \vec{\mathbb{D}}\cdot\overset{\leftrightarrow}{\mathbf{F}}^{\mathrm{EC,GLM}}, \mathbf{W} \right\rangle_N - \left\langle \overset{\leftrightarrow}{\vec{\Phi}}^{\mathrm{GLM}} \cdot \vec{\mathbb{D}}_{\mathrm{grad}}^{\mathrm{NC}}\psi, \mathbf{W} \right\rangle_N + \left\langle \mathbb{I}^N(J)\,\mathbf{R}, \mathbf{W} \right\rangle_N \le 0, \qquad (4.88)$$

since

$$\left\langle \mathbb{I}^N(J)\,\mathbf{R}, \mathbf{W} \right\rangle_N = - \sum_{i,j,k=0}^{N} J_{ijk}\omega_{ijk}\left(2\alpha\beta_{ijk}\psi_{ijk}^2\right) \le 0, \qquad (4.89)$$

for $\alpha, \beta_{ijk} \ge 0$. This result corresponds to discrete entropy stability instead of conservation and will be excluded for the following discussion of the remaining advective parts.

All together, this leads us to the following result:

Corollary 3 (Entropy contribution of the curvilinear advective volume terms)**.**
For each element the sum of all curvilinear advective volume contributions plus the non-conservative volume terms in (4.1) *yields*

$$\left\langle \vec{\mathbb{D}}\cdot\overset{\leftrightarrow}{\mathbf{F}}^{\mathrm{EC}}, \mathbf{W} \right\rangle_N + \left\langle \mathbf{\Phi}^{\mathrm{MHD}}\vec{\mathbb{D}}_{\mathrm{div}}^{\mathrm{NC}}\cdot\vec{\mathbf{B}}, \mathbf{W} \right\rangle_N + \left\langle \overset{\leftrightarrow}{\vec{\Phi}}^{\mathrm{GLM}} \cdot \vec{\mathbb{D}}_{\mathrm{grad}}^{\mathrm{NC}}\psi, \mathbf{W} \right\rangle_N = \int\limits_{\partial\mathfrak{E},N}\left(\vec{F}^S \cdot \vec{n}\right)\hat{s}\,\mathrm{dS}.$$
$$(4.90)$$

Proof. Again we first split the volume flux in Euler, MHD and GLM parts according to (4.27). From Lemmas 5 and 6 we know, that the curvilinear MHD and GLM volume terms together with the non-conservative terms vanish. Moreover, we know from [41, 53], that the volume contributions of the Euler components become the entropy flux evaluated at the boundary

$$\left\langle \vec{\mathbb{D}}\cdot\overset{\leftrightarrow}{\mathbf{F}}^{\mathrm{EC,Euler}}, \mathbf{W} \right\rangle_N = \int\limits_{\partial\mathfrak{E},N}\left(\vec{F}^S \cdot \vec{n}\right)\hat{s}\,\mathrm{dS}, \qquad (4.91)$$

which is equivalent to the steps (2.68) and (2.93) in the continuous analysis with $\vec{F}^S$ being the discrete evaluation of the entropy flux. □

The results of Lemmas 5, 6 and Corollary 3 demonstrate that many of the volume contributions cancel in entropy space and the remaining terms move to the interfaces of the contracted DG approximation. Thus, in the next section we include this additional interface contribution containing the entropy fluxes.

4.2.2. Surface contributions

We are now prepared to examine the advective surface terms of the contracted DG approximation (4.1) incorporating the now known additional surface part that comes from the volume terms due to the result of Corollary 3. On each element the surface terms are given in compact notation as

$$
G_\iota = \int\limits_{\partial\mathfrak{E}_\iota,N} \mathbf{W}^T \left[\mathbf{F}_n^{\mathrm{EC}} - \mathbf{F}_n^a \right] \hat{s}\,\mathrm{dS} + \int\limits_{\partial\mathfrak{E}_\iota,N} \mathbf{W}^T \left[\left(\boldsymbol{\Phi}^{\mathrm{MHD}} B_n \right)^\lozenge - \boldsymbol{\Phi}^{\mathrm{MHD}} B_n \right] \hat{s}\,\mathrm{dS}
$$
$$
+ \int\limits_{\partial\mathfrak{E}_\iota,N} \mathbf{W}^T \left[\left(\boldsymbol{\Phi}_n^{\mathrm{GLM}}\psi \right)^\lozenge - \boldsymbol{\Phi}_n^{\mathrm{GLM}}\psi \right] \hat{s}\,\mathrm{dS} + \int\limits_{\partial\mathfrak{E}_\iota,N} \left(\vec{F}^S \cdot \vec{n} \right) \hat{s}\,\mathrm{dS}.
$$
(4.92)

To determine the total surface contributions from the advective and non-conservative terms in the contracted DG approximation (4.1) we sum over all elements, $\iota = 1, \ldots, N_{\mathrm{el}}$ similar to Gassner et al. [53]. We introduce notation for states at the LGL node of the one side of the interface between two elements to be a primary "$-$" and complement the notation with a secondary "$+$" to denote the value at the LGL nodes on the opposite side. This allows us to define the orientated jump and the arithmetic mean at the interfaces to be

$$
\llbracket \cdot \rrbracket = (\cdot)^+ - (\cdot)^-, \quad \{\!\{ \cdot \}\!\} = \frac{1}{2} \left((\cdot)^+ + (\cdot)^- \right).
$$
(4.93)

When applied to vectors, the average and jump operators are evaluated separately for each vector component. The physical normal vector $\vec{n}$ is then defined uniquely to point from the "$-$" to the "$+$" side, so that $\vec{n} = (\vec{n})^- = -(\vec{n})^+$.

We consider the discrete total entropy evolution in a closed system and thus focus on fully periodic domains, so that all interfaces in the domain have two adjacent elements. We investigate the total surface contributions from (4.92) term by term. The sum over all elements for the first term generates jumps in the fluxes and entropy variables, where we also use the uniqueness of the numerical surface flux function, $\mathbf{F}_n^{\mathrm{EC}} = \overset{\leftrightarrow}{\mathbf{F}}^{\mathrm{EC}} \cdot \vec{n}$, yielding

$$
\sum_{\iota=1}^{N_{\mathrm{el}}} \int\limits_{\partial\mathfrak{E}_\iota,N} \mathbf{W}^T \left(\overset{\leftrightarrow}{\mathbf{F}}^{\mathrm{EC}} - \overset{\leftrightarrow}{\mathbf{F}}^a \right) \cdot \vec{n}\,\hat{s}\,\mathrm{dS} = - \sum_{\mathrm{faces}} \int\limits_N \left(\llbracket \mathbf{W} \rrbracket^T \left(\overset{\leftrightarrow}{\mathbf{F}}^{\mathrm{EC}} \cdot \vec{n} \right) - \llbracket \mathbf{W}^T \overset{\leftrightarrow}{\mathbf{F}}^a \rrbracket \cdot \vec{n} \right) \hat{s}\,\mathrm{dS}.
$$
(4.94)

Next, we examine the behavior of the GLM part of the entropy conservative flux at the interfaces that come from (4.92). Also, we account for the surface contribution of the GLM non-conservative term (2.32).

Lemma 7 (Entropy contribution of GLM surface terms).
The contribution from the GLM part of the entropy conservative scheme vanishes at element interfaces, i.e.,

$$\int_N \left([\![\mathbf{W}]\!]^T \overset{\leftrightarrow}{\mathbf{F}}^{\mathrm{EC,GLM}} - [\![\mathbf{W}^T \overset{\leftrightarrow}{\mathbf{F}}^{a,\mathrm{GLM}}]\!] \right) \cdot \vec{n}\, \hat{s} \, \mathrm{dS} = 0. \tag{4.95}$$

For the non-conservative term surface contribution we define the interface coupling as

$$\left(\mathbf{\Phi}_n^{\mathrm{GLM}} \psi \right)^{\Diamond} = \left(\left(\overset{\leftrightarrow}{\tilde{\mathbf{\Phi}}}^{\mathrm{GLM}} \right)^- \cdot \vec{n} \right) \{\!\{ \psi \}\!\} \tag{4.96}$$

to ensure that the associated non-conservative terms from (4.92) *vanish locally at each element face.*

Proof. The proof of (4.95) follows directly from the definition of the GLM components of the entropy conservative flux (4.36)

$$\left([\![\mathbf{W}]\!]^T \overset{\leftrightarrow}{\mathbf{F}}^{\mathrm{EC,GLM}} - [\![\mathbf{W}^T \overset{\leftrightarrow}{\mathbf{F}}^{a,\mathrm{GLM}}]\!] \right) \cdot \vec{n} = \left([\![\mathbf{W}]\!]^T \overset{\leftrightarrow}{\mathbf{F}}^{\mathrm{EC,GLM}} - [\![\overset{\rightarrow}{\Psi}^{\mathrm{GLM}}]\!] \right) \cdot \vec{n} = 0. \tag{4.97}$$

To demonstrate the behavior of the non-conservative term on each element face we examine the appropriate part from (4.92) and substitute the coupling term (4.96) at a single interface to find

$$\begin{aligned}
\mathbf{W}^T \left[\left(\mathbf{\Phi}_n^{\mathrm{GLM}} \psi \right)^{\Diamond} - \mathbf{\Phi}_n^{\mathrm{GLM}} \psi \right] &= (\mathbf{W}^-)^T \left[\left(\left(\overset{\leftrightarrow}{\tilde{\mathbf{\Phi}}}^{\mathrm{GLM}} \right)^- \cdot \vec{n} \right) \{\!\{ \psi \}\!\} - \left(\left(\overset{\leftrightarrow}{\tilde{\mathbf{\Phi}}}^{\mathrm{GLM}} \right)^- \cdot \vec{n} \right) \psi^- \right] \\
&= \left(\left[(\mathbf{W}^-)^T \left(\overset{\leftrightarrow}{\tilde{\mathbf{\Phi}}}^{\mathrm{GLM}} \right)^- \right] \cdot \vec{n} \right) \frac{1}{2} \left(\psi^+ - \psi^- \right) \\
&= \left(\left[(\mathbf{W}^-)^T \left(\overset{\leftrightarrow}{\tilde{\mathbf{\Phi}}}^{\mathrm{GLM}} \right)^- \right] \cdot \vec{n} \right) \frac{1}{2} [\![\psi]\!] .
\end{aligned} \tag{4.98}$$

It is straightforward to verify that each part of $\left(\overset{\leftrightarrow}{\tilde{\mathbf{\Phi}}}^{\mathrm{GLM}} \right)^-$ contracts to zero in entropy space, i.e.,

$$(\mathbf{W}^-)^T \left(\mathbf{\Phi}_l^{\mathrm{GLM}} \right)^- = 0, \quad l = 1, 2, 3, \tag{4.99}$$

such that

$$\begin{aligned}
\mathbf{W}^T \left[\left(\mathbf{\Phi}_n^{\mathrm{GLM}} \psi \right)^{\Diamond} - \mathbf{\Phi}_n^{\mathrm{GLM}} \psi \right] &= \left(\left[(\mathbf{W}^-)^T \left(\overset{\leftrightarrow}{\tilde{\mathbf{\Phi}}}^{\mathrm{GLM}} \right)^- \right] \cdot \vec{n} \right) \frac{1}{2} [\![\psi]\!] \\
&= \left(\vec{0} \cdot \vec{n} \right) \frac{1}{2} [\![\psi]\!] \\
&= 0.
\end{aligned} \tag{4.100}$$

Thus, the surface contribution of the GLM non-conservative terms directly vanish at each element face. □

Before we investigate the remaining contributions of the Euler and ideal MHD components, we define $\left(\boldsymbol{\Phi}^{\mathrm{MHD}}B_n\right)^{\Diamond}$ and examine the contribution of the second non-conservative term from (4.92). What we will find is that the surface contribution of the MHD non-conservative terms generates an additional boundary term that cancels an extraneous term left over from the analysis of the ideal MHD part of the advective fluxes.

Lemma 8 (Discretization of the non-conservative ideal MHD surface term)**.**
For the second term in (4.92) *we define*

$$\left(\boldsymbol{\Phi}^{\mathrm{MHD}}B_n\right)^{\Diamond} = \left(\boldsymbol{\Phi}^{\mathrm{MHD}}\right)^{-} \left\{\!\!\left\{\vec{B}\right\}\!\!\right\} \cdot \vec{n}, \tag{4.101}$$

to obtain the total contribution of the non-conservative ideal MHD surface terms

$$\sum_{\iota=1}^{N_{\mathrm{el}}} \int_{\partial \mathfrak{E}_{\iota},N} \mathbf{W}^{T}\left(\left(\boldsymbol{\Phi}^{\mathrm{MHD}}B_n\right)^{\Diamond} - \boldsymbol{\Phi}^{\mathrm{MHD}}B_n\right)\hat{s}\,\mathrm{dS} = \sum_{\mathrm{faces}} \int_{N} \{\!\!\{\theta\}\!\!\}\left[\!\!\left[\vec{B}\right]\!\!\right]\cdot\vec{n}\,\hat{s}\,\mathrm{dS}. \tag{4.102}$$

Proof. We first substitute the definition (4.101) into the second term of (4.92), where, for clarity, we explicitly state that values from the current element $\mathfrak{E}_{\iota}$ to be primary ("$-$"), since $\vec{n}$ is outward pointing

$$
\begin{aligned}
&\int_{\partial \mathfrak{E}_{\iota},N} \mathbf{W}^{T}\left(\left(\boldsymbol{\Phi}^{\mathrm{MHD}}B_n\right)^{\Diamond} - \boldsymbol{\Phi}^{\mathrm{MHD}}B_n\right)\hat{s}\,\mathrm{dS} \\
&= \int_{\partial \mathfrak{E}_{\iota},N} (\mathbf{W}^{-})^{T}\left(\left(\boldsymbol{\Phi}^{\mathrm{MHD}}\right)^{-}\left\{\!\!\left\{\vec{B}\right\}\!\!\right\} - \left(\boldsymbol{\Phi}^{\mathrm{MHD}}\right)^{-}\vec{B}^{-}\right)\cdot\vec{n}\,\hat{s}\,\mathrm{dS}.
\end{aligned}
\tag{4.103}
$$

Note that the values of $\mathbf{W}$ and $\boldsymbol{\Phi}^{\mathrm{MHD}}$ in the contribution (4.103) are evaluated from the current element, so we have a discrete version of the property (2.59)

$$(\mathbf{W}^{-})^{T}\left(\boldsymbol{\Phi}^{\mathrm{MHD}}\right)^{-} = \theta^{-}. \tag{4.104}$$

Thus,

$$\int_{\partial \mathfrak{E}_{\iota},N} (\mathbf{W}^{-})^{T}\left(\left(\boldsymbol{\Phi}^{\mathrm{MHD}}\right)^{-}\left\{\!\!\left\{\vec{B}\right\}\!\!\right\} - \left(\boldsymbol{\Phi}^{\mathrm{MHD}}\right)^{-}\vec{B}^{-}\right)\cdot\vec{n}\,\hat{s}\,\mathrm{dS} = \int_{\partial \mathfrak{E}_{\iota},N} \theta^{-}\left(\left\{\!\!\left\{\vec{B}\right\}\!\!\right\} - \vec{B}^{-}\right)\cdot\vec{n}\,\hat{s}\,\mathrm{dS}. \tag{4.105}$$

Next, we expand the arithmetic mean to get

$$\int_{\partial \mathfrak{E}_{\iota},N} \theta^{-}\left(\left\{\!\!\left\{\vec{B}\right\}\!\!\right\} - \vec{B}^{-}\right)\cdot\vec{n}\,\hat{s}\,\mathrm{dS} = \frac{1}{2}\int_{\partial \mathfrak{E}_{\iota},N} \theta^{-}\left(\vec{B}^{+} - \vec{B}^{-}\right)\cdot\vec{n}\,\hat{s}\,\mathrm{dS}. \tag{4.106}$$

The total surface contribution of (4.106) requires delicate consideration due to the inherent non-uniqueness of the non-conservative term at the interface. Each interface actually contributes twice to the contracted DG approximation and it is important to choose, again, a unique normal vector for each interface $\vec{n}$. The sum over all elements gives for an arbitrary interface contribution of the integrand

$$\frac{1}{2}\left(\theta^-\left(\vec{B}^+-\vec{B}^-\right)\cdot\vec{n}\right)+\frac{1}{2}\left(\theta^+\left(\vec{B}^--\vec{B}^+\right)\cdot(-\vec{n})\right)=\{\!\{\theta\}\!\}\left[\!\left[\vec{B}\right]\!\right]\cdot\vec{n}, \qquad (4.107)$$

yielding the desired result

$$\sum_{\iota=1}^{N_{\mathrm{el}}}\int_{\partial\mathfrak{E}_\iota,N}\mathbf{W}^T\left(\left(\mathbf{\Phi}^{\mathrm{MHD}}B_n\right)^\Diamond-\mathbf{\Phi}^{\mathrm{MHD}}B_n\right)\hat{s}\,\mathrm{dS}=\sum_{\mathrm{faces}}\int_N\{\!\{\theta\}\!\}\left[\!\left[\vec{B}\right]\!\right]\cdot\vec{n}\,\hat{s}\,\mathrm{dS}. \qquad (4.108)$$

$\square$

Remark 5. The prescription of non-conservative surface contributions for high-order DG methods have been previously investigated by Cheng and Shu [24] in the context of the Hamilton-Jacobi equations. Recently, these methods from the Hamilton-Jacobi community have been applied to approximate the solution of the ideal MHD equations at high-order on two-dimensional Cartesian meshes [48, 97]. The current work built upon these previous results to fully generalize the extension of the non-conservative surface contributions into the three-dimensional, unstructured, curvilinear hexahedral mesh framework and re-contextualize the non-conservative surface term discretization based on specific non-conservative numerical surface approximations.

The sum over all elements on the third term in (4.92) generates a jump in the entropy fluxes

$$\sum_{\iota=1}^{N_{\mathrm{el}}}\int_{\partial\mathfrak{E}_\iota,N}\left(\vec{F}^S\cdot\vec{n}\right)\hat{s}\,\mathrm{dS}=-\sum_{\mathrm{faces}}\int_N\left[\!\left[\vec{F}^S\right]\!\right]\cdot\vec{n}\,\hat{s}\,\mathrm{dS}. \qquad (4.109)$$

Now, with the results of Lemmas 7 and 8 as well as the results (4.94) and (4.109) we can address the remaining contributions of the Euler and ideal MHD components at the surface:

Corollary 4 (Entropy contributions of total advective surface terms)**.**
Summing over all elements in (4.92) *shows that the contribution of the curvilinear advective and non-conservative terms on the surface cancel, meaning*

$$\sum_{\iota=1}^{N_{\mathrm{el}}}G_\iota=0. \qquad (4.110)$$

Proof. We note that from Lemma 7 we have accounted for the cancellation of the GLM terms. Similar to the volume term analysis in Corollary 3 we again separate the contributions of the Euler and ideal MHD terms. It is immediate that the Euler terms drop out from the definition of the entropy flux potential for the Euler part (2.62) and the separation of the entropy conserving flux condition (4.34)

$$\left([\![\mathbf{W}]\!]^T \overset{\leftrightarrow}{\mathbf{F}}^{\text{EC,Euler}} - [\![(\mathbf{W})^T \overset{\leftrightarrow}{\mathbf{F}}^{a,\text{Euler}}]\!] + [\![\vec{F}^S]\!] \right) \cdot \vec{n} = \left([\![\mathbf{W}]\!]^T \overset{\leftrightarrow}{\mathbf{F}}^{\text{EC,Euler}} - [\![\vec{\Psi}^{\text{Euler}}]\!] \right) \cdot \vec{n} = 0. \tag{4.111}$$

For the ideal MHD contributions we make use of the entropy flux potential (2.63) to write

$$
\begin{aligned}
&\left([\![\mathbf{W}]\!]^T \overset{\leftrightarrow}{\mathbf{F}}^{\text{EC,MHD}} - [\![\mathbf{W}^T \overset{\leftrightarrow}{\mathbf{F}}^{a,\text{MHD}}]\!] \right) \cdot \vec{n} \\
&= \left([\![\mathbf{W}]\!]^T \left(\overset{\leftrightarrow}{\mathbf{F}}^{\text{EC,MHD}} \right) - [\![\vec{\Psi}^{\text{MHD}}]\!] + [\![\theta \vec{B}]\!] \right) \cdot \vec{n} \\
&= \left([\![\mathbf{W}]\!]^T \left(\overset{\leftrightarrow}{\mathbf{F}}^{\text{EC,MHD}} \right) - [\![\vec{\Psi}^{\text{MHD}}]\!] + [\![\theta]\!] \{\!\{\vec{B}\}\!\} + \{\!\{\theta\}\!\} [\![\vec{B}]\!] \right) \cdot \vec{n},
\end{aligned}
\tag{4.112}
$$

where we use a property of the jump operator

$$[\![ab]\!] = \{\!\{a\}\!\} [\![b]\!] + \{\!\{b\}\!\} [\![a]\!]. \tag{4.113}$$

We see that the first three terms on the last line of (4.112) are the entropy conservative flux condition of the magnetic field components (4.35) and cancel. This leaves the remainder term

$$-\sum_{\text{faces}} \int_N \left([\![\mathbf{W}]\!]^T \overset{\leftrightarrow}{\mathbf{F}}^{\text{EC,MHD}} - [\![\mathbf{W}^T \overset{\leftrightarrow}{\mathbf{F}}^{a,\text{MHD}}]\!] \right) \cdot \vec{n}\hat{s} \, \mathrm{dS} = -\sum_{\text{faces}} \int_N \{\!\{\theta\}\!\} [\![\vec{B}]\!] \cdot \vec{n}\hat{s} \, \mathrm{dS}. \tag{4.114}$$

This term is identical to the surface contribution of the non-conservative term from Lemma 8 but with opposite sign. Thus the final two terms cancel and we get the desired result

$$\sum_{\iota=1}^{N_{\text{el}}} G_\iota = 0. \tag{4.115}$$

$\square$

4.3. Discrete entropy analysis of the resistive GLM-MHD equations

Lastly, since the discussion of the curvilinear advective and non-conservative parts is now complete, we focus on the resistive parts, namely the last row of the first equation in (4.1). Again, we first have to select appropriate numerical fluxes at the interfaces. Thus, we use the computationally simple BR1 type approximation [10] in terms of the discrete entropy variables and gradients [53]

$$\mathbf{F}_n^{v,*} = \left\{\!\!\left\{ \overset{\leftrightarrow}{\mathbf{F}}^v \right\}\!\!\right\} \cdot \vec{n}, \quad \mathbf{W}^* = \{\!\{\mathbf{W}\}\!\}. \tag{4.116}$$

With the results from the previous section we are able to prove the main result of this chapter:

Theorem 2 (Discrete entropy stability of the curvilinear DGSEM for the resistive GLM-MHD equations)**.**
The curvilinear DGSEM for the resistive GLM-MHD equations (3.51) *with*

$$\left(\mathbf{\Phi}_n^{\mathrm{GLM}} \psi \right)^{\lozenge} = \left(\left(\overset{\leftrightarrow}{\mathbf{\Phi}}^{\mathrm{GLM}} \right)^- \cdot \vec{n} \right) \{\!\{\psi\}\!\}, \quad \left(\mathbf{\Phi}^{\mathrm{MHD}} B_n \right)^{\lozenge} = \left(\mathbf{\Phi}^{\mathrm{MHD}} \right)^- \left\{\!\!\left\{ \vec{B} \right\}\!\!\right\} \cdot \vec{n},$$

$$\mathbf{F}_n^{a,*} = \overset{\leftrightarrow}{\mathbf{F}}^{a,\#} \cdot \vec{n} = \overset{\leftrightarrow}{\mathbf{F}}^{\mathrm{EC}} \cdot \vec{n} \tag{4.117}$$

and the viscous interface fluxes (4.116) *is entropy stable, i.e. for a closed system (periodic boundary conditions) the discrete total entropy is a decreasing function in time*

$$\frac{d\bar{S}}{dt} \le 0. \tag{4.118}$$

Proof. From Corollaries 3 and 4 we know that the volume, surface and non-conservative terms of the advective portions of the resistive GLM-MHD equations cancel in entropy space. The remaining parts of the contracted DG approximation are

$$\left\langle \mathbb{I}^N(J)\,\mathbf{U}_t, \mathbf{W} \right\rangle_N = \left\langle \vec{\mathbb{D}}^{\mathrm{S}} \cdot \overset{\leftrightarrow}{\mathbf{F}}^v, \mathbf{W} \right\rangle_N + \int_{\partial\mathfrak{E},N} \mathbf{W}^T \left(\mathbf{F}_n^{v,*} - \mathbf{F}_n^v \right) \hat{s}\,\mathrm{dS} + \left\langle \mathbb{I}^N(J)\,\mathbf{R}, \mathbf{W} \right\rangle_N,$$

$$\left\langle \mathbb{I}^N(J)\,\overset{\leftrightarrow}{\mathbf{Q}}, \overset{\leftrightarrow}{\mathbf{F}}^v \right\rangle_N = \int_{\partial\mathfrak{E},N} \mathbf{W}^{*,T} \left(\overset{\leftrightarrow}{\mathbf{F}}^v \cdot \vec{n} \right) \hat{s}\,\mathrm{dS} - \left\langle \mathbf{W}, \vec{\mathbb{D}}^{\mathrm{S}} \cdot \overset{\leftrightarrow}{\mathbf{F}}^v \right\rangle_N.$$

$$\tag{4.119}$$

We consider the first term of the second equation and insert the alternate form of the viscous flux rewritten in terms of the gradient of the entropy variables as in the continuous analysis (2.80). We use the known property that the viscous and resistive coefficient

matrix $\underline{\mathsf{K}}$ is symmetric positive semi-definite for the resistive MHD equations to see that

$$\left\langle \mathbb{I}^N(J)\,\overset{\leftrightarrow}{\mathbf{Q}}, \overset{\leftrightarrow}{\mathbf{F}}_v \right\rangle_N = \left\langle \mathbb{I}^N(J)\,\overset{\leftrightarrow}{\mathbf{Q}}, \underline{\mathsf{K}}\,\overset{\leftrightarrow}{\mathbf{Q}} \right\rangle_N \geq \min_{i,j,k=0,\ldots,N}(J_{ijk}) \left\langle \overset{\leftrightarrow}{\mathbf{Q}}, \underline{\mathsf{K}}\,\overset{\leftrightarrow}{\mathbf{Q}} \right\rangle_N \geq 0. \qquad (4.120)$$

Next, we insert the second equation of (4.119) into the first and use the estimate (4.120) to get

$$\left\langle \mathbb{I}^N(J)\,\mathbf{U}_t, \mathbf{W} \right\rangle_N \leq \int_{\partial\mathfrak{E},N} \left(\mathbf{W}^T\left(\mathbf{F}_n^{v,*} - \mathbf{F}_n^v\right) + \mathbf{W}^{*,T}\mathbf{F}_n^v \right) \hat{s}\,\mathrm{dS} + \left\langle \mathbb{I}^N(J)\,\mathbf{R}, \mathbf{W} \right\rangle_N. \qquad (4.121)$$

From Remark 4 we know, that we can also ignore the discrete damping source term without violating the inequality. After summing over all elements we can replace the left hand side by the total entropy derivative according to (4.2) and obtain

$$\frac{d\overline{S}}{dt} \leq -\sum_{\text{faces}}\int_N \left([\![\mathbf{W}]\!]^T\,\mathbf{F}_n^{v,*} - [\![\mathbf{W}^T\overset{\leftrightarrow}{\mathbf{F}}^v]\!] \cdot \vec{n} + (\mathbf{W}^*)^T\,[\![\overset{\leftrightarrow}{\mathbf{F}}^v]\!] \cdot \vec{n} \right) \hat{s}\,\mathrm{dS}. \qquad (4.122)$$

In Gassner et al. [53] it is shown that for the BR1 choice (4.116) all the surface terms in (4.122) vanish, if periodic boundary conditions are considered, yielding our desired result

$$\frac{d\overline{S}}{dt} \leq 0, \qquad (4.123)$$

which shows that the discrete total entropy is decreasing in time, i.e. that the DGSEM for the resistive GLM-MHD equations is entropy stable. $\qquad\square$

Remark 6. It is desirable to introduce additional upwind-type dissipation for advection dominated problems through the choice of the numerical advection fluxes by replacing the EC fluxes at element interfaces with e.g. the ES fluxes (4.38).

5. Shock capturing

In this chapter we equip the derived entropy stable DGSEM with additional shock capturing mechanisms in order to stabilize the approximation for discontinuous solutions. Particularly, we present two different approaches, whereas the first one is a common technique based on adding an adjustable amount of artificial viscosity and the second one is a novel approach designed by a local filtering procedure. We conclude this chapter by presenting a limiter for the DG approximation to maintain discrete positivity of the density and pressure, which is necessary for a flow to remain physically meaningful in the presence of shocks.

For general non-linear systems of hyperbolic conservation laws, discontinuities in terms of shocks may develop in finite time regardless on the smoothness of the initial data, as pointed out in Sec. 2.1. Although shocks are unproblematic for first-order approximations as in finite volume schemes due to their monotonicity and high numerical dissipation, they present a challenge in high-order methods. Indeed, schemes with a formal accuracy higher than first order exhibit large spurious oscillations near discontinuities in the solution, termed as the *Gibbs phenomenon* [57]. Consequently, this might lead to catastrophic numerical instabilities or even unphysical solution states, e.g. negative density or pressure.

In the numerics community many counter mechanisms have been developed for overshoot control during the recent decades, which are all constructed to stabilize high-order approximations in shocked regions. Altogether, these methods can be subdivided into three main categories, which are slope limiters, solution filters and artificial dissipation techniques.

Concerning limiters, the first approaches were formulated in the early eighties by many researchers including Harten et al. [63] and are based on shock capturing upwind-biased schemes. To handle shocks, famous algorithms have been developed such as the total variation diminishing (TVD) schemes making use of flux or slope limiters [64], the essentially non-oscillatory (ENO) and weighted ENO (WENO) schemes, in which adaptive stencils are applied in order to adjust the smoothness of the approximation [120]. Even though these schemes ensure high stability, they are in general of low spatial order, especially for time-dependent problems, e.g. [49]. Moreover, they are not well-suited for parallel computations due to the strong element-coupling inside the stencils. Therefore, many attempts have been made to improve the performance of these limiters by modifying their design or by increasing their formal order, e.g. [6, 7].

An alternative shock capturing strategy is based on filters originating from sound and image processing, in which noisy signals and ringing are smoothed out. Already in 1975, Kramer and Bruckner have proposed the first shock filter in their morphological segmentation method [86], which is based on a Laplacian detector. The basic idea is to iteratively use a dilation process near maxima and an erosion process around minima. From this baseline approach, a number of modifications have been developed in order to improve the performance of shock filters. For instance, increased robustness against small scale details was achieved by Alvarez and Mazorra [5], who convolved the data by a Gaussian. Thus, applying such filters to shocked regions of our approximation is a promising tool to smooth the oscillations caused by Gibbs phenomenon. Additionally, the filtering is usually performed locally, easy to implement and cheap from a computational point of view. We will introduce a novel filter for our DGSEM approximation in Sec. 5.2.

Further, artificial dissipation or viscosity has first been a common approach in the context of stream-wise upwind Petrov–Galerkin finite element methods, as proposed by Hughes et al. [72]. The idea to use explicit artificial viscosity for shock capturing dates back to von Neumann in 1950 [136] and has been popularized in the 70s and 80s by MacCormack [98] and Jameson [74]. Later, such approaches were successfully adapted for DG methods, albeit only for second order approximations, e.g. [2, 66]. Remarkably, Persson and Peraire [106] introduced an element-wise constant artificial viscosity scaled by the resolution length as well as the polynomial degree, such that shocks can be captured locally in single DG elements. Since this approach is not only well-suited for our DGSEM but also produces reasonable results for a broad variety of shock tests, we introduce this method first.

5.1. Artificial viscosity approach

For the general framework introducing artificial viscosity, we consider the modified system of conservation laws

$$\mathbf{u}_t + \vec{\nabla} \cdot \overleftrightarrow{\mathbf{f}}^a(\mathbf{u}) - \vec{\nabla} \cdot \overleftrightarrow{\mathbf{f}}^v(\mathbf{u}, \vec{\nabla}\mathbf{u}) - \vec{\nabla} \cdot (\nu\vec{\nabla}\mathbf{u}) + \boldsymbol{\Upsilon} = \mathbf{r} \qquad (5.1)$$

with the (element-wise) constant scaling parameter $\nu \geq 0$. We note, that for $\nu = 0$, (5.1) reduces to the original resistive GLM-MHD equations (2.39).

The basic idea is to adjust the scaling parameter for each element $\nu_\iota, \iota = 1, \ldots, N_{\text{el}}$, so that it is equal to zero in smooth areas and positive in regions where shocks have to be dissipated. One crucial point in this methodology is the definition of the shock detector, which has to distinguish between shocks and gradients of any other kind in order to limit the range of the shock capturing dissipation specifically to the regions containing shocks. Furthermore, in these regions, we have to determine the proper amount of artificial viscosity. Both issues are solved by the following degrees of freedom (DOF) energy indicator.

5.1.1. DOF energy indicator

Persson and Peraire proposed an indicator, which not only helps to detect elements containing shocks, but also measures the local smoothness of the approximation and, thus, can be used to define ν_ι for the affected elements $\iota = 1, \ldots, N_{\text{el}}$. Therefore, we first transform the current DG approximation of the considered element into a modal representation by the inverse Vandermonde matrix applied in a tensor product fashion, i.e.

$$\hat{\mathbf{U}}_{ijk} = \sum_{m=0}^{N} \mathcal{V}_{im}^{-1}\mathbf{U}_{mjk} + \sum_{m=0}^{N} \mathcal{V}_{jm}^{-1}\mathbf{U}_{imk} + \sum_{m=0}^{N} \mathcal{V}_{km}^{-1}\mathbf{U}_{ijm}, \tag{5.2}$$

for $i, j, k = 0, \ldots, N$, where the entries of the Vandermonde matrix are defined as

$$\mathcal{V}_{ij} = \tilde{L}_j(\xi_i) \tag{5.3}$$

for $i, j = 0, \ldots, N$. The modal basis functions of choice are the orthonormal Legendre polynomials [106], i.e.

$$\tilde{L}_j = \frac{L_j}{\|L_j\|} = L_j\sqrt{j + \frac{1}{2}} \tag{5.4}$$

for $j = 0, \ldots, N$. As a matter of fact, we pre-compute the inverse Vandermonde matrix with the help of a numerical projection

$$\mathcal{V}_{ij}^{-1} = \left\langle \ell_j, \tilde{L}_i \right\rangle = \left\langle \ell_j, \tilde{L}_i \right\rangle_M \tag{5.5}$$

for $i, j = 0, \ldots, N$, where we use a Gauss quadrature with a sufficient accuracy $M = N$ to evaluate the discrete integrals exactly.

By the modal representation of our approximation we define the *DOF energy indicator* as

$$\sigma^{\text{DOF}}(\mathbf{U}) = \log_{10}\left\{ \max\left[\frac{\|\mathbf{U} - \hat{\mathbf{U}}^{\prec}\|}{\|\mathbf{U}\|}, \frac{\|\hat{\mathbf{U}}^{\prec} - \hat{\mathbf{U}}^{\prec\prec}\|}{\|\hat{\mathbf{U}}^{\prec}\|} \right] \right\} \tag{5.6}$$

with the truncated modal approximations

$$\begin{aligned}
\hat{\mathbf{U}}^{\prec} &= \sum_{i,j,k=0}^{N-1} \hat{\mathbf{U}}_{ijk}\tilde{L}_i(\xi)\tilde{L}_j(\eta)\tilde{L}_k(\zeta), \\
\hat{\mathbf{U}}^{\prec\prec} &= \sum_{i,j,k=0}^{N-2} \hat{\mathbf{U}}_{ijk}\tilde{L}_i(\xi)\tilde{L}_j(\eta)\tilde{L}_k(\zeta).
\end{aligned} \tag{5.7}$$

Consequently, this indicator is only applicable to approximations with a polynomial degree of $N \geq 2$, which is acceptable, since shocks are more problematic for high-order. We use a discrete L_2 norm in (5.6), the orthogonality of the Legendre polynomials and

the discrete identity $\mathbf{U} \equiv \hat{\mathbf{U}}$ to find a simplified expression of the DOF energy indicator by replacing

$$
\begin{aligned}
\|\mathbf{U} - \hat{\mathbf{U}}^{\prec}\| &= \sum_{i,j,k=0}^{N-1} \left(\hat{\mathbf{U}}_{Njk}^2 + \hat{\mathbf{U}}_{iNk}^2 + \hat{\mathbf{U}}_{ijN}^2 \right) + \hat{\mathbf{U}}_{NNN}^2, \\
\|\hat{\mathbf{U}}^{\prec} - \hat{\mathbf{U}}^{\prec\!\prec}\| &= \sum_{i,j,k=0}^{N-2} \left(\hat{\mathbf{U}}_{(N-1)jk}^2 + \hat{\mathbf{U}}_{i(N-1)k}^2 + \hat{\mathbf{U}}_{ij(N-1)}^2 \right) + \hat{\mathbf{U}}_{(N-1)(N-1)(N-1)}^2
\end{aligned}
\tag{5.8}
$$

in (5.6). With this equivalent formulation we can interpret the DOF energy indicator as a measurement of how much the highest mode influences the total approximation. More precisely, for high leading coefficients in the modal representation it is more likely, that steep gradients in form of shocks or oscillations are present. Further, (5.8) guarantees that both, influences of even and odd modes, are taken into account.

Since shocks are particularly troublesome in system variables like the density or pressure, we rather consider these quantities instead of the influences of all conserved variables in (5.6). So, we decide beforehand, if we use the density, the pressure or the product of both as an indicator. In our experience, the latter choice is the best one for most applications, since it indicates shocks as well as contact discontinuities.

Next, we consider

$$
\nu^*(\sigma^{\mathrm{DOF}}(\mathbf{U})) = \begin{cases} \epsilon_0 & , \text{ if } \sigma^{\mathrm{DOF}} \geq \sigma_{\max}^{\mathrm{DOF}} \\ \frac{\epsilon_0}{2}\delta & , \text{ if } \sigma_{\min}^{\mathrm{DOF}} \leq \sigma^{\mathrm{DOF}} \leq \sigma_{\max}^{\mathrm{DOF}} \\ 0 & , \text{ if } \sigma_{\min}^{\mathrm{DOF}} \geq \sigma^{\mathrm{DOF}} \end{cases}
\tag{5.9}
$$

with the smooth transition function

$$
\delta = 1 + \sin\left(\frac{\pi\left[\sigma^{\mathrm{DOF}} - \frac{1}{2}\left(\sigma_{\max}^{\mathrm{DOF}} + \sigma_{\min}^{\mathrm{DOF}} \right) \right]}{\sigma_{\max}^{\mathrm{DOF}} - \sigma_{\min}^{\mathrm{DOF}}} \right)
\tag{5.10}
$$

and the user defined parameters $\epsilon_0, \sigma_{\min}^{\mathrm{DOF}}$ and $\sigma_{\max}^{\mathrm{DOF}}$. Finally, we scale (5.9) by the local wave speed, element size and polynomial degree in order to obtain the artificial viscosity in the considered element

$$
\nu = \lambda_{\max}\frac{h}{N+1}\nu^*.
\tag{5.11}
$$

We note, that the maximum eigenvalue is computed locally by (2.23) and the element size is approximated as in (3.54).

Inserting the artificial viscosity computed element-wise by (5.6), (5.9) and (5.11) into (5.1) gives an overall scheme, that smooths the approximation locally, if shocks are present. But, one major drawback of this approach is, that we change the physical system by introducing additional diffusive effects. Hence, we must adapt the viscous timestep,

too. We do so by simply including the artificial viscosity in (3.55). In particular, we change the approximation of the diffusive eigenvalues (3.57) to be

$$v^\iota = \max\left\{\nu_\iota, \mu_R, \mu_{NS} \max\left[\frac{\gamma}{\mathrm{Pr}}, \frac{4}{3}\right] \max_{i,j,k=0,\dots,N} \frac{1}{\varrho_{ijk}}\right\} \qquad (5.12)$$

for $\iota = 1, \dots, N_{el}$. With this restriction, the artificial viscosity method is implemented into our curvilinear DGSEM for the three-dimensional resistive GLM-MHD equations. Next, we investigate the entropic properties of this modification.

5.1.2. Entropy stability for artificial viscosity

In this section, we show, that the modification in (5.1) is compatible with the previous entropy analysis, i.e. that the final DG approximation containing artificial viscosity is still entropy stable. Thus, we start on the continuous level, before we extend the result to the discrete DGSEM formulation.

Lemma 9 (Entropy inequality for the resistive GLM-MHD equations with artificial viscosity)**.**
Solutions of the resistive GLM-MHD equations including artificial viscosity (5.1) *with the non-conservative terms* (2.31), (2.32) *and $\alpha \geq 0$ in* (2.38) *satisfy the entropy inequality*

$$\int_\Omega S_t \, \mathrm{dV} + \int_{\partial\Omega} (\vec{f}^S \cdot \vec{n}) - \mathbf{w}^T(\overset{\leftrightarrow}{\mathbf{f}}^{v,\nu} \cdot \vec{n}) \, \mathrm{dS} \leq 0 \qquad (5.13)$$

with

$$\overset{\leftrightarrow}{\mathbf{f}}^{v,\nu} = \overset{\leftrightarrow}{\mathbf{f}}^v(\mathbf{u}, \vec{\nabla}\mathbf{u}) + \nu\vec{\nabla}\mathbf{u}. \qquad (5.14)$$

Proof. We know from Lemma 1 that the advective and non-conservative parts of (5.1) result in the entropy conservation law (2.48). Moreover from the original proof of Theorem 1 we know, that the damping source term $\mathbf{r}$ is entropy dissipative and that by contraction with the entropy variables (2.56) we obtain the entropy inequality (2.49), as long as we can express the viscous fluxes by the product of a symmetric positive semi-definite matrix and the entropy gradients as in (2.72). Hence, it is sufficient to show, that there is a similar expression for the artificial viscosity, i.e.

$$\nu\vec{\nabla}\mathbf{u} = \nu\underline{H}\vec{\nabla}\mathbf{w}. \qquad (5.15)$$

We note, that the matrix $\underline{H} \in \mathbb{R}^{27\times27}$ is zero everywhere except for the three 9×9

diagonal blocks, which are built from the entropy Jacobians (2.54) defined by

$$
\mathsf{H} = \begin{bmatrix}
\varrho & \varrho v_1 & \varrho v_2 & \varrho v_3 & \varrho e & 0 & 0 & 0 & 0 \\
\varrho v_1 & \varrho v_1^2 + p & \varrho v_1 v_2 & \varrho v_1 v_3 & \varrho h v_1 & 0 & 0 & 0 & 0 \\
\varrho v_2 & \varrho v_1 v_2 & \varrho v_2^2 + p & \varrho v_2 v_3 & \varrho h v_2 & 0 & 0 & 0 & 0 \\
\varrho v_3 & \varrho v_1 v_3 & \varrho v_2 v_3 & \varrho v_3^2 + p & \varrho h v_3 & 0 & 0 & 0 & 0 \\
\varrho e & \varrho h v_1 & \varrho h v_2 & \varrho h v_3 & \varrho h^2 - \frac{a^2 p}{\gamma-1} + \frac{a^2 \|\vec{B}\|^2}{\gamma} + \frac{a^2 \psi^2}{\gamma} & \frac{pB_1}{\varrho} & \frac{pB_2}{\varrho} & \frac{pB_3}{\varrho} & \frac{p\psi}{\varrho} \\
0 & 0 & 0 & 0 & \frac{pB_1}{\varrho} & \frac{p}{\varrho} & 0 & 0 & 0 \\
0 & 0 & 0 & 0 & \frac{pB_2}{\varrho} & 0 & \frac{p}{\varrho} & 0 & 0 \\
0 & 0 & 0 & 0 & \frac{pB_3}{\varrho} & 0 & 0 & \frac{p}{\varrho} & 0 \\
0 & 0 & 0 & 0 & \frac{p\psi}{\varrho} & 0 & 0 & 0 & \frac{p}{\varrho}
\end{bmatrix}
\tag{5.16}
$$

with

$$
a^2 = \frac{p\gamma}{\varrho}, \quad \varrho e = \frac{p}{\gamma-1} + \frac{\varrho}{2}\|\vec{v}\|^2, \quad h = \frac{a^2}{\gamma-1} + \frac{1}{2}\|\vec{v}\|^2.
\tag{5.17}
$$

These matrices are obviously symmetric and have already been shown to be positive semi-definite, see e.g. [141]. Together with the original matrix $\underline{\mathsf{K}}$ from (2.72) and our new viscous fluxes as in (5.14) we can define a matrix $\underline{\mathsf{P}} = \underline{\mathsf{K}} + \nu\underline{\mathsf{H}}$, such that

$$
\overset{\leftrightarrow}{\mathbf{f}}^{v,\nu} = \underline{\mathsf{P}}\vec{\nabla}\mathbf{w}.
\tag{5.18}
$$

The new matrix $\underline{\mathsf{P}} \in \mathbb{R}^{27\times27}$ is obviously symmetric and positive semi-definite, since we have

$$
\begin{aligned}
&\mathsf{q}^T\underline{\mathsf{K}}\mathsf{q} \geq 0 \quad \text{and} \quad \mathsf{q}^T\underline{\mathsf{H}}\mathsf{q} \geq 0 \quad \forall\mathsf{q} \in \mathbb{R}^{27} \\
&\Rightarrow \mathsf{q}^T\underline{\mathsf{P}}\mathsf{q} = \mathsf{q}^T[\underline{\mathsf{K}} + \nu\underline{\mathsf{H}}]\mathsf{q} = \mathsf{q}^T\underline{\mathsf{K}}\mathsf{q} + \nu\mathsf{q}^T\underline{\mathsf{H}}\mathsf{q} \geq 0
\end{aligned}
\tag{5.19}
$$

with $\nu \geq 0$. Hence, adding artificial viscosity in terms of (5.1) is compatible with entropy stability on a continuous level. $\qquad\square$

Remark 7. Alternatively, we can add artificial viscosity in terms of the entropy gradients instead of the solution gradients, so that $\underline{\mathsf{H}}$ becomes the identity matrix and again we have entropy stability.

As in the previous entropy analysis, we are again able to write the viscous fluxes in terms of a symmetric and positive semi-definite matrix times the gradients of entropy variables. But this time the dissipation matrices also include the entropy Jacobians and the artificial viscosity coefficients. We now repeat all the necessary steps of the discrete entropy analysis, include the artificial viscosity in the BR1 evaluation of the viscous Riemann fluxes and arrive at the following result:

Corollary 5 (Discrete entropy stability of the curvilinear DGSEM for the resistive GLM-MHD equations with artificial viscosity)**.**
The curvilinear DGSEM for the resistive GLM-MHD equations (3.51) *with artificial viscosity as in* (5.1),

$$\left(\mathbf{\Phi}_n^{\mathrm{GLM}}\psi\right)^\diamond = \left(\left(\overset{\leftrightarrow}{\mathbf{\Phi}}{}^{\mathrm{GLM}}\right)^- \cdot \vec{n}\right)\{\!\{\psi\}\!\}, \quad \left(\mathbf{\Phi}^{\mathrm{MHD}}B_n\right)^\diamond = \left(\mathbf{\Phi}^{\mathrm{MHD}}\right)^- \left\{\!\left\{\vec{B}\right\}\!\right\} \cdot \vec{n},$$

$$\mathbf{F}_n^{a,*} = \overset{\leftrightarrow}{\mathbf{F}}{}^{a,\#} \cdot \vec{n} = \overset{\leftrightarrow}{\mathbf{F}}{}^{\mathrm{EC}} \cdot \vec{n} \tag{5.20}$$

and the viscous interface fluxes (4.116) *is entropy stable, i.e. for a closed system (periodic boundary conditions) the discrete total entropy is a decreasing function in time*

$$\frac{d\bar{S}}{dt} \le 0. \tag{5.21}$$

Proof. The proof is identical to the one of Theorem 2 besides that we now use (5.18) to bound the viscous fluxes, i.e.

$$\left\langle \mathbb{I}^N(J)\overset{\leftrightarrow}{\mathbf{Q}}, \overset{\leftrightarrow}{\mathbf{F}}{}^{v,\nu}\right\rangle_N = \left\langle \mathbb{I}^N(J)\overset{\leftrightarrow}{\mathbf{Q}}, \underline{\mathsf{P}}\overset{\leftrightarrow}{\mathbf{Q}}\right\rangle_N \geqslant \min_{E,N}(\mathbb{I}^N(J))\left\langle \overset{\leftrightarrow}{\mathbf{Q}}, \underline{\mathsf{P}}\overset{\leftrightarrow}{\mathbf{Q}}\right\rangle_N \geq 0. \tag{5.22}$$

Moreover, we have to be careful and also include the artificial viscosity at the cell interfaces by simple averages, so that everything cancels after summing over the elements. Besides that, the entire discrete entropy analysis remains the same. $\qquad\square$

Remark 8. This is a general result, independent of the considered system, since the mathematical entropy is assumed to be a convex function. Thus, the entropy Jacobian (inverse Hessian) is always symmetric and positive semi-definite.

5.2. Filtering by Dirac-delta kernels

In this approach, we avoid unphysical approximations caused by Gibbs oscillations at shocks by applying a filter matrix to the discrete solution after each time step. In particular, the filter matrix is constructed by a convolution against the Dirac-delta kernel, which is defined by the following delta sequence

$$\delta_\varepsilon^{m,k}(x) = \begin{cases} \frac{1}{\varepsilon}P^{m,k}\left(\frac{x}{\varepsilon}\right) & |x| \le \varepsilon \\ 0 & |x| > \varepsilon \end{cases}. \tag{5.23}$$

The kernel is built from the polynomial $P^{m,k}$, which is uniquely determined by the following conditions [125, 143]

$$\int_{-1}^{1} P^{m,k}(\xi)d\xi = 1, \tag{5.24}$$

$$\left(P^{m,k}\right)^{(i)}(\pm1) = 0 \quad \text{for} \quad i = 0, \ldots, k, \tag{5.25}$$

$$\int_{-1}^{1} \xi^i P^{m,k}(\xi)d\xi = 0 \quad \text{for} \quad i = 1, \ldots, m. \tag{5.26}$$
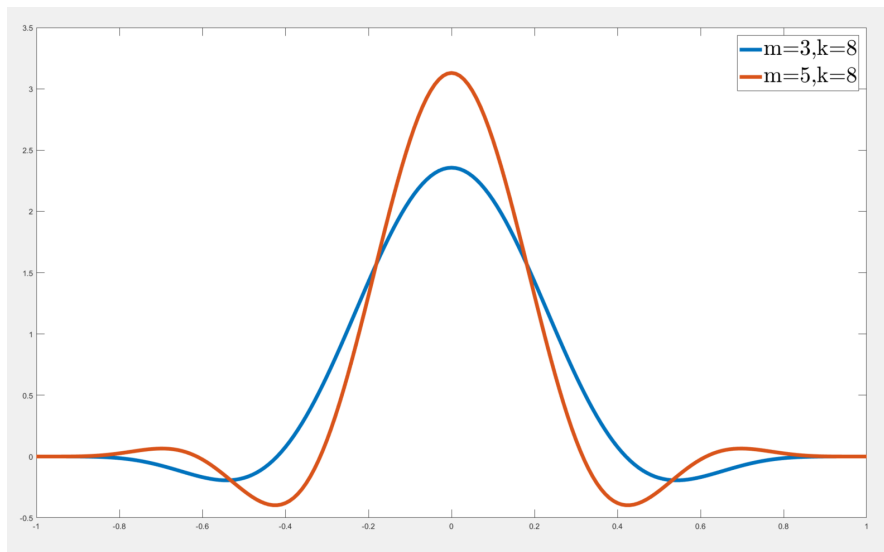
Figure 5.1.: Visualization of the Dirac-delta kernel for $\varepsilon = 1$.

In Fig. 5.1 we illustrate two choices of the delta kernel with $\varepsilon = 1$. The convolution against such kernels was originally used in the context of data post-processing by so-called smoothness increasing accuracy conserving (SIAC) Dirac-delta filtering, see e.g. [101, 115, 135]. We first present the original Dirac-delta filtering approach for a one-dimensional spectral collocation method in Sec. 5.2.1, before we derive a local filter applicable to approximations of single DG elements in Sec. 5.2.2 and extend it to higher spatial dimensions in Sec. 5.2.3.

5.2.1. Global filter

In this section we focus on global spectral collocation methods ($N_{\text{el}} = 1$) and start with a derivation of the filtering matrix in one spatial dimension. According to the SIAC

filtering strategy [115, 143] we regularize the global solution produced by the spectral method with the point-wise manipulation

$$
\begin{aligned}
\check{\mathbf{U}}(x,t) &= \int_{x-\varepsilon}^{x+\varepsilon} \mathbf{U}(\tau,t)\delta_\varepsilon^{m,k}(x-\tau)d\tau \\
&\approx \int_{x-\varepsilon}^{x+\varepsilon} \left[\sum_{i=0}^{N} \mathbf{U}_i(t)\ell_i(\tau)\right] \delta_\varepsilon^{m,k}(x-\tau)d\tau \\
&= \sum_{i=0}^{N} \mathbf{U}_i(t) \int_{x-\varepsilon}^{x+\varepsilon} \ell_i(\tau)\delta_\varepsilon^{m,k}(x-\tau)d\tau.
\end{aligned}
\tag{5.27}
$$

For compact notation we introduce the filter matrix Ξ and approximate its values with the LGL quadrature by mapping the corresponding integration area $[x - \varepsilon, x + \varepsilon]$ into the reference element $E = [-1, 1]$

$$
\begin{aligned}
\Xi_{ij} &= \int_{x_i-\varepsilon}^{x_i+\varepsilon} \ell_j(\tau)\delta_\varepsilon^{m,k}(x_i-\tau)d\tau \\
&= \varepsilon \int_{-1}^{1} \ell_j(\varepsilon x + x_i)\delta_\varepsilon^{m,k}(\varepsilon x)dx \\
&\approx \varepsilon \sum_{l=0}^{N^*} \omega_l \ell_j(\varepsilon x_l + x_i)\delta_\varepsilon^{m,k}(\varepsilon x_l)
\end{aligned}
\tag{5.28}
$$

for $i, j = 0, \ldots, N$, where $\{x_l\}_{l=0}^{N^*}$ and $\{\omega_l\}_{l=0}^{N^*}$ are the LGL quadrature points and weights for the sufficient degree of $N^* = 2\left(\frac{m}{2} + k + 1\right)$ to maintain the desired high-order accuracy of the approximation [125]. Further, we choose

$$
\varepsilon = \cos\left(\frac{\pi\left[\frac{N-N_d}{2}\right]}{N}\right)
\tag{5.29}
$$

with N_d determined empirically to ensure stable converging results [125, 143].

Finally, we can express the filtering process in terms of a matrix vector multiplication, i.e.

$$
\check{\mathbf{U}}(t) = \Xi\, \mathbf{U}(t).
\tag{5.30}
$$

For the global SIAC filtering technique we must address how the filter matrix is applied at the physical boundaries of the domain. However, at the physical boundaries no ε-stencils are defined. Thus, oscillations caused by shocks as well as by re-interpolation (Runge phenomena) cannot be smoothed in these areas. In the original approach for the global collocation method the affected parts of the discretization are set to the analytical solution [143]. Using a local version of the filter we can avoid identifying interior points by an analytical reference solution, as discussed in the next section.

Moreover, by construction, the filter conserves mass solely for polynomial data of degree up to m, which especially in a global collocation method is difficult to realize. Thus, small conservation errors might be introduced by applying the filter matrix (5.28).

5.2.2. Local filter

We next determine a method, in which we apply the SIAC filter to local DG solutions on one-dimensional domains decomposed into multiple elements ($N_{\mathrm{el}} > 1$) of equal size. Particularly, we want to apply the smoothing matrix Ξ locally to the solution of single elements [15]. Thus, we only require to couple the filtering across interfaces of neighboring elements to determine a *multi-element* SIAC filtering technique.

We begin with (5.27), where, in one spatial dimension, we know that the approximation of the solution $\mathbf{U}$ is a union of piecewise polynomials over all elements $\iota = 1, \ldots, N_{\mathrm{el}}$, i.e.

$$
\begin{aligned}
\check{\mathbf{U}}(x,t) &= \int_{x-\varepsilon}^{x+\varepsilon} \mathbf{U}(\tau,t)\delta_\varepsilon^{m,k}(x-\tau)d\tau \\
&= \int_{x-\varepsilon}^{x+\varepsilon} \left[\sum_{\iota=1}^{N_{\mathrm{el}}} \mathbf{U}^\iota(\tau,t)\right]\delta_\varepsilon^{m,k}(x-\tau)d\tau \\
&= \sum_{\iota=1}^{N_{\mathrm{el}}} \int_{x-\varepsilon}^{x+\varepsilon} \mathbf{U}^\iota(\tau,t)\delta_\varepsilon^{m,k}(x-\tau)d\tau.
\end{aligned} \tag{5.31}
$$

Next, we focus on one physical node $x_i := X^n(\xi_i)$ within one specific element $\mathfrak{E}_n$ and define the following sets

$$
Q_{i,n}^\varepsilon := [x_i - \varepsilon, x_i + \varepsilon] \cap \mathfrak{E}_n, \tag{5.32}
$$

$$
Q_{i,n-1}^\varepsilon := [x_i - \varepsilon, x_i + \varepsilon] \cap \mathfrak{E}_{n-1}, \tag{5.33}
$$

$$
Q_{i,n+1}^\varepsilon := [x_i - \varepsilon, x_i + \varepsilon] \cap \mathfrak{E}_{n+1}. \tag{5.34}
$$

Since ε is sufficiently small, we assume that the ε-stencil is imbedded in these three sets and thus

$$
\begin{aligned}
\check{\mathbf{U}}_i^n(t) &= \sum_{\iota=1}^{N_{\mathrm{el}}} \int_{x_i-\varepsilon}^{x_i+\varepsilon} \mathbf{U}^\iota(\tau,t)\delta_\varepsilon^{m,k}(x_i-\tau)d\tau \\
&= \int_{Q_{i,n}^\varepsilon} \mathbf{U}^n(\tau,t)\delta_\varepsilon^{m,k}(x_i-\tau)d\tau + \int_{Q_{i,n-1}^\varepsilon} \mathbf{U}^{n-1}(\tau,t)\delta_\varepsilon^{m,k}(x_i-\tau)d\tau \\
&\quad + \int_{Q_{i,n+1}^\varepsilon} \mathbf{U}^{n+1}(\tau,t)\delta_\varepsilon^{m,k}(x_i-\tau)d\tau.
\end{aligned} \tag{5.35}
$$

If we now define similar sets for the corresponding LGL node

$$E_i^\varepsilon := [\xi_i - \varepsilon, \xi_i + \varepsilon] \cap [-1, 1], \tag{5.36}$$

$$E_{i,L}^\varepsilon := [\xi_i - \varepsilon, \xi_i + \varepsilon] \cap [\xi_i - \varepsilon, -1], \tag{5.37}$$

$$E_{i,R}^\varepsilon := [\xi_i - \varepsilon, \xi_i + \varepsilon] \cap [1, \xi_i + \varepsilon], \tag{5.38}$$

we can transform everything to reference space again and obtain

$$\begin{aligned}
\check{\mathbf{U}}_i^n(t) = \varepsilon &\int_{E_i^\varepsilon} \sum_{j=0}^{N} \ell_j(\varepsilon x + \xi_i) \mathbf{U}_j^n(t) \delta_\varepsilon^{m,k}(\varepsilon x) dx \\
&+ \varepsilon \int_{E_{i,L}^\varepsilon} \sum_{j=0}^{N} \ell_j(\varepsilon x + \xi_i - 2) \mathbf{U}_j^{n-1}(t) \delta_\varepsilon^{m,k}(\varepsilon x) dx \\
&+ \varepsilon \int_{E_{i,R}^\varepsilon} \sum_{j=0}^{N} \ell_j(\varepsilon x + \xi_i + 2) \mathbf{U}_j^{n+1}(t) \delta_\varepsilon^{m,k}(\varepsilon x) dx.
\end{aligned} \tag{5.39}$$

Note, that we shift the arguments of the Lagrange basis functions in the left and right elements by ± 2 to guarantee the correct evaluation points. We can write (5.39) in compact notation by applying a modified $(N+1) \times 3(N+1)$ smoothing matrix to the solution, i.e.

$$\check{\mathbf{U}}^n(t) = \underbrace{\begin{pmatrix} \Xi^{n-1} & \Xi^n & \Xi^{n+1} \end{pmatrix}}_{=: \, \boldsymbol{\Xi}} \begin{pmatrix} \mathbf{U}^{n-1}(t) \\ \mathbf{U}^n(t) \\ \mathbf{U}^{n+1}(t) \end{pmatrix} \tag{5.40}$$

with the block matrices defined by

$$\Xi_{i,j}^n = \varepsilon \int_{E_i^\varepsilon} \ell_j(\varepsilon x + \xi_i) \delta_\varepsilon^{m,k}(\varepsilon x) dx \tag{5.41}$$

$$\Xi_{i,j}^{n-1} = \varepsilon \int_{E_{i,L}^\varepsilon} \ell_j(\varepsilon x + \xi_i - 2) \delta_\varepsilon^{m,k}(\varepsilon x) dx \tag{5.42}$$

$$\Xi_{i,j}^{n+1} = \varepsilon \int_{E_{i,R}^\varepsilon} \ell_j(\varepsilon x + \xi_i + 2) \delta_\varepsilon^{m,k}(\varepsilon x) dx \tag{5.43}$$

for $i, j = 0, \ldots, N$. Again, we evaluate these integrals by a Legendre-Gauss-Lobatto quadrature with $N^* = 2 \left(\frac{m}{2} + k + 1 \right)$ points as in (5.28).

Note, that since the neighboring elements only enter in the smoothing matrix at grid points near to the element boundaries, Ξ^{n-1} and Ξ^{n+1} are block matrices with mostly zero entries, especially when N is large. In particular, only the first several rows of Ξ^{n-1} and the last several rows of Ξ^{n+1} are non-zero. We see that the multi-element SIAC filtering process is not entirely local to element $\mathfrak{E}_n$; however, we only need solution information from its direct neighbors in the mesh. Further we note, that the local filter

matrix $\boldsymbol{\Xi}$ is independent of the current solution and, thus, can be pre-computed and stored, before the simulation is started.

An additional advantage in the design of this multi-element filtering technique is the treatment of elements located at physical boundaries. We already noted that there is no ε-stencil defined in these boundary areas. Thus, we cannot apply the filter. However, from the multi-element technique we can introduce *ghost elements*, in which we define a consistent solution depending on the physical boundary condition, e.g. for reflecting wall or Dirichlet values. This procedure removes Runge phenomena from the solution without the need to identify interior points by analytical values as in [143].

Furthermore, we can use the locally filtered solution as a *shock detector* to adaptively apply the multi-element filter only in elements where it is necessary. To do so, we define an indicator to measure the difference between the filtered and unfiltered solutions

$$\epsilon_{\mathrm{FIL}}(\mathbf{U}) := \max_{i=0,\ldots,N} \left| \mathbf{U}_i - \check{\mathbf{U}}_i \right|. \tag{5.44}$$

Next, we normalize this indicator with respect to the polynomial order and the number of elements and check in each element $\iota = 1, \ldots, N_{\mathrm{el}}$, if

$$\frac{\epsilon_{\mathrm{FIL}}^{\iota}}{(N+1)N_{\mathrm{el}}} > \texttt{TOL} \tag{5.45}$$

for a given user defined tolerance $\texttt{TOL} > 0$. If this condition is fulfilled, we replace the current element solution with the filtered solution. Otherwise the approximation is deemed to be sufficiently smooth and no filtering is applied. As for the DOF energy indicator, we use single variables to compute ϵ_{FIL}, e.g. the density or pressure for the resistive GLM-MHD equations.

Moreover, for convenience, we define

$$\sigma^{\mathrm{FIL}} = \log_{10}\left(\epsilon_{\mathrm{FIL}}\right) \tag{5.46}$$

and introduce a transition area between two tolerance levels, $\sigma_{\min}^{\mathrm{FIL}} \leq \sigma^{\mathrm{FIL}} \leq \sigma_{\max}^{\mathrm{FIL}}$, to smoothly blend the filtered and unfiltered solutions. As such we introduce a parameter $0 \leq \varkappa \leq 1$ and then define the updated solution on a given element $\mathfrak{E}_n$ to be a convex combination of the two solutions

$$\hat{\mathbf{U}}^n = \varkappa\check{\mathbf{U}}^n + (1-\varkappa)\mathbf{U}^n \tag{5.47}$$

with

$$\varkappa = \frac{1}{2}\left[1 + \sin\left(\pi\left(\sigma^{\mathrm{FIL},n} - \frac{1}{2}\frac{\sigma_{\max}^{\mathrm{FIL}} + \sigma_{\min}^{\mathrm{FIL}}}{\sigma_{\max}^{\mathrm{FIL}} - \sigma_{\min}^{\mathrm{FIL}}}\right)\right)\right]. \tag{5.48}$$

A major concern for any shock capturing method is to maintain conservation, which ensures the correct shock speeds are maintained discretely [92]. But, in its current

incarnation the multi-element SIAC filter *does not* conserve the solution quantities, e.g., density, momentum and total energy for the Euler equations. The unfiltered standard DGSEM as well as the artificial viscosity approach conserve the solution variables up to machine precision, e.g. [28, 106]. However, the application of the global or local SIAC filter after each time step is no longer conservative because we re-distribute solution data, e.g. the mass, by the filtering process. Whereas the conservation errors for the global filter are introduced by the necessary large interpolation order $N >> m$, we can easily assure $N \leq m$ for the local element-wise filtering. Though, we run into a different problem, because our global approximation is no longer a polynomial, but solely built from piecewise polynomial data. Thus, again, we introduce conservation errors in our approximation, which are usually small, but unavoidable [15].

5.2.3. Two-dimensional filter

Next, we extend the one-dimensional local SIAC filter to higher spatial dimensions, whereas we restrict to Cartesian meshes. For the filtering process we apply the same local smoothing matrix $\mathbf{\Xi}$ as in the one-dimensional case in each spatial direction to the unfiltered element solutions. Conveniently, this is possible due to the tensor product ansatz of the DGSEM and the definition of the Dirac-delta kernel (5.23).

We begin, again, from the filtering assumption of (5.27) and find for the piecewise polynomial solution $\mathbf{U}$ that

$$
\begin{aligned}
\check{\mathbf{U}}(x,y,t) &= \int_{x-\varepsilon}^{x+\varepsilon} \int_{y-\varepsilon}^{y+\varepsilon} \mathbf{U}(\tau,\varsigma,t)\delta_\varepsilon^{m,k}(x-\tau,y-\varsigma)d\tau d\varsigma \\
&= \sum_{\iota=1}^{N_{\text{el}}} \int_{x-\varepsilon}^{x+\varepsilon} \int_{y-\varepsilon}^{y+\varepsilon} \mathbf{U}^\iota(\tau,\varsigma,t)\delta_\varepsilon^{m,k}(x-\tau,y-\varsigma)d\tau d\varsigma,
\end{aligned}
\tag{5.49}
$$

where we define the multi-variable delta function to have the form

$$
\delta(x,y) := \delta_\varepsilon^{m,k}(x,y) = \delta_\varepsilon^{m,k}(x)\delta_\varepsilon^{m,k}(y) =: \delta(x)\delta(y).
\tag{5.50}
$$

Again, we focus on the approximation in one particular element $\mathfrak{E}_n$ at one LGL node $(\xi_i, \eta_j) \in [-1,1]^2$, transform into the reference space and use the tensor product property

to split the integrand, i.e.

$$
\begin{aligned}
\check{\mathbf{U}}^n_{ij}(t) &= \sum_{\iota=1}^{N_{\mathrm{el}}} \int_{x_i-\varepsilon}^{x_i+\varepsilon} \int_{y_j-\varepsilon}^{y_j+\varepsilon} \mathbf{U}^\iota(\tau,\varsigma,t)\delta(x_i-\tau,y_j-\varsigma)d\tau d\varsigma \\
&= \sum_{\iota=1}^{N_{\mathrm{el}}} \varepsilon^2 \int_{-1}^{1} \int_{-1}^{1} \mathbf{U}^\iota(\varepsilon x + \xi_i, \varepsilon y + \eta_j, t)\delta(\varepsilon x, \varepsilon y)dxdy \\
&= \varepsilon^2 \int_{-1}^{1} \int_{-1}^{1} \sum_{k,l=0}^{N} \bar{\ell}_k(\varepsilon x + \xi_i)\bar{\ell}_l(\varepsilon y + \eta_j)\mathbf{U}^{\bar{\iota}}_{kl}(t)\delta(\varepsilon x)\delta(\varepsilon y)dxdy \\
&= \sum_{k,l=0}^{N} \underbrace{\varepsilon \int_{-1}^{1} \bar{\ell}_k(\varepsilon x + \xi_i)\delta(\varepsilon x)dx}_{=\Xi_{ik}}\; \underbrace{\varepsilon \int_{-1}^{1} \bar{\ell}_l(\varepsilon y + \eta_j)\delta(\varepsilon y)dy}_{=\Xi_{jl}}\; \mathbf{U}^{\bar{\iota}}_{kl}(t).
\end{aligned}
\tag{5.51}
$$

Here, the $\bar{\iota}$ points to the correct solution entry, which includes neighboring elements and is dependent on the storing data structure. The shifting of the evaluation points for the Lagrange basis function is also hidden in the bar notation, i.e.

$$
\bar{\ell}(x) := \begin{cases} \ell(x), & x \in [-1,1] \\ \ell(x-2), & x > 1 \\ \ell(x+2), & x < -1 \end{cases}.
\tag{5.52}
$$

From this definition of the filtering matrices it is possible to write the filtering process in a compact notation

$$
\check{\mathbf{U}}^n = \mathbf{\Xi}\,\mathbf{U}^n_{\mathrm{env}}\,\mathbf{\Xi}^T
\tag{5.53}
$$

with

$$
\mathbf{\Xi} = \begin{pmatrix} \Xi^{n-1} & \Xi^n & \Xi^{n+1} \end{pmatrix} \quad \text{and} \quad \mathbf{U}^n_{\mathrm{env}} = \begin{pmatrix} \mathbf{U}^{n+N^x_{\mathrm{el}}-1} & \mathbf{U}^{n+N^x_{\mathrm{el}}} & \mathbf{U}^{n+N^x_{\mathrm{el}}+1} \\ \mathbf{U}^{n-1} & \mathbf{U}^n & \mathbf{U}^{n+1} \\ \mathbf{U}^{n-N^x_{\mathrm{el}}-1} & \mathbf{U}^{n-N^x_{\mathrm{el}}} & \mathbf{U}^{n-N^x_{\mathrm{el}}+1} \end{pmatrix}, \tag{5.54}
$$

provided the elements are labeled from bottom-left to top-right and N^x_{el} denotes the number of elements in the x-direction. In this case, we design the smoothing matrix $\mathbf{\Xi} = \begin{pmatrix} \Xi^{n-1} & \Xi^n & \Xi^{n+1} \end{pmatrix}$ exactly as in one spatial dimension (5.40).

We want the resulting shock capturing DG scheme to be as local as possible and implement the 2D multi-element SIAC filter in a way to reflect this goal. First, we define

$$
\begin{pmatrix} \hat{\mathbf{U}}^{n+N^x_{\mathrm{el}}} \\ \hat{\mathbf{U}}^n \\ \hat{\mathbf{U}}^{n-N^x_{\mathrm{el}}} \end{pmatrix} := \mathbf{U}^n_{\mathrm{env}}\mathbf{\Xi}^T = \begin{pmatrix} \Xi^{n-1}\mathbf{U}^{n+N^x_{\mathrm{el}}-1} + \Xi^n\mathbf{U}^{n+N^x_{\mathrm{el}}} + \Xi^{n+1}\mathbf{U}^{n+N^x_{\mathrm{el}}-1} \\ \Xi^{n-1}\mathbf{U}^{n-1} + \Xi^n\mathbf{U}^n + \Xi^{n+1}\mathbf{U}^{n+1} \\ \Xi^{n-1}\mathbf{U}^{n-N^x_{\mathrm{el}}-1} + \Xi^n\mathbf{U}^{n-N^x_{\mathrm{el}}} + \Xi^{n+1}\mathbf{U}^{n-N^x_{\mathrm{el}}-1} \end{pmatrix}, \tag{5.55}
$$

which is nothing more than the solution vector of the three considered adjacent cells filtered in the x-direction. To filter in the y-direction, we simply apply the smoothing matrix $\boldsymbol{\Xi}$ from the left and obtain an overall filtered solution $\check{\mathbf{U}}^n$ from (5.53). A major advantage of this approach is that the filtering procedure is performed dimension by dimension. So for all elements $\iota = 1, \ldots, N_{\text{el}}$ we first filter in the x-direction to find $\hat{\mathbf{U}}^\iota$ with coupling only from the right and left neighbor cells. Next, we filter in the y-direction and compute the fully filtered solution $\check{\mathbf{U}}^\iota$ from the information stored in the intermediate array $\hat{\mathbf{U}}^\iota$ with coupling from the upper and lower neighbor elements. That is, we simply apply the one-dimensional filter twice for each grid point using only information from the direct neighbors. Additionally, we note, that this filtering procedure has no preferred direction such that the order of x, y directions makes no difference.

An extension to three-dimensional SIAC filters on Cartesian meshes is straightforward. But in addition to the conservation issues stressed in the previous section, there is no theory available for SIAC filtering on unstructured or curved elements. Additionally, we have not investigated the entropic properties of such a smoothing filter yet. Nonetheless, we will present some promising results for two-dimensional shock problems on Cartesian grids in Sec. 7.1.5.

5.3. Positivity preserving limiter

Even though it technically does not belong to the shock capturing methods, we broadly present the positivity preserving limiter developed by Perthame, Shu and Zhang [107, 146]. As mentioned above, shocks can cause spurious oscillations in the DG approximation, which we can greatly reduce by the counter-mechanisms discussed in the previous sections. But, especially in regions close to vacuum, the oscillations are most problematic, because the simulation might crash due to the generation of negative density and/or pressure values. Hence, an additional mechanism is required, that strictly enforces the positivity of these quantities without destroying accuracy, conservation or locality of the entropy stable DGSEM for the resistive GLM-MHD equations.

In e.g. [146] the authors have developed a positivity preserving limiter based on a linear scaling around element averages. Particularly, for all elements $\iota = 1, \ldots, N_{\text{el}}$ a simple limiting procedure is applied in each Runge-Kutta step, which for a given tolerance $\epsilon > 0$ can be summarized in four steps:

1. compute $\bar{\mathbf{u}} = \frac{1}{|\mathfrak{E}_\iota|} \int\limits_{\mathfrak{E}_\iota} \mathbf{u} \, \mathrm{dV} \approx \frac{1}{8} \sum\limits_{i,j,k=0}^{N} J_{ijk} \mathbf{U}_{ijk} \omega_{ijk}$ and $\varrho_{\min} = \min\limits_{i,j,k=0,\ldots,N} \varrho_{ijk}$

2. if $\varrho_{\min} < 0$, then modify the density by $\hat{\varrho} = \theta_1 \varrho + (1-\theta_1)\bar{\varrho}$ with $\theta_1 = \frac{\bar{\varrho}-\epsilon}{\bar{\varrho}-\varrho_{\min}}$

3. compute $\bar{p} = \frac{1}{|\mathfrak{E}_\iota|} \int\limits_{\mathfrak{E}_\iota} p \, \mathrm{dV} \approx \frac{1}{8} \sum\limits_{i,j,k=0}^{N} J_{ijk} p_{ijk} \omega_{ijk}$ and $p_{\min} = \min\limits_{i,j,k=0,\ldots,N} p_{ijk}$

4. if $p_{\min} < 0$, then modify the solution vector by $\hat{\mathbf{u}} = \theta_2 \mathbf{u} + (1-\theta_2)\bar{\mathbf{u}}$ with $\theta_2 = \frac{\bar{p}-\epsilon}{\bar{p}-p_{\min}}$

We note, that in steps 3 and 4 we use the limited density value $\hat{\varrho}$ for the computation of the pressure as well as in the correction of the solution vector.

It has been shown, that this limiting procedure preserves non-negative average densities and pressures for the Euler equations (2.5) on Cartesian meshes [107]. Further, all the proofs in [107] are based on a specific set of *positivity preserving* numerical fluxes, which are derived for finite volume discretizations, directly translate to DG methods on Cartesian meshes and cover e.g. the global and local Lax-Friedrichs numerical fluxes [146]. The positivity preserving property is only shown for explicit Euler time integration and introduces an additional time step restriction by a factor of $\frac{1}{2\omega_0}$. By such an adjustment of the CFL condition it naturally extends to *strong stability preserving* (SSP) Runge-Kutta methods, as these are convex combinations of Euler time steps [122].

Moreover, these profs have recently been extended to DG approximations of the ideal MHD equations (2.18) on Cartesian meshes, provided a positivity preserving numerical fluxes is used and the magnetic field is divergence-free [25, 145]. Obviously, this is discretely not true for our scheme. Further, our time integration method is not SSP and our elements might be curved. Nonetheless, the limiting strategy still works well for the few numerical tests we needed it, but in fact, we solely applied it to simulations on Cartesian meshes and circumvented the effects of the time integration by simply reducing the CFL number.

In addition to the missing theory concerning non-divergence-free magnetic fields and curvilinear meshes, studying the compatibility of such a positivity limiter with the discrete entropic properties of the resistive GLM-MHD equations is future work. Such research results are especially desired, since positive density and pressure are an essential assumption for the entire entropy analysis. Thus, discretely guaranteeing the positivity of these quantities in an entropy consistent way would complete the circle and provide a very robust physically relevant numerical approximation.

6. Implementation

Before we provide the numerical verification of the novel entropy stable DG solver for the resistive GLM-MHD equations as well as the discussed shock capturing methods, we present some details on the actual implementation. In fact, the developed entropy stable DGSEM has been implemented in two different coding environments. The first code introduced in Sec. 6.1 is a serial implementation, that covers all the presented methods, but is restricted to two-dimensional Cartesian meshes. A fully parallelized, three-dimensional and curved version of the derived method, except for the SIAC filter, has been programmed into the open source MHD solver `FLUXO` (`https://github.com/project-fluxo`), which we discuss in Sec. 6.2. Both codes are written in the programming language `Fortran` (`http://www.fortran90.org/`).

6.1. Serial Cartesian code

During the process of deriving an entropy stable DG solver for the resistive GLM-MHD equations it was desired to validate the developed methods numerically, first for simple one- and two-dimensional test cases. Hence, a reduced implementation was required, which could be used to verify the expected numerical behavior of the scheme in serial, before moving to a high performance computing level. For this purpose, the author implemented a two-dimensional Cartesian version of the entropy stable DGSEM for the resistive GLM-MHD equations including both shock capturing strategies as well as the positivity preserving limiter from Sec. 5. In order to refer to this implementation, we call it `SerCart` throughout this work.

In particular, `SerCart` is written in the language `Fortran90` and operated in the `eclipse` environment for open source software collaboration and innovation (`https://www.eclipse.org/`). We run all our `SerCart` simulations under Windows 8.1 Enterprise on a 2.2 GHz Intel Core i7-4702MQ CPU quad-core processor. Data post processing is done with the open source visualization, animation and analysis tools `visit` (`https://wci.llnl.gov/simulation/computer-codes/visit/`) and `paraview` (`https://www.paraview.org/`). Some plots are also created with `Matlab` (`https://de.mathworks.com/products/matlab.html`) and the `matplot` library provided by `Python` (`https://www.python.org/`).

Since there is much literature available about implementing spectral element methods in general, or more precisely discontinuous Galerkin schemes, e.g. [81], we refer to

these books for details on coding the numerical schemes. From an implementation stand-point, the only necessary changes to obtain the entropy stable DGSEM from its standard version are to replace the volume integral by its flux differencing counterpart, include the discretizations of the non-conservative terms and use the entropy stable numerical flux on the interfaces. However, in Algorithm 1 we present the general code structure of the entropy stable DGSEM with optional shock capturing as it is implemented in `SerCart`.

Algorithm 1: *DGmain:* General body of entropy stable DGSEM with optional shock capturing.

Input : Mesh data, polynomial degree N, final time T, boundary conditions,
            initial data, shock capturing flags, simulation specified parameters

Output: Final solution array $\mathbf{u}(x, y, T) \approx \mathbf{U}_{n=1,i=0,j=0,\iota=1}^{N_{\mathrm{eq}},N,N,N_{\mathrm{el}}}$

Procedure *DGmain*
initializeSolutionArray
computeFilterMatrix   `// optional`
while $t < T$ **do**
   | *computeTimeStep*   `//` Δt
   | **for** $RK\,step = 1 : 5$ **do**
   | | *updateGradientEdgeFluxes*
   | | **for** $\iota = 1 : N_{\mathrm{el}}$ **do**
   | | | *computeGradients*
   | | **end**
   | | *computeGLMwavespeed*   `//` c_h
   | | *computeArtificialViscosity*   `// optional`
   | | *updateEdgeFluxesAndNonCons*
   | | **for** $\iota = 1 : N_{\mathrm{el}}$ **do**
   | | | *computeVolumeFluxesAndNonCons*
   | | | *updateSolutionTimeDerivative*
   | | **end**
   | | *makeSolutionPositive* `// optional`
   | **end**
   | *filterSolution*   `// optional`
   | $t = t + \Delta t$
end
writeSolutionToPlot

Note, that for the shock capturing we either use the artificial viscosity approach from Sec. 5.1 or the filtering technique from Sec. 5.2, whereas the positivity limiter can always be applied on top. Further, one has to be careful implementing the correct orientation of the non-conservative terms at the element interfaces.

Especially for the nine equation GLM-MHD system a serial computation of all split form volume discretizations for the advective fluxes and non-conservative terms is computationally expensive. The evaluations of all the averages in the EC and ES fluxes plus the computations of the gradients generate additional runtime and memory consumptions. Thus, the `SerCart` code is not applicable for bigger simulations. Consequently, we require a parallelized version of the entropy stable DG solver for real three-dimensional problems including curved geometries.

6.2. Parallel curved code

A fully three-dimensional version of the entropy stable DGSEM for the resistive GLM-MHD equations on curved elements is implemented in the open source MHD solver `FLUXO` (`https://github.com/project-fluxo`). The general code structure is similar to Algorithm 1. `FLUXO` is written in modern Fortran and its non-blocking pure Message Passing Interface (MPI) parallelization shows excellent strong and weak scaling on modern HPC architectures. The three-dimensional high-order meshes for our simulations are generated with the open source tool `HOPR` (`www.hopr-project.org`).

The author would like to emphasize, that `FLUXO` has been developed in collaboration with the IAG Stuttgart and the Max-Planck Insitut in Garching over the recent years. Especially, the extension of the original Navier-Stokes solver `FLEXI` (`https://www.flexi-project.org/`), see e.g. [70], to the full resistive GLM-MHD system in an entropy stable fashion has mostly been coded by Florian Hindenlang. The author himself implemented the shock capturing by the artificial viscosity approach from Sec. 5.1 into the existing framework, which includes an additional module to calculate the element-wise artificial viscosity by the DOF energy indicator from Sec. 5.1.1 and a modification of the viscous fluxes as in (5.14). Moreover, he embedded the necessary modifications for the final space physics applications presented in Sec. 8.

All three-dimensional simulations in this work are run with `FLUXO` on the HPC cluster `CHEOPS`, which is provided by the Regional Computing Centre of Cologne (RRZK) together with the HPC expert Bull. With more than 100 TFlop/s peak and 85.9 TFlop/s Linpack performance, `CHEOPS` was ranked to be the 89th fastest supercomputer worldwide in the Top500 list from November 2010 [1]. In particular, `CHEOPS` is an InfiniBand coupled HPC cluster with dual socket INCA compute nodes, which consist of 210×2 Nehalem EP quad-core processors (Xeon X5550, 2.66 GHz, 24 GB RAM), 5×2 Nehalem EP quad-core processors (Xeon X5550, 2.66 GHz, 48 GB RAM), 432×2 Westmere hexa-core processors (Xeon X5650, 2.66GHz, 24 GB RAM) and 170×2 Westmere hexa-core processors (Xeon X5650, 2.66 GHz, 48 GB RAM), as well as quad socket MESCA compute nodes divided into 24×4 Nehalem EX octo-core processors (Xeon X7560, 2.27 GHz, 512 GB RAM) [1]. The node interconnect is based on InfiniBand QDR, which is a broadband bus technology with exceptionally small latency. Further, `CHEOPS` uses

General Parallel File System and Lustre as parallel file systems. To provide the required performance, four object storage servers deliver the data to the compute nodes. The meta data is stored on an EMC box, which is exposed through two meta data servers. For more details on the hardware structure see [1].

Even though we do not discuss all implementation details of `FLUXO`, we highlight two important aspects in this section: We provide a general overview of the parallelization including MPI communication and scaling on HPC clusters in Sec. 6.2.1. Additionally, we point out some optimization strategies for a more efficient implementation of the scheme in Sec. 6.2.2.

6.2.1. Parallelization aspects

As three-dimensional simulations on curvilinear meshes are computationally very demanding and computer resources constantly cheapen, the scalability of numerical algorithms has become more important to tackle large scale computations or to decrease the runtime of simulations. Besides the high-order accuracy, entropic properties and divergence cleaning, a main advantage of the derived entropy stable DGSEM is its HPC capability due to its local structure, where elements communicate only with their direct neighbors via solution and flux exchange. The following descriptions of the parallel structure as it is implemented in `FLUXO` were originally proposed in [69].

As a first step to run a parallel simulation, we have to decompose the mesh and assign partial domains to each core. Further, we mark the inter-element connections of the mesh, especially domain-to-domain interfaces for data communication. These steps are typically global operations and have to be done in a pre-processing stage. Advantageously, the mesh generator `HOPR` supports such domain decompositions for HPC structures in form of a space-filling curve approach [69]. Particularly, `HOPR` provides mesh files using the binary HDF5 format, which is parallel readable and includes element connectivity lists as well as high-order curved element information. The resulting one-dimensional list of elements is sorted along a space-filling curve enabling fast parallel communication. Note, that `HOPR` only needs to be run once for a given mesh and the simulation code reads this file in parallel at each start or restart of a simulation, whereas the number of cores can be arbitrarily chosen.

The labeling of elements by space-filling curves is just one possibility to manage the domain decomposition and dynamic load balancing [4, 62]. They map positions in multi-dimensional space to points on a one-dimensional curve, whereas neighboring positions are located as close as possible on the curve. Alternatively, quadtrees or octrees are often used to split the domain in quadrants or octants, respectively [19]. More details on space-filling curves and other mesh decomposition strategies can be found in [69].

Now, that we have divided the computational domain onto several cores and marked the shared surfaces termed as *MPI-sides*, we address the communication between different processors. In fact, it is possible to send surface data while simultaneously performing

other local operations, as depicted in Fig. 6.1 and realized via non-blocking send and receive commands provided by the MPI standard library [59]. Here, the receive buffer acts like a mailbox, whereas the receive checks the mail and would only wait if the communication has not finished [69].
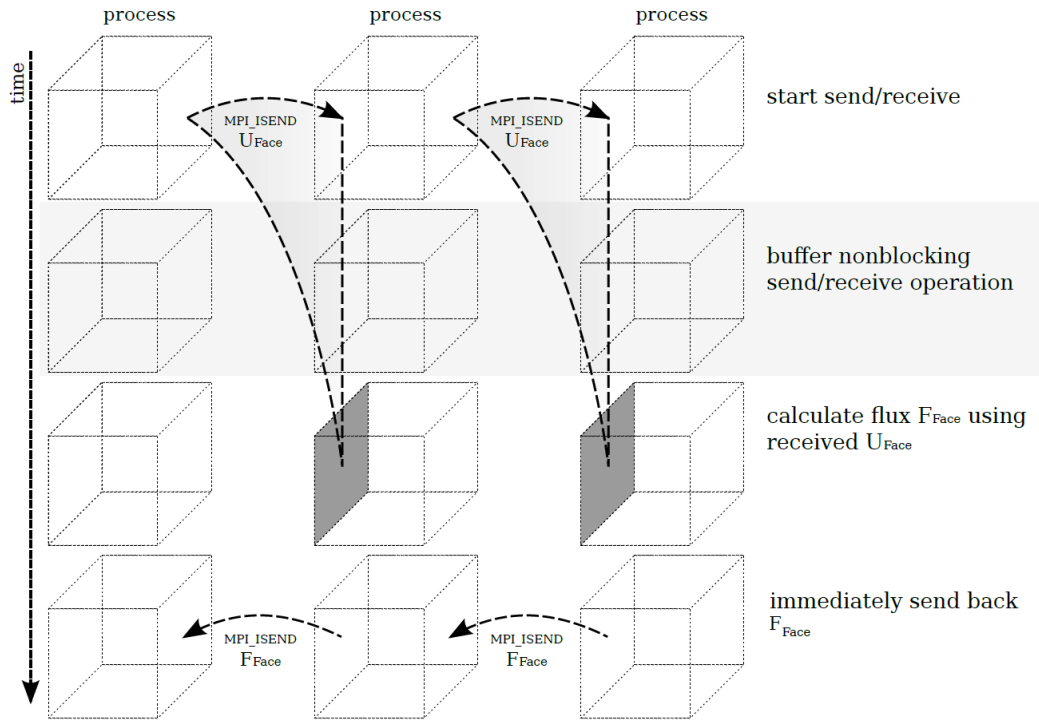
Figure 6.1.: Communication pattern for inter-processor computation with non-blocking communication [69].

Similar as in Sec. 4.2.2, FLUXO identifies element sides either as primary or secondary. Neglecting boundary surfaces for now, the element coupling is performed by the numerical fluxes, which are unique for each side, and the non-conservative terms, which are also identical for neighboring elements except for the sign. Therefore, all these components are computed once per side.

For MPI-sides, the solution is sent from the secondary to the primary side, so that the flux and non-conservative terms are only computed on the primary side. Then, these shared components are sent back to the secondary side, as shown in Fig. 6.1. Hence, except for communication, no additional operations are introduced, which is an important property of a scalable algorithm. In the overall workflow, MPI-sides are treated first and the data is sent immediately. Meanwhile, as a buffer, the remaining surface data is

exchanged and volume integrals are computed. After the communication of the surface data is finished over the entire domain, the surface fluxes and non-conservative terms can be calculated. Again, the flux at MPI-sides is computed first and sent, followed by the flux computations and the surface integrals at the other sides. When the flux is received, the surface integration adds the surface flux and non-conservative contributions at the MPI-sides to the volume data and the evaluation of the parallel DGSEM operator is finished.

On unstructured meshes the number of MPI-sides per domain varies. Thus, they are divided into subgroups associated to each neighbor domain and reassigned, such that half of each subgroup sides are primary and the other secondary sides. By this procedure we equally distribute the sent and receive commands over the entire domain and minimize the communication time, which is one example of *load balancing*. For more details on the parallelization aspects implemented in `FLUXO` we refer to [69].

In order to verify, that the entropy stable DGSEM is indeed well suited for such a parallel implementation, the performance of the code can be analyzed in terms of its *weak* and *strong scaling* capabilities. Whereas the first measures the scaling of the simulation time over the number of cores for constant loads per core and, thus, an increasing problem size, the latter measures the scaling of the simulation time over the number of processors for a fixed total problem size. In Sec. 7.2.2, we present some evidence for the strong scaling abilities of the entropy stable DGSEM for the resistive GLM-MHD equations as it is implemented in `FLUXO`. These results are computed on the `CHEOPS` cluster and underline, that the described parallelization approach indeed speeds up the simulation time by the expected optimal rate. Further, in the same section, we present the performance index (PID) defined by

$$\text{PID} = \frac{\text{runtime} \times \#\text{cores}}{\#\text{timesteps} \times \text{DOF}} \tag{6.1}$$

for different numbers of processors in order to assess the efficiency of the code. We find, that up to a minimum load an optimal scaling is obtained independent of the polynomial degree of the DG solution.

6.2.2. Efficient implementation

As highlighted in the second paper of our entropy stable DGSEM for the resistive GLM-MHD equations series [68], there are many possibilities to optimize the implementation of the derived method. Besides an appropriate data structure for storing the solution vector as well as its gradient, we require fast and efficient algorithms to update them in each Runge-Kutta step. Respectively, for all elements we compute the right hand side of both equations in our final DG approximation (3.51), which consists of several volume and surface discretizations.

Regarding the surface coupling, we have no other option than solving the point-wise Riemann problems for the advective, viscous and non-conservative terms. This can be implemented most efficiently by looping over all element interfaces and providing fast and logical access to adjacent element data as presented in the previous section. Further, we make use of the rotational invariance of the numerical fluxes as well as the non-conservative terms. Consequently, the according routines are solely implemented in the ξ-direction and before they are called, the corresponding fluxes and non-conservative terms are rotated once and afterward rotated back into the normal direction.

For the volume and interior surface contributions though, we can achieve a significant performance speed-up in the simulations. In order to do so, we first recall these contributions for the the advective pieces

$$\langle \mathcal{L}(\mathbf{U}), \boldsymbol{\varphi} \rangle_N := \left\langle \vec{\mathbb{D}} \cdot \overset{\leftrightarrow}{\tilde{\mathbf{F}}}^{a,\#}, \boldsymbol{\varphi} \right\rangle_N + \int\limits_{\partial \mathfrak{E}, N} \boldsymbol{\varphi}^T \left\{ \mathbf{F}_n^{a,*} - \mathbf{F}_n^a \right\} \hat{s} \, \mathrm{dS}. \tag{6.2}$$

Restricting to the differentiation in the first spatial direction and inserting the DG test functions

$$\varphi_{ijk}(\xi, \eta, \zeta) = \ell_i(\xi)\ell_j(\eta)\ell_k(\zeta) \tag{6.3}$$

for $i, j, k = 0, \ldots, N$ and each system variable, we can write (6.2) at one particular grid point (i, j, k) as

$$\mathcal{L}_\xi(\mathbf{U})_{ijk} = 2 \sum_{m=0}^{N} \mathcal{D}_{im} \tilde{\mathbf{F}}_1^{a,\#}(\mathbf{U}_{ijk}, \mathbf{U}_{mjk}) + \frac{\delta_{iN}}{\omega_N} \left[\tilde{\mathbf{F}}^{a,*} - \tilde{\mathbf{F}}_1^a \right]_{Njk} - \frac{\delta_{i0}}{\omega_0} \left[\tilde{\mathbf{F}}^{a,*} - \tilde{\mathbf{F}}_1^a \right]_{0jk}. \tag{6.4}$$

Here, δ denotes the Kronecker-delta and ω_0, ω_N the outermost LGL quadrature weights, so that the interface distributions solely enter at the 0-th and N-th entry of the solution array. Hence, we can implement the equivalent *quasi-weak* form

$$\mathcal{L}_\xi(\mathbf{U})_{ijk} = \sum_{m=0}^{N} \hat{\mathcal{D}}_{mi} \tilde{\mathbf{F}}_1^{a,\#}(\mathbf{U}_{ijk}, \mathbf{U}_{mjk}) + \frac{\delta_{iN}}{\omega_N} \tilde{\mathbf{F}}_{Njk}^{a,*} - \frac{\delta_{i0}}{\omega_0} \tilde{\mathbf{F}}_{0jk}^{a,*} \tag{6.5}$$

with

$$\hat{\mathcal{D}}_{ji} = 2\mathcal{D}_{ij} - \frac{\delta_{iN} - \delta_{i0}}{\omega_i} \tag{6.6}$$

for $i, j = 0, \ldots, N$. So, we pulled the additional surface contributions caused by the strong form back into the volume integral and modified the discrete derivative matrix, such that a most efficient evaluation in a quasi-weak sense is implemented. Similarly, the modification of the $\mathcal{D}$ matrix in (6.6) is sufficient to immediately obtain efficient evaluations of discrete derivatives in the η- and ζ-directions.

Moreover, this result also applies to both non-conservative terms, even though we have to be careful with the dimensionality, especially in the gradient version for the

Galilean term (3.49). Thus, we never split away the discrete Powell $\boldsymbol{\Phi}^{\text{MHD}}$ nor the other scaling term $\overset{\leftrightarrow}{\boldsymbol{\Phi}}{}^{\text{GLM}}$ in the actual implementation. The viscous volume terms are still computed in the standard form, which cannot be optimized in such a way.

We update each 1D operator line-by-line, e.g. with a loop over j, k for (6.5), to have small memory consumption and vectorization. Finally, we insert the already computed surface coupling terms for each direction, add source terms, e.g. for the damping of the divergence errors, and are ready to update the solution in time. For the computation of the gradients we use the common weak form DG implementation [81].

Overall, we could observe an significant speed-up depending on the polynomial degree of the approximation when using the quasi-weak formulation (6.5) for the advective and non-conservative terms. We can even improve the efficiency by exploiting the symmetry of the two-point volume fluxes. More details can be found in [68].

7. Numerical verification

In this chapter we present numerical tests to validate the theoretical findings of the numerical method derived herein. We first focus on demonstrating the high-order accuracy, discrete entropy conservation and stability, GLM divergence cleaning capabilities and shock capturing performance on two-dimensional Cartesian meshes in Sec. 7.1. Subsequently, we show the most important properties of the entropy stable DGSEM on three-dimensional, unstructured and curvilinear meshes next in Sec. 7.2. In both sections we highlight the increased robustness of the novel solver.

7.1. Results on two-dimensional Cartesian meshes

The following simulation results are obtained by the two-dimensional Cartesian solver implemented in the `SerCart` code from Sec. 6.1. Consequently, throughout this section we consider two-dimensional domains discretized by uniform quadrilateral elements of size $\Delta x = \Delta y$. If not stated otherwise, we turn off the divergence error damping $\alpha = 0$, bound the divergence cleaning speed c_h as in (2.37) and use the ES flux (4.38) with local Lax-Friedrichs type dissipation (4.44) at element interfaces.

We begin in Sec. 7.1.1 with verifying the high-order nature of the entropy stable DGSEM for the ideal and resistive GLM-MHD equations. In Sec. 7.2.3, through an academic test case, we numerically show the entropy conservative property of the ideal GLM-MHD DG approximation using a weak shock tube with periodic boundaries. The divergence cleaning properties of the high-order ideal GLM-MHD scheme are given in Sec. 7.1.3. Moreover, a viscous version of the well-known Orszag-Tang vortex (OTV) in Sec. 7.1.4 provides an example where every piece of the presented numerical solver is exercised. It demonstrates the entropy stability as well as the increased robustness of the entropy stable DGSEM for the resistive GLM-MHD equations on Cartesian meshes. Finally, we conclude this section with some two-dimensional shock examples for ideal GLM-MHD equations in Sec. 7.1.5 to verify the functionality of the shock capturing methods from Sec. 5.

7.1.1. Convergence studies

A substantial property of DG schemes is the high-order accuracy of the approximation for smooth solutions. Thus, we first consider an academic test case with a known analytical solution for the ideal GLM-MHD equations, that allows us to compute numerical

errors measured in a discrete L_2-norm. With the help of these error values for different discretization levels, we are able to compute the experimental order of convergence (EOC), which for the DGSEM is expected to agree with the theoretical order of $N+1$ as the mesh is refined. To show this result, we begin with a smooth Alfvén convergence test for the ideal GLM-MHD equations. Next, we apply the method of manufactured solutions to verify the high-order nature of the entropy stable DGSEM also for the resistive GLM-MHD system.

Ideal smooth Alfvén wave test

We use the smooth Alfvén wave test [133] to compute the numerical errors and experimental convergence rates for the approximation of the ideal GLM-MHD equations (2.34). The problem is defined in $\Omega = \left[0, \sqrt{2}\right]^2$ with the initialized primitives

$$\varrho = 1, \ \vec{v} = \begin{pmatrix} -0.1\sin(2\pi\kappa)\sin(\omega) \\ 0.1\sin(2\pi\kappa)\cos(\omega) \\ 0.1\cos(2\pi\kappa) \end{pmatrix}, \ p = 0.1, \ \vec{B} = \begin{pmatrix} \cos(\omega) \\ \sin(\omega) \\ 0 \end{pmatrix} + \vec{v} \qquad (7.1)$$

and $\kappa(x, y) = x\cos(\omega) + y\sin(\omega)$. Advantageously, the solution of this test case is smooth as well as periodic in Ω and the velocity of the Alfvén-wave remains a constant equal to one. Thus, the solution adopts the initial values for each time $t \in \mathbb{N}$. For the following EOC results we set $\omega = \pi/4, \gamma = 5/3$ and $\texttt{CFL} = 0.5$. The final time is $T = 1$. Further, we neglect all viscous and resistive effects as well as the damping of the divergence errors. We first investigate the errors and convergence rates for the strictly entropy conservative discretization. As such, we turn off any interface dissipation and use the EC flux (4.33) as a Riemann solver, too.

Due to the symmetry of the test case, the errors of v_2 and B_2 are identical to the ones of v_1 and B_1. In Tables 7.1 and 7.2 we observe odd-even effects in some variables. Particularly, we lose one order of convergence for $N = 3$, but overshoot the theoretical result for $N = 4$, which is a previously observed behavior for high-order entropy conservative approximations (see e.g. [54]). If we enable the interface dissipation in the numerical flux (4.38) we remove such odd-even effects from the convergence order of the approximation. We demonstrate this in Tables 7.3 and 7.4, where we use the local Lax-Friedrichs type dissipation term (4.44) at the interfaces.

For completeness, in Tables 7.5 and 7.6, we also provide the EOC results for the entropy stable Riemann solver with the nine-wave dissipation term from (4.48) and appendix A.2. We note, that applying this particular numerical flux function at the cell interfaces produces remarkably clean convergence rates compared to the LLF solver for this setup.

Δx	$L^2(\varrho)$	$L^2(v_1)$	$L^2(v_3)$	$L^2(p)$	$L^2(B_1)$	$L^2(B_3)$	$L^2(\psi)$
$\sqrt{2}/5$	2.55E-04	1.47E-04	3.57E-04	4.25E-05	2.85E-04	3.62E-04	2.92E-04
$\sqrt{2}/10$	3.92E-05	4.41E-05	1.30E-05	6.34E-06	6.04E-05	1.43E-05	1.24E-05
$\sqrt{2}/20$	4.12E-06	6.36E-06	9.28E-07	6.59E-07	7.63E-06	8.07E-07	4.58E-07
$\sqrt{2}/40$	5.21E-07	8.16E-07	1.03E-07	8.24E-08	9.52E-07	9.01E-08	6.66E-08
EOC	2.98	2.50	3.92	3.00	2.74	3.99	4.03

Table 7.1.: L^2-errors and average EOC for smooth Alfvén wave test with EC flux and $N = 3$ on a 2D Cartesian mesh.

Δx	$L^2(\varrho)$	$L^2(v_1)$	$L^2(v_3)$	$L^2(p)$	$L^2(B_1)$	$L^2(B_3)$	$L^2(\psi)$
$\sqrt{2}/5$	1.96E-05	2.58E-05	2.33E-05	3.21E-06	2.16E-05	2.32E-05	1.02E-05
$\sqrt{2}/10$	3.35E-07	4.11E-07	7.39E-07	5.63E-08	3.90E-07	7.46E-07	1.80E-07
$\sqrt{2}/20$	1.17E-08	1.07E-08	2.29E-08	1.96E-09	1.12E-08	2.30E-08	5.97E-09
$\sqrt{2}/40$	2.63E-10	3.57E-10	3.62E-10	4.38E-11	3.62E-10	3.63E-10	2.22E-10
EOC	5.40	5.38	5.32	5.39	5.29	5.32	5.16

Table 7.2.: L^2-errors and average EOC for smooth Alfvén wave test with EC flux and $N = 4$ on a 2D Cartesian mesh.

Δx	$L^2(\varrho)$	$L^2(v_1)$	$L^2(v_3)$	$L^2(p)$	$L^2(B_1)$	$L^2(B_3)$	$L^2(\psi)$
$\sqrt{2}/5$	2.17E-04	1.87E-04	3.76E-04	3.74E-05	2.15E-04	3.88E-04	1.81E-04
$\sqrt{2}/10$	2.00E-05	1.25E-05	1.89E-05	3.31E-06	1.48E-05	1.91E-05	1.24E-05
$\sqrt{2}/20$	1.08E-06	7.89E-07	1.14E-06	1.79E-07	9.24E-07	1.14E-06	7.89E-07
$\sqrt{2}/40$	6.65E-08	4.90E-08	7.03E-08	1.11E-08	5.82E-08	7.04E-08	4.96E-08
EOC	3.89	3.97	4.13	3.91	3.95	4.14	3.94

Table 7.3.: L^2-errors and average EOC for smooth Alfvén wave test with LLF ES flux and $N = 3$ on a 2D Cartesian mesh.

Δx	$L^2(\varrho)$	$L^2(v_1)$	$L^2(v_3)$	$L^2(p)$	$L^2(B_1)$	$L^2(B_3)$	$L^2(\psi)$
$\sqrt{2}/5$	1.61E-05	1.40E-05	2.24E-05	2.97E-06	1.27E-05	2.15E-05	1.08E-05
$\sqrt{2}/10$	4.46E-07	4.58E-07	7.95E-07	7.70E-08	4.39E-07	7.81E-07	3.43E-07
$\sqrt{2}/20$	1.14E-08	1.40E-08	2.70E-08	1.81E-09	1.42E-08	2.68E-08	1.09E-08
$\sqrt{2}/40$	2.53E-10	4.52E-10	8.68E-10	4.02E-11	4.58E-10	8.66E-10	3.40E-10
EOC	5.32	4.97	4.89	5.39	4.92	4.87	4.98

Table 7.4.: L^2-errors and average EOC for smooth Alfvén wave test with LLF ES flux and $N = 4$ on a 2D Cartesian mesh.

Δx	$L^2(\varrho)$	$L^2(v_1)$	$L^2(v_3)$	$L^2(p)$	$L^2(B_1)$	$L^2(B_3)$	$L^2(\psi)$
$\sqrt{2}/5$	2.59E-04	1.87E-04	3.66E-04	4.34E-05	2.14E-04	3.74E-04	1.78E-04
$\sqrt{2}/10$	1.80E-05	1.33E-05	2.25E-05	2.96E-06	1.49E-05	2.23E-05	1.21E-05
$\sqrt{2}/20$	1.11E-06	8.49E-07	1.41E-06	1.83E-07	9.55E-07	1.40E-06	7.75E-07
$\sqrt{2}/40$	6.88E-08	5.34E-08	8.84E-08	1.14E-08	6.01E-08	8.74E-08	4.87E-08
EOC	3.96	3.92	4.01	3.96	3.93	4.02	3.94

Table 7.5.: L^2-errors and average EOC for smooth Alfvén wave test with NW ES flux and $N = 3$ on a 2D Cartesian mesh.

Δx	$L^2(\varrho)$	$L^2(v_1)$	$L^2(v_3)$	$L^2(p)$	$L^2(B_1)$	$L^2(B_3)$	$L^2(\psi)$
$\sqrt{2}/5$	1.34E-05	1.13E-05	2.18E-05	2.17E-06	1.30E-05	2.13E-05	1.11E-05
$\sqrt{2}/10$	3.42E-07	3.85E-07	6.28E-07	5.55E-08	4.44E-07	6.27E-07	3.57E-07
$\sqrt{2}/20$	9.14E-09	1.18E-08	2.01E-08	1.51E-09	1.40E-08	2.01E-08	1.13E-08
$\sqrt{2}/40$	2.73E-10	3.68E-10	6.36E-10	4.54E-11	4.39E-10	6.36E-10	3.55E-10
EOC	5.19	4.97	5.02	5.18	4.95	5.01	4.98

Table 7.6.: L^2-errors and average EOC for smooth Alfvén wave test with NW ES flux and $N = 4$ on a 2D Cartesian mesh.

Manufactured solution test for viscous equations

In order to also verify the high-order approximation of the entropy stable DG discretization (3.51) for the resistive GLM-MHD system (2.39), we run an additional convergence test with the method of manufactured solutions. To do so, we assume a solution of the form

$$\mathbf{u} = (h, h, h, 0, 2h^2, h, -h, 0, 0)^T \text{ with } h = h(x, y, t) = \sin(2\pi(x + y) - 4t) + 4. \quad (7.2)$$

This choice generates a residual for the viscous PDE system defined as

$$\mathbf{u}_t + \nabla \cdot \overset{\leftrightarrow}{\mathbf{f}}^a(\mathbf{u}) - \nabla \cdot \overset{\leftrightarrow}{\mathbf{f}}^v(\mathbf{u}, \nabla\mathbf{u}) = \begin{pmatrix} h_t + 2h_x \\ h_t + h_x + 4hh_x \\ h_t + h_x + 4hh_x \\ 0 \\ 4hh_t + 16hh_x - 2h_x - 4\mu_{\mathrm{R}}(h_x^2 + hh_{xx}) - 4\mu_{\mathrm{NS}}h_{xx}/\mathrm{Pr} \\ h_t + 2h_x - 2\mu_{\mathrm{R}}h_{xx} \\ -h_t - 2h_x + 2\mu_{\mathrm{R}}h_{xx} \\ 0 \\ 0 \end{pmatrix}$$

$$(7.3)$$

for $\gamma = 2$ and $\mathrm{Pr} = 0.72$. To solve the inhomogeneous problem we subtract this residual from the approximate solution in each Runge-Kutta step. We run the test case on the periodic domain $\Omega = [0, 1]^2$ with `CFL = DFL = 0.5` up to the final time $T = 0.5$. Furthermore, we set $\mu_{\mathrm{NS}} = \mu_{\mathrm{R}} = 0.05$ and turn off the divergence damping ($\alpha = 0$). Finally, we obtain the convergence results illustrated in Tables 7.7 and 7.8 for the ES flux (4.38) with local Lax-Friedrichs type dissipation (4.44) as well as the ones in Tables 7.9 and 7.10 for the ES flux (4.38) with the nine-wave dissipation (4.48). Again, the errors of v_2 and B_2 are identical to the ones of v_1 and B_1, whereas v_3 and B_3 are equal to zero for all time.

Δx	$L^2(\varrho)$	$L^2(v_1)$	$L^2(p)$	$L^2(B_1)$	$L^2(\psi)$
1/5	2.98E-03	1.28E-03	1.22E-02	1.74E-03	1.79E-03
1/10	2.15E-04	9.18E-05	7.66E-04	1.00E-04	1.31E-04
1/20	1.46E-05	6.12E-06	5.24E-05	5.38E-06	8.64E-06
1/40	8.24E-07	3.51E-07	3.14E-06	3.07E-07	5.48E-07
EOC	3.94	3.94	3.97	4.16	3.89

Table 7.7.: L^2-errors and average EOC for manufactured solution test with LLF ES flux and $N = 3$ on a 2D Cartesian mesh.

Δx	$L^2(\varrho)$	$L^2(v_1)$	$L^2(p)$	$L^2(B_1)$	$L^2(\psi)$
1/5	1.73E-04	8.85E-05	1.00E-03	9.85E-05	1.16E-04
1/10	5.26E-06	2.75E-06	4.03E-05	2.77E-06	3.50E-06
1/20	1.98E-07	7.33E-08	1.47E-06	8.16E-08	1.08E-07
1/40	7.66E-09	1.57E-09	5.80E-08	2.53E-09	3.37E-09
EOC	4.82	5.26	4.69	5.08	5.02

Table 7.8.: L^2-errors and average EOC for manufactured solution test with LLF ES flux and $N = 4$ on a 2D Cartesian mesh.

Δx	$L^2(\varrho)$	$L^2(v_1)$	$L^2(p)$	$L^2(B_1)$	$L^2(\psi)$
1/5	3.10E-03	1.41E-03	1.21E-02	1.96E-03	1.61E-03
1/10	2.87E-04	1.15E-04	8.29E-04	1.19E-04	1.15E-04
1/20	1.97E-05	9.31E-06	6.72E-05	7.41E-06	7.57E-06
1/40	1.09E-06	6.86E-07	5.68E-06	5.78E-07	4.82E-07
EOC	3.82	3.67	3.69	3.91	3.90

Table 7.9.: L^2-errors and average EOC for manufactured solution test with NW ES flux and $N = 3$ on a 2D Cartesian mesh.

Δx	$L^2(\varrho)$	$L^2(v_1)$	$L^2(p)$	$L^2(B_1)$	$L^2(\psi)$
1/5	1.75E-04	1.15E-04	1.82E-03	1.40E-04	1.29E-04
1/10	1.53E-05	4.89E-06	6.92E-05	4.11E-06	3.76E-06
1/20	6.02E-07	9.88E-08	2.32E-06	9.55E-08	1.15E-07
1/40	1.95E-08	1.86E-09	8.34E-08	2.66E-09	3.57E-09
EOC	4.38	5.30	4.80	5.23	5.05

Table 7.10.: L^2-errors and average EOC for manufactured solution test with NW ES flux and $N = 4$ on a 2D Cartesian mesh.

7.1.2. Entropy conservation

In order to demonstrate the entropy conservation of the high-order DG scheme numerically, we solely consider the advective parts of the system, i.e. the ideal GLM-MHD equations (2.34) without any damping of the divergence errors. Additionally, we use the EC flux (4.33) also at the interfaces to omit any dissipative effects there. To make the problem more challenging, we consider a generic test case on the periodic domain $\Omega = [0, 1]^2$ initialized by a small diagonal shock (see e.g. [133]) stated in Table 7.11.

	ϱ	v_1	v_2	v_3	p	B_1	B_2	B_3
$x < y$	1.0	0.0	0.0	0.0	1.0	$2.0/\sqrt{4.0\pi}$	$4.0/\sqrt{4.0\pi}$	$2.0/\sqrt{4.0\pi}$
$x \geq y$	1.08	0.6	0.01	0.5	0.95	$2.0/\sqrt{4.0\pi}$	$3.6/\sqrt{4.0\pi}$	$2.0/\sqrt{4.0\pi}$

Table 7.11.: Initialized primitive variables for the 2D entropy conservation test.

Further, we set $\gamma = 5/3, \Delta x = \Delta y = 1/20$ and $T = 0.5$. The discrete entropy change is computed by

$$\epsilon_S = \left| 1 - \frac{\bar{S}(T)}{\bar{S}(0)} \right|, \tag{7.4}$$

whereas the total entropy at a given time is

$$\bar{S}(t) = \sum_{\iota=1}^{N_{\mathrm{el}}} \langle J^\iota S^\iota(t), 1 \rangle_N. \tag{7.5}$$

We know, that the entropy conservative DGSEM for the ideal GLM-MHD equations is essentially dissipation-free. Therefore, in the case of discontinuous solutions, the only dissipation introduced into the approximation is through the time integration scheme. Hence, we can use the error in the total entropy as a measure of the temporal convergence of the method. We know that by shrinking the `CFL` number, the dissipation of the time integration scheme is lessened and entropy conservation is captured more accurately, e.g. [43].

In the following log-log plots we illustrate the numerical results for different polynomial degrees N, which confirm the reduction of the entropy conservation error according to the order of the time integration scheme for decreasing `CFL` numbers (Figure 7.1). In fact, the observed reduction rates are slightly better than the theoretical prediction given by the fourth order time integration method.

7.1.3. Divergence cleaning

In order to demonstrate the reduction of the divergence error in the magnetic field, we use a maliciously chosen non-divergence-free initialization in $\Omega = [-1, 1]^2$ defined by a Gaussian pulse in the $x-$component of the magnetic field proposed in [3]:

$$\varrho = 1, \quad E = 6, \quad B_1 = \exp\left(-0.5 \, \frac{x^2 + y^2}{0.11^2} \right) \tag{7.6}$$

The other initial values are set to zero and the boundaries are periodic. Again we set $\gamma = 5/3, \mathtt{CFL} = 0.5$ and use the local Lax-Friedrichs numerical ES flux.
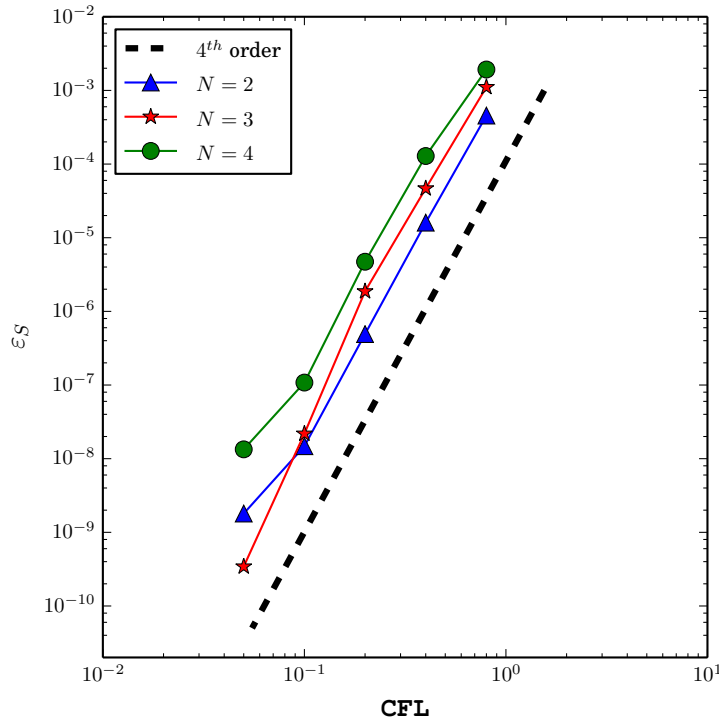
Figure 7.1.: Log-log plot of entropy conservation error for $N = 2, N = 3$ and $N = 4$ on a 20×20 Cartesian mesh at $T = 0.5$.

In Figure 7.2 we illustrate the time evolution of the discrete divergence error measured in terms of

$$\|\nabla \cdot \vec{B}\|_{L^2(\Omega)} \approx \sum_{\iota=1}^{N_{\mathrm{el}}} \left\langle J^\iota (\nabla \cdot \vec{B})^\iota, 1 \right\rangle_N \tag{7.7}$$

for $N = 3$ and 20×20 elements, where the element-wise discrete divergence is computed by the gradient approximation $\overset{\leftrightarrow}{\mathbf{Q}}$.

We show the simulation results of the ideal GLM-MHD approximation without any divergence cleaning mechanism as well as the approximation, in which the divergence error is solely propagated through the domain ($\alpha = 0$). However, due to the periodic nature of the boundaries it is known that the divergence errors will simply advect back into the domain [30] with only minimal damping due to the high-order nature of the DG scheme. Therefore, we use the same configuration but add additional damping for different values of α in (2.38). We see that the damping improves the overall divergence error in Figure 7.2. Also, our results here compare well to those presented in [3, 34].
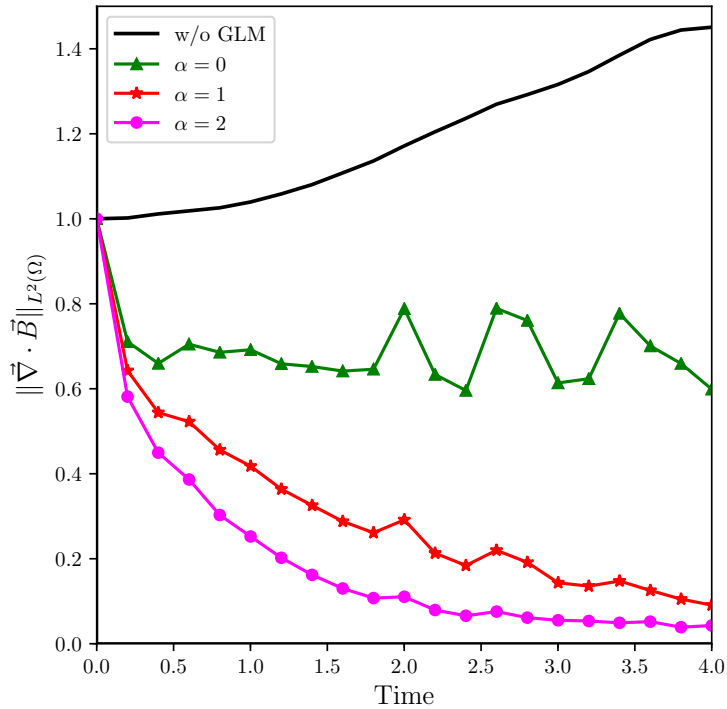
Figure 7.2.: Temporal evolution of the normalized discrete L^2 error in the divergence-free condition on a 20×20 Cartesian mesh with $N = 3$ and $T = 4$.

7.1.4. Robustness test

Next, we use a viscous version of the Orszag-Tang vortex [3, 34, 105] to demonstrate the increased robustness of the entropy stable approximation including GLM divergence cleaning. The initial conditions are simple and smooth, but evolve to contain complex structures and energy exchanges between the velocity and magnetic fields. The domain is $\Omega = [0, 1]^2$ with periodic boundary conditions, initial data

$$
\begin{aligned}
&\varrho = 1, && v_1 = -\sin(2\pi y), && v_2 = \sin(2\pi x), \\
&p = \frac{1}{\gamma}, && B_1 = -\frac{1}{\gamma}\sin(2\pi y), && B_2 = \frac{1}{\gamma}\sin(4\pi x)
\end{aligned}
\tag{7.8}
$$

and $\gamma = 5/3$. To include diffusivity in the simulation we select the Prandtl number to be $\mathrm{Pr} = 0.72$ and the viscosity and resistivity parameters to be

$$
\mu_{\mathrm{NS}} = 8.5 \times 10^{-4}, \quad \mu_{\mathrm{R}} = 10^{-5}.
\tag{7.9}
$$

This selection of the diffusive coefficients corresponds to a kinematic Reynolds number (Re) of approximately 1170 and a magnetic Reynolds number (Re$_m$) of 100,000. The initial conditions evolve to a final time of $T = 0.5$.

Moreover, the simulation uses a polynomial order $N = 7$ in each spatial direction on a 20×20 Cartesian grid and we use the local Lax-Friedrichs numerical ES flux. We run three variants of the DG approximation to demonstrate the necessity of the entropy stable scheme as well as the GLM modification for numerical stability of this particular test case configuration in Table 7.12.

CONFIGURATION	$N = 7$, 20×20 mesh
Standard DGSEM with GLM divergence cleaning	*crash*
Entropy stable DGSEM without GLM divergence cleaning	*crash*
Entropy stable DGSEM with GLM divergence cleaning	*result*

Table 7.12.: Comparison of the numerical stability of the standard DGSEM against the entropy stable version with and without GLM divergence cleaning, applied to the viscous Orszag-Tang vortex problem.

These results demonstrate that the entropy stable formulation as well as numerical treatment of the divergence-free constraint are needed to create a robust scheme for this configuration. Further, we shrink the time step by setting `CFL = DFL = 0.25` and find the same numerical stability results for the three configurations presented in Table 7.12. This reinforces that the numerical instabilities in the approximate flow are caused by errors other than those introduced by the time integration scheme.

For the entropy stable DG simulation with GLM divergence cleaning we illustrate the density together with contour lines of the magnetic field at the final time in Figure 7.3. We also provide a time-dependent plot of the normalized total entropy for the case `CFL = DFL = 0.5` to show the entropy stability of the entire approximation in Figure 7.4.

We note that the high-order entropy stable approximation is not guaranteed to be oscillation-free near shocks, e.g. [139]. Thus, there are still observable, albeit small, numerical artifacts in the approximate solution (Figure 7.3). But, due to the viscous and resistive terms, the entropy stable DGSEM applied to this setup of the Orszag-Tang problem can run without any additional shock capturing method.
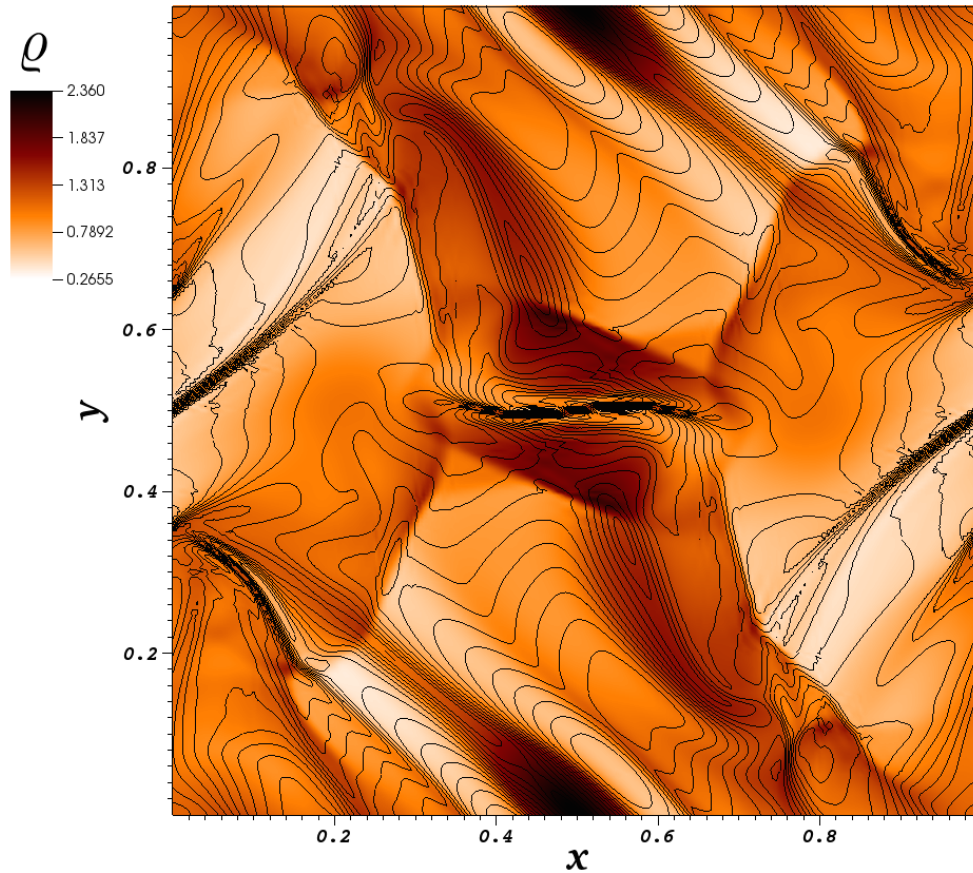
Figure 7.3.: Density pseudo-color plot with overlaid magnetic field lines for the viscous Orszag-Tang vortex at $T = 0.5$ with $N = 7$ on a 20×20 Cartesian mesh and diffusivity coefficients (7.16).

7.1.5. Shock capturing examples

Concluding, we provide some two-dimensional shock problems in order to demonstrate results, that require the presented shock capturing methods from Sec. 5 to stabilize the approximation. Hence, for both of the following tests we turn off any viscous or resistive effects and restrict to the advective parts of the governing equations. We begin with the original, inviscid version of the previously presented Orszag-Tang vortex and then show results for the magnetic rotor test , see e.g. [3]. In all simulations we compare the artificial viscosity results according to Sec. 5.1 with those obtained by the SIAC filter from Sec. 5.2.
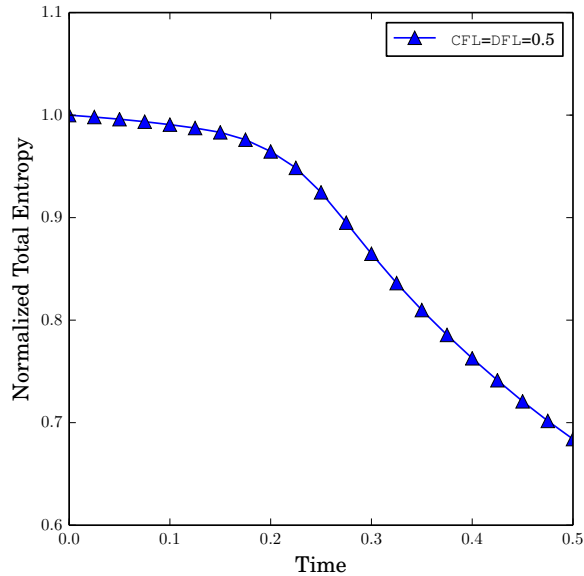
Figure 7.4.: Time evolution plot of the total entropy in the viscous Orszag-Tang vortex with $N = 7$ on 20×20 elements with diffusivity coefficients (7.16).

Inviscid Orszag-Tang vortex

The first shock problem describing the evolution of a turbulent plasma cloud is initialized as in (7.8) on the periodic domain $\Omega = [0,1]^2$. Viscous effects as well as divergence error damping are turned off and we use the ES flux with LLF dissipation for all simulations, since it is better suited in the presence of discontinuities. Furthermore, we use CFL $= 0.5$, polynomials of degree $N = 5$ and 40×40 elements.

We note, that due to the absence of stabilizing viscous and resistive effects the simulation of this test crashes at $t \approx 0.2$, because various shocks develop and interact all over the domain. Thus, we use the shock capturing mechanisms from Sec. 5 to regularize the approximation and compare the solution quality of both approaches.

We show the evolution of the density in the plots below (Fig. 7.5) smoothed by the derived two-dimensional SIAC filter with $m = 3, k = 8$ and a fixed $\varepsilon = 1.6$. We use the smoothing matrix $\mathbf{\Xi}$ from (5.40) and do the filtering adaptively as in (5.47) with the pressure as a shock indicator, $\sigma_{\min}^{\mathrm{FIL}} = -9$ and $\sigma_{\max}^{\mathrm{FIL}} = -6$. Further, we show the distribution of the cell-wise constant convex parameter $\varkappa$ from (5.47) at the same stages in Fig. 7.6, which confirms the correct tracking of shocks as they evolve.

In order to assess the performance of the two-dimensional Dirac-delta filter, we compare the simulation results to the ones obtained by the common artificial viscosity
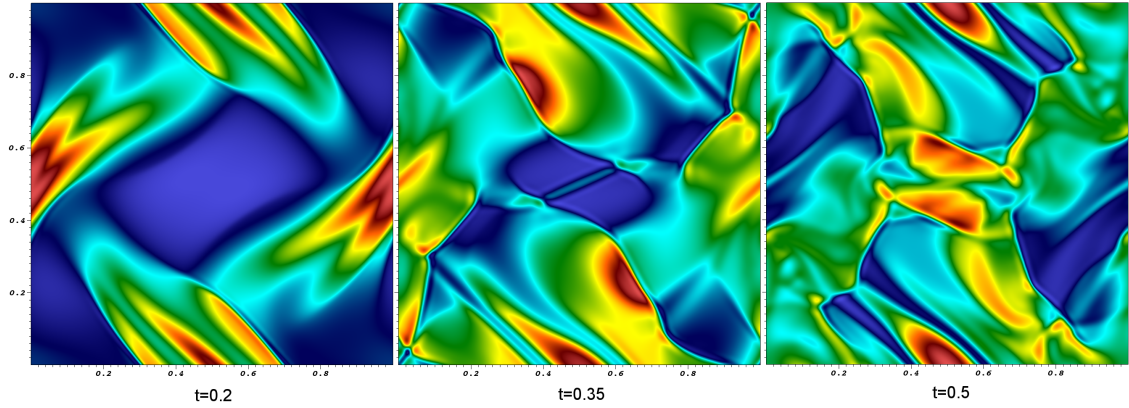
Figure 7.5.: Time evolution of Orszag-Tang vortex density on 40×40 elements with $N = 5$ filtered adaptively by $\boldsymbol{\Xi}$ with $\sigma_{\min}^{\text{FIL}} = -9, \sigma_{\max}^{\text{FIL}} = -6, m = 3, k = 8$ and $\varepsilon = 1.6$.
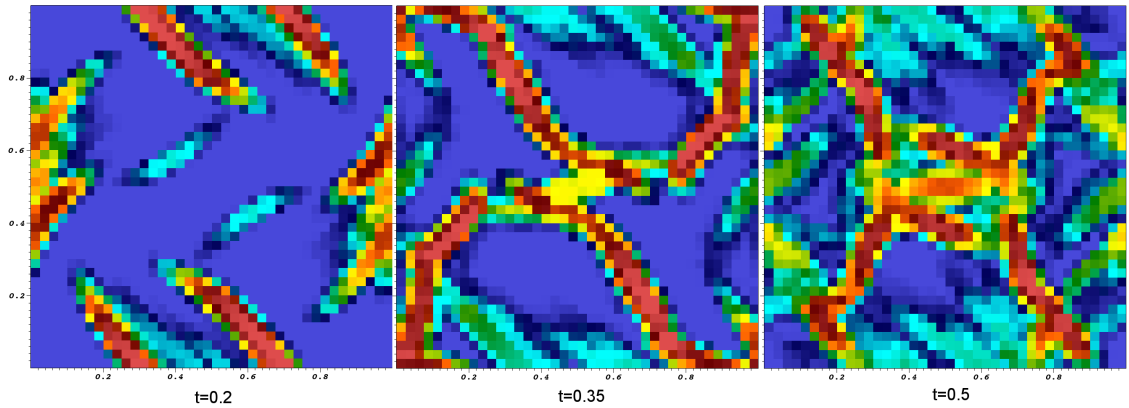
Figure 7.6.: Time evolution of convex parameter $\varkappa$ on 40×40 elements with $N = 5$ for adaptive Dirac-delta filter $\boldsymbol{\Xi}$ with $\sigma_{\min}^{\text{FIL}} = -9, \sigma_{\max}^{\text{FIL}} = -6, m = 3, k = 8$ and $\varepsilon = 1.6$.

approach. For both methods we use the pressure as a shock indicator and introduce a smooth transition area as in (5.9) and (5.47), respectively. The according user defined parameters for the DOF energy indicator are $\sigma_{\min}^{\text{DOF}} = -6, \sigma_{\max}^{\text{DOF}} = -4$ and $\epsilon_0 = 0.1$ in (5.9). We note, that for both shock capturing methods, the results vary sensitively with respect to the choice of parameters, which in the demonstrated simulations are set as optimal as possible in terms of an appropriate balance between smoothing oscillatory regions and avoiding too much dissipation.
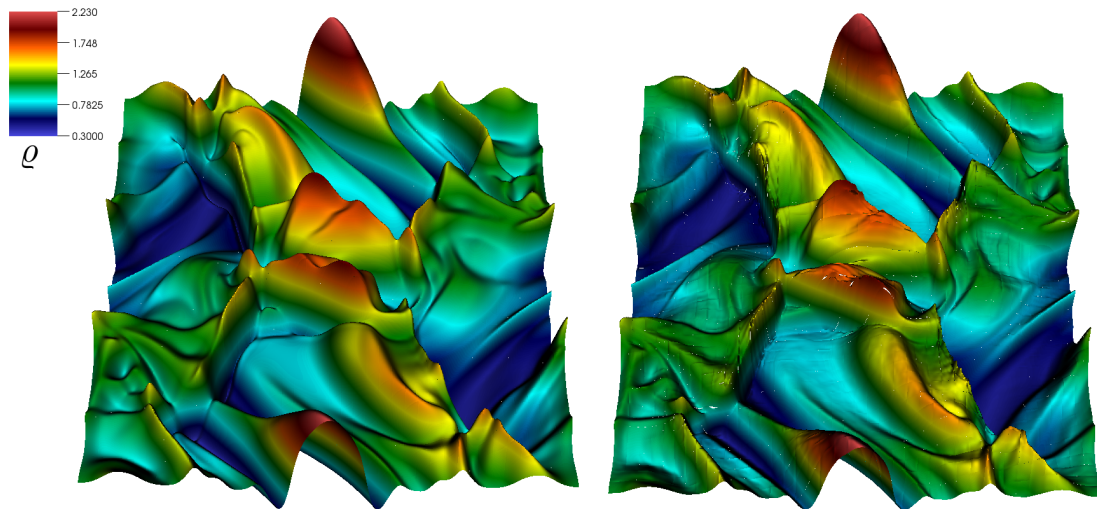
Figure 7.7.: Orszag-Tang vortex density at $T = 0.5$ for $\texttt{CFL} = 0.5, N = 5$ and 40×40 elements smoothed by Dirac-delta filter (left) and artificial viscosity (right).

As we can see in the plots (Fig. 7.7), on first sight, the Dirac-delta filter performs slightly better than the artificial viscosity, since it is able to smooth out almost all spurious oscillations, whereas in the right hand figure some mesh artifacts are still observable. In order to investigate the performance of both methods, we provide two slices (Figures 7.8 and 7.9), in which we cut through the density distribution at $x = y$ and $y = 0.3$ to compare the profiles obtained by both shock capturing methods against a reference solution.

This highly resolved reference solution is computed by a second order MUSCL-Hancock finite volume method (see e.g. [137]) on 1024×1024 elements with the publicly available high performance application code $\texttt{FLASH}$ ($\texttt{http://flash.uchicago.edu/site/flashcode/}$).

Whereas the oscillations are smoothed out by both approaches, we see that the filtering technique produces more overshoots at shocks. On the other hand, the viscous approach is more dissipative and causes longer simulation times due to the expensive computation of the gradients in each Runge-Kutta step as well as the additional time step restriction. In the end, both approaches generate reasonable approximations for this shock test and it is up to the user, which method he or she prefers for the mentioned reasons.
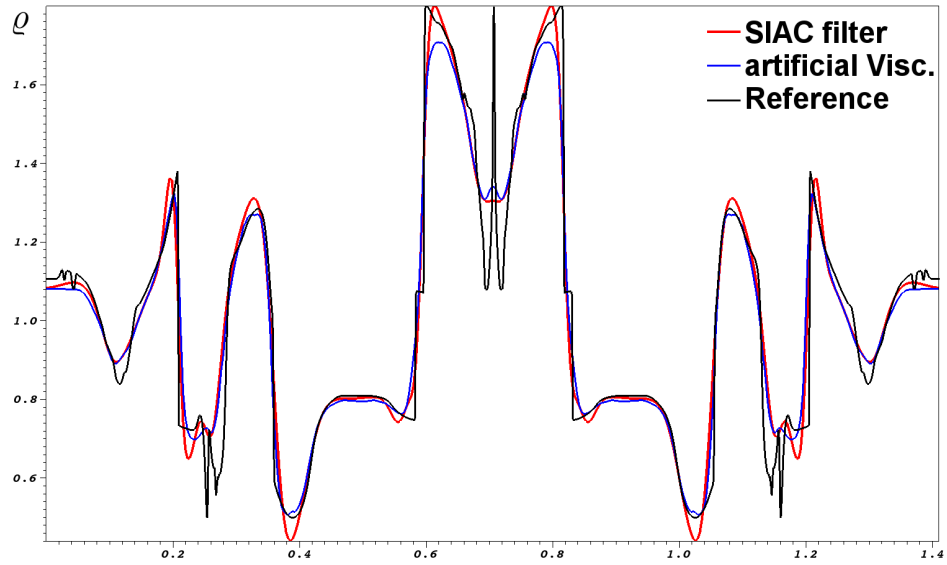
Figure 7.8.: Orszag-Tang-Vortex density slice at $x = y$ and $T = 0.5$ for $\mathtt{CFL}\!=\!0.5, N\!=\!5$ and 40×40 elements.
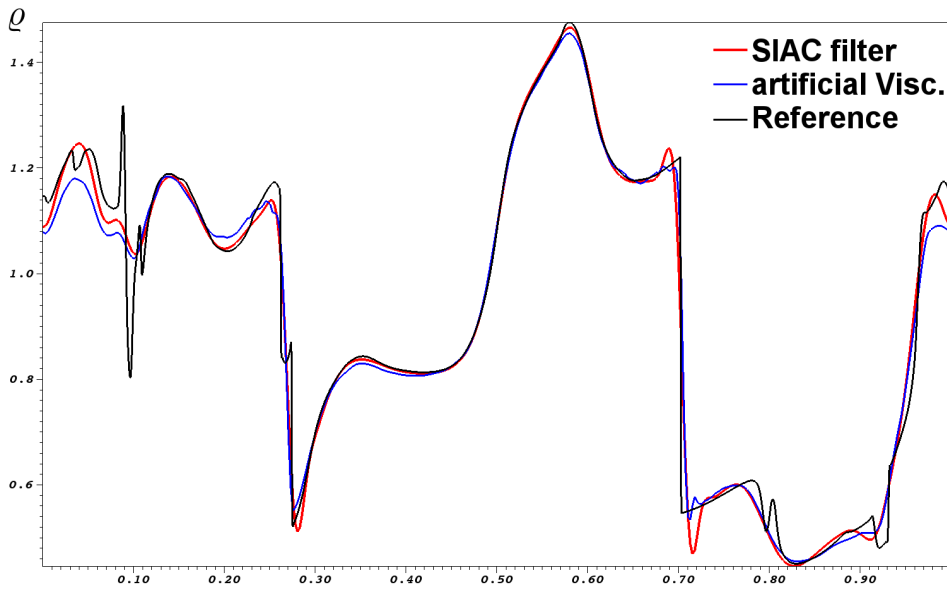
Figure 7.9.: Orszag-Tang-Vortex density slice at $y = 0.3$ and $T = 0.5$ for $\mathtt{CFL}\!=\!0.5, N\!=\!5$ and 40×40 elements.

Magnetic rotor

The second test case describes a rotating dense circle in a static fluid, that generates strong circular shock waves [3]. In general this benchmark problem is defined in the same periodic domain $\Omega = [0,1]^2$, by the radius $r = \sqrt{(x-0.5)^2 + (y-0.5)^2}$ and the slope $s = \frac{r_1 - r}{r_1 - r_0}$. The initial primitive variables for the magnetic rotor are stated in Table 7.13, where the unlisted quantities are initially zero in the entire domain and $\gamma = 1.4$.

	ϱ	v_1	v_2	p	B_1
$r < r_0$	10	$\frac{u_0}{r_0}\left(\frac{1}{2} - y\right)$	$\frac{u_0}{r_0}\left(x - \frac{1}{2}\right)$	1	$\frac{5}{\sqrt{4\pi}}$
$r_0 \leq r \leq r_1$	$1 + 9s$	$\frac{su_0}{r_0}\left(\frac{1}{2} - y\right)$	$\frac{su_0}{r_0}\left(x - \frac{1}{2}\right)$	1	$\frac{5}{\sqrt{4\pi}}$
$r > r_1$	1	0	0	1	$\frac{5}{\sqrt{4\pi}}$

Table 7.13.: Initial primitive states for the magnetic rotor test.

In our simulations we define $r_0 = 0.1, r_1 = 0.115$ and $u_0 = 2$. We use `CFL` = 0.5, a polynomial degree of $N = 4$ and 100×100 elements. We show the density and pressure at $T = 0.15$ for both shock capturing methods in the plots below, Figures 7.10 and 7.11 respectively. Due to the strong circular shocks combined with the oscillatory split form evaluation of the EC volume flux this test case is extremely sensitive and unstable. Therefore, we apply the SIAC filtering matrix constructed by a Dirac-delta kernel with only one vanishing moment $m = 1$ and $k = 5$. Again, we smooth the approximation adaptively with the density as a shock indicator, $\sigma_{\min}^{\mathrm{FIL}} = -9, \sigma_{\max}^{\mathrm{FIL}} = -6$ and a fixed $\varepsilon = 1.4$. For the stabilization by artificial viscosity we use the same parameters as for the previous test, i.e. $\sigma_{\min}^{\mathrm{DOF}} = -6, \sigma_{\max}^{\mathrm{DOF}} = -4$ and $\epsilon_0 = 0.1$ in (5.9).

In Figures 7.10 and 7.11 we see, that both shock capturing techniques perform well in terms of stabilizing the approximation and regularizing oscillatory regions. As in the previous test, the artificial viscosity approach is more dissipative, but this time the filtered solution is polluted by small mesh artifacts, which is particularly visible at the generated Alfvén waves in the pressure profile. We note, that these artifacts do not occur when using the SIAC filter in combination with the standard DGSEM approximation, see e.g. [15].
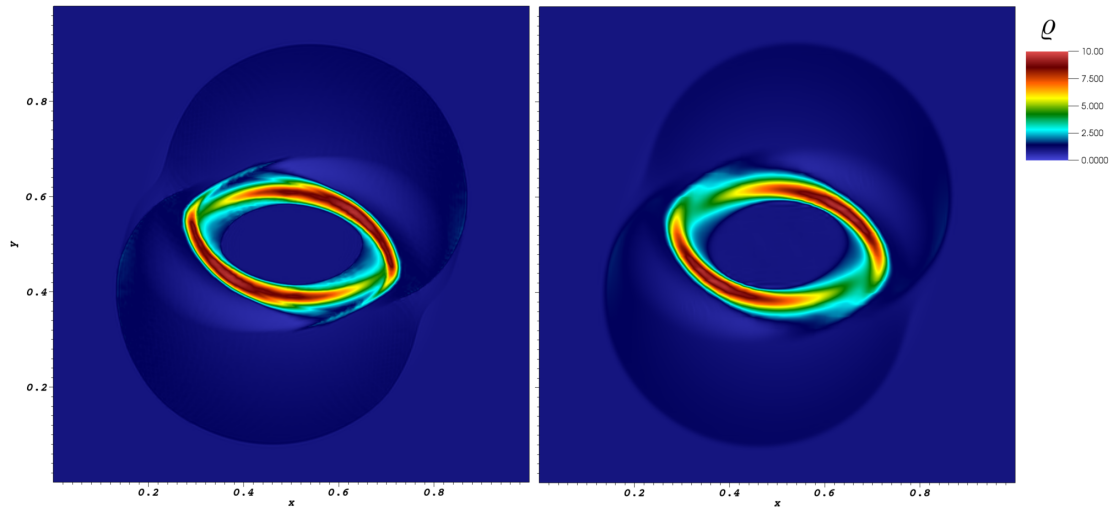
Figure 7.10.: Magnetic rotor density at $T = 0.15$ for CFL $= 0.5, N = 4$ and 100×100 elements smoothed by Dirac-delta filter (left) and artificial viscosity (right).
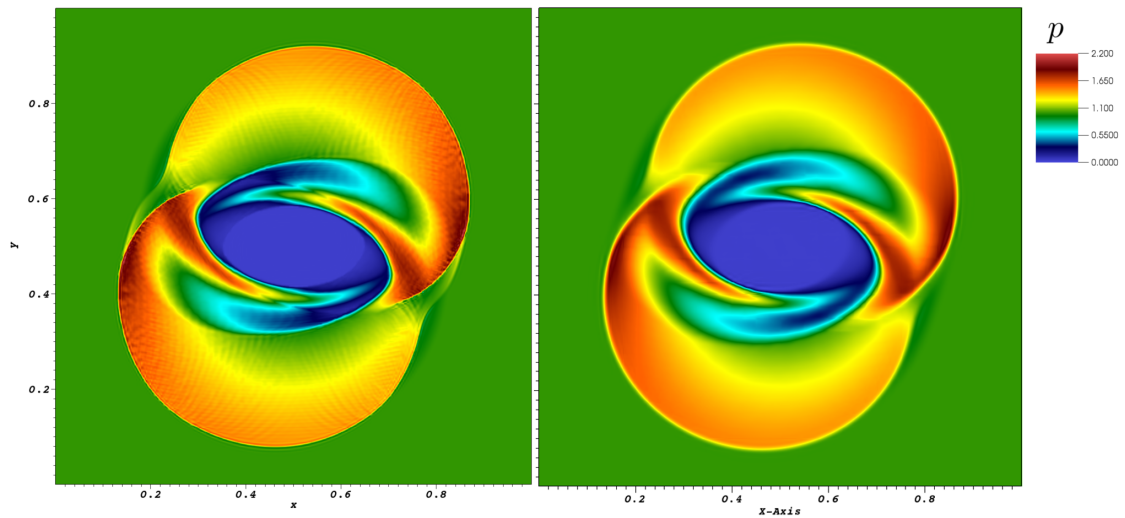
Figure 7.11.: Magnetic rotor pressure at $T = 0.15$ for CFL $= 0.5, N = 4$ and 100×100 elements smoothed by Dirac-delta filter (left) and artificial viscosity (right).

7.2. Results on three-dimensional curved meshes

In this section, we provide numerical validation for the theoretical findings on three-dimensional, unstructured and curved meshes. As pointed out in Sec. 6.2, we perform these numerical computations with the open source, three-dimensional curvilinear split form DG framework for the resistive GLM-MHD equations `FLUXO` (`www.github.com/project-fluxo`). Further, we use the open source tool `HOPR` (`www.hopr-project.org`) to create the three-dimensional high-order meshes and run all simulations in parallel on the HPC cluster `CHEOPS`.

As in the previous section, we start with a demonstration of the high-order accuracy for the resistive GLM-MHD system by a manufactured solution, but on three-dimensional curvilinear meshes. With the same setup we verify the strong scaling of the parallel implementation. Next, we demonstrate the entropy conservation for the ideal GLM-MHD system, before we verify the GLM divergence cleaning capability of the scheme with a similar configuration as in the previous section, both for curved elements. Finally, we provide two examples, in which every piece of the presented numerical solver is exercised, to demonstrate the increased robustness and applicability of the entropy stable DG approximation for the ideal and resistive GLM-MHD equations. Specifically, we use a three-dimensional, viscous version of the OTV and a MHD extension of the Taylor-Green vortex to show the value of the entropy stable framework in conjunction with GLM hyperbolic divergence cleaning in providing numerical stability. Unless otherwise stated, we set the damping parameter $\alpha = 0$ and the GLM propagation speed c_h to be proportional to the maximum advective wave speed. For all simulations, we use the ES flux (4.38) with local Lax-Friedrichs type dissipation (4.44) at element interfaces.

Moreover, in this section, all numerical results are obtained on fully periodic curved meshes. To generate such a mesh, we first define the high-order element nodes on a standard Cartesian mesh with periodic boundary conditions, in the space variables $\vec{\chi} = (\chi_1, \chi_2, \chi_3)^T$. The curved mesh is then generated by applying a transformation function to all high-order nodes mapping them to physical space $\vec{x}$ defined by

$$x_l = \chi_l + 0.1 \sin(\pi\chi_1) \sin(\pi\chi_2) \sin(\pi\chi_3), \quad l = 1, 2, 3. \tag{7.10}$$

As shown in Figure 7.12, two mesh types will be considered throughout this section. Type (a) with flat periodic boundaries and curved element faces inside, using $\vec{\chi} \in [0, 1]^3$ and type (b) with curved element interfaces, using $\vec{\chi} \in [-0.6, 1.4] \times [-0.8, 1.2] \times [-0.7, 1.3]$, being still fully periodic and conforming.

(a)
$\vec{\chi} \in [0,1]^3$

(b)
$\vec{\chi} \in [-0.6, 1.4] \times [-0.8, 1.2] \times [-0.7, 1.3]$
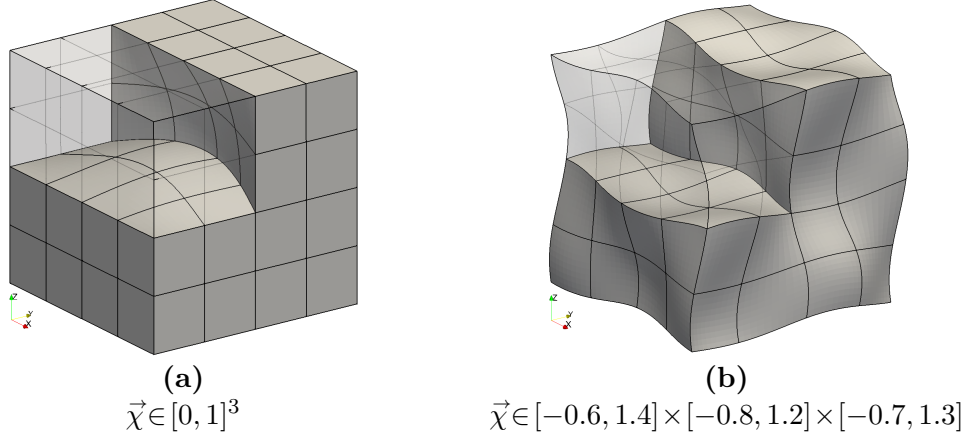
Figure 7.12.: Two types of fully periodic curved meshes, shown for 4^3 elements, generated via the transformation function (7.10) [16].

7.2.1. Convergence test

As in the two-dimensional Cartesian case, we use the method of manufactured solutions to verify the high-order accuracy of the entropy stable DG discretization (3.51) for the resistive GLM-MHD system (2.39) on curved elements. Therefore, we assume a solution of the form

$$\mathbf{u} = \left[h, h, h, 0, 2h^2 + h, h, -h, 0, 0 \right]^T \quad \text{with } h = h(x, y, z, t) = 0.5 \sin(2\pi(x + y + z - t)) + 2, \tag{7.11}$$

which has the advantage, that it is symmetric and spatial derivatives cancel with temporal derivatives, i.e.

$$h_x = h_y = h_z = -h_t. \tag{7.12}$$

Hence, the additional residual for the resistive GLM-MHD system reads

$$\mathbf{u}_t + \vec{\nabla} \cdot \overleftrightarrow{\mathbf{f}}^a(\mathbf{u}) - \vec{\nabla} \cdot \overleftrightarrow{\mathbf{f}}^v(\mathbf{u}, \vec{\nabla}\mathbf{u}) = \begin{pmatrix} h_x \\ h_x + 4hh_x \\ h_x + 4hh_x \\ 4hh_x \\ h_x + 12hh_x - 6\mu_R(h_x^2 + hh_{xx}) - 6\mu_{NS}h_{xx}/\text{Pr} \\ h_x - 3\mu_R h_{xx} \\ -h_x + 3\mu_R h_{xx} \\ 0 \\ 0 \end{pmatrix} \tag{7.13}$$

115

for $\gamma = 2$ and $\mathrm{Pr} = 0.72$. In order to solve the inhomogeneous problem, we again subtract the residual from the approximate solution in each Runge-Kutta step. Moreover, we run the test case up to the final time $T = 1.0$ and set $\mu_{\mathrm{NS}} = \mu_{\mathrm{R}} = 0.005$. For all computations we use mesh type (b) from Figure 7.12 with a varying number of elements.

Finally, we obtain the convergence results illustrated in Tables 7.14 and 7.15 that confirm the high-order accuracy of the scheme on curvilinear meshes in three spatial dimensions. The errors of v_2 and B_2 are similar to the ones of v_1 and B_1 and, thus, not presented in the tables.

N_{el}	$L^2(\varrho)$	$L^2(v_1)$	$L^2(v_3)$	$L^2(p)$	$L^2(B_1)$	$L^2(B_3)$	$L^2(\psi)$
4^3	1.78E-01	1.90E-01	1.55E-01	3.78E-01	1.38E-01	1.74E-02	2.05E-02
8^3	6.17E-03	8.43E-03	6.03E-03	1.59E-02	3.45E-03	2.18E-03	1.19E-03
16^3	2.33E-04	4.97E-04	3.29E-04	1.17E-03	1.38E-04	1.05E-04	6.31E-05
32^3	1.90E-05	2.51E-05	1.50E-05	7.34E-05	7.64E-06	2.68E-06	3.51E-06
EOC	4.40	4.30	4.45	4.11	4.71	4.22	4.17

Table 7.14.: L^2-errors and average EOC for manufactured solution test with LLF ES flux and $N = 3$ on a 3D curvilinear mesh, Fig. 7.12 (b).

N_{el}	$L^2(\varrho)$	$L^2(v_1)$	$L^2(v_3)$	$L^2(p)$	$L^2(B_1)$	$L^2(B_3)$	$L^2(\psi)$
4^3	1.12E-01	1.65E-01	1.04E-01	2.74E-01	7.58E-02	5.91E-02	1.87E-02
8^3	2.43E-03	4.88E-03	3.79E-03	1.15E-02	2.34E-03	1.97E-03	8.54E-04
16^3	7.25E-05	1.44E-04	1.01E-04	3.88E-04	5.84E-05	4.48E-05	3.17E-05
32^3	1.88E-06	3.45E-06	2.14E-06	1.12E-05	1.41E-06	7.39E-07	1.52E-06
EOC	5.29	5.18	5.19	4.86	5.24	5.43	4.53

Table 7.15.: L^2-errors and average EOC for manufactured solution test with LLF ES flux and $N = 4$ on a 3D curvilinear mesh, Fig. 7.12 (b).

Further, we used the ES flux (4.38) with local Lax-Friedrichs type dissipation (4.44) at the element surfaces. We note, if we apply an entropy conservative approximation to this test case, the convergence order would exhibit an odd-even effect as in the two-dimensional studies.

In order to finalize the convergence studies on three-dimensional curvilinear meshes, we present the convergence rates for the identical setup obtained by the entropy stable scheme with the nine-wave dissipation (4.48) at the element surfaces in Tables 7.16 and 7.17.

N_{el}	$L^2(\varrho)$	$L^2(v_1)$	$L^2(v_3)$	$L^2(p)$	$L^2(B_1)$	$L^2(B_3)$	$L^2(\psi)$
4^3	1.97E-01	2.01E-01	1.88E-01	4.11E-01	1.54E-01	1.90E-02	2.01E-01
8^3	6.36E-03	1.06E-02	6.75E-03	1.84E-02	4.34E-03	1.98E-03	1.43E-03
16^3	2.69E-04	5.77E-04	3.25E-04	1.22E-03	1.86E-04	9.30E-05	9.17E-05
32^3	2.12E-05	3.06E-05	1.48E-05	7.28E-05	1.13E-05	2.79E-06	6.11E-06
EOC	4.39	4.23	4.54	4.15	4.58	4.25	3.89

Table 7.16.: L^2-errors and average EOC for manufactured solution test with NW ES flux and $N\!=\!3$ on a 3D curvilinear mesh, Fig. 7.12 (b).

N_{el}	$L^2(\varrho)$	$L^2(v_1)$	$L^2(v_3)$	$L^2(p)$	$L^2(B_1)$	$L^2(B_3)$	$L^2(\psi)$
4^3	1.14E-01	1.69E-01	1.06E-01	2.79E-01	7.60E-02	5.90E-02	1.85E-02
8^3	2.40E-03	5.05E-03	3.72E-03	1.14E-02	2.32E-03	1.89E-03	9.12E-04
16^3	8.17E-05	1.59E-04	1.09E-04	3.86E-04	6.32E-05	5.04E-05	3.75E-05
32^3	2.86E-06	4.92E-06	2.52E-06	1.17E-05	1.66E-06	9.82E-07	1.28E-06
EOC	5.09	5.02	5.12	4.85	5.16	5.29	4.61

Table 7.17.: L^2-errors and average EOC for manufactured solution test with NW ES flux and $N\!=\!4$ on a 3D curvilinear mesh, Fig. 7.12 (b).

7.2.2. Strong scaling

To verify the HPC capabilities of the entropy stable DGSEM as it is presented in this work, we provide some scaling results obtained on `CHEOPS`. Particularly, we demonstrate the strong scaling of our DGSEM implementation, which is defined by the variation of the solution time with the number of processors for a fixed total problem size. Hence, we consider the same setup as in the previous section for the manufactured solution test with a fixed number of elements $N_{\text{el}} = 16^3$ and final time $T\!=\!5.0$. All other parameters are identical to the ones of the convergence tests, i.e. $\gamma = 2, \text{Pr}\!=\!0.72, \mu_{\text{NS}} = \mu_{\text{R}}\!=\!0.005$, and we use the ES flux (4.38) with local Lax-Friedrichs type dissipation (4.44) at element interfaces.

In Fig. 7.13 we show, that the relative simulation time indeed scales with the number of processors for $N = 5$ and $N = 8$, where we started with a serial run and doubled the number of processors up to 1024. We observe, that for both polynomial degrees the scaling is initially almost perfect, but at a certain decomposition level decays, since the latency limit seems to be reached, meaning that the computation time for the buffer routines is less than the communication time [69].
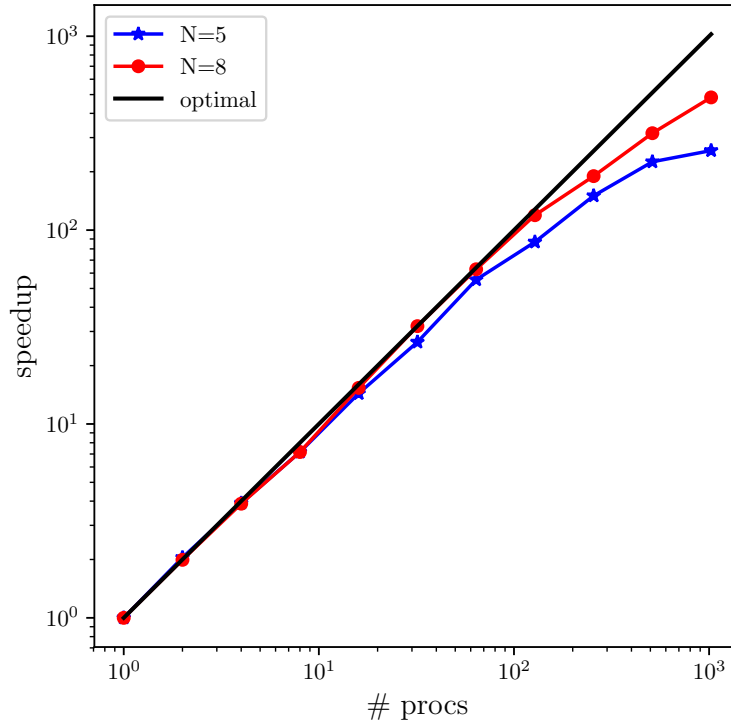
Figure 7.13.: Strong scaling of the entropy stable DGSEM for $N = 5$ and $N = 8$ applied to the manufactured solution test on 16^3 curved elements with $T = 0.5$ computed by one up to 1024 processors.

Further, we computed the performance index (6.1) in each run, which for $N = 5$ and $N = 8$ are given in Table 7.18. We see, that these values are in the same order of magnitude as expected, whereas the small growth for the highest decomposition levels arises from the communication overhead [69]. We also note, that the limit of the ideal speedup as well as the performance index depend on the architecture of the used HPC cluster, since the ratio of computation and communication bandwidth differ.

#procs	#DOF's/proc	PID	#procs	#DOF's/proc	PID
1	884 736	17.13	1	2 985 984	21.41
2	442 368	19.21	2	1 492 992	22.65
4	221 184	17.55	4	746 496	23.48
8	110 592	19.13	8	373 248	25.42
16	55 296	19.06	16	186 624	23.38
32	27 648	20.71	32	93 312	22.80
64	13 824	19.72	64	46 656	23.20
128	6 912	25.16	128	23 328	24.41
256	3 456	28.90	256	11 664	30.67
512	1 728	37.65	512	5 832	36.73
1024	864	61.87	1024	2 916	47.55

Table 7.18.: Local DOF's and performance index (in μs) of the entropy stable DGSEM for $N = 5$ (left) and $N = 8$ (right) applied to the manufactured solution test on 16^3 curved elements with $T = 0.5$ computed by one up to 1024 processors.

7.2.3. Entropy conservation

Next, we demonstrate the discrete entropy conservation of the scheme on curvilinear meshes, both with and without the GLM terms. As such, we deactivate the numerical dissipation introduced by the interface stabilization terms (4.38) and set $\mu_{NS} = \mu_R = 0$ to remove the resistive terms, because entropy conservation only applies to the ideal GLM-MHD equations.

We choose mesh type (b) from Figure 7.12 with a resolution of $7^3 = 343$ elements. As well-resolved smooth solutions would result in very small changes of total entropy anyway, we purposely select a more challenging test case initializing a moving spherical blast wave in a constant magnetic field. The inner and outer states are given in Table 7.19 and are blended over a distance of approximately δ_0 with the blending function

$$\mathbf{u} = \frac{\mathbf{u}_{\text{inner}} + \lambda \mathbf{u}_{\text{outer}}}{1 + \lambda}, \quad \lambda = \exp\left[\frac{5}{\delta_0}(r - r_0)\right], \quad r = \|\vec{x} - \vec{x}_c\|. \tag{7.14}$$

The parameters are $\vec{x}_c = (0.3, 0.4, 0.2), r_0 = 0.3, \delta_0 = 0.1$ and we set $\gamma = 5/3$. A visualization of the initial state is shown in Figure 7.15.

Since the entropy conservative scheme is essentially dissipation-free by construction, we can use the error in the total entropy as a measure of the temporal convergence of the method. In particular, the total entropy at time t is computed by the discrete approximation (7.5). As in the two-dimensional studies, we reduce the CFL number to demonstrate that the dissipation of the time integration scheme decreases and entropy conservation is captured more accurately.

	ϱ	v_1	v_2	v_3	p	B_1	B_2	B_3	ψ
inner	1.2	0.1	0.0	0.1	0.9	1.0	1.0	1.0	0.0
outer	1.0	0.2	−0.4	0.2	0.3	1.0	1.0	1.0	0.0

Table 7.19.: Inner and outer primitive states for the 3D entropy conservation test.

Figure 7.14 confirms this precise behavior for $N = 4$ and $N = 5$ using a fourth order Runge-Kutta time integrator. For small enough time steps, the EC scheme conserves entropy discretely up to numerical round-off even for this discontinuous test case. The same behavior is observed for the EC scheme without the GLM terms. We also demonstrate, that the entropy change for the entropy stable scheme including additional dissipation through the numerical surface fluxes is independent of the time step.
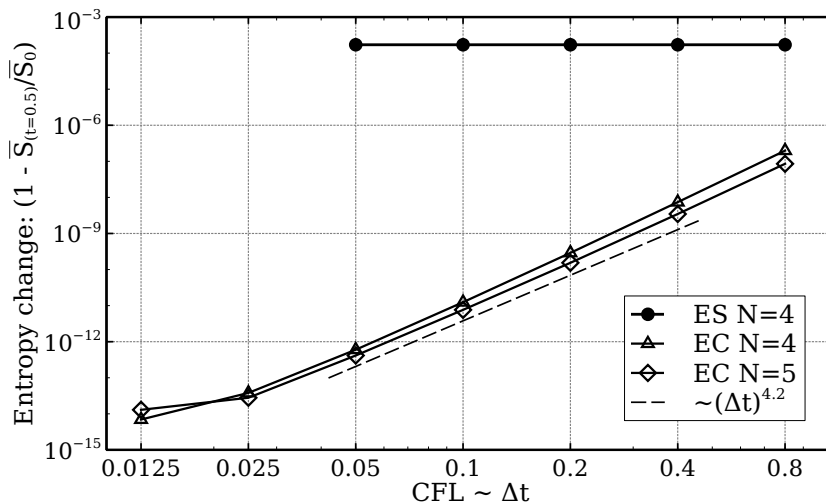
Figure 7.14.: Log-log plot of entropy change from the initial entropy $\overline{S}_0$ to $\overline{S}(t = 0.5)$ over the timestep on $7^3 = 343$ curved elements [16].

As the EC scheme has virtually no built-in dissipation, all EC simulations crash due to negative pressure, independently of the CFL number, after $T \approx 0.72, 0.61$ for $N = 4, 5$ respectively. In Figure 7.15, the $N = 4$ simulation results at $T = 0.5$ of the EC and ES scheme are visualized and clearly underline the difference between the EC and the ES results, although dissipation is only added at the element interfaces.

In all simulations, we use the discretely divergence-free metric terms computed via the discrete curl form [80], a necessary condition pointed out in the entropy conservation proofs. We note that, when using the $N = 4$ EC scheme with cross-product metrics instead, the discrete entropy conservation property is broken with an absolute entropy change $\varepsilon_S > 10^{-8}$ and even with the wrong sign for CFL numbers $\texttt{CFL} \le 0.4$.
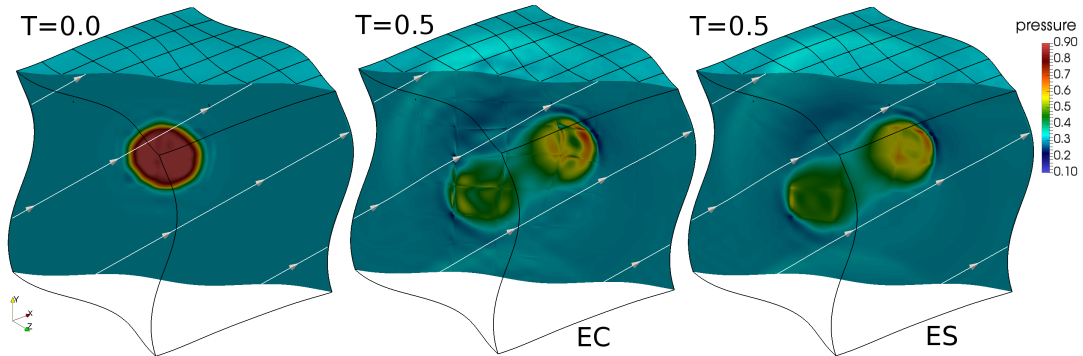
Figure 7.15.: Entropy conserving test of ideal GLM-MHD equations for $N = 4$ on $7^3 = 343$ curved elements: Pressure distribution, left at initialization, the EC scheme in the middle and the ES scheme on the right, both at $T = 0.5$ [16].

7.2.4. Divergence cleaning

For the demonstration of the divergence cleaning capabilities, we use a three-dimensional extension of the non-divergence-free initialization from Sec. 7.1.3. On $\Omega = [0, 1]^3$ we initially define a Gaussian pulse in the $x-$component of the magnetic field, i.e.

$$\varrho = 1, \quad E = 6, \quad B_1 = \exp\left(-\frac{1}{8}\frac{(x - 0.5)^2 + (y - 0.5)^2 + (z - 0.5)^2}{0.0275^2}\right). \quad (7.15)$$

Again, all other initial values are set to zero and the boundaries are periodic. Further, we set $\gamma = 5/3$, turn off physical viscosity and use the ES flux (4.38) with local Lax-Friedrichs type dissipation (4.44) at element interfaces.

In Figure 7.16 we show the time evolution of the discrete divergence error $\|\vec{\nabla}\cdot\vec{B}\|_{L^2(\Omega)}$ from (7.7) normalized by the initial divergence for $N = 3$ and mesh type (a) with 20^3 elements. Similar to the previous two-dimensional studies, we present the simulation results of the ideal GLM-MHD approximation, in which the divergence error is solely propagated through the domain, as well as reference results without any divergence cleaning ($c_h = 0$) and with additional damping for varying values of α in (2.38). We see in Figure 7.2 that without GLM divergence cleaning the simulation even crashes at $t \approx 3.4$ and for $\alpha > 0$ the divergence error decays over time.

7.2.5. Robustness tests

Lastly, we again verify the increased robustness of the entropy stable approximation including GLM divergence cleaning. In order to do so, we present two different plasma flows, which both crash for the standard DGSEM, e.g. [70], but produce reasonable simulation results for the entropy stable DGSEM presented herein.
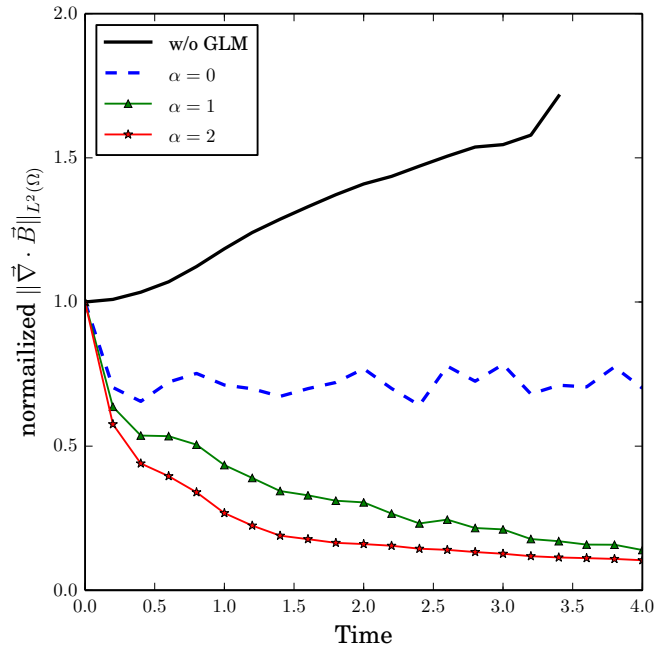
Figure 7.16.: Temporal evolution of the normalized discrete L^2 error in the divergence-free condition for $N = 3$ in each spatial direction on 20^3 curved elements and $T = 4$ [16].

Viscous 3D Orszag-Tang vortex

We use a three-dimensional extension of the common Orszag-Tang vortex proposed by Elizarova and Popov [37] as well as consider a viscous version of the standard test problem, similar to Altmann [3]. The domain is $\Omega = [0,1]^3$ with periodic boundary conditions and the initial data given in Table 7.20.

ϱ	v_1	v_2	v_3	p	B_1	B_2	B_3
$\frac{25}{36\pi}$	$-\sin(2\pi z)$	$\sin(2\pi x)$	$\sin(2\pi y)$	$\frac{5}{12\pi}$	$-\frac{1}{4\pi}\sin(2\pi z)$	$\frac{1}{4\pi}\sin(4\pi x)$	$\frac{1}{4\pi}\sin(4\pi y)$

Table 7.20.: Initial condition for the 3D Orzag-Tang vortex in primitive variables.

We choose $\gamma = 5/3$, a Prandtl number of $\mathrm{Pr} = 0.72$ and set the viscosity and resistivity parameters to be

$$\mu_{\mathrm{NS}} = 10^{-3}, \quad \mu_{\mathrm{R}} = 6 \times 10^{-4}, \tag{7.16}$$

which correspond to a kinematic Reynolds number (Re) of 1000 and a magnetic Reynolds number ($\mathrm{Re_m}$) of approximately 1667. We run this test to a final time of $T = 0.5$ with a polynomial order of $N = 7$ in each spatial direction on a $10 \times 10 \times 10$ element internally curved hexahedral mesh, Fig. 7.12(a).

We successfully run the entropy stable DGSEM for the resistive GLM-MHD equations up to the final time. The magnetic energy, $\frac{1}{2}\|\vec{B}\|^2$, is visualized in Fig. 7.17 for the initialization, time $t = 0.25$ as well as the final time $T = 0.5$.
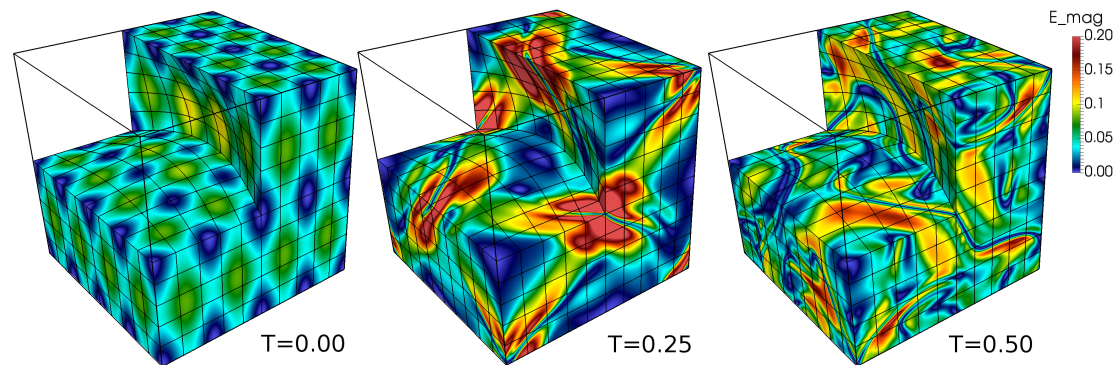
Figure 7.17.: Time evolution of the magnetic energy for the three-dimensional viscous Orszag-Tang vortex with polynomial order $N = 7$ in each spatial direction on a $10 \times 10 \times 10$ internally curved hexahedral mesh, Fig. 7.12(a) [16].

Further, we find that the standard DGSEM, e.g. [70], for this resistive GLM-MHD model crashes at $t \approx 0.42$ due to the generation of negative pressure values. Also, we shrank the time step for the entropy stable as well as the standard DG runs and find the same numerical stability results. This reinforces that the numerical instabilities in the approximate flow are caused by errors other than those introduced by the time integration scheme. These results demonstrate the strong benefits of using an entropy stable formulation for such a complex configuration.

Insulating Taylor-Green vortex

Lastly, we consider a modification of the well-known Taylor-Green vortex (TGV) to include magnetic fields [17, 93, 94] as a final example to demonstrate the increased robustness of the entropy stable DG approximation. The TGV flow was first introduced for the incompressible Navier-Stokes equations in [131] as a model problem for the analysis of transition and turbulence decay in a cubic domain with periodic boundary conditions. The test case is particularly interesting, because a simple set of initial conditions evolve to include a wide range of spatial scales as well as turbulent structures. Several extensions of the TGV are available for the ideal MHD equations to model turbulent

123

plasmas, e.g. [94]. Here we consider a particular insulating version of the TGV for the ideal GLM-MHD equations [93].

We adopt a modified version of the initial conditions suited for compressible flow solvers. To create an initial condition for the pressure involves solving a Poisson equation from the incompressible ideal MHD equations. Because the definition of the pressure is unique up to a constant, we select the initial pressure such that the flow is nearly incompressible with a maximum Mach number of Ma = 0.1. The initial conditions prescribe a state in $\Omega = [0, 2\pi]^3$ with the density, velocity components, pressure, and magnetic field components defined as

$$\varrho = 1,$$

$$\vec{v} = \left(\sin(x)\cos(y)\cos(z), \, -\cos(x)\sin(y)\cos(z), \, 0\right)^T,$$

$$p = \frac{100}{\gamma} + \frac{1}{16}\left(\cos(2x) + \cos(2y)\right)\left(2 + \cos(2z)\right) + \frac{1}{16}\left(\cos(4x) + \cos(4y)\right)\left(2 - \cos(4z)\right),$$

$$\vec{B} = \left(\cos(2x)\sin(2y)\sin(2z), \, -\sin(2x)\cos(2y)\sin(2z), \, 0\right)^T,$$

$$(7.17)$$

where $\gamma = 1.4$ and $\mu_{\mathrm{NS}} = \mu_{\mathrm{R}} = 0$. We evolve this initial state up to the final time $T = 20$, such that turbulent structures can develop. We note that, for a compressible simulation the initial condition of the pressure will change, if other insulating or conducting TGV formulations from [93] are chosen.

Again, we use this turbulent test case of the insulated TGV (7.17) to demonstrate the increased robustness of the proposed solver described in this work. To do so, we scale mesh type (a) from Fig. 7.12 up to a length of 2π in each direction, discretize it into 16^3 elements and set the polynomial order of the approximation to $N = 3$. In Figure 7.18, by a rendering volume plot, we visualize the magnetic energy, $\frac{1}{2}\|\vec{B}\|^2$, obtained by the entropy stable solver at the final time.

As in the previous stability investigations, we perform a comparison of the standard DGSEM against the entropy stable DGSEM, both with GLM divergence cleaning. Again, we find that the simulation crashes for the standard DGSEM, already at $t \approx 3.6$, whereas the entropy stable solver successfully runs up to the final time. We underline, that the same result has been observed for lower CFL numbers as well as different spatial discretizations and polynomial orders. This highlights that the entropy stable DG method with GLM divergence cleaning is more numerically stable for under-resolved turbulence computations, too.

We note, that the low Mach number insulating TGV (7.17) considered here is used purely as a robustness test case. An analysis of the turbulence modeling capabilities obtained by the entropy stable DGSEM with GLM divergence cleaning is outside the scope of the current work, but is the focus of future research. However, these results underline that controlling aliasing errors in a high-order numerical approximation of the ideal GLM-MHD equations with an entropy stable formulation offers increased robustness.
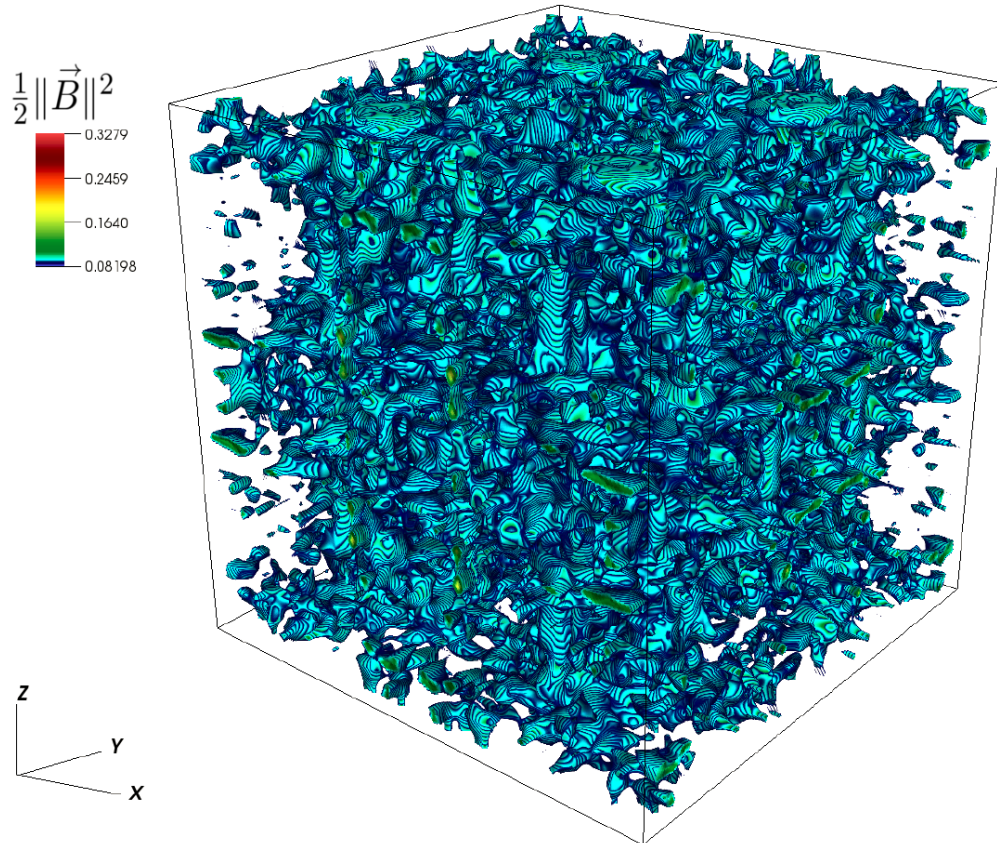
Figure 7.18.: Rendered magnetic energy distribution of the insulating Taylor-Green vortex at $T = 20$ obtained by the entropy stable DGSEM with polynomial order $N\!=\!3$ on a internally curved mesh with 16^3 elements, Fig. 7.12(a).

8. Geophysics application

Finally, we apply the novel entropy stable DG solver to MHD flows, which arise from real space physics models describing atmospheric plasma interactions. In particular, we consider moons with sub-alfvénic plasma interactions like Io, Europa or Enceladus. As these moons are embedded in dense luminous plasma tori caused by the magnetosphere of Jupiter or Saturn, respectively, they exhibit exceptionally interesting plasma flow characteristics containing steep gradients and discontinuities [116, 118, 123]. In addition to analytical models and observation data acquired by e.g. the Galileo spacecraft flybys, numerical simulations of the far-field atmospheric plasma interactions have become a powerful tool to gain a better understanding of the underlying physical processes in recent decades.

We start this chapter with a broad overview of the general setup for such simulations including the physical background knowledge in Sec. 8.1. Next, in Sec. 8.2 we show simulation results for a simplified cylindrical version of the problem, for which we have an analytical solution, before we provide results for the more physically relevant spherical setup in Sec. 8.3.

8.1. Physical setup

As a representative example, we focus on the moon Io, which was discovered in 1610 and is the innermost of Jupiter's four Galilean moons. It has the highest density, the least amount of water and the fourth-largest size of all moons in our solar system. Moreover, Io is the most volcanically active body and embedded in the largest magnetosphere of the solar system. Hence, Io's electrodynamic interaction is unique due to Jupiter's strong magnetic field as well as its fast rotation and the tenuous and patchy atmosphere caused by its strong volcanism [116]. Plasma interactions with Io's atmosphere lead to mass loss in form of ions and neutrons [14]. The latter are then ionized by ultraviolet radiation and electron impact ionization, such that ions and electrons accumulate around the orbit of Io forming a plasma torus [118]. The plasma mostly consists of heavy sulfur dioxide ions and is subject to electrodynamic forces accelerating it to the local bulk plasma velocity. Consequently, this flow of magnetized plasma past the obstacle Io, together with its tenuous atmosphere, is the engine of Io's plasma interaction [116]. The general setup is illustrated in Figure 8.1.
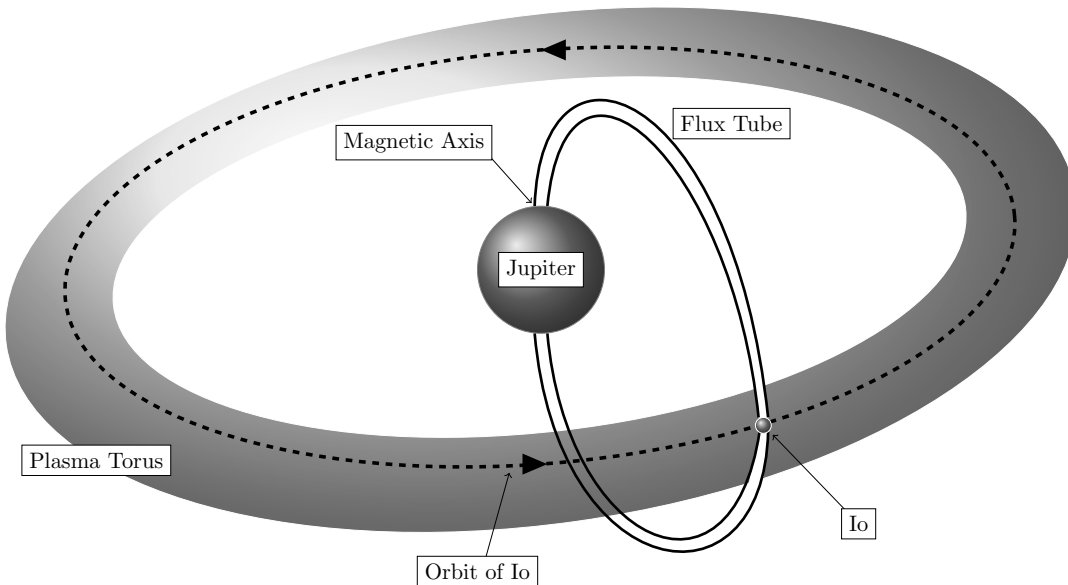
Figure 8.1.: Illustration of Io's plasma torus.

Neglecting neutral density, relativistic, viscous and Hall effects, the considered magneto-hydrodynamic flow inside Io's plasma torus can be modeled by the ideal GLM-MHD equations (2.34). As pointed out, there is more energy in the magnetic field than in the bulk velocity or the thermal velocity, which results in a low Alfvénic Mach number of $\text{Ma}_\text{m} \approx 0.03$. Further important characteristic parameters are the sonic Mach number, which is larger than one, and the plasma beta $\beta_\text{m} \approx 0.04$. Due to these numbers the stiffness of the strong background magnetic field of Jupiter plays the dominant role in determining the topology of the interaction, which is essentially anisotropic [116, 118].

In most common approaches, the basic physical mechanisms of Io's plasma interaction are divided into the local interaction, which occurs within a few satellite radii of Io, and the far-field interaction region including Io's plasma torus, Jupiter's ionosphere and the high magneto-spheric latitudes [116]. We note, that these two interaction regions are very strongly coupled.

The local interaction area comprises Io's atmosphere, where plasma from the torus streams in and forms an ionosphere by electron impact ionization and photo-ionization. Since the conductivity is very high perpendicular to the magnetic field in the ionosphere, the motional electric field drives an ionospheric electric current. Consequently, the electric field is modified by polarization charges, which changes the local Lorentz force and damps the electron and ion flow close to Io. As a result the plasma flow is strongly reduced inside Io's atmosphere, which can be modeled by an additional source term on

the right-hand side of the ideal GLM-MHD model, i.e.

$$\mathbf{u}_t + \nabla \cdot \overset{\leftrightarrow}{\mathbf{f}} + \boldsymbol{\Upsilon} = \mathbf{r}_{\mathrm{c}} \tag{8.1}$$

with the neutral collision term

$$\mathbf{r}_{\mathrm{c}} = \left(0, \ -\varpi \varrho \vec{v}, \ -\frac{1}{2}\varpi \varrho \|\vec{v}\|^2, \ \vec{0}, \ 0 \right)^T \tag{8.2}$$

and the collision frequency

$$\varpi = \begin{cases} \varpi_{\mathrm{in}} & , \vec{x} \in \mathfrak{A} \\ \varpi_{\mathrm{in}} \exp\left(\frac{r_{\mathfrak{A}} - r}{d} \right) & , \vec{x} \in \mathfrak{I} \\ 0 & , \vec{x} \notin \mathfrak{A} \cup \mathfrak{I} \end{cases} , \tag{8.3}$$

where $\varpi_{\mathrm{in}} \geq 0$. It is straight-forward to prove, that this additional source term does not violate the entropy inequality, since

$$\mathbf{w}^T \mathbf{r}_{\mathrm{c}} = -\beta \varpi \varrho \|\vec{v}\|^2 \leq 0 \tag{8.4}$$

for $\beta, \varpi, \varrho \geq 0$. Similar to the damping source term of the divergence cleaning, we interpolate the collision source term at the LGL nodes, so that entropy stability is guaranteed discretely, too.

Moreover, in (8.3), $\mathfrak{A}$ denotes the neutral gas cloud representing the inner atmosphere, in which the collision frequency $\varpi_{\mathrm{in}} > 0$ is constant. In order to model the ionosphere, we also introduce a smooth transition area $\mathfrak{I}$ by an exponential blending dependent on the radii $r_{\mathfrak{A}}, r$ and the dilatation factor d. In this region the neutral atmosphere gets thinner, so that the ionospheric conductivities become smaller and cannot maintain the ionospheric current perpendicular to the magnetic field. Eventually, electric current is continued along the magnetic field lines out of Io's ionosphere, where it is finally fed into Io's *Alfvén wings*.

That is, where the far-field interaction takes place as described by many approaches, e.g. the unipolar-inductor model [56] or the ideal Alfvén wing model [104]. In general, when Io moves along the constant flow velocity v_1 across the constant background field lines B_3, it generates a standing magneto-spheric disturbance that propagates away along field lines at the Alfvén wave speed in both directions. Thus, in the rest frame of the co-rotating plasma there is a standing disturbance spread out downstream along the Alfvén characteristics of the ambient flow described as a pair of standing Alfvén current tubes and termed as *Alfvén wings*. The main reason for these perturbations are elastic collisions between the ions and the neutrals in addition to charge exchanges and ionization [13]. In particular, the development of the Alfvén wings is observable in the regions with decreasing plasma bulk velocity v_1 and perturbed B_1 north and south of

Io in the xz plane. Moreover, the Alfvén current tubes are bent back by a constant angle with respect to the unperturbed background magnetic field. The perturbation of the magnetic field is positively correlated with the perturbation of the velocity field in the northern Alfvén wing and negatively correlated in the southern wing [104]. These phenomena have been observed by many flybys [116, 118] and are illustrated in Fig. 8.2.
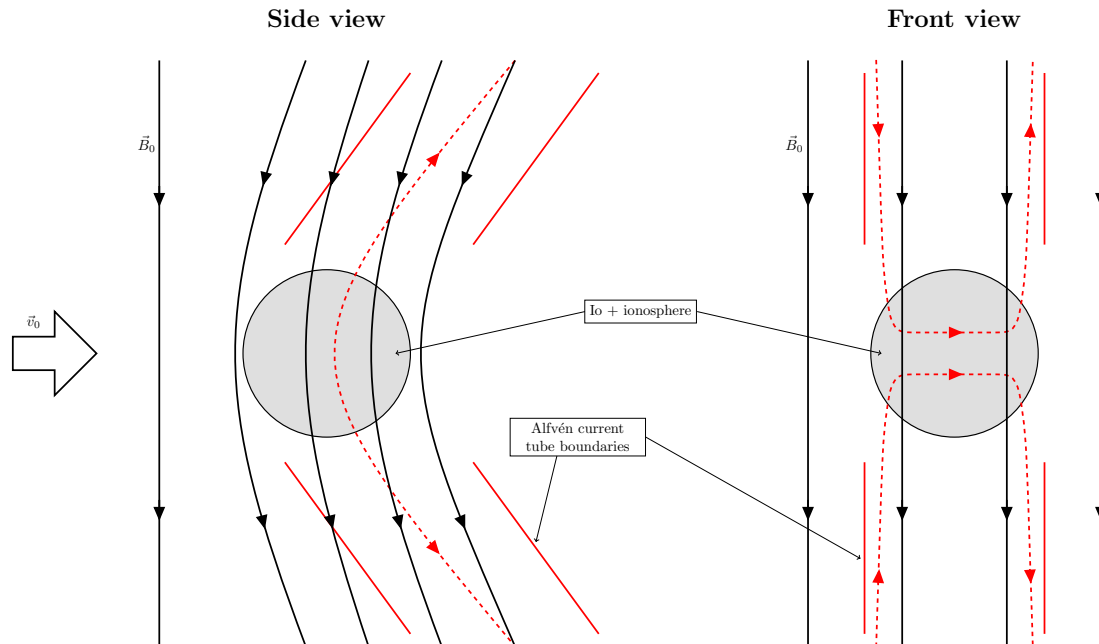
Figure 8.2.: Front and side view of Io's plasma torus with Alfvén wings.

Since the real astronomical quantities vary over many length scales from thousands of kilometers to the order of Nano-Tesla, we introduce dimensionless units in order to normalize the values for our final simulations. The most important quantities for the considered setup can be found in Table 8.1, where we state both, the initial values in real units and the dimensionless values.

	l	ϱ	v_1	p	B_3	ϖ_{in}	t
real	1820 km	42300 $\frac{\text{amu}}{\text{cm}^3}$	57 $\frac{\text{km}}{\text{s}}$	34 nPa	-1840 nT	4 Hz	522.72 s
normalized	1	1	1	0.148	-3.41	127.6	16.36

Table 8.1.: Real and dimensionless (initial) values inside Io's plasma torus

All other variables are initially zero and in the following simulations we consider the ideal GLM-MHD equation, so that we set both, the viscosity and resistivity, to zero, i.e. $\mu_{\text{NS}} = \mu_{\text{R}} = 0$.

Further, we note that in all simulations we ignore local interactions at Io's surface, which can be modeled by non-conducting inner boundary conditions [35]. This approach is based on solving an elliptical problem for the magnetic potentials over the entire surface in each time step. Hence, it would violate the local structure of our entropy stable DGSEM and is not well suited for a parallel implementation. However, even without considering the effects at the moon's surface, we are able to simulate the local and far-field interactions around Io as presented in the next sections.

8.2. Plasma flow through cylindrical gas cloud

In this first configuration we consider a neutral gas cloud of a cylindrical shape. Particularly, the cylinder is placed with its center at the origin, has a radius of one unit and a height of two units, so that we model the inner atmosphere by

$$\mathfrak{A} = \mathfrak{C} = \{\vec{x} \in \Omega \mid x_1^2 + x_2^2 \leq 1, |x_3| \leq 1\}. \tag{8.5}$$

In this setup, we neglect physical processes inside the ionosphere $\mathfrak{I}$, i.e. $d \to 0$, which causes a strong discontinuity of the additional collision source term right at the cylinder's surfaces. We initialize the primitive variables according to Table 8.1 by a constant state in the entire domain, i.e.

$$\varrho = 1, \quad \vec{v} = (1,0,0)^T, \quad p = 0.148, \quad \vec{B} = (0,0,-3.41)^T, \tag{8.6}$$

and let them evolve to a final time $T = 5$. Further, we set $\gamma = 5/3$ and turn off viscous effects as well as the damping of the divergence error. The boundary states at the left, front and back boundary faces are constant to this reference solution, whereas we define outflow boundary conditions at the right, top and bottom of the domain.

As we have the freedom of discretizing the domain by an unstructured curvilinear mesh, we adapt it to the shape of the cylinder as well as the developing Alfvén wings in order to capture the flow motion and evolving shocks, see Fig. 8.3. This particular mesh contains the inner structure of a tilted cylinder and is built from 14,336 curved elements.

We run simulations on the tilted cylinder mesh with both schemes, the standard and the entropy stable DGSEM, using polynomial approximations of degree $N = 3$, which corresponds to 917,504 spatial DOF's in total. Since both schemes are high-order and shocks close to the cylinder and Alfvén wings cause strong oscillations in the density and pressure, we require an additional shock capturing method. In order to regularize the approximation in these oscillatory areas we use the DOF energy indicator and cell-wise artificial viscosity as presented in Sec. 5.1. The shock capturing parameters for all simulations are chosen to be $\sigma_{\min}^{\mathrm{DOF}} = -9, \sigma_{\max}^{\mathrm{DOF}} = -6$ and $\epsilon_0 = 0.03$ in (5.9), where we use the product of density and pressure as the shock indicator.
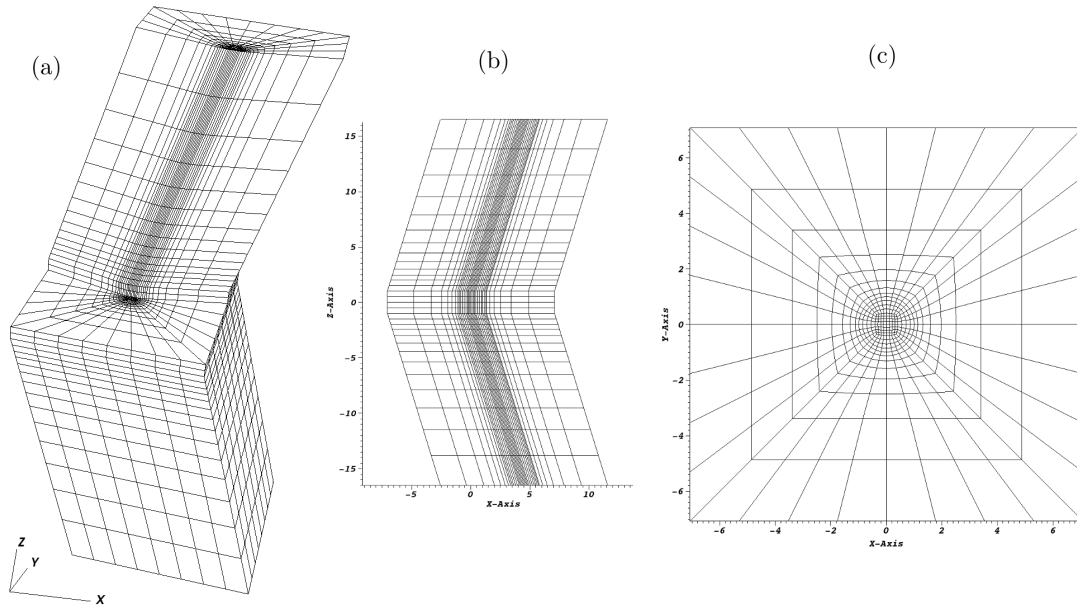
Figure 8.3.: Tilted cylinder mesh for the neutral gas cloud test, (a) 3D view, (b) side view at $y = 0$, (c) top view at $z = 0$.

We also stabilize the approximation between neighboring elements with the standard Lax-Friedrichs flux, see e.g. [114], respectively the ES flux (4.38) with local Lax-Friedrichs type dissipation (4.44) at element interfaces. The CFL number is always set to CFL $= 0.5$.

We provide pseudo-color plots of the density and pressure at $z = 0$ and $T = 5$ in Figure 8.4. We see, that the density decays right behind the cylinder, whereas the pressure increases inside the neutral gas cloud. The rise in pressure is related to atmospheric heating driven by the particle collisions.

Most importantly, in Figure 8.5 we illustrate the mentioned Alfvén wings observed in the B_1 and v_1 components of the solution vector at $y = 0$ and the final time $T = 5$. As described in the previous section, they evolve at the northern and southern poles of the neutral gas cloud and are bent back by the same constant angle we considered in the construction of the mesh. Even though we focus on the simplified cylindrical version of the problem without an ionosphere, we observe the expected physical features.

We compare our results to a first order approximation computed by the open-source software ZEUS (https://www.astro.princeton.edu/~jstone/zeus.html). This solver uses a first order finite volume approximation of the considered problem on a Cartesian mesh with spherical coordinates and a simple explicit Euler time integration, which for this setup results in 10 mill DOF's.
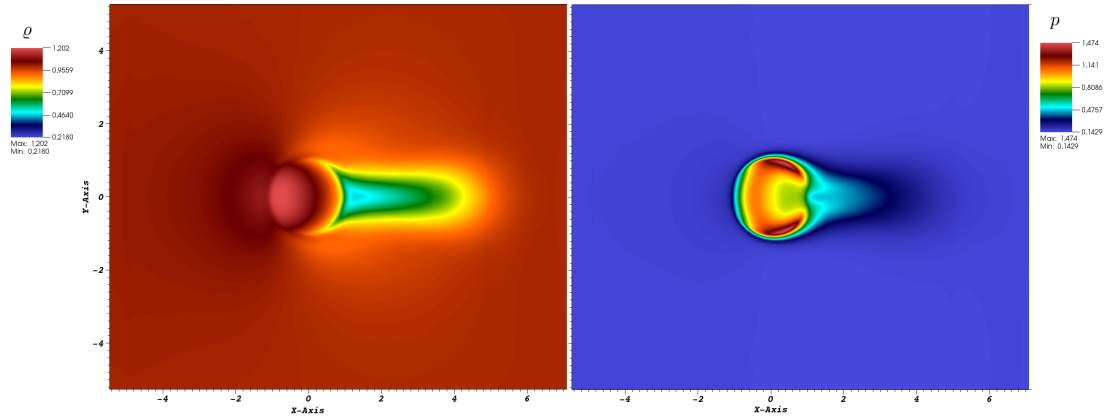
Figure 8.4.: Density (left) and pressure (right) at $z = 0$ and $T = 5$ for the cylindrical neutral gas cloud test computed by the ES DGSEM with artificial viscosity and $N = 3$.
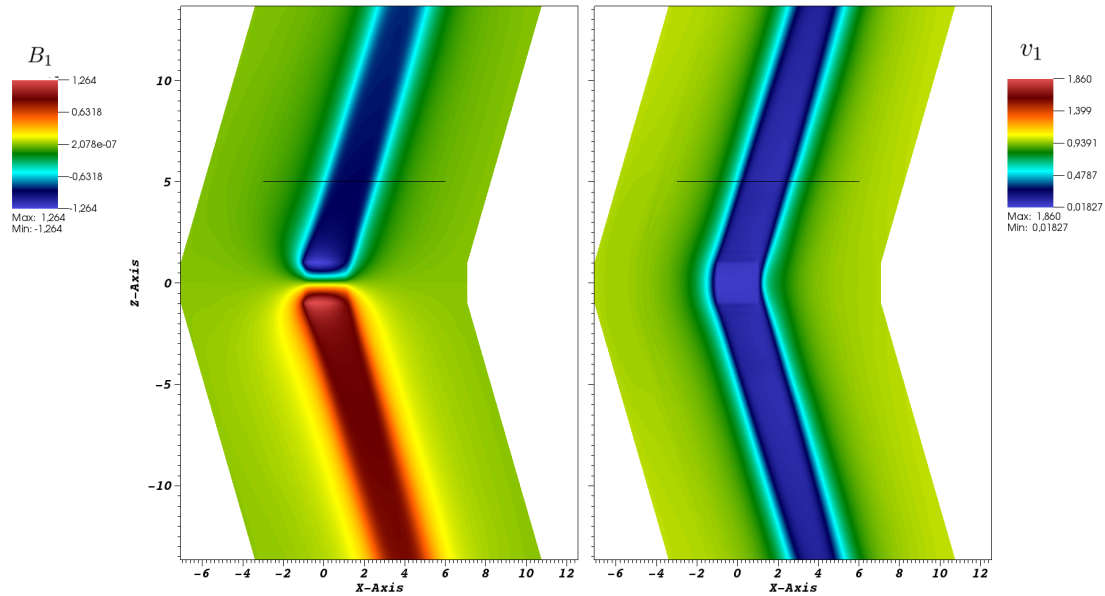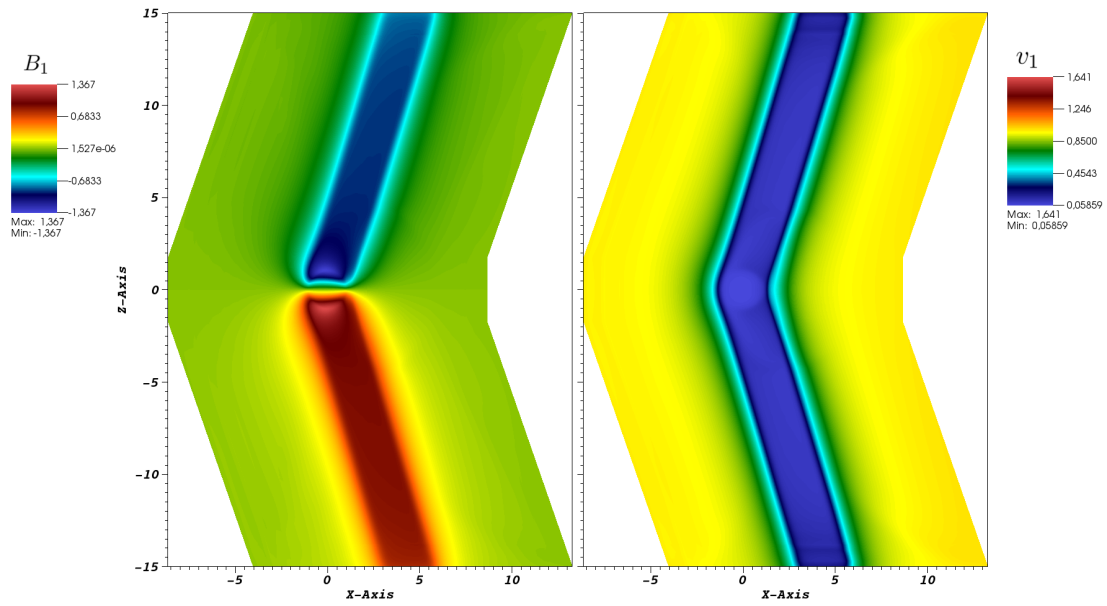

Figure 8.5.: Alfvén wings in B_1 (left) and v_1 (right) at $y = 0$ and $T = 5$ for the cylindrical neutral gas cloud test computed by the ES DGSEM with artificial viscosity and $N = 3$.

Moreover, due to the simplicity of this configuration, we compare it to an analytical reference solution derived in [118]. For this final comparison we perform an additional slicing at $z = 5$ as highlighted by the black lines in Figure 8.5.
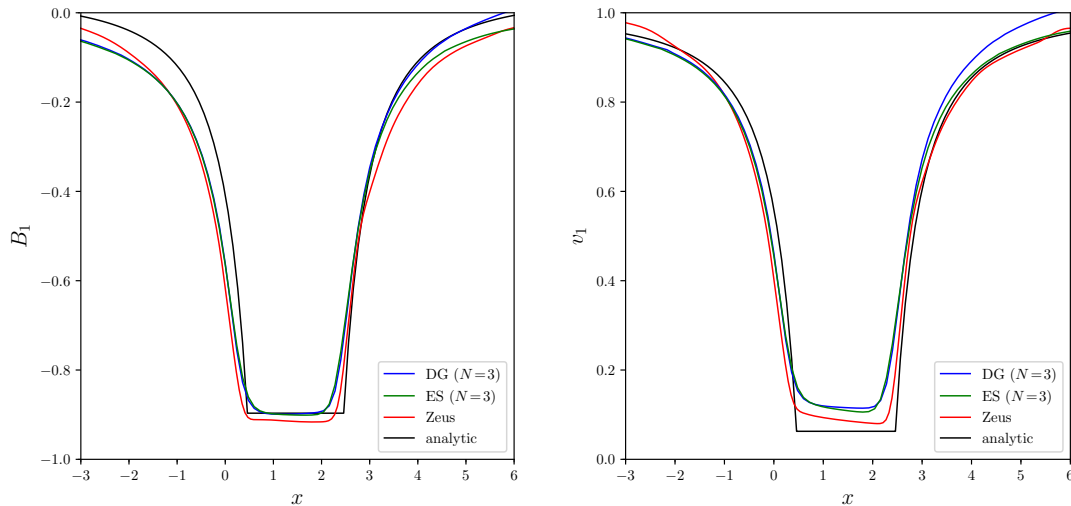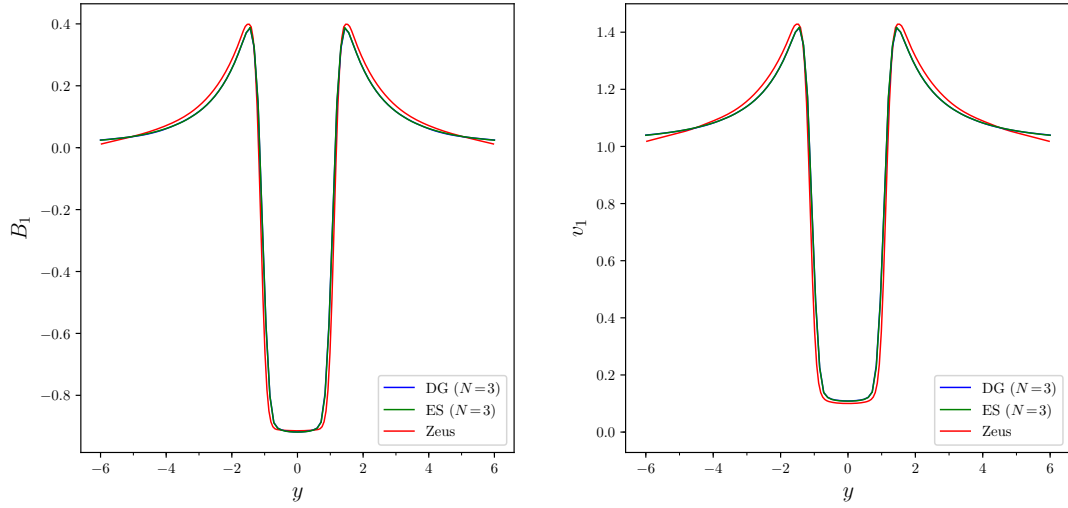

Figure 8.6.: Profile comparison of B_1 (left) and v_1 (right) at $y = 0, z = 5$ and $T = 5$ for the cylindrical neutral gas cloud test.

Subsequently, in Figure 8.6 we show the profiles of the B_1 and v_1 components, which we obtain by slicing through the Alfvén wings at $z = 5$ for the three simulation results of the entropy stable, the standard DGSEM and the ZEUS solver. As we can see, all approximations are close to the analytical profile derived by Saur et al. [118], but of course they are not entirely matching by reasons of numerical dissipation, either caused by the low order scheme or by the artificial viscosity. Whereas the DG approximations reproduce the B_1 profile better, they deviate even more than the ZEUS approximation from the analytical v_1 solution. We note, that in the derivation of the analytical reference solution additional physical restrictions are involved, too [118].

Next, we consider additional slices at $x = 1, z = 5$ and $x = 2, z = 10$ (Fig. 8.7) to investigate how the steep gradients and discontinuities are captured by the different approximations. Regarding this matter, we visualize the resulting profiles in Figures 8.8 and 8.9, where we again observe, that all approximations get close to the analytical reference solution. Obviously, the first order approach reproduces the discontinuities best, where the DG approximations are almost identical. At this point, we highlight, that for this applied test problem we also found configurations with less artificial viscosity, for which the standard scheme crashed, but the ES DGSEM successfully produced the desired, albeit oscillatory, data.
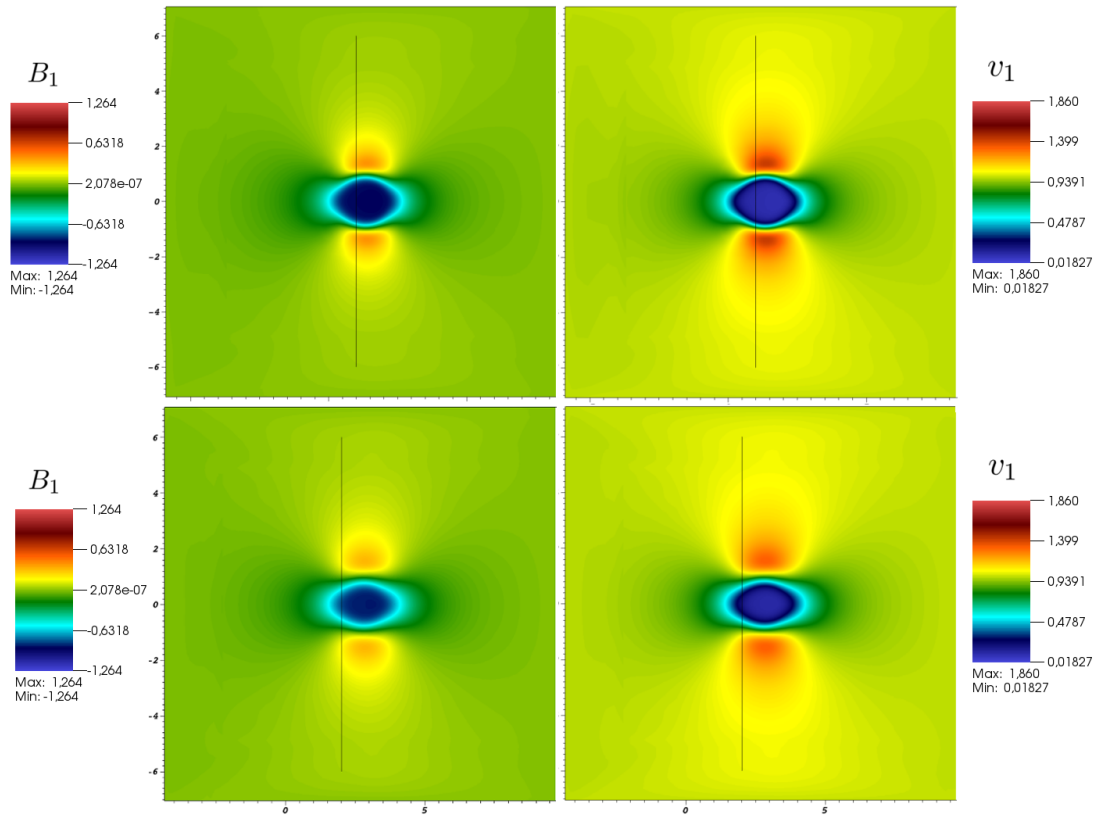
Figure 8.7.: Additional slices in B_1 (left) and v_1 (right) at $z = 5$ (top) and $z = 10$ (bottom) for the cylindrical neutral gas cloud test computed by the ES DGSEM with artificial viscosity and $N = 3$.

Even though the `ZEUS` approximations are closest to the analytical profile, we note, that the million DOF's of this simulation result in extremely long runtimes. Indeed, we observed a speed-up for the simulation results of the DG schemes by a factor of 10 compared to the `ZEUS` approximations. Although we use a 4th order time integrator, the overall degrees of freedom are way less for the DG schemes due to the mesh flexibility and high-order nature. Thus, especially the more robust ES DGSEM offers a promising alternative to state-of-the-art finite volume solvers.
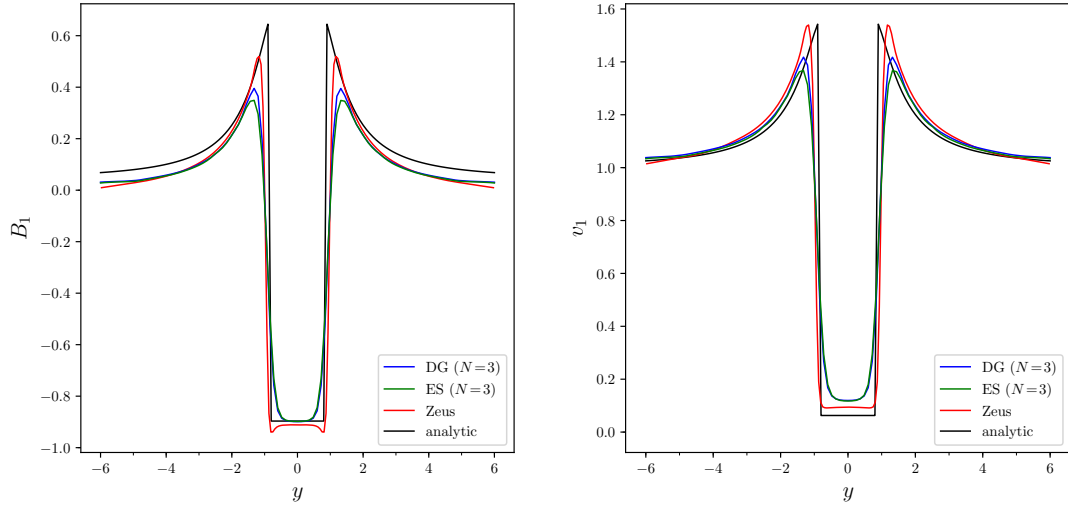
Figure 8.8.: Profile comparison of B_1 (left) and v_1 (right) at $x = 1, z = 5$ and $T = 5$ for the cylindrical neutral gas cloud test.
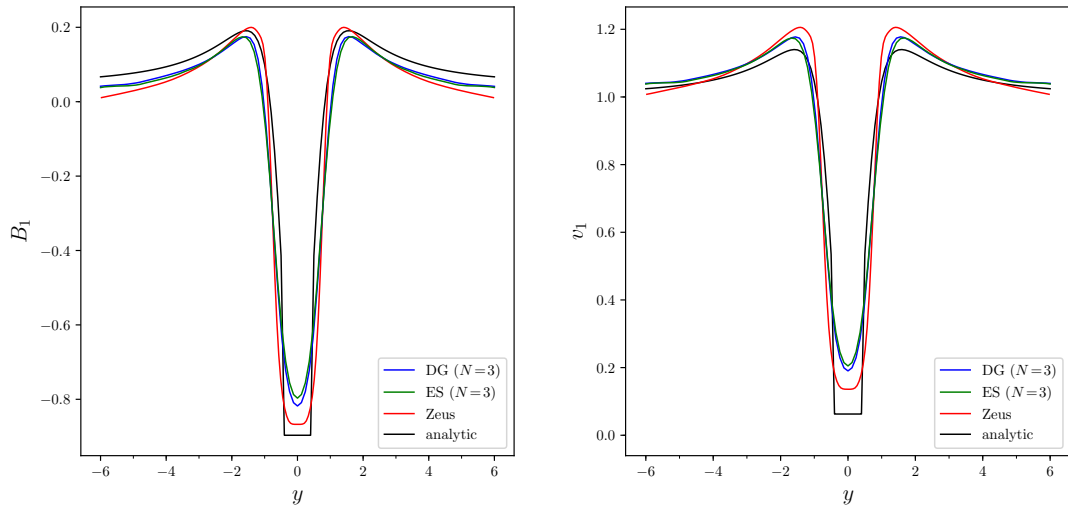
Figure 8.9.: Profile comparison of B_1 (left) and v_1 (right) at $x = 2, z = 10$ and $T = 5$ for the cylindrical neutral gas cloud test.

135

8.3. Plasma flow through spherical gas cloud

As a final application, we now replace the cylindrical gas cloud by a more realistic spherical shape. In the dimensionless computational domain we scale the radius of the atmosphere to be one unit, $r_{\mathfrak{A}} = 1$, and locate the center of the sphere at the origin, i.e.

$$\mathfrak{A} = \mathfrak{S} = \{\vec{x} \in \Omega \mid \|\vec{x}\| \leq r_{\mathfrak{A}} = 1\}. \tag{8.7}$$

Further, we include the ionospheric processes by an exponential blending of the collision frequency as in (8.3). To do so, we define the dilatation factor by $d = 150/1820$ according to the normalized measured data. By its definition the ionosphere $\mathfrak{I}$ is of infinite size, but with this choice of d we find that for $r = 2$ the collision frequency already becomes less than 0.001.

We initialize the primitive variables as in (8.6) and Table 8.1. Again, we turn off viscous and divergence damping effects, set $\gamma = 5/3$ and run to a final time of $T = 5.0$. The left, front and back boundary states are constant to the initial solution and at the right, top and bottom of the domain we define outflow boundary conditions. In order to capture the physical interactions at the sphere as well as the development of the Alfvén wings best, we discretize the computational domain by the unstructured and curvilinear, but conforming, mesh illustrated in Figure 8.10, which is built from 79,872 curved elements.

As for the cylinder, we run the simulations with both, the standard and the entropy stable DGSEM, using polynomials of degree $N = 3$, which results in approximately five million spatial DOF's. The CFL number is `CFL = 0.5` and we regularize oscillations caused by shocks with the artificial viscosity approach. Troubled elements are identified by the DOF energy indicator applied to the pressure times density and the according parameters are defined as $\sigma_{\min}^{\mathrm{DOF}} = -9, \sigma_{\max}^{\mathrm{DOF}} = -3$ and $\epsilon_0 = 0.01$ in (5.9). So, compared to the cylinder we add less artificial dissipation, because the upper threshold is smaller and the smoothing interval is larger, before we eventually add the maximum amount of viscosity. Obviously, this is related to the involvement of the ionosphere, which already smooths the additional collision source term and, thereby, the strength of the physical shocks. Additionally, we again use the local Lax-Friedrichs flux, [114], for the standard DGSEM and the ES flux (4.38) with local Lax-Friedrichs type dissipation (4.44) at element interfaces.

In Figure 8.11 we visualize the density and pressure at $z = 0$ and $T = 5$, which exhibit similar physical features as in the cylindrical setup. Moreover, in Figure 8.12 we show the B_1 and v_1 components of the entropy stable approximation at $y = 0$ and $T = 5$ revealing the Alfvén wings of the spherical problem. Again, the northern wing contains negative perturbations of both field variables, whereas in the southern wing only the velocity is reduced and the magnetic field component grows.

(a)

(b)

(c)
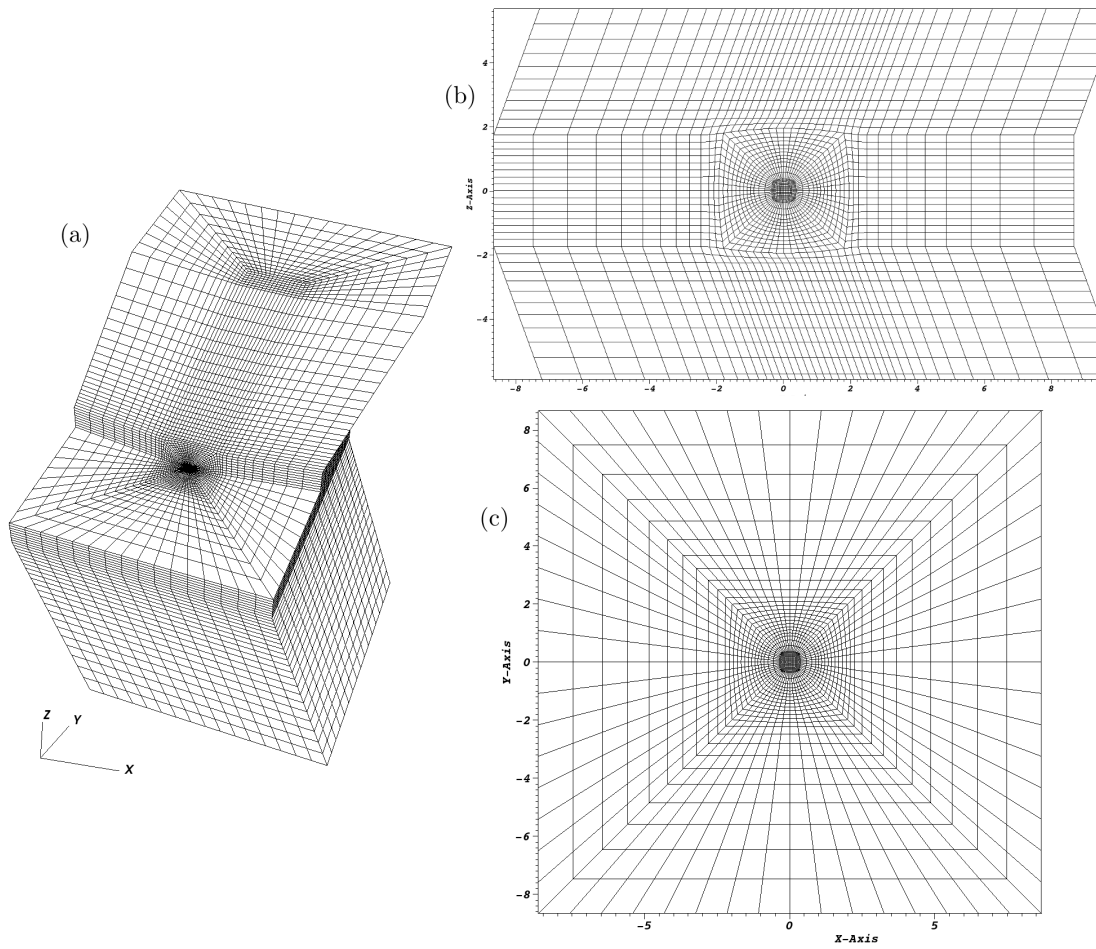
Figure 8.10.: Tilted sphere mesh for the neutral gas cloud test, (a) 3D view, (b) side view at $y = 0$, (c) top view at $z = 0$.
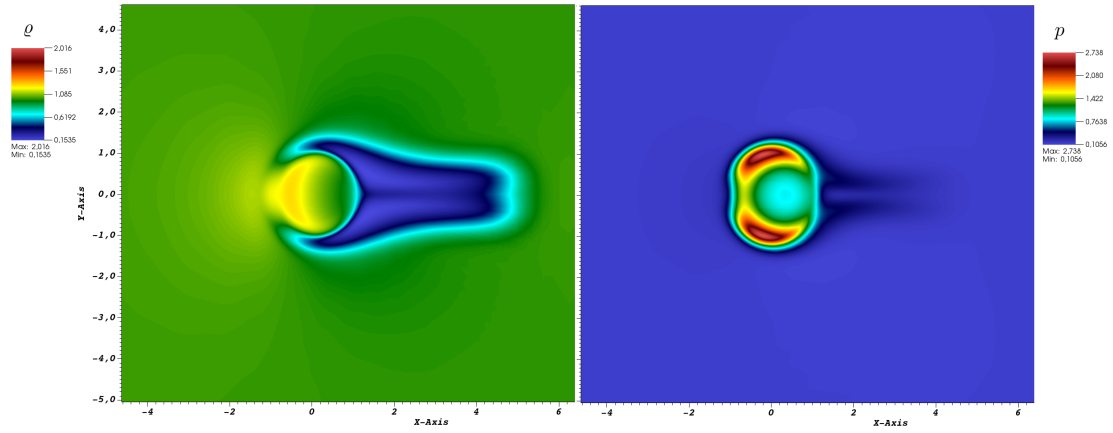
Figure 8.11.: Density (left) and pressure (right) at $z = 0$ and $T = 5$ for the spherical neutral gas cloud test computed by the ES DGSEM with artificial viscosity and $N = 3$.

Figure 8.12.: Alfvén wings in B_1 (left) and v_1 (right) at $y = 0$ and $T = 5$ for the spherical neutral gas cloud test computed by the ES DGSEM with artificial viscosity and $N = 3$.

Finally, we consider the same B_1 and v_1 profile slices as before, which we obtain by slicing through the final approximations at $y = 0, z = 5$ as well as $x = 1, z = 5$ and $x = 2, z = 10$. Since there is no analytical reference solution available for the spherical setup, we solely present the profiles of both DG approximations and the one computed by the ZEUS solver in Figures 8.13 - 8.15.
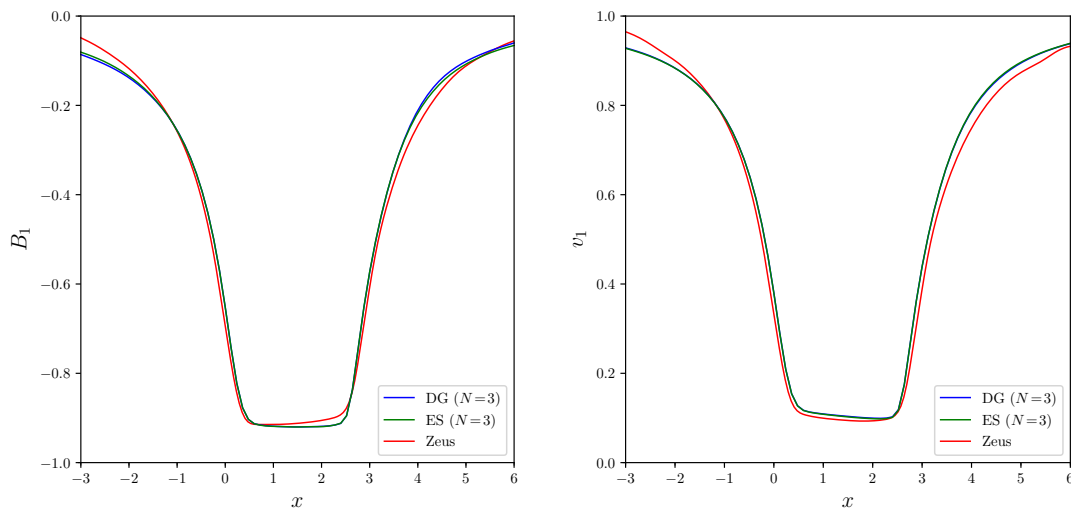
Figure 8.13.: Profile comparison of B_1 (left) and v_1 (right) at $y = 0, z = 5$ and $T = 5$ for the spherical neutral gas cloud test.

In all six plots we see, that the three different approximations are relatively close to each other. Even though the DG results are more dissipative for v_1 inside the Alfvén wing (Fig. 8.13 and 8.14), they are less dissipative close to the borders of the wing (Fig. 8.15). Explanations for this behavior are the weaker shocks and the finer discretization by more elements in contrast to the cylindrical problem. We note again, that there are configurations possible with less artificial viscosity, for which the standard scheme crashes, but the ES DGSEM successfully runs through. However, we adjusted the artificial viscosity for both DG simulations such that stability, no spurious oscillations and a fair comparison are ensured.

Even though we increased the number of mesh elements for the DG simulations, we still found a significant speed-up in runtime compared to the ZEUS simulation. This result together with the high-order accuracy in smooth areas, the increased robustness of the entropy stable discretization and the geometrical flexibility are essential advantages of the ES DGSEM presented herein. Especially, we verified, that the novel method is indeed applicable to real space physics problems, too.

Figure 8.14.: Profile comparison of B_1 (left) and v_1 (right) at $x = 1, z = 5$ and $T = 5$ for the spherical neutral gas cloud test.
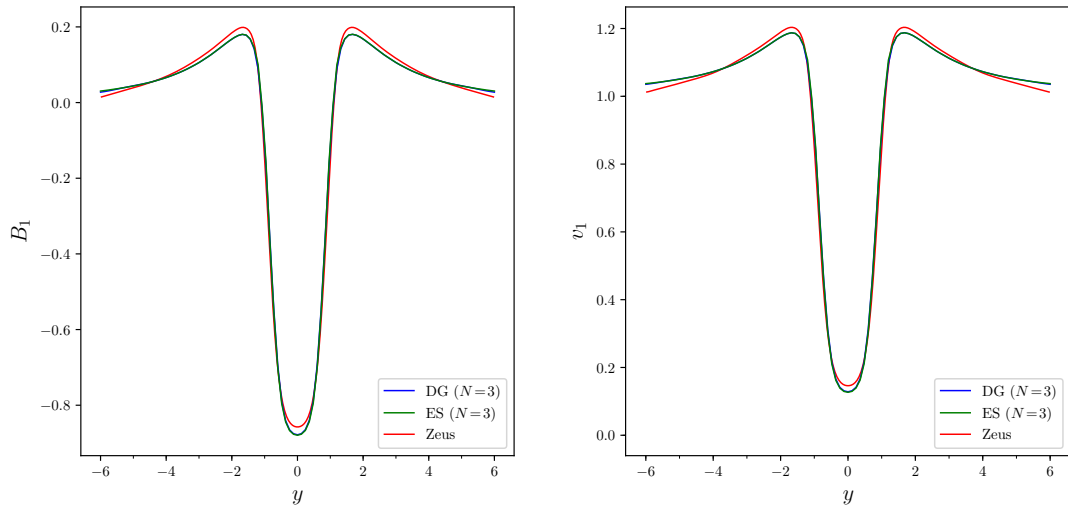
Figure 8.15.: Profile comparison of B_1 (left) and v_1 (right) at $x = 2, z = 10$ and $T = 5$ for the spherical neutral gas cloud test.

9. Conclusions and outlook

The major goals of this thesis were the development of an entropy stable discontinuous Galerkin method for the three-dimensional resistive MHD equations and its application to a real space physics setup. In this regard, the numerical method has been designed such that it could operate on complex curved geometries and evolving shocks could be handled sufficiently well.

In order to construct the novel entropy stable nodal DG scheme we first investigated the continuous entropic properties of the underlying system in order to demonstrate that the resistive GLM-MHD equations satisfy the entropy inequality. This also provided guidance for the semi-discrete analysis, where we carefully split the different terms in the DGSEM and analyzed the individual discrete entropy contributions step-by-step. Special attention has been given to the discretizations of the non-conservative Powell and the GLM terms as well as the curvilinear nature of the elements and the resistive parts. The key ingredients establishing entropy stability for the DGSEM are the split formulation based on diagonal norm SBP operators, the discrete satisfaction of the metric identities and specific discretizations of the numerical fluxes and non-conservative terms inside the volume integrals as well as at interfaces connecting elements. Combining all these components led to an entropy stable nodal DG method for the resistive GLM-MHD equations.

Furthermore, we extended the resulting ES DGSEM by several shock capturing approaches to stabilize the approximation against spurious oscillations caused by high-order interpolations of discontinuities inside the volume. We first introduced artificial viscosity based on the detector by Persson and Peraire to the system [106] and showed that this modification maintains the entropy stability of the scheme. Albeit unrelated to the entropy analysis, we presented a multi-element version of the SIAC filter constructed from Dirac-delta kernels as an alternative shock capturing strategy. For the worst case scenario we further suggested the positivity preserving limiter of Shu et al. [146].

Advantageously, the ES DGSEM naturally inherits the HPC capabilities of discontinuous Galerkin methods as no additional communication between elements is required. We broadly discussed the parallelization of the scheme together with some helpful notes on the actual implementation. In doing so, we have introduced the open source framework `FLUXO` that implements the high-order, entropy stable, nodal DGSEM for the resistive GLM-MHD equations.

Most importantly, we validated our theoretical analysis with several numerical results. In particular, we showed that the entropy stable DGSEM solver described in this

thesis is high-order accurate on curvilinear meshes. We also verified the entropy conservative nature as well as the GLM divergence cleaning of the underlying scheme for the ideal part of the equations on two-dimensional Cartesian and on three-dimensional curvilinear meshes. Finally, we provided numerical tests that revealed significant improvement in the robustness of the entropy stable discretization with hyperbolic divergence cleaning compared to the standard DGSEM.

The applicability of the entropy stable DG solver to real space physics problems was demonstrated in the final chapter. Here, we used the novel entropy stable DG solver to simulate sub-alfvénic plasma interactions in the atmosphere of Jupiter's Galilean moon Io. Even though we did not take all the relevant physical processes into account, we were able to reproduce the evolution of the northern and southern Alfvén wings developing inside Io's plasma torus as observed by several spacecraft flybys. We compared our results to an analytical profile of a simplified problem as well as to other numerical simulations to find, that the entropy stable DGSEM indeed supplies physically meaningful solutions.

An extension of the neutral gas cloud problem by incorporating more physics is one desirable aim for future projects. Especially, the implementation of inner boundary conditions to represent the non-conductive surface of Io would be a promising step towards more realistic simulations. In addition, the internal production and loss of plasma as well as an improved description of the atmosphere including inhomogeneities like water plumes would update the current solver significantly. With such a code, physicists could numerically model rotational discontinuities as they are provided by observation data and reason the existence of plumes for e.g. Enceladus or Europa.

Moreover, there are still some theoretical gaps to fill. Most importantly, the closure of discretely guaranteed positive density and pressure is essential to complete the entire entropy analysis. Investigating the entropic properties of the SIAC filter and augmenting it to curvilinear elements could also be pursued. However, one of the most pressing questions for discontinuous Galerkin approximations is to find a general and reliable treatment of shocks.

A. Appendix

A.1. Dissipation matrices for entropy variables

In this section we explicitly state the missing block matrices necessary to define the diffusion terms for the entropy stable approximation of the resistive GLM-MHD equations from Lemma 2:

$$
\mathsf{K}_{12} = \frac{1}{w_5}
\begin{pmatrix}
0 & 0 & 0 & 0 & 0 & 0 & 0 & 0 & 0 \\
0 & 0 & \frac{2\mu_{\mathrm{NS}}}{3} & 0 & -\frac{2\mu_{\mathrm{NS}}w_3}{3w_5} & 0 & 0 & 0 & 0 \\
0 & -\mu_{\mathrm{NS}} & 0 & 0 & \frac{\mu_{\mathrm{NS}}w_2}{w_5} & 0 & 0 & 0 & 0 \\
0 & 0 & 0 & 0 & 0 & 0 & 0 & 0 & 0 \\
0 & \frac{\mu_{\mathrm{NS}}w_3}{w_5} & -\frac{2\mu_{\mathrm{NS}}w_2}{3w_5} & 0 & -\frac{\mu_{\mathrm{NS}}w_2w_3}{3w_5^2} & 0 & 0 & 0 & 0 \\
0 & 0 & 0 & 0 & \frac{\mu_{\mathrm{R}}w_6w_7}{w_5^2} & -\frac{\mu_{\mathrm{R}}w_7}{w_5} & 0 & 0 & 0 \\
0 & 0 & 0 & 0 & 0 & 0 & 0 & 0 & 0 \\
0 & 0 & 0 & 0 & -\frac{\mu_{\mathrm{R}}w_6}{w_5} & \mu_{\mathrm{R}} & 0 & 0 & 0 \\
0 & 0 & 0 & 0 & 0 & 0 & 0 & 0 & 0
\end{pmatrix}
\tag{A.1}
$$

$$
\mathsf{K}_{13} = \frac{1}{w_5}
\begin{pmatrix}
0 & 0 & 0 & 0 & 0 & 0 & 0 & 0 & 0 \\
0 & 0 & 0 & \frac{2\mu_{\mathrm{NS}}}{3} & -\frac{2\mu_{\mathrm{NS}}w_4}{3w_5} & 0 & 0 & 0 & 0 \\
0 & 0 & 0 & 0 & 0 & 0 & 0 & 0 & 0 \\
0 & -\mu_{\mathrm{NS}} & 0 & 0 & \frac{\mu_{\mathrm{NS}}w_2}{w_5} & 0 & 0 & 0 & 0 \\
0 & \frac{\mu_{\mathrm{NS}}w_4}{w_5} & 0 & -\frac{2\mu_{\mathrm{NS}}w_2}{3w_5} & -\frac{\mu_{\mathrm{NS}}w_2w_4}{3w_5^2} + \frac{\mu_{\mathrm{R}}w_6w_8}{w_5^2} & -\frac{\mu_{\mathrm{R}}w_8}{w_5} & 0 & 0 & 0 \\
0 & 0 & 0 & 0 & 0 & 0 & 0 & 0 & 0 \\
0 & 0 & 0 & 0 & 0 & 0 & 0 & 0 & 0 \\
0 & 0 & 0 & 0 & -\frac{\mu_{\mathrm{R}}w_6}{w_5} & \mu_{\mathrm{R}} & 0 & 0 & 0 \\
0 & 0 & 0 & 0 & 0 & 0 & 0 & 0 & 0
\end{pmatrix}
\tag{A.2}
$$

$$
\mathsf{K}_{21} = \frac{1}{w_5}
\begin{pmatrix}
0 & 0 & 0 & 0 & 0 & 0 & 0 & 0 & 0 \\
0 & 0 & -\mu_{\mathrm{NS}} & 0 & \frac{\mu_{\mathrm{NS}} w_3}{w_5} & 0 & 0 & 0 & 0 \\
0 & \frac{2\mu_{\mathrm{NS}}}{3} & 0 & 0 & -\frac{2\mu_{\mathrm{NS}} w_2}{3 w_5} & 0 & 0 & 0 & 0 \\
0 & 0 & 0 & 0 & 0 & 0 & 0 & 0 & 0 \\
0 & -\frac{2\mu_{\mathrm{NS}} w_3}{3 w_5} & \frac{\mu_{\mathrm{NS}} w_2}{w_5} & 0 & -\frac{\mu_{\mathrm{NS}} w_2 w_3}{3 w_5^2} & 0 & 0 & 0 & 0 \\
0 & 0 & 0 & 0 & \frac{\mu_{\mathrm{R}} w_6 w_7}{w_5^2} & 0 & -\frac{\mu_{\mathrm{R}} w_6}{w_5} & 0 & 0 \\
0 & 0 & 0 & 0 & -\frac{\mu_{\mathrm{R}} w_7}{w_5} & 0 & \mu_{\mathrm{R}} & 0 & 0 \\
0 & 0 & 0 & 0 & 0 & 0 & 0 & 0 & 0 \\
0 & 0 & 0 & 0 & 0 & 0 & 0 & 0 & 0
\end{pmatrix}
\tag{A.3}
$$

$$
\mathsf{K}_{22} = \frac{1}{w_5}
\begin{pmatrix}
0 & 0 & 0 & 0 & 0 & 0 & 0 & 0 & 0 \\
0 & -\mu_{\mathrm{NS}} & 0 & 0 & \frac{\mu_{\mathrm{NS}} w_2}{w_5} & 0 & 0 & 0 & 0 \\
0 & 0 & -\frac{4\mu_{\mathrm{NS}}}{3} & 0 & \frac{4\mu_{\mathrm{NS}} w_3}{3 w_5} & 0 & 0 & 0 & 0 \\
0 & 0 & 0 & -\mu_{\mathrm{NS}} & \frac{\mu_{\mathrm{NS}} w_4}{w_5} & 0 & 0 & 0 & 0 \\
0 & \frac{\mu_{\mathrm{NS}} w_2}{w_5} & \frac{4\mu_{\mathrm{NS}} w_3}{3 w_5} & \frac{\mu_{\mathrm{NS}} w_4}{w_5} & -\frac{\mu_{\mathrm{NS}} w_2^2}{w_5^2} - \frac{4\mu_{\mathrm{NS}} w_3^2}{3 w_5^2} - \frac{\mu_{\mathrm{NS}} w_4^2}{w_5^2} + \frac{\kappa}{R w_5} - \frac{\mu_{\mathrm{R}} w_6^2}{w_5^2} - \frac{\mu_{\mathrm{R}} w_8^2}{w_5^2} & \frac{\mu_{\mathrm{R}} w_6}{w_5} & 0 & \frac{\mu_{\mathrm{R}} w_8}{w_5} & 0 \\
0 & 0 & 0 & 0 & \frac{\mu_{\mathrm{R}} w_6}{w_5} & -\mu_{\mathrm{R}} & 0 & 0 & 0 \\
0 & 0 & 0 & 0 & 0 & 0 & 0 & 0 & 0 \\
0 & 0 & 0 & 0 & \frac{\mu_{\mathrm{R}} w_8}{w_5} & 0 & 0 & -\mu_{\mathrm{R}} & 0 \\
0 & 0 & 0 & 0 & 0 & 0 & 0 & 0 & 0
\end{pmatrix}
\tag{A.4}
$$

$$
\mathsf{K}_{23} = \frac{1}{w_5}
\begin{pmatrix}
0 & 0 & 0 & 0 & 0 & 0 & 0 & 0 & 0 \\
0 & 0 & 0 & 0 & 0 & 0 & 0 & 0 & 0 \\
0 & 0 & 0 & \frac{2\mu_{\mathrm{NS}}}{3} & -\frac{2\mu_{\mathrm{NS}} w_4}{3 w_5} & 0 & 0 & 0 & 0 \\
0 & 0 & -\mu_{\mathrm{NS}} & 0 & \frac{\mu_{\mathrm{NS}} w_3}{w_5} & 0 & 0 & 0 & 0 \\
0 & 0 & \frac{\mu_{\mathrm{NS}} w_4}{w_5} & -\frac{2\mu_{\mathrm{NS}} w_3}{3 w_5} & -\frac{\mu_{\mathrm{NS}} w_3 w_4}{3 w_5^2} + \frac{\mu_{\mathrm{R}} w_7 w_8}{w_5^2} & 0 & -\frac{\mu_{\mathrm{R}} w_8}{w_5} & 0 & 0 \\
0 & 0 & 0 & 0 & 0 & 0 & 0 & 0 & 0 \\
0 & 0 & 0 & 0 & 0 & 0 & 0 & 0 & 0 \\
0 & 0 & 0 & 0 & -\frac{\mu_{\mathrm{R}} w_7}{w_5} & 0 & \mu_{\mathrm{R}} & 0 & 0 \\
0 & 0 & 0 & 0 & 0 & 0 & 0 & 0 & 0
\end{pmatrix}
\tag{A.5}
$$

$$\mathsf{K}_{31} = \frac{1}{w_5}\begin{pmatrix}
0 & 0 & 0 & 0 & 0 & 0 & 0 & 0 & 0 \\
0 & 0 & 0 & -\mu_{\mathrm{NS}} & \frac{\mu_{\mathrm{NS}}w_4}{w_5} & 0 & 0 & 0 & 0 \\
0 & 0 & 0 & 0 & 0 & 0 & 0 & 0 & 0 \\
0 & \frac{2\mu_{\mathrm{NS}}}{3} & 0 & 0 & -\frac{2\mu_{\mathrm{NS}}w_2}{3w_5} & 0 & 0 & 0 & 0 \\
0 & -\frac{2\mu_{\mathrm{NS}}w_4}{3w_5} & 0 & \frac{\mu_{\mathrm{NS}}w_2}{w_5} & -\frac{\mu_{\mathrm{NS}}w_2 w_4}{3w_5^2} + \frac{\mu_{\mathrm{R}}w_6 w_8}{w_5^2} & 0 & 0 & -\frac{\mu_{\mathrm{R}}w_6}{w_5} & 0 \\
0 & 0 & 0 & 0 & -\frac{\mu_{\mathrm{R}}w_8}{w_5} & 0 & 0 & \mu_{\mathrm{R}} & 0 \\
0 & 0 & 0 & 0 & 0 & 0 & 0 & 0 & 0 \\
0 & 0 & 0 & 0 & 0 & 0 & 0 & 0 & 0 \\
0 & 0 & 0 & 0 & 0 & 0 & 0 & 0 & 0
\end{pmatrix} \quad \text{(A.6)}$$

$$\mathsf{K}_{32} = \frac{1}{w_5}\begin{pmatrix}
0 & 0 & 0 & 0 & 0 & 0 & 0 & 0 & 0 \\
0 & 0 & 0 & 0 & 0 & 0 & 0 & 0 & 0 \\
0 & 0 & 0 & -\mu_{\mathrm{NS}} & \frac{\mu_{\mathrm{NS}}w_4}{w_5} & 0 & 0 & 0 & 0 \\
0 & 0 & \frac{2\mu_{\mathrm{NS}}}{3} & 0 & -\frac{2\mu_{\mathrm{NS}}w_3}{3w_5} & 0 & 0 & 0 & 0 \\
0 & 0 & -\frac{2\mu_{\mathrm{NS}}w_4}{3w_5} & \frac{\mu_{\mathrm{NS}}w_3}{w_5} & -\frac{\mu_{\mathrm{NS}}w_3 w_4}{3w_5^5} + \frac{\mu_{\mathrm{R}}w_7 w_8}{w_5^2} & 0 & 0 & -\frac{\mu_{\mathrm{R}}w_7}{w_5} & 0 \\
0 & 0 & 0 & 0 & 0 & 0 & 0 & 0 & 0 \\
0 & 0 & 0 & 0 & -\frac{\mu_{\mathrm{R}}w_8}{w_5} & 0 & 0 & \mu_{\mathrm{R}} & 0 \\
0 & 0 & 0 & 0 & 0 & 0 & 0 & 0 & 0 \\
0 & 0 & 0 & 0 & 0 & 0 & 0 & 0 & 0
\end{pmatrix} \quad \text{(A.7)}$$

$$\mathsf{K}_{33} = \frac{1}{w_5}\begin{pmatrix}
0 & 0 & 0 & 0 & 0 & 0 & 0 & 0 & 0 \\
0 & -\mu_{\mathrm{NS}} & 0 & 0 & \frac{\mu_{\mathrm{NS}}w_2}{w_5} & 0 & 0 & 0 & 0 \\
0 & 0 & -\mu_{\mathrm{NS}} & 0 & \frac{\mu_{\mathrm{NS}}w_3}{w_5} & 0 & 0 & 0 & 0 \\
0 & 0 & 0 & -\frac{4\mu_{\mathrm{NS}}}{3} & \frac{4\mu_{\mathrm{NS}}w_4}{3w_5} & 0 & 0 & 0 & 0 \\
0 & \frac{\mu_{\mathrm{NS}}w_2}{w_5} & \frac{\mu_{\mathrm{NS}}w_3}{w_5} & \frac{4\mu_{\mathrm{NS}}w_4}{3w_5} & -\frac{\mu_{\mathrm{NS}}w_2^2}{w_5^2} - \frac{\mu_{\mathrm{NS}}w_3^2}{w_5^2} - \frac{4\mu_{\mathrm{NS}}w_4^2}{3w_5^2} + \frac{\kappa}{Rw_5} - \frac{\mu_{\mathrm{R}}w_6^2}{w_5^2} - \frac{\mu_{\mathrm{R}}w_6^2}{w_5^2} & \frac{\mu_{\mathrm{R}}w_6}{w_5} & \frac{\mu_{\mathrm{R}}w_7}{w_5} & 0 & 0 \\
0 & 0 & 0 & 0 & \frac{\mu_{\mathrm{R}}w_6}{w_5} & -\mu_{\mathrm{R}} & 0 & 0 & 0 \\
0 & 0 & 0 & 0 & \frac{\mu_{\mathrm{R}}w_7}{w_5} & 0 & -\mu_{\mathrm{R}} & 0 & 0 \\
0 & 0 & 0 & 0 & 0 & 0 & 0 & 0 & 0 \\
0 & 0 & 0 & 0 & 0 & 0 & 0 & 0 & 0
\end{pmatrix} \quad \text{(A.8)}$$

3

A.2. Dissipation matrices for nine-wave ES numerical flux

Here, we state the explicit form of the necessary matrices in the entropy stable numerical interface flux with the nine-wave dissipation term (4.48). First, we recall the dissipation matrix, which reads

$$\Lambda_n^{\mathrm{NW}} = \mathsf{R}|\hat{\Lambda}|\mathsf{T}\mathsf{R}^T \tag{A.9}$$

and contains the yet undefined matrices $\mathsf{R}, \hat{\Lambda}$ and T. Due to the rotational invariance of the numerical flux functions, it is sufficient to derive these matrices only for the x-direction.

The mean state for the diagonal scaling matrix is

$$\mathsf{T} = \mathrm{diag}\left(\frac{1}{2\gamma\varrho^{\ln}}, \frac{1}{4\,\{\!\{\beta\}\!\}\,(\varrho^{\ln})^2}, \frac{1}{2\gamma\varrho^{\ln}}, \frac{1}{4\,\{\!\{\beta\}\!\}}, \frac{\varrho^{\ln}(\gamma-1)}{\gamma}, \frac{1}{4\,\{\!\{\beta\}\!\}}, \frac{1}{2\gamma\varrho^{\ln}}, \frac{1}{4\,\{\!\{\beta\}\!\}\,(\varrho^{\ln})^2}, \frac{1}{2\gamma\varrho^{\ln}}\right), \tag{A.10}$$

and the diagonal matrix of eigenvalues for the resistive GLM-MHD system in the first spatial direction is

$$\hat{\Lambda} = \mathrm{diag}\left(\hat{\boldsymbol{\lambda}}\right) \tag{A.11}$$

with

$$\hat{\boldsymbol{\lambda}} = \begin{pmatrix} \hat{\lambda}_{+f} \\ \hat{\lambda}_{+a} \\ \hat{\lambda}_{+s} \\ \hat{\lambda}_{+\psi} \\ \hat{\lambda}_{E} \\ \hat{\lambda}_{-\psi} \\ \hat{\lambda}_{-s} \\ \hat{\lambda}_{-a} \\ \hat{\lambda}_{-f} \end{pmatrix} = \begin{pmatrix} \{\!\{v_1\}\!\} + \hat{c}_f \\ \{\!\{v_1\}\!\} + \hat{c}_a \\ \{\!\{v_1\}\!\} + \hat{c}_s \\ \{\!\{v_1\}\!\} + c_h \\ \{\!\{v_1\}\!\} \\ \{\!\{v_1\}\!\} - c_h \\ \{\!\{v_1\}\!\} - \hat{c}_s \\ \{\!\{v_1\}\!\} - \hat{c}_a \\ \{\!\{v_1\}\!\} - \hat{c}_f \end{pmatrix}. \tag{A.12}$$

For the computation of the average Alfvén and magneto-acoustic sound speeds

$$\hat{c}_a^2 = \bar{b}_1^2, \quad \hat{c}_{f,s}^2 = \frac{1}{2}\left((\bar{a}^2 + \bar{b}^2) \pm \sqrt{(\bar{a}^2 + \bar{b}^2)^2 - 4\bar{a}^2\bar{b}_1^2}\right) \tag{A.13}$$

we introduce the additional mean values

$$\bar{a}^2 = \gamma\frac{\bar{p}}{\varrho^{\ln}}, \quad \bar{b}_{1,2,3}^2 = \frac{\{\!\{B_{1,2,3}\}\!\}^2}{\varrho^{\ln}}, \quad \bar{b}^2 = \bar{b}_1^2 + \bar{b}_2^2 + \bar{b}_3^2. \tag{A.14}$$

Due to the complicated structure of the eigenvectors, we have to define even more specific

averages for several convenience variables, i.e.

$$\hat{\Psi}_{\pm s} = \frac{\hat{\alpha}_s \varrho^{\ln} \overline{\|\vec{v}\|^2}}{2} - a^\beta \hat{\alpha}_f \varrho^{\ln} \bar{b}_\perp + \frac{\hat{\alpha}_s \varrho^{\ln} (a^{\ln})^2}{\gamma - 1} \pm \hat{\alpha}_s \hat{c}_s \varrho^{\ln} \{\!\{v_1\}\!\} \pm \hat{\alpha}_f \hat{c}_f \varrho^{\ln} \sigma(\bar{b}_1)(\{\!\{v_2\}\!\} \bar{\chi}_2 + \{\!\{v_3\}\!\} \bar{\chi}_3),$$

$$\hat{\Psi}_{\pm f} = \frac{\hat{\alpha}_f \varrho^{\ln} \overline{\|\vec{v}\|^2}}{2} + a^\beta \hat{\alpha}_s \varrho^{\ln} \bar{b}_\perp + \frac{\hat{\alpha}_f \varrho^{\ln} (a^{\ln})^2}{\gamma - 1} \pm \hat{\alpha}_f \hat{c}_f \varrho^{\ln} \{\!\{v_1\}\!\} \mp \hat{\alpha}_s \hat{c}_s \varrho^{\ln} \sigma(\bar{b}_1)(\{\!\{v_2\}\!\} \bar{\chi}_2 + \{\!\{v_3\}\!\} \bar{\chi}_3)$$

$$\text{(A.15)}$$

with

$$\overline{\|\vec{v}\|^2} = 2\left(\{\!\{v_1\}\!\}^2 + \{\!\{v_2\}\!\}^2 + \{\!\{v_3\}\!\}^2\right) - \left(\{\!\{v_1^2\}\!\} + \{\!\{v_2^2\}\!\} + \{\!\{v_3^2\}\!\}\right),$$

$$(a^{\ln})^2 = \gamma \frac{p^{\ln}}{\varrho^{\ln}}, \quad (a^\beta)^2 = \gamma \frac{1}{2\{\!\{\beta\}\!\}}, \quad \bar{b}_\perp^2 = \bar{b}_2^2 + \bar{b}_3^2, \quad \bar{\chi}_{2,3} = \frac{\bar{b}_{2,3}}{\bar{b}_\perp},$$

$$\hat{\alpha}_f^2 = \frac{\bar{a}^2 - \hat{c}_s^2}{\hat{c}_f^2 - \hat{c}_s^2}, \quad \hat{\alpha}_s^2 = \frac{\hat{c}_f^2 - \bar{a}^2}{\hat{c}_f^2 - \hat{c}_s^2}, \quad \sigma(\omega) = \begin{cases} +1 & \text{if } \omega \geq 0, \\ -1 & \text{otherwise} \end{cases}.$$

$$\text{(A.16)}$$

Finally, we present the average of the right eigenvector matrix in the first spatial direction

$$\mathsf{R} = [\, \mathbf{r}_{+f} \,|\, \mathbf{r}_{+a} \,|\, \mathbf{r}_{+s} \,|\, \mathbf{r}_{+\psi} \,|\, \mathbf{r}_E \,|\, \mathbf{r}_{-\psi} \,|\, \mathbf{r}_{-s} \,|\, \mathbf{r}_{-a} \,|\, \mathbf{r}_{-f} \,], \tag{A.17}$$

where each of the discrete eigenvectors are

$$\mathbf{r}_E = \begin{bmatrix} 1 \\ \{\!\{v_1\}\!\} \\ \{\!\{v_2\}\!\} \\ \{\!\{v_3\}\!\} \\ \frac{1}{2}\overline{\|\vec{v}\|^2} \\ 0 \\ 0 \\ 0 \\ 0 \end{bmatrix}, \quad \mathbf{r}_{\pm\psi} = \begin{bmatrix} 0 \\ 0 \\ 0 \\ 0 \\ \{\!\{B_1\}\!\} \pm \{\!\{\psi\}\!\} \\ 1 \\ 0 \\ 0 \\ \pm 1 \end{bmatrix}, \quad \mathbf{r}_{\pm a} = \begin{bmatrix} 0 \\ 0 \\ \pm \varrho^{\ln}\sqrt{\{\!\{\varrho\}\!\}}\, \bar{\chi}_3 \\ \mp \varrho^{\ln}\sqrt{\{\!\{\varrho\}\!\}}\, \bar{\chi}_2 \\ \mp \varrho^{\ln}\sqrt{\{\!\{\varrho\}\!\}}(\bar{\chi}_2 \{\!\{v_3\}\!\} - \bar{\chi}_3 \{\!\{v_2\}\!\}) \\ 0 \\ -\varrho^{\ln}\bar{\chi}_3 \\ \varrho^{\ln}\bar{\chi}_2 \\ 0 \end{bmatrix},$$

$$\text{(A.18)}$$

$$\mathbf{r}_{\pm\mathrm{f}} = \begin{bmatrix} \hat{\alpha}_{\mathrm{f}}\varrho^{\ln} \\ \hat{\alpha}_{\mathrm{f}}\varrho^{\ln}(\{\!\{v_1\}\!\} \pm \hat{c}_f) \\ \varrho^{\ln}\left(\hat{\alpha}_{\mathrm{f}}\{\!\{v_2\}\!\} \mp \hat{\alpha}_{\mathrm{s}}\hat{c}_{\mathrm{s}}\bar{\chi}_2\sigma(\bar{b}_1)\right) \\ \varrho^{\ln}\left(\hat{\alpha}_{\mathrm{f}}\{\!\{v_3\}\!\} \mp \hat{\alpha}_{\mathrm{s}}\hat{c}_{\mathrm{s}}\bar{\chi}_3\sigma(\bar{b}_1)\right) \\ \hat{\Psi}_{\pm\mathrm{f}} \\ 0 \\ \hat{\alpha}_{\mathrm{s}}a^{\beta}\bar{\chi}_2\sqrt{\varrho^{\ln}} \\ \hat{\alpha}_{\mathrm{s}}a^{\beta}\bar{\chi}_3\sqrt{\varrho^{\ln}} \\ 0 \end{bmatrix}, \qquad \mathbf{r}_{\pm\mathrm{s}} = \begin{bmatrix} \hat{\alpha}_{\mathrm{s}}\varrho^{\ln} \\ \hat{\alpha}_{\mathrm{s}}\varrho^{\ln}\left(\{\!\{v_1\}\!\} \pm \hat{c}_{\mathrm{s}}\right) \\ \varrho^{\ln}\left(\hat{\alpha}_{\mathrm{s}}\{\!\{v_2\}\!\} \pm \hat{\alpha}_{\mathrm{f}}\hat{c}_{\mathrm{f}}\bar{\chi}_2\sigma(\bar{b}_1)\right) \\ \varrho^{\ln}\left(\hat{\alpha}_{\mathrm{s}}\{\!\{v_3\}\!\} \pm \hat{\alpha}_{\mathrm{f}}\hat{c}_{\mathrm{f}}\bar{\chi}_3\sigma(\bar{b}_1)\right) \\ \hat{\Psi}_{\pm\mathrm{s}} \\ 0 \\ -\hat{\alpha}_{\mathrm{f}}a^{\beta}\bar{\chi}_2\sqrt{\varrho^{\ln}} \\ -\hat{\alpha}_{\mathrm{f}}a^{\beta}\bar{\chi}_3\sqrt{\varrho^{\ln}} \\ 0 \end{bmatrix}. \tag{A.19}$$

We note, that in the actual implementation, one has to be careful when evaluating certain averages. Especially, numerical cancellation errors, square roots of negative values and division by zero have to be avoided numerically. More details on the nine-wave solver can be found in [34, 141].

Bibliography

[1] Viktor Achter, Stefan Borowski, Lech Nieroda, Lars Packschies, and Volker Winkelmann. Cheops. *Cologne High Efficient Operating Platform for Science, Regional Computing Centre Cologne, University of Cologne*, 2013.

[2] Shahrouz Aliabadi, Shuangzhang Tu, and Marvin Watts. An alternative to limiter in discontinous Galerrkin finite element method for simulation of compressible flows. In *42nd AIAA Aerospace Sciences Meeting and Exhibit*, page 76, 2004.

[3] Christoph Altmann. *Explicit discontinuous Galerkin methods for magnetohydrodynamics*. PhD thesis, University of Struttgart, 2012.

[4] Srinivas Aluru and Fatih Erdogan Sevilgen. Parallel domain decomposition and load balancing using space-filling curves. In *High-Performance Computing, 1997. Proceedings. Fourth International Conference on*, pages 230–235. IEEE, 1997.

[5] Luis Alvarez and Luis Mazorra. Signal and image restoration using shock filters and anisotropic diffusion. *SIAM Journal on Numerical Analysis*, 31(2):590–605, 1994.

[6] Mohit Arora and Philip L. Roe. A well-behaved TVD limiter for high-resolution calculations of unsteady flow. *Journal of Computational Physics*, 132(1):3–11, 1997.

[7] Dinshaw S. Balsara and Chi-Wang Shu. Monotonicity preserving weighted essentially non-oscillatory schemes with increasingly high order of accuracy. *Journal of Computational Physics*, 160(2):405–452, 2000.

[8] Dinshaw S. Balsara and Daniel Spicer. A staggered mesh algorithm using high order Godunov fluxes to ensure solenoidal magnetic fields in magnetohydrodynamic simulations. *Journal of Computational Physics*, 149(2):270–292, 1999.

[9] Timothy J. Barth. Numerical methods for gasdynamic systems on unstructured meshes. In Dietmar Kröner, Mario Ohlberger, and Christian Rohde, editors, *An Introduction to Recent Developments in Theory and Numerics for Conservation Laws*, volume 5 of *Lecture Notes in Computational Science and Engineering*, pages 195–285. Springer Berlin Heidelberg, 1999.

[10] F. Bassi and S. Rebay. A high order accurate discontinuous finite element method for the numerical solution of the compressible Navier-Stokes equations. *Journal of Computational Physics*, 131:267–279, 1997.

[11] Nicholas A. Battista. An introduction to magnetohydrodynamics. *Stony Brook University, New York*, 2010.

[12] Dieter Biskamp. *Magnetohydrodynamic turbulence.* Cambridge University Press, 2003.

[13] Aljona Bloecker, Joachim Saur, and Lorenz Roth. Europa's plasma interaction with an inhomogeneous atmosphere: Development of Alfvén winglets within the Alfvén wings. *Journal of Geophysical Research: Space Physics*, 121(10):9794–9828, 2016.

[14] Aljona Bloecker, Joachim Saur, and Lorenz Roth. Io's plasma interaction with Jupiter's magnetosphere: Influence of global asymmetries in Io's atmosphere and volcanic plumes on the plasma environment. In *AGU Fall Meeting Abstracts*, 2016.

[15] Marvin Bohm, Sven Schermeng, Andrew R. Winters, Gregor J. Gassner, and Gustaaf Jacobs. Multi-element SIAC filter for shock capturing applied to high-order discontinuous Galerkin spectral element methods (working title). 2019.

[16] Marvin Bohm, Andrew R. Winters, Gregor J. Gassner, Dominik Derigs, Florian Hindenlang, and Joachim Saur. An entropy stable nodal discontinuous Galerkin method for the resistive MHD equations. Part I: Theory and numerical verification. *Journal of Computational Physics*, 2018.

[17] M. E. Brachet, M. D. Bustamante, G. Krstulovic, P. D. Mininni, A. Pouquet, and D. Rosenberg. Ideal evolution of MHD turbulence when imposing Taylor-Green symmetries. *Physical Review E*, 87(1):013110, 2013.

[18] J. U. Brackbill and D. C. Barnes. The effect of nonzero $\nabla \cdot B$ on the numerical solution of the magnetohydrodynamic equations. *Journal of Computational Physics*, 35(3):426 – 430, 1980.

[19] Carsten Burstedde, Lucas C. Wilcox, and Omar Ghattas. Scalable algorithms for parallel adaptive mesh refinement on forests of octrees. *SIAM Journal on Scientific Computing*, 33(3):1103–1133, 2011.

[20] M. Carpenter, T. Fisher, E. Nielsen, and S. Frankel. Entropy stable spectral collocation schemes for the Navier–Stokes equations: Discontinuous interfaces. *SIAM Journal on Scientific Computing*, 36(5):B835–B867, 2014.

[21] M. Carpenter and C. Kennedy. Fourth-order $2N$-storage Runge-Kutta schemes. Technical Report NASA TM 109111, NASA Langley Research Center, 1994.

[22] Praveen Chandrashekar, Juan Pablo Gallego-Valencia, and Christian Klingenberg. A Runge-Kutta discontinuous Galerkin scheme for the ideal magnetohydrodynamical model. In *XVI International Conference on Hyperbolic Problems: Theory, Numerics, Applications*, pages 335–344. Springer, 2016.

[23] Praveen Chandrashekar and Christian Klingenberg. Entropy stable finite volume scheme for ideal compressible MHD on 2-D cartesian meshes. *SIAM Journal of Numerical Analysis*, 54(2):1313–1340, 2016.

[24] Yingda Cheng and Chi-Wang Shu. A discontinuous Galerkin finite element method for directly solving the Hamilton-Jacobi equations. *Journal of Computational Physics*, 223:398–415, 2007.

[25] Yue Cheng, Fengyan Li, Jianxian Qiu, and Liwei Xu. Positivity-preserving DG and central DG methods for ideal MHD equations. *Journal of Computational Physics*, 238:255–280, 2013.

[26] Elisabetta Chiodaroli. A counterexample to well-posedness of entropy solutions to the compressible Euler system. *Journal of Hyperbolic Differential Equations*, 11(03):493–519, 2014.

[27] B. Cockburn and C. W. Shu. Runge-Kutta discontinuous Galerkin methods for convection-dominated problems. *Journal of Scientific Computing*, 16(3):173–261, 2001.

[28] Bernardo Cockburn, George E. Karniadakis, and Chi-Wang Shu. The development of discontinuous Galerkin methods. In *Discontinuous Galerkin Methods*, pages 3–50. Springer, 2000.

[29] Peter Alan Davidson. An introduction to magnetohydrodynamics, 2002.

[30] Andreas Dedner, Friedemann Kemm, Dietmar Kröner, C.-D. Munz, Thomas Schnitzer, and Matthias Wesenberg. Hyperbolic divergence cleaning for the MHD equations. *Journal of Computational Physics*, 175(2):645–673, 2002.

[31] Richard O. Dendy. *Plasma physics: An introductory course*. Cambridge University Press, 1995.

[32] Dominik Derigs, Gregor J. Gassner, Stefanie Walch, and Andrew R. Winters. Entropy stable finite volume approximations for ideal magnetohydrodynamics. *Jahresbericht der Deutschen Mathematiker-Vereinigung*, 120(3):153–219, 2018.

[33] Dominik Derigs, Andrew R. Winters, Gregor J. Gassner, and Stefanie Walch. A novel averaging technique for discrete entropy stable dissipation operators for ideal MHD. *Journal of Computational Physics*, 330:624–632, 2016.

[34] Dominik Derigs, Andrew R. Winters, Gregor J. Gassner, Stefanie Walch, and Marvin Bohm. Ideal GLM-MHD: About the entropy consistent nine-wave magnetic field divergence diminishing ideal magnetohydrodynamics equations. *Journal of Computational Physics*, 364:420–467, 2018.

[35] Stefan Duling, Joachim Saur, and Johannes Wicht. Consistent boundary conditions at nonconducting surfaces of planetary bodies: Applications in a new Ganymede MHD model. *Journal of Geophysical Research: Space Physics*, 119(6):4412–4440, 2014.

[36] Pravir Dutt. Stable boundary conditions and difference schemes for Navier-Stokes equations. *SIAM Journal on Numerical Analysis*, 25(2):245–267, 1988.

[37] T. G. Elizarova and M. V. Popov. Numerical simulation of three-dimensional quasi-neutral gas flows based on smoothed magnetohydrodynamic equations. *Computational Mathematics and Mathematical Physics*, 55(8):1330–1345, 2015.

[38] C. R. Evans and J. F. Hawley. Simulation of magnetohydrodynamic flows - A constrained transport method. *Astrophysical Journal*, 332:659–677, September 1988.

[39] Lawrence Evans. A survey of entropy methods for partial differential equations. *Bulletin of the American Mathematical Society*, 41(4):409–438, 2004.

[40] Lawrence Evans. *Partial differential equations*. American Mathematical Society, 2010.

[41] Travis C. Fisher and Mark H. Carpenter. High-order entropy stable finite difference schemes for nonlinear conservation laws: Finite domains. *Journal of Computational Physics*, 252:518–557, 2013.

[42] Travis C. Fisher, Mark H. Carpenter, Jan Nordström, Nail K. Yamaleev, and Charles Swanson. Discretely conservative finite-difference formulations for nonlinear conservation laws in split form: Theory and boundary conditions. *Journal of Computational Physics*, 234:353–375, 2013.

[43] Ulrik S. Fjordholm, Siddhartha Mishra, and Eitan Tadmor. Well-blanaced and energy stable schemes for the shallow water equations with discontiuous topography. *Journal of Computational Physics*, 230(14):5587–5609, 2011.

[44] Ulrik Skre Fjordholm. *High-order accurate entropy stable numerical schemes for hyperbolic conservation laws.* ETH Zurich, 2013.

[45] Jeffrey P. Freidberg. Ideal magnetohydrodynamics. 1987.

[46] Lucas Friedrich, Gero Schnücke, Andrew R. Winters, David C. Fernández, Gregor J. Gassner, and Mark H. Carpenter. Entropy stable space-time discontinuous Galerkin schemes with summation-by-parts property for hyperbolic conservation laws. *arXiv preprint arXiv:1808.08218*, 2018.

[47] Lucas Friedrich, Andrew R. Winters, David C. Del Rey Fernández, Gregor J. Gassner, Matteo Parsani, and Mark H. Carpenter. An entropy stable h/p non-conforming discontinuous Galerkin method with the summation-by-parts property. *Journal of Scientific Computing*, pages 1–37, 2018.

[48] Juan Pablo Gallego-Valencia. *On Runge-Kutta Discontinuous Galerkin Methods for the Compressible Euler Equations and the Ideal Magneto-Hydrodynamical Model.* PhD thesis, Univeristy of Wuerzburg, 2017.

[49] Eric Garnier, Michele Mossi, Pierre Sagaut, Pierre Comte, and Michel Deville. On the use of shock-capturing schemes for large-eddy simulation. *Journal of computational Physics*, 153(2):273–311, 1999.

[50] Gregor J. Gassner. *Discontinuous Galerkin methods for the unsteady compressible Navier-Stokes equations.* 2009.

[51] Gregor J. Gassner. A skew-symmetric discontinuous Galerkin spectral element discretization and its relation to SBP-SAT finite difference methods. *SIAM Journal on Scientific Computing*, 35(3):A1233–A1253, 2013.

[52] Gregor J. Gassner, Florian Hindenlang, and Claus-Dieter Munz. A Runge-Kutta based discontinuous Galerkin method with time accurate local time stepping. *Adaptive High-Order Methods in Computational Fluid Dynamics*, 2:95–118, 2011.

[53] Gregor J. Gassner, Andrew R. Winters, Florian Hindenlang, and David A. Kopriva. The BR1 scheme is stable for the compressible Navier-Stokes equations. *Journal of Scientific Computing (under revision)*, 2017.

[54] Gregor J. Gassner, Andrew R. Winters, and David A. Kopriva. Split form nodal discontinuous Galerkin schemes with summation-by-parts property for the compressible Euler equations. *Journal Of Computational Physics*, 327:39–66, 2016.

[55] S. K. Godunov. Symmetric form of the equations of magnetohydrodynamics. *Numerical Methods for Mechanics of Continuum Medium*, 1:26–34, 1972.

[56] Peter Goldreich and Donald Lynden-Bell. Io, a Jovian unipolar inductor. *The Astrophysical Journal*, 156:59–78, 1969.

[57] David Gottlieb and Chi-Wang Shu. On the Gibbs phenomenon and its resolution. *SIAM review*, 39(4):644–668, 1997.

[58] Sigal Gottlieb, Chi-Wang Shu, and Eitan Tadmor. Strong stability-preserving high-order time discretization methods. *SIAM Review*, 43(1):89–112, 2001.

[59] William D. Gropp, William Gropp, Ewing Lusk, Anthony Skjellum, and Argonne Distinguished Fellow Emeritus Ewing Lusk. *Using MPI: Portable parallel programming with the message-passing interface*, volume 1. MIT press, 1999.

[60] Thomas Guillet, Rüdiger Pakmor, Volker Springel, Praveen Chandrashekar, and Christian Klingenberg. High-order magnetohydrodynamics for astrophysics with an adaptive mesh refinement discontinuous Galerkin scheme. *arXiv preprint arXiv:1806.02343*, 2018.

[61] E. Hairer, S. P. Nørsett, and G. Wanner. *Solving Ordinary Differential Equations I: Nonstiff Problems*. Springer-Verlag, Berlin, Heidelberg, 1993.

[62] Daniel F. Harlacher, Harald Klimach, Sabine Roller, Christian Siebert, and Felix Wolf. Dynamic load balancing for unstructured meshes on space-filling curves. In *Parallel and Distributed Processing Symposium Workshops & PhD Forum (IPDPSW), 2012 IEEE 26th International*, pages 1661–1669. IEEE, 2012.

[63] Ami Harten. High resolution schemes for hyperbolic conservation laws. *Journal of computational physics*, 49(3):357–393, 1983.

[64] Ami Harten, Bjorn Engquist, Stanley Osher, and Sukumar R. Chakravarthy. Uniformly high order accurate essentially non-oscillatory schemes, III. In *Upwind and high-resolution schemes*, pages 218–290. Springer, 1987.

[65] Amiram Harten. On the symmetric form of systems of conservation laws with entropy. *Journal of Computational Physics*, 49:151–164, 1983.

[66] Ralf Hartmann. Adaptive discontinuous Galerkin methods with shock-capturing for the compressible Navier-Stokes equations. *International Journal for Numerical Methods in Fluids*, 51(9-10):1131–1156, 2006.

[67] J.S. Hesthaven and T. Warburton. *Nodal Discontinuous Galerkin Methods: Algorithms, Analysis, and Applications*. Springer, 2008.

[68] Florian Hindenlang, Marvin Bohm, Andrew R. Winters, and Gregor J. Gassner. An entropy stable nodal discontinuous Galerkin method for the resistive MHD equations. Part II: Efficient implementation and applications (working title). 2019.

[69] Florian Hindenlang, Thomas Bolemann, and Claus-Dieter Munz. Mesh curving techniques for high order discontinuous Galerkin simulations. In *IDIHOM: Industrialization of High-Order Methods-A Top-Down Approach*, pages 133–152. Springer, 2015.

[70] Florian Hindenlang, Gregor J. Gassner, Christoph Altmann, Andrea Beck, Marc Staudenmaier, and Claus-Dieter Munz. Explicit discontinuous Galerkin methods for unsteady problems. *Computers and Fluids*, 61(0):86 – 93, 2012.

[71] Florian Hindenlang, Eric Sonnendrücker, and Matthias Hölzl. A parallel 3D discontinuous Galerkin framework for nonlinear resistive MHD simulations in Tokamak and stellerator geometries. In *43rd EPS Conference on Plasma Physics*. European Physical Society, 2016.

[72] Thomas J.R. Hughes, L.P. Franca, and M. Mallet. A new finite element formulation for computational fluid dynamics: I. Symmetric forms of the compressible Euler and Navier-Stokes equations and the second law of thermodynamics. *Computer Methods in Applied Mechanics and Engineering*, 54(2):223–234, 1986.

[73] Farzad Ismail and Philip L. Roe. Affordable, entropy-consistent Euler flux functions II: Entropy production at shocks. *Journal of Computational Physics*, 228(15):5410–5436, 2009.

[74] Antony Jameson, Wolfgang Schmidt, and Eli Turkel. Numerical solution of the Euler equations by finite volume methods using Runge Kutta time stepping schemes. In *14th fluid and plasma dynamics conference*, page 1259, 1981.

[75] P. Janhunen. A positive conservative method for magnetohydrodynamics based on HLL and Roe methods. *Journal of Computational Physics*, 160(2):649–661, 2000.

[76] Christopher A. Kennedy and Andrea Gruber. Reduced aliasing formulations of the convective terms within the Navier-Stokes equations for a compressible fluid. *Journal of Computational Physics*, 227:1676–1700, 2008.

[77] R.M. Kirby and S.J. Sherwin. Aliasing errors due to quadratic nonlinearities on triangular spectral h/p element discretisations. *JOURNAL OF ENGINEERING MATHEMATICS*, 56:273–288, 2006.

[78] Christian Klingenberg. Numerical methods for astrophysics. In *Handbook of Numerical Analysis*, volume 18, pages 465–477. Elsevier, 2017.

[79] Christian Klingenberg, Frank Pörner, and Yinhua Xia. An efficient implementation of the divergence free constraint in a discontinuous Galerkin method for magnetohydrodynamics on unstructured meshes. *Communications in Computational Physics*, 21(2):423–442, 2017.

13

[80] David A. Kopriva. Metric identities and the discontinuous spectral element method on curvilinear meshes. *The Journal of Scientific Computing*, 26(3):301–327, March 2006.

[81] David A. Kopriva. *Implementing Spectral Methods for Partial Differential Equations*. Scientific Computation. Springer, May 2009.

[82] David A. Kopriva. A polynomial spectral calculus for analysis of DG spectral element methods. *ArXiv e-prints arXiv:1704.00709*, 2017.

[83] David A. Kopriva and Gregor J. Gassner. Geometry effects in nodal discontinuous Galerkin methods on curved elements that are provably stable. *Applied Mathematics and Computation*, 272, Part 2:274 – 290, 2016.

[84] David A. Kopriva and Edwin Jimenez. An assessment of the efficiency of nodal discontinuous Galerkin spectral element methods. In *Recent Developments in the Numerics of Nonlinear Hyperbolic Conservation Laws*, pages 223–235. Springer, 2013.

[85] David A. Kopriva, Andrew R. Winters, Marvin Bohm, and Gregor J. Gassner. A provably stable discontinuous Galerkin spectral element approximation for moving hexahedral meshes. *Computers & Fluids*, 139:148–160, 2016.

[86] Henry P. Kramer and Judith B. Bruckner. Iterations of a non-linear transformation for enhancement of digital images. *Pattern recognition*, 7(1-2):53–58, 1975.

[87] Stanislav N. Kružkov. First order quasilinear equations in several independent variables. *Mathematics of the USSR-Sbornik*, 10(2):217, 1970.

[88] Pijush K. Kundu, Ira M. Cohen, and D. W. Dowling. *Fluid Mechanics 4th*. Elsevier, Oxford, 2008.

[89] L. D. Landau. *Fluid Mechanics*, volume 6. Pergamon, 1 1959.

[90] Peter D. Lax. Hyperbolic systems of conservation laws II. *Communications on pure and applied mathematics*, 10(4):537–566, 1957.

[91] Peter D. Lax. *Hyperbolic systems of conservation laws and the mathematical theory of shock waves*, volume 11. SIAM, 1973.

[92] Peter D. Lax and Burton Wendroff. Systems of conservation laws. *Communications on Pure and Applied mathematics*, 13(2):217–237, 1960.

[93] E. Lee, M. E. Brachet, A. Pouquet, P. D. Mininni, and D. Rosenberg. Paradigmatic flor for small-scale magnetohydrodynamics: Properties of the ideal case and collision of current sheets. *Physical Review E*, 78(6):066401, 2008.

[94] E. Lee, M. E. Brachet, A Pouquet, P. D. Mininni, and D. Rosenberg. Lack of universality in decaying magnetohydrodynamic turbulence. *Physical Review E*, 81(1):016318, 2010.

[95] Randall J. LeVeque. *Numerical Methods for Conservation Laws*. Birkhäuser, 2nd edition, 1992.

[96] Randall J. LeVeque. *Finite volume methods for hyperbolic problems*, volume 31. Cambridge university press, 2002.

[97] Yong Liu, Chi-Wang Shu, and Mengping Zhang. Entropy stable high order discontinuous Galerkin methods for ideal compressible MHD on structured meshes. *Journal of Computational Physics*, 354:163–178, 2017.

[98] Robert W. MacCormack. The effect of viscosity in hypervelocity impact cratering. In *Frontiers of Computational Fluid Dynamics 2002*, pages 27–43. World Scientific, 2002.

[99] Maxima. Maxima, a computer algebra system. version 5.38.1, 2016.

[100] Marshal L. Merriam. *An entropy-based approach to nonlinear stability*. NASA Technical Memorandum, 1989.

[101] Hanieh Mirzaee, Liangyue Ji, Jennifer K. Ryan, and Robert M. Kirby. Smoothness-increasing accuracy-conserving (SIAC) postprocessing for discontinuous Galerkin solutions over structured triangular meshes. *SIAM Journal on Numerical Analysis*, 49(5):1899–1920, 2011.

[102] Michael S. Mock. Systems of conservation laws of mixed type. *Journal of Differential Equations*, 37(1):70–88, 1980.

[103] V.M. Nakariakov, L. Ofman, E.E. DeLuca, B. Roberts, and J.M. Davila. TRACE observation of damped coronal loop oscillations: Implications for coronal heating. *Science*, 285(5429):862–864, 1999.

[104] F.M. Neubauer. Nonlinear standing Alfvén wave current system at Io: Theory. *Journal of Geophysical Research: Space Physics*, 85(A3):1171–1178, 1980.

[105] Steven A. Orszag and Cha-Mei Tang. Small-scale structure of two-dimensional magnetohydrodynamic turbulence. *Journal of Fluid Mechanics*, 90(01):129–143, 1979.

[106] Per-Olof Persson and Jaime Peraire. Sub-cell shock capturing for discontinuous Galerkin methods. In *44th AIAA Aerospace Sciences Meeting and Exhibit*, page 112, 2006.

[107] Benoit Perthame and Chi-Wang Shu. On positivity preserving finite volume schemes for Euler equations. *Numerische Mathematik*, 73(1):119–130, 1996.

[108] Sergio Pirozzoli. Numerical methods for high-speed flows. *Annual Review of Fluid Mechanics*, 43:163–194, 2011.

[109] Kenneth G. Powell, Philip L. Roe, Timur J. Linde, Tamas I. Gombosi, and Darren L. De Zeeuw. A solution-adaptive upwind scheme for ideal magnetohydrodynamics. *Journal of Computational Physics*, 154(2):284–309, 1999.

[110] William H. Reed and T.R. Hill. Triangular mesh methods for the neutron transport equation. Technical report, Los Alamos Scientific Lab., N. Mex.(USA), 1973.

[111] Paul Harry Roberts. *An introduction to magnetohydrodynamics*, volume 6. Longmans London, 1967.

[112] P. L. Roe and D. S. Balsara. Notes on the eigensystem of magnetohydrodynamics. *SIAM Journal on Applied Mathematics*, 56(1):57–67, 1996.

[113] James A. Rossmanith. High-order discontinuous Galerkin finite element methods with globally divergence-free constrained transport for ideal MHD. *ArXiv e-prints: arXiv:1310.4251*, 2013.

[114] Viktor Vladimirovich Rusanov. The calculation of the interaction of non-stationary shock waves with barriers. *Zhurnal Vychislitel'noi Matematiki i Matematicheskoi Fiziki*, 1(2):267–279, 1961.

[115] Jennifer K. Ryan, Xiaozhou Li, Robert M. Kirby, and Kees Vuik. One-sided position-dependent smoothness-increasing accuracy-conserving (SIAC) filtering over uniform and non-uniform meshes. *Journal of Scientific Computing*, 64(3):773–817, 2015.

[116] Joachim Saur, Fritz M. Neubauer, J.E.P. Connerney, Philippe Zarka, and Margaret G. Kivelson. Plasma interaction of Io with its plasma torus. *Jupiter: The Planet, Satellites and Magnetosphere*, 1:537–560, 2004.

[117] Joachim Saur, Fritz M. Neubauer, and Nico Schilling. Hemisphere coupling in Enceladus' asymmetric plasma interaction. *Journal of Geophysical Research: Space Physics*, 112(A11), 2007.

[118] Joachim Saur, Fritz M. Neubauer, Darrell F. Strobel, and Michael E. Summers. Three-dimensional plasma simulation of Io's interaction with the Io plasma torus: Asymmetric plasma flow. *Journal of Geophysical Research: Space Physics*, 104(A11):25105–25126, 1999.

[119] Kevin Schaal, Andreas Bauer, Praveen Chandrashekar, Rüdiger Pakmor, Christian Klingenberg, and Volker Springel. Astrophysical hydrodynamics with a high-order discontinuous Galerkin scheme and adaptive mesh refinement. *Monthly Notices of the Royal Astronomical Society*, 453(4):4278–4300, 2015.

[120] Chi-Wang Shu. Essentially non-oscillatory and weighted essentially non-oscillatory schemes for hyperbolic conservation laws. In *Advanced numerical approximation of nonlinear hyperbolic equations*, pages 325–432. Springer, 1998.

[121] Chi-Wang Shu. High-order finite difference and finite volume WENO schemes and discontinuous Galerkin methods for CFD. *International Journal of Computational Fluid Dynamics*, 17(2):107–118, 2003.

[122] Chi-Wang Shu and Stanley Osher. Efficient implementation of essentially non-oscillatory shock-capturing schemes. *Journal of computational physics*, 77(2):439–471, 1988.

[123] Sven Simon, Joachim Saur, Shari C. Treeck, Hendrik Kriegel, and Michele K. Dougherty. Discontinuities in the magnetic field near Enceladus. *Geophysical Research Letters*, 41(10):3359–3366, 2014.

[124] Björn Sjögreen, Helen C. Yee, and Dmitry Kotov. Skew-symmetric splitting and stability of high order central schemes. *Journal of Physics: Conference Series*, 837(1), 2017.

[125] Jean-Piero Suarez and Gustaaf B. Jacobs. Regularization of singularities in the weighted summation of Dirac-delta functions for the spectral solution of hyperbolic conservation laws. *Journal of Scientific Computing*, 72(3):1080–1092, 2017.

[126] Eitan Tadmor. Skew-selfadjoint form for systems of conservation laws. *Journal of Mathematical Analysis and Applications*, 103(2):428–442, 1984.

[127] Eitan Tadmor. Entropy functions for symmetric systems of conservation laws. *Journal of Mathematical Analysis and Applications*, 122(2):355–359, 1987.

[128] Eitan Tadmor. The numerical viscosity of entropy stable schemes for systems of conservation laws. *Mathematics of Computation*, 49(179):91–103, 1987.

[129] Eitan Tadmor. Entropy stability theory for difference approximations of nonlinear conservation laws and related time-dependent problems. *Acta Numerica*, 12:451–512, 5 2003.

[130] Eitan Tadmor. Perfect derivatives, conservative differences and entropy stable computation of hyperbolic conservation laws. *Discrete and Continuous Dynamical Systems-A*, 36(8):4579–4598, 2016.

[131] G. I. Taylor and A. E. Green. Mechanism of the production of small eddies from large ones. *Proceedings of the Royal Society of London (A)*, 158(895):499–521, 1937.

[132] Eleuterio F. Toro. *Riemann solvers and numerical methods for fluid dynamics: A practical introduction*. Springer Science & Business Media, 2013.

[133] Gábor Tóth. The $\nabla \cdot B = 0$ Constraint in Shock-Capturing Magnetohydrodynamics Codes. *Journal of Computational Physics*, 161(2):605 – 652, 2000.

[134] Terrence S. Tricco and Daniel J. Price. Constrained hyperbolic divergence cleaning for smoothed particle magnetohydrodynamics. *Journal of Computational Physics*, 231(21):7214 – 7236, 2012.

[135] Paulien van Slingerland, Jennifer K. Ryan, and Cornelis Vuik. Position-dependent smoothness-increasing accuracy-conserving (SIAC) filtering for improving discontinuous Galerkin solutions. *SIAM Journal on Scientific Computing*, 33(2):802–825, 2011.

[136] John Von Neumann and Robert D. Richtmyer. A method for the numerical calculation of hydrodynamic shocks. *Journal of applied physics*, 21(3):232–237, 1950.

[137] Knut Waagan. A positive MUSCL-Hancock scheme for ideal magnetohydrodynamics. *Journal of Computational Physics*, 228(23):8609–8626, 2009.

[138] T. C. Warburton and G. E. Karniadakis. A discontinuous Galerkin method for the viscous MHD equations. *Journal of Computational Physics*, 152:608–641, 1999.

[139] Niklas Wintermeyer, Andrew R. Winters, Gregor J. Gassner, and David A. Kopriva. An entropy stable discontinuous Galerkin method for the two dimensional shallow water equations with discontinuous bathymetry. *Journal of Computational Physics*, 340:200–242, 2017.

[140] Andrew R. Winters. *Discontinuous Galerkin spectral element approximations for the reflection and transmission of waves from moving material interfaces*. PhD thesis, The Florida State University, 2014.

[141] Andrew R. Winters and Gregor J. Gassner. Affordable, Entropy Conserving and Entropy Stable Flux Functions for the Ideal MHD Equations. *Journal of Computational Physics*, 304:72–108, 2016.

[142] Andrew R. Winters and David A. Kopriva. High-order local time stepping on moving DG spectral element meshes. *Journal of Scientific Computing*, 58(1):176–202, 2014.

[143] B.W. Wissink, G.B. Jacobs, J.K. Ryan, W.S. Don, and E.T.A. van der Weide. Shock regularization with smoothness-increasing accuracy-conserving Dirac-delta polynomial kernels. *Journal of scientific computing*, 77:579–596, 2018.

[144] Leslie Colin Woods. *An introduction to the kinetic theory of gases and magneto-plasmas*. Oxford University Press, 1993.

[145] Kailiang Wu and Chi-Wang Shu. A provably positive discontinuous Galerkin method for multidimensional ideal magnetohydrodynamics. *SIAM Journal on Scientific Computing*, 40(5):B1302–B1329, 2018.

[146] Xiangxiong Zhang and Chi-Wang Shu. On positivity-preserving high order discontinuous Galerkin schemes for compressible Euler equations on rectangular meshes. *Journal of Computational Physics*, 229(23):8918–8934, 2010.

List of Tables

List of Figures

Erklärung

Ich versichere, dass ich die von mir vorgelegte Dissertation selbständig angefertigt, die benutzten Quellen und Hilfsmittel vollständig angegeben und die Stellen der Arbeit - einschließlich Tabellen, Karten und Abbildungen -, die anderen Werken im Wortlaut oder dem Sinn nach entnommen sind, in jedem Einzelfall als Entlehnung kenntlich gemacht habe; dass diese Dissertation noch keiner anderen Fakultät oder Universität zur Prüfung vorgelegen hat; dass sie - abgesehen von unten angegebenen Teilpublikationen - noch nicht veröffentlicht worden ist, sowie, dass ich eine solche Veröffentlichung vor Abschluss des Promotionsverfahrens nicht vornehmen werde. Die Bestimmungen der Promotionsordnung sind mir bekannt. Die von mir vorgelegte Dissertation ist von Prof. Dr. Gregor Gassner betreut worden.

Köln, den 25.02.2019

_____

(Marvin Bohm)

Curriculum Vitae

Persönliche Daten:

Name	Marvin Bohm
Geburtstag	23.05.1988
Geburtsort	Bielefeld, Deutschland
Nationalität	Deutsch

Bildungsweg:

2014-2019	Promotionsstudium in Mathematik Universität zu Köln
2011-2014	Masterstudium in Wirtschaftsmathematik Universität zu Köln
2008-2011	Bachelorstudium in Wirtschaftsmathematik Universität zu Köln
1998-2007	Gymnasiales Abitur Helmholtz-Gymnasium Bielefeld

Köln, den 25.02.2019

_____

(MARVIN BOHM)

Publikationsliste

Verzeichnis veröffentlichter Wissenschaftlicher Arbeiten

1. An entropy stable nodal discontinuous Galerkin method for the resistive MHD equations. Part I: Theory and Numerical Verification (submittiert an Journal of Computational Physics) [16]

2. Ideal GLM-MHD: About the entropy consistent nine-wave magnetic field divergence diminishing ideal magnetohydrodynamics equations (publiziert im Journal of Computational Physics) [34]

3. A Provably Stable Discontinuous Galerkin Spectral Element Approximation for Moving Hexahedral Meshes (publiziert in Computers & Fluids) [85]

4. An entropy stable nodal discontinuous Galerkin method for the resistive MHD equations. Part II: Efficient implementation and applications (Arbeitstitel, in Entwicklung) [68]

5. Multi-element SIAC filter for shock capturing applied to high-order discontinuous Galerkin spectral element methods (Arbeitstitel, in Entwicklung) [15]

Köln, den 25.02.2019

_____

(Marvin Bohm)